Proximity-induced spin-orbit and exchange coupling in van der Waals heterostructures

Dissertation zur Erlangung des Doktorgrades
der Naturwissenschaften (Dr. rer. nat.)
der Universität Regensburg
der Fakultät für Physik

vorgelegt im Jahr 2020 von

Klaus Zollner

geboren am 31.10.1991 in Bogen

Promotionsgesuch eingereicht am: *07.10.2020*
Die Arbeit wurde angeleitet von: *Prof. Dr. Jaroslav Fabian*

Prüfungsausschuss:
Vorsitzender: *Prof. Dr. Vladimir Braun*
1. Gutachter: *Prof. Dr. Jaroslav Fabian*
2. Gutachter: *PD Dr. Jonathan Eroms*
Weiterer Prüfer: *Prof. Dr. Andrea Donarini*

Termin Promotionskolloquium: *26.01.2021*

Abstract

Two-dimensional materials and their van der Waals heterostructures offer unforeseen potential for electronics and spintronics. At present, the available two-dimensional material repertoire covers semiconductors, ferromagnets, superconductors, and topological insulators, which already feature highly interesting physics. Remarkably, one can manipulate the properties of a two-dimensional material by proximity effects, while still preserving a great degree of its own autonomy. The ability to control and modify the electronic, spin, and optical properties of two-dimensional materials is extremely valuable for investigating novel physical phenomena, as well as a potential knob for device applications. In this thesis, we investigate graphene, bilayer graphene, and transition-metal dichalcogenides in proximity to various two-dimensional materials. We quantify the spin-orbit and magnetic proximity effects by fitting suitable model Hamiltonians, which capture the relevant low energy electronic and spin properties, to realistic first-principles calculations. As we show, the obtained results can be used for calculating charge and spin transport or optical properties, and are vital for the interpretation of experiments.

Zusammenfassung

Zweidimensionale Materialien und ihre van der Waals Heterostrukturen bieten unvorhergesehene Möglichkeiten für konventionelle und spin-basierte Elektronik. Momentan stehen viele verschiedene zweidimensionale Materialien zur Verfügung, wie zum Beispiel Halbleiter, Ferromagnete, Supraleiter und topologische Isolatoren, welche bereits selbst außerordentliche physikalische Eigenschaften besitzen. Erstaunlicherweise lassen sich diese Eigenschaften von zweidimensionalen Materialen durch sogenannte Näherungseffekte manipulieren. Dadurch, dass man die intrinsischen elektronischen, spin-basierten und optischen Eigenschaften kontrolliert verändern kann, eröffnen sich neue Möglichkeiten für Forschung und Industrie. In dieser Dissertation untersuchen wir Ein- und Zweischicht Graphen, sowie Übergangsmetall-Dichalkogenide, welche durch Näherungseffekte, ausgehend von verschiedensten anderen zweidimensionalen Materialien, beinflusst werden. Wir berechnen dafür die Bandstrukturen für eine Reihe von interessanten van der Waals Heterostrukturen mit Hilfe von Dichtefunktionaltheorie. Die Spin-Bahn-Kopplung und magnetischen Näherungseffekte werden näher charakterisiert, indem wir die relevanten Energiebänder der Bandstruktur durch geeignete Modelle und passende Parameter beschreiben. Wir zeigen, dass die daraus resultierenden Modellbeschreibungen verwendet werden können, um sowohl Spin- und Ladungstransport, als auch optische Eigenschaften zu berechnen, was wiederum essentiell ist, um experimentelle Ergebnisse zu interpretieren.

Contents

Part I Motivation and Overview 1

1 Spintronics . . . 3

2 2D materials and van der Waals heterostructues . . . 9

Part II Graphene 19

3 The basics of monolayer graphene . . . 21
- 3.1 Unit cell, Brillouin zone, and band structure . . . 21
- 3.2 Hamiltonian of spin-orbit and exchange proximitized graphene . . . 23
- 3.3 Band structure topologies of proximitized graphene . . . 26

4 Spin relaxation anisotropy in graphene/hBN structures . . . 29
- 4.1 Introduction . . . 29
- 4.2 Geometry, computational details, and band structure . . . 31
- 4.3 Graphene on hBN . . . 34
  - 4.3.1 Low energy bands . . . 34
  - 4.3.2 Distance study . . . 36
  - 4.3.3 Transverse electric field . . . 38
  - 4.3.4 Spin relaxation anisotropy . . . 40
- 4.4 hBN encapsulated graphene . . . 44
  - 4.4.1 Low energy bands . . . 44
  - 4.4.2 Transverse electric field . . . 47
  - 4.4.3 Spin relaxation anisotropy . . . 48
- 4.5 Summary and conclusion . . . 49

5 Proximity spin-orbit coupling in graphene on Bi_2Se_3 . . . 51
- 5.1 Introduction . . . 51
- 5.2 Geometry and computational details . . . 53
- 5.3 Band structures and fit results . . . 54
- 5.4 Transverse electric field . . . 58
- 5.5 Distance study . . . 59
- 5.6 Different topological insulators . . . 61
- 5.7 Summary and conclusion . . . 62

6 Proximity exchange in graphene on $MnPSe_3$ . . . 63
6.1 Introduction . . . 63
6.2 Computational details and geometry . . . 65
6.3 Band structure and fit results . . . 66
6.4 Summary and conclusion . . . 71

Part III Bilayer graphene 73

7 The basics of bilayer graphene . . . 75
7.1 Unit cell, Brillouin zone, and band structure . . . 75
7.2 Hamiltonian of spin-orbit and exchange proximitized bilayer graphene . . . 77
7.3 Band structure topologies of proximitized bilayer graphene . . . 78

8 Heterostructures of bilayer graphene, WS_2, and $Cr_2Ge_2Te_6$ . . . 81
8.1 Introduction . . . 81
8.2 Computational details . . . 83
8.3 Exchange valve in bilayer graphene on $Cr_2Ge_2Te_6$ . . . 83
8.4 Spin-orbit valve in bilayer graphene on WS_2 . . . 88
8.5 Doubly proximitized bilayer graphene . . . 90
8.6 Summary and conclusion . . . 94

Part IV Transition-Metal Dichalcogenides 95

9 The basics and strain effects of TMDCs . . . 97
9.1 Introduction . . . 97
9.2 Geometry, band structure, and model Hamiltonian . . . 99
9.3 Strain effects on orbital and spin-orbit properties . . . 103
9.4 Strain tunable optical transitions . . . 106
9.5 Summary and conclusion . . . 108

10 Proximity exchange effects in $MoSe_2$ and WSe_2 on CrI_3 . . . 111
10.1 Introduction . . . 111
10.2 Geometry and computational details . . . 114
10.3 Band structure and twist effects . . . 116
10.4 Short-rangeness of proximity effects . . . 120
10.5 Gate tunable proximity exchange and valley splitting . . . 123
10.6 Summary and conclusion . . . 125

Part V Summary and Outlook 127

11 Recapitulation . . . 129

12 Novel 2D materials . . . 133

Part VI Appendix 137

A Supplementary Material . . . 139
A.1 Supporting Information for chapter 6 . . . 139
A.2 Supporting Information for chapter 8 . . . 140
A.3 Supporting Information for chapter 9 . . . 144

B Employed program packages . . . 147

Acronyms . . . 149

References . . . 151

List of Publications . . . 179

Acknowledgments . . . 181

PART I

Motivation and Overview

CHAPTER 1

Spintronics

What is spintronics?

Conventional electronics is based on the *charge* degree of freedom of the electron. Any information can be encoded into two discrete binary states, 1 and 0, represented by a finite or absent flow of charge in an electronic circuit. In contrast, modern spintronics [1–4] is based on another degree of freedom of the electron: *the spin*. The two degrees of freedom, charge and spin of the electron, are linked and cannot be directly decoupled from each other. Imagine the electron as a tiny charged sphere that can rotate either clockwise or counter-clockwise around its own axis, while moving in the Coulomb field of the atomic nuclei. This intrinsic rotational sense of the electron is called spin, which can be either *up* or *down* with respect to the chosen quantization axis, usually the z one. Similarly, the earth is rotating around its own axis while moving in the gravitational field of the sun. However, *spin* is of purely quantum mechanical nature, while the rotating earth can be described by classical physics. Binary data, 1 and 0, can now be encoded in those two spin states, up and down, similarly to the presence or absence of charge in electronics. We can measure the spin, because it is associated with a magnetic moment of a rotating charge. Some materials, such as cobalt, nickel, and iron are magnetic, because enough electron spins are aligned (rotate in the same direction), generating a global magnetization.

The field of spintronics rooted in the early 1920s, when O. Stern and W. Gerlach first demonstrated the quantization of the atomic magnetic moment in a magnetic field [5]. Only a few years later, W. Pauli formulated the quantum mechanical description of the electron's spin with the help of simple matrices [6]. When people then started to study spin-polarized transport, they found out that electrons of majority and minority spin flow rather independently in a ferromagnet [7, 8], and charge currents can be spin-polarized. A major role in the understanding of spin-polarized transport is attributed to tunneling experiments through metal/ferromagnetic insulator (FMI)/metal junctions [9]. An unpolarized current can become spin-polarized when passing through the FMI tunnel layer, as proven by the magnetic field dependence of the current-voltage characteristics [10–12]. Experimentalists also studied ferromagnet/insulator/superconductor [13, 14] and ferromagnet/insulator/ferromagnet junctions, and M. Julliére was able to derive a formula for the tunneling magnetoresitance (TMR), which depends on the spin polarization of the ferromagnets [15]. In a ferromagnet/insulator/ferromagnet junction, the relative direction of the two magnetizations affects tunneling, founding the basis of the spin-valve effect, see Fig. 1.1. A subsequent major discovery, that was awarded with the Nobel Prize [16] and revolutionized hard disk technology, is the giant magnetoresitance (GMR) effect [17–19]. In ferromagnet/metal/ferromagnet junctions, parallel and antiparallel aligned ferromagnets lead to significantly different resistances when passing a current through the junction. For TMR and GMR, the magnetization switching of the ferromagnet is therefore essential to control the flow of spin-polarized currents. Also the reverse process is possible: a spin-polarized current can switch the magnetization of a ferromagnet, due to transfer of angular momentum. This effect is known as the spin-transfer torque (STT) [20].

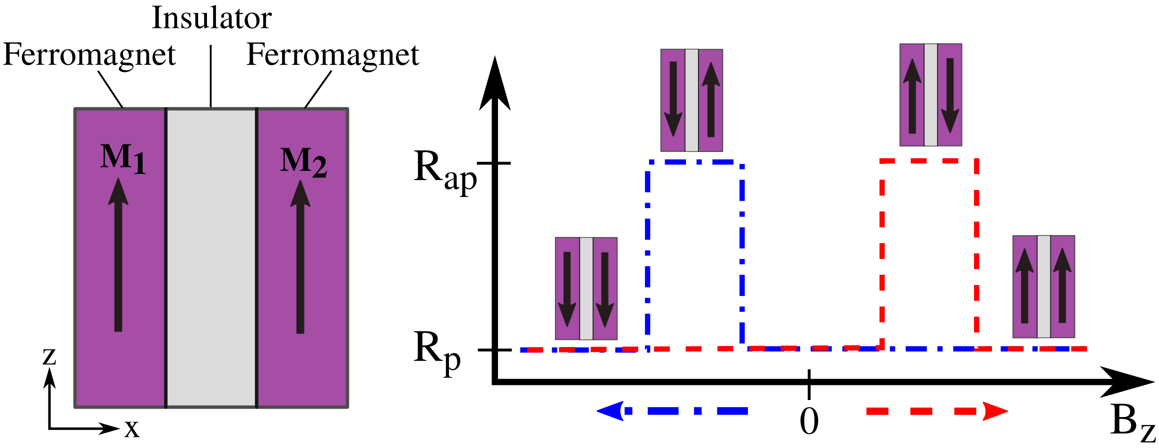

Figure 1.1: Left: Schematic structure employed for the TMR effect, consisting of two ferromagnetic layers separated by an insulating tunnel barrier. The magnetizations M_1 and M_2 of the two ferromagnets are aligned parallel, but can be switched with an external magnetic field B_z along the z axis. Right: The tunneling resistance as function of the magnetic field B_z (red = up-sweep, blue = down-sweep), when current is injected along the x axis across the ferromagnet/insulator/ferromagnet junction. For parallel M_1 and M_2, the junction resistance is low (R_p), while for antiparallel alignment, the resistance is high (R_ap), due to spin-dependent electron tunneling and scattering. The relative resistance change is given by $(R_\mathrm{ap} - R_\mathrm{p})/R_\mathrm{p}$ and defines the efficiency of the TMR effect.

Applications and challenges of spintronics

In electronic devices, e. g., personal computers, millions of transistors are responsible for logic operations, which require special semiconducting materials that control the charge flow. In spintronics, we actually do not need these specially designed materials, as spin can be measured by common ferromagnets and metals. People also argue that the power consumption is much lower in spintronics [21]. By applying electric fields, the magnetization, or equivalently the spin polarization can be changed quite easily, while in electronics a lot of power is consumed by maintaining the charge flow. Additionally, the switching rates for spin states are very high. Because *spin* is an intrinsic property of the electron and not energy dependent, spins can in principle maintain their direction, even after shutdown of the power source. Especially this last property is important for the design of novel nonvolatile memory devices, where the information could be practically stored forever without power consumption. However, these considerations are very idealistic. For example, spins will always interact with their surroundings, especially in solid media, such that scattering leads to the loss of the spin information. In addition, the amount of energy to generate and maintain the spin dependent properties of a device might overcome the low power consumption needed for the actual spin operations. Moreover, to master the mentioned obstacles for spintronics, we are also bound to special materials and novel device designs.

Is spintronics ready for the mass market industry? Certainly, the answer is *Yes!* In 2007, when A. Fert and P. Grünberg received the Nobel Prize for the GMR effect [16], their discovery had entered industry for about 10 years. In 1997, IBM was the first company to implement GMR structures in hard disk read heads [22]. By employing the GMR effect, storage densities were drastically increased, while simultaneously decreasing resistance and thus speeding up the reading and writing processes. The key ingredient for the GMR effect is a ferromagnet/metal/ferromagnet junction. One of these ferromagnets can easily switch its magnetization direction (soft ferromagnet), while the magnetization direction of the other ferromagnet is practically fixed (hard ferromagnet). The bits are stored in magnetic units on rotating disks. When the read head is above a magnetic unit of the disk, the soft ferromagnet adapts its magnetization direction. Whenever the soft ferromagnet switches its magnetization direction, the junction resistance of the read head will drastically change, which can be measured by passing a current across the junction. Similar things hold for the TMR effect, where the metal layer is replaced by a tunneling barrier, see Fig. 1.1. Microscopically, electrons with their spin parallel to the magnetization of the ferromagnet will experience less scattering than electrons with antiparallel spin, leading to giant magnetization dependent differences in resistance. Of course, the efficiency of the GMR effect is a matter of device engineering and the search for optimal material combinations with appropriate thicknesses. The current generation of data storage solutions are based on this magnetic random access memory (MRAM) technology, which employs even more advanced spin-based phenomena, such as the TMR effect, STT, and spin-orbit torque (SOT), leading to even smaller devices with giant storage densities and ultrafast information processing [23]. At this point, two-dimensional (2D) materials enter the game, which are promising for pushing this field to the ultimate limits, regarding size and efficiency.

Despite these very general advantages and first applications, there are also some challenges. The main goal in spintronics is to transport information, represented by the spin of the electron, while optimally no net charge current flows in the transport channel. In order to do so, we need to efficiently generate, inject, on-demand manipulate, and detect the spin information. The injection of spins can be achieved electrically by conventional ferromagnet/insulator tunnel junctions, where the conductivity mismatch plays a major role [24]. Another possibility is the hot-electron spin injection [25] method, which circumvents conductivity mismatch. Spins can be also injected optically in semiconductors [26], employing the difference in the absorption of left- and right-handed circularly polarized light and the special optical selection rules. More advanced spin injection methods are based on spin pumping, driven by magnetization dynamics [27], or by current-induced spin orientation via spin Hall effect (SHE) and spin-orbit interaction [28]. The detection of the spin information is typically just the inverse of one of the injection processes.

Once the spins are injected into the desired material, we need to transport the information that they carry. There are several mechanisms that can influence the spin information and lead to a temporal evolution of the spin density [3], according to

$$\frac{\partial \boldsymbol{s}}{\partial t} = -v_d \nabla \boldsymbol{s} + D\nabla^2 \boldsymbol{s} + \boldsymbol{s} \times \boldsymbol{\omega}_0 - \frac{\boldsymbol{s}}{\tau_s}. \tag{1.1}$$

The four terms correspond to spin drift, diffusion, precession, and relaxation. The final spin density $\boldsymbol{s}(\boldsymbol{r}, t)$ depends then on the initial spin density $s_0(\boldsymbol{r})$, the spin diffusivity D of the system, the drift velocity v_d due to an applied electric field, the precession frequency $\boldsymbol{\omega}_0$ due to an applied magnetic field, and the spin relaxation (SR) via a characteristic lifetime τ_s. As we can see, there are a lot of external influences on the spin density, which are strongly determined by the actual materials that are used. For example, the drift velocity depends on the electron mobility and the actual band structure. The relaxation rate depends on the impurity and doping density, temperature, spin-orbit coupling (SOC), etc. Of course, the individual parameters also mutually influence each other. In the end, everything boils down to find the most adequate material combinations and the optimal settings, suitable to achieve the desired spin transport qualities, while simultaneously maintaining an efficient way to control the spin information. However, this is a highly nontrivial task and a lot of efforts are necessary to bridge the gap between the basic idea and final mass market devices.

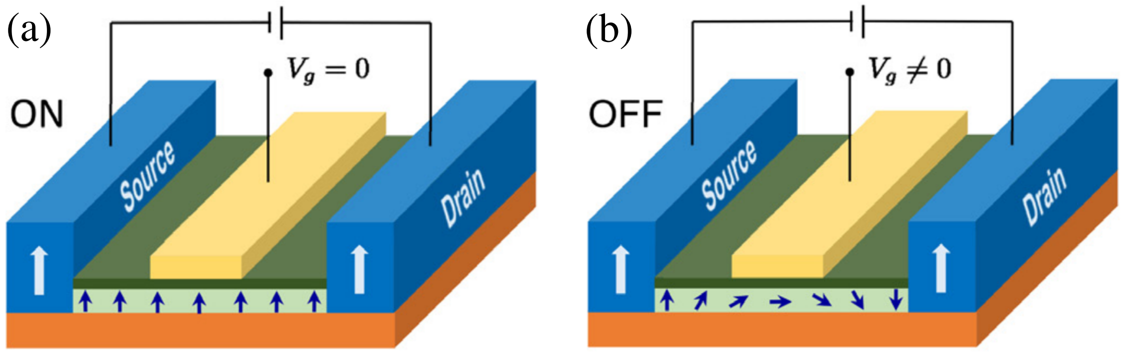

Figure 1.2: Schematics of the Datta-Das spin field-effect transistor (FET) [29]. Source and drain ferromagnetic contacts with parallel magnetizations are used to inject and detect the spins (small arrows). The transport in the 2D electron gas channel depends on the precession of the electron spins, which is due to SOC, i. e., an effective magnetic field. The SOC in the channel can be manipulated with a gate voltage V_g. (a) In the ON state, when there is no gate voltage applied, spins experience no precession and keep their original alignment. The current is large. (b) In the OFF state, spins precess and have opposite alignment compared to the ferromagnetic drain contact. The current is small. Figures are from Ref. [30].

A particular example of this is the still elusive Datta-Das spin FET, shown in Fig. 1.2, which has been proposed 30 years ago [29]. The basic idea is to inject spin polarized electrons from the ferromagnetic source contact into a, for example, 2D electron gas formed at a GaAs/AlGaAs interface. The electrons flow ballistically along the transport channel and arrive at the ferromagnetic drain contact. Depending on the orientation of the electron spin with respect to the drain contact magnetization, they can either enter the contact or not, i. e., current flows or not. The gate voltage V_g is responsible for generating an effective magnetic field in the transport channel, which is due to SOC and leads to precession of the spins. Depending on the gate voltage, precession and consequently the current flow can be turned on and off.

The current generation of spintronics devices employs hybrid geometries consisting of several ultrathin 2D materials in order to overcome intrinsic limitations of the transport medium via proximity effects. For example, the previously introduced concept of the spin FET can be potentially realized in a bilayer graphene (BLG)/transition-metal dichalcogenide (TMDC) heterostructure [31]. In addition, TMR structures have been investigated, which exclusively consist of 2D materials and show giant efficiencies [32]. As a result, a new branch of condensed matter physics has emerged, which is solely dedicated to the interface and band structure engineering of 2D layers. In this context, also new subfields such as straintronics, valleytronics, and optospintronics have emerged, where additional control possibilities and degrees of freedom enter the game. The ability to precisely control and modify the electronic, spin, and optical properties of materials would be extremely valuable for investigating novel physical phenomena, as well as a potential knob for device applications. In this thesis, we consider several such 2D material heterostructures and analyze the proximity effects, always with regard to possible spintronics applications. In the next chapter, we will first introduce 2D materials and van der Waals (vdW) heterostructures, and summarize some application prospects.

CHAPTER 2

2D materials and van der Waals heterostructues

What are 2D materials?

In solid state theory, one typically deals with crystals that have finite extensions along all three spatial directions. Such materials, where the electronic motion is unconfined within the crystal, is called three-dimensional (3D) or commonly termed *bulk*. Even if the material is only a micrometer in size, we still call it a bulk crystal because the spatial extensions along all directions x_i of the crystal are much larger than the thermal de Broglie wavelength $\lambda = \sqrt{2\pi\hbar^2/mk_BT}$ of the electron ($\lambda \approx 4.3$ nm for $T = 300$ K). Consequently, electrons will effectively not feel the surface boundary of such a bulk crystal. Conversely, this means that if the motion of the electron is spatially confined, we talk about *quantum confinement* and new physical phenomena can appear [33]. A very general classification of crystals can be done via their dimensionality.

If we confine the electronic motion within a layer with thickness $d < \lambda$, for example by thinning down a material, we get a two-dimensional (2D) system. A typical example for quantum confinement in 2D is a AlGaAs/GaAs/AlGaAs heterostructure. If the central GaAs region is thin enough, we speak of a *quantum well*, where the electronic and optical properties can be strongly altered compared to the bulk GaAs crystal. In this scenario, the confinement is due to the potential well that forms in the GaAs layer because of the surrounding AlGaAs layers. Similarly, one can apply confinement along two spatial dimensions and we end up with a one-dimensional system, a so-called *quantum wire*. It is even possible to confine electrons in all three spatial dimensions and the system is then zero-dimensional. Such a zero-dimensional system is called *quantum dot*, which can be regarded as an artificial atom with discrete energy levels. Nowadays, when we speak of 2D materials, we actually mean true monolayers of a crystal. Their bulk materials are formed by individual ultrathin layers that are held together by weak van der Waals (vdW) forces. These monolayers have interesting physical properties and can even be combined in a lego-like fashion in vdW heterostructures [34].

The most prominent and prototypical example of a 2D material is graphene. It is a single layer of carbon atoms that are arranged in a honeycomb lattice [35, 36]. Consequently, it is the ultimate limit that can be reached for quantum confinement because the thickness of graphene equals the size of an atom. Remarkably, graphene displays extraordinary properties [37, 38], such as giant mobility, mechanical robustness, optical transparency, and much more. Therefore, it is applicable in several devices in diverse fields, such as chemical sensors [39] and flexible electronics [40]. If we replace the carbon atoms in graphene by boron and nitrogen atoms, we get its insulating "analog" hexagonal boron nitride (hBN) [38]. hBN is a wide band gap insulator and, due to its chemical inertness, it is frequently used as encapsulation material for other 2D materials to protect them from the environment and degradation [41].

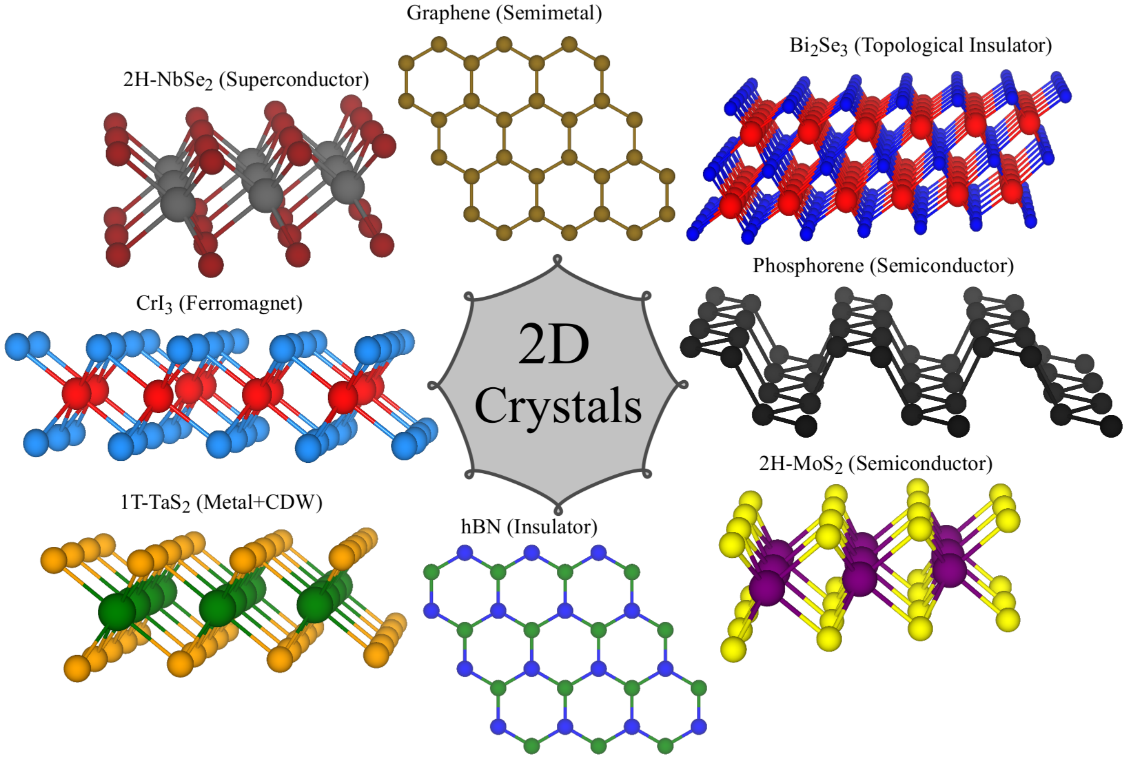
Graphene (Semimetal)
Bi_2Se_3 (Topological Insulator)
2H-$NbSe_2$ (Superconductor)
Phosphorene (Semiconductor)
CrI_3 (Ferromagnet)
2D Crystals
2H-MoS_2 (Semiconductor)
1T-TaS_2 (Metal+CDW)
hBN (Insulator)

Figure 2.1: Examples of a few different and important 2D vdW crystals with diverse properties. For each material, we show the structure of a "monolayer".

A huge class of 2D materials are transition-metal dichalcogenides (TMDCs) [42]. Bulk TMDCs are layered vdW crystals, where each monolayer is formed by a layer of transition-metal atoms surrounded by top and bottom layers of chalcogen atoms. Interestingly, several different polytypes of TMDCs exist, such as the 2H, 1T, and 1T′ forms, that only differ by the relative arrangement of transition-metal and chalcogen atoms in the unit cell, which can have drastic consequences for electronic properties. For example, the bulk 2H-form of MoS_2 is an indirect band gap semiconductor, while a monolayer has a direct band gap in the visible optical range [43, 44]. In contrast, the 1T-form of, for example, TaS_2 is a metal and can exhibit a series of rather exotic electronic states, including superconductivity or a charge density wave (CDW) phase [45]. Even though TMDCs are experimentally known since about the 1920s [46], the monolayers have been prepared and properly characterized just recently, as in the case of MoS_2 [43]. Especially the semiconducting TMDCs are technologically important building blocks for spintronics, optics, and transistors [47–49].

Another important class of 2D materials are the magnetic ones [50–53], which are indispensable for devices that require magnetism, such as the giant magnetoresitance (GMR) and tunneling magnetoresitance (TMR) effects. Examples of vdW layered magnetic crystals are the transition-metal trihalides (TMTHs) CrI_3 and $CrBr_3$, as well as transition-metal trichalcogenides (TMTCs), such as $Cr_2Ge_2Te_6$ (CGT), in which ferromagnetic order is present in the monolayer limit [51, 52]. For a long time, people believed that long-range magnetic order could not be present in a 2D system [54]. However, since these materials have perpendicular magnetic anisotropy (PMA), ferromagnetic order is stabilized even for the monolayers. Similarly to the TMDCs, the vdW magnets are known to physicists for quite some time, but just recently monolayers were successfully fabricated and characterized [55]. A drawback for applications is the reduced Curie temperature of the monolayers compared to their bulk counterparts, which is already well below room temperature [51]. Another issue is the stability of these magnetic materials under ambient conditions [50], an obstacle that can be overcome by the encapsulation with hBN.

Above are just a few examples of 2D materials with diverse properties. Fortunately, for every 3D material class, we now have at least one 2D analog available, be it metal, insulator, superconductor, ferromagnet, antiferromagnet, semiconductor, or topological insulator. In Fig. 2.1, we summarize a few very important representatives of 2D crystals, which offer unforeseen opportunities, but also challenges, to electronics, spintronics, optics, and magnetism.

How to create a 2D material?

The creation of a 2D material is a delicate task and a lot of efforts are needed to achieve large scale and high purity samples, which are the ultimate requirement for mass market applications. In general, two different approaches can be distinguished: 1) separation of individual monolayers from the bulk compound and 2) direct growth of the monolayer material via assembling the atomic constituents.

The first technique is, from a theoretical point of view, a very simple one. Take a piece of sticky tape and apply it to the material of interest, provided that it is a vdW layered crystal. Eventually, one will peel off a monolayer of the vdW crystal, which is sticking to the tape. The tape will then be pressed on a suitable substrate, such that the peeled off monolayer will be transferred from the tape to the substrate. This process is called mechanical exfoliation or Scotch-tape method [56]. Typically, the peel off process is repeated many times to enhance the probability for monolayer generation, before the tape is pressed on the substrate. Subsequent scanning of the substrate via an optical microscope is often used to search for regions where a monolayer is present. The advantage of this method is that no chemical reactants are present during the exfoliation process, which could degrade the sample quality. However, one has no direct control of monolayer generation and the sample sizes are usually small. This technique, which is still frequently used, was the first one to peel off graphene layers from the graphite crystal [57], which initialized the whole field of 2D material research.

Another technique to separate the monolayers from each other is the liquid exfoliation method [58–60], where several fine tuning options exist. The basic idea is to suspend the vdW material, typically in powder form, in a special liquid solvent. Among sonication of the liquid mixture, microbubbles are created and annihilated due to the pressure pulsations. The bubble cavitation lead to shock waves which provide the normal and shear forces that act on the vdW material, separating the layers from each other. The success of monolayer generation strongly depends on the sonication power, but primarily on the solvent that is used to efficiently overcome the vdW forces between the layers. The exfoliated flakes can be extracted via filtration or drop casing, typically including some residuals from the exfoliation process, which is just one drawback of this method. In addition, the monolayer yield is usually low and the flake sizes are small, having also high defect densities.

One of the most frequently used growth techniques for large scale production of 2D materials is the chemical vapour deposition (CVD) [61–63]. For the CVD growth process, some precursor materials are necessary, which already contain the atomic constituents of the desired monolayer material. In the case of graphene, typically a mixture of CH_4/H_2 gas is used, for which the flow rate can be easily controlled. For TMDCs, metal oxides or foils in combination with sulfur or selenium powders are heated to create the gasified solid precursors. These precursor gases are lead into a heated furnace, where they react with each other such that the desired 2D material will grow on a suitable substrate. The substrate itself can have an additional catalytic functionality to improve the overall growth success. Especially for the CVD growth process, it is vital to stick to specific guidelines, concerning temperature, gas pressure, and time duration, to get high quality monolayer samples [61]. Remarkably, under well-controlled growth conditions, many features, such as grain sizes, number of layers, the orientation, or crystal phase (especially important for TMDCs), can be precisely tuned. It is even possible to grow vdW heterostructures with CVD-based techniques. Already in 2010, macroscopic graphene films were grown on Cu-foils [64], showing the indispensable role of CVD for the mass market production of 2D monolayers.

Another technique to create 2D materials is the molecular beam epitaxy (MBE) [65], which is one of the most important methods for industry, as it allows to easily grow clean semiconductor heterostructures with sharp interfaces. The MBE growth process takes place in an ultrahigh vacuum chamber to reduce impurities from residual atmospheric gases. Effusion cells, containing the pure atomic constituents, are heated such that directed molecular beams can be shot on a substrate within the chamber. The whole growth process can be monitored *in situ* with the help of the reflection high-energy electron diffraction (RHEED) technique. Several control knobs, such as temperature and substrate material, decide on the overall growth process, quality, and resulting deposited crystal. MBE holds promise for continuous and scalable growth, especially for TMDC mono- and multilayers [66–68], but also for graphene [69] and hBN [70].

The mentioned creation techniques are briefly summarized in Fig. 2.2. For industrial purposes, it is incredibly important to grow 2D materials in a large scale, cheap, and reproducible way. Remarkably, since the first mechanical exfoliation of graphene, researchers made a great progress towards realizing this, especially by customizing CVD and MBE for the growth of monolayers.

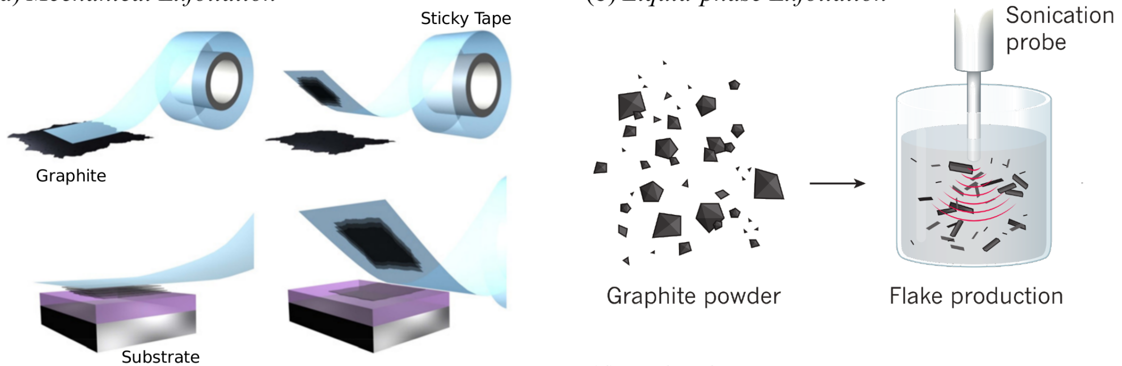

(a) *Mechanical Exfoliation* (b) *Liquid-phase Exfoliation*

Sticky Tape
Graphite
Substrate
Sonication probe
Graphite powder
Flake production

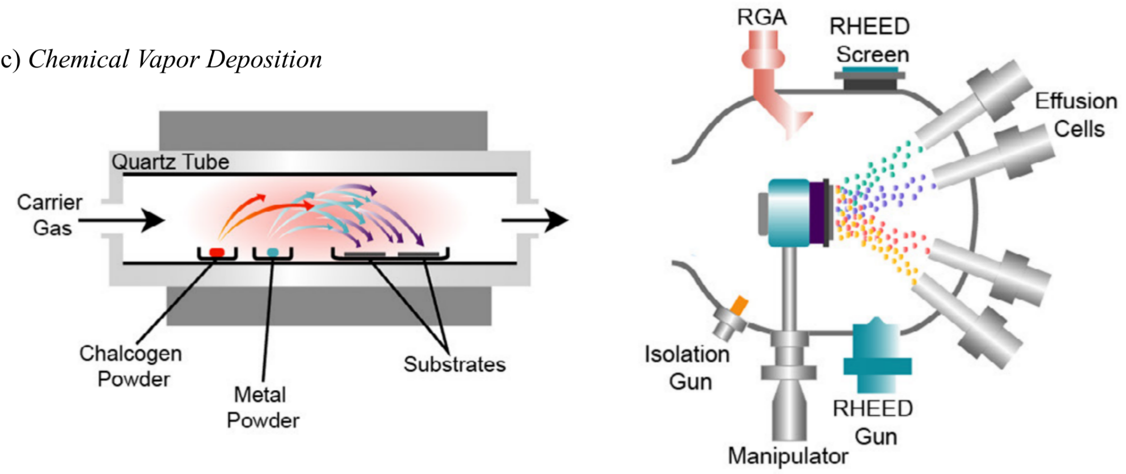

(c) *Chemical Vapor Deposition* (d) *Molecular Beam Epitaxy*

Quartz Tube
Carrier Gas
Chalcogen Powder
Metal Powder
Substrates
RGA
RHEED Screen
Effusion Cells
Isolation Gun
RHEED Gun
Manipulator

Figure 2.2: Creation techniques for 2D materials. (a) Micromechanical exfoliation with the help of an adhesive tape and subsequent transfer on a substrate. (b) Liquid exfoliation method, where graphite powder is placed in a liquid solution and among sonication the mono- and multilayer flakes are created. (c) Powder-based CVD method, where a carrier gas transports the source powders to the substrate within a heated quartz tube. (d) MBE method, where directed molecular beams from effusion cells are shot on a substate. Figure (a) from Ref. [71], (b) from Ref. [72], and (c,d) from Ref. [73].

Application prospects of 2D materials and their heterostructures

For field-effect transistor (FET) device applications, operating at high frequencies, it is important that the channel material has a large carrier mobility [74]. Conventional bulk semiconductors (Si, Ge) have mobilites typically ranging in between 10^2–10^4 cm^2/Vs, while III-V compounds (InAs, InSb) can even reach up to 10^5 cm^2/Vs [75, 76]. In contrast, 2D monolayer graphene flakes, grown by CVD on copper and encapsulated in hBN, show mobilities of around 10^6 cm^2/Vs [77]. Recent experiments could even demonstrate that graphene in a vdW heterostructure with a TMDC can have a giant room temperature mobility as high as 350.000 cm^2/Vs [78], well above the predicted limits due to acoustic phonons [79]. Graphene-based FETs begin now to outperform Si-based technology [80–82]. Moreover, charge carriers in graphene are ultra-sensitive to external influences, such as adatoms and admolecules that are attached to it. Even single molecule absorption can be detected, due to relatively large changes in graphene's resistivity [39]. Thus, graphene can be used as a powerful detector for poisonous gases.

Nevertheless, for transistor applications, semiconducting materials with a band gap are advantageous to semimetallic graphene. One such 2D material is phosphorene, which shows good ambipolar device performance with relatively high mobilities and on/off ratios [83, 84]. In addition, the anisotropic transport, optical, and mechanical properties of phosphorene, which originate from its puckered crystal structure, could be relevant for novel flexible device designs [85], see Fig. 2.3(d). Furthermore, phosphorene shows a layer dependent band gap ranging from 0.3 eV (bulk) to 2 eV (monolayer), thus bridging the gap between near-infrared and the visible spectrum. Phosphorene is also a superior thermoelectric material and can be used in photodetectors with similar response times as graphene [83, 86]. Recent studies also demonstrate that phosphorene-based heterostructures are suitable candidates as water splitting photocatalysts [87].

Also TMDCs are semiconductors, with band gaps in the visible spectrum, that can be used for ambipolar FET device applications, which are highly efficient when an electric double layer (ionic liquid) is used as gate dielectric [42, 48, 91]. One pecularity of TMDCs is the spin-valley locking, the helicity selective optical excitation of carriers with certain spin in a certain valley[1] at the same excitation energy. The spin-valley locking provides another degree of protection for charge carriers, important for information technology. In particular, it is a very attractive property for the field of valleytronics [92], for example as a spin and valley-polarized current source. Another possible application area for TMDCs is in photonics devices [48, 93, 94], as they are highly sensitive to polarized light and can be used in photodetectors and light emitting devices with controllable emission helicity.

The recently discovered magnetic materials, such as CGT and CrI_3 are long-awaited building blocks in spintronics for nonvolatile magnetic random access memory (MRAM) technology [50–52, 95]. For example, magnetic tunnel junctions consisting of CrI_3 [90, 96], showing giant magnetoresistance ratios up to 10.000%, are ideally suited for novel TMR devices, see Fig. 2.3(c). Furthermore, the distinct resistance states can be controlled and tuned fully electrically by gating and doping in multilayer CrI_3 structures. Unfortunately, the operation is limited to low temperatures due to the Curie temperature of the currently known 2D magnetic materials.

Heterostructures formed by 2D materials are also very attractive from another point of view, since we can easily stack them in a lego-like fashion so that proximity effects can play an important role. The first demonstration of proximity-induced phenomena dates back to 1932 in normal-metal/superconductor junctions, where superconductivity "leaks" into the normal-metal [97]. Similarly, combining a strong spin-orbit coupling (SOC)[2] or magnetic material, with a generic 2D crystal layer, one can induce spin-orbit or exchange coupling

---

[1] The term "valley" denotes a local minimimum/maximum in the conduction band (CB)/valence band (VB) of the band structure. For the direct band gap semiconducting monolayer TMDCs, the valleys are located at the K and K′ points of the Brillouin zone (BZ).

[2] A strong SOC material would be for example a TMDC or a topological insulator (TI), where the characteristic band structure features are dominated by SOC.

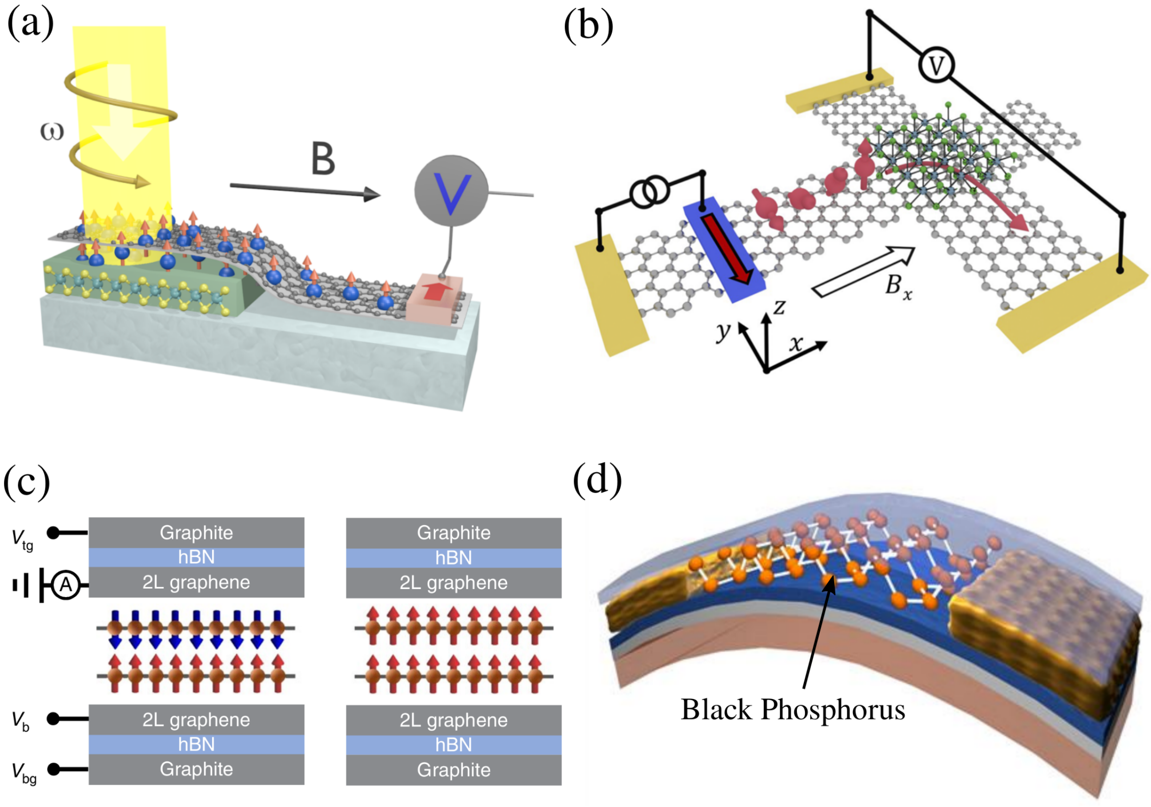

Figure 2.3: Device schemes employing 2D materials and their heterostructures. (a) Optical spin injection into graphene with the help of a semiconducting TMDC. The circularly polarized light generates spin-polarized electrons in the TMDC, which are transferred to graphene and subsequently detected as a Hanle signal by the ferromagnetic electrode. (b) Sketch of the geometry to measure the proximity-induced inverse spin Hall effect (SHE) in graphene/TMDC heterostructures. The precession of the spins and the spin-to-charge conversion is sketched. (c) Schematics of a spin tunnel FET based on a gate-tunable ferromagnet-to-antiferromagnet transition in bilayer CrI_3 and the spin filtering in the tunnel junction. Arrows indicate the magnetization in each CrI_3 layer. The left and right panels correspond to a low and a high tunnel conductance state, respectively. (d) Illustration of the device structure of a flexible back-gated black phosphorus FET on a polyimide substrate. Even after 5.000 bending cycles, the device performance did not degrade. Figure (a) from Ref. [88], (b) from Ref. [89], (c) from Ref. [90], and (d) from Ref. [85].

by the proximity effect [30]. Therefore, one can effectively add multiple spin interactions to a 2D material which intrinsically lacks superconductivity, strong spin-orbit, or magnetic exchange coupling. Nowadays, vdW heterostructures are considered for proximity effects, exclusively consisting of 2D crystal layers. In fact, proximity effects offer new opportunities in condensed matter physics. On the one hand, different materials can mutually benefit from each other and allows for the efficient manipulation of electronic and spin properties. On the other hand, proximity effects in 2D vdW materials typically leave the characteristic intrinsic properties of the individual materials intact.

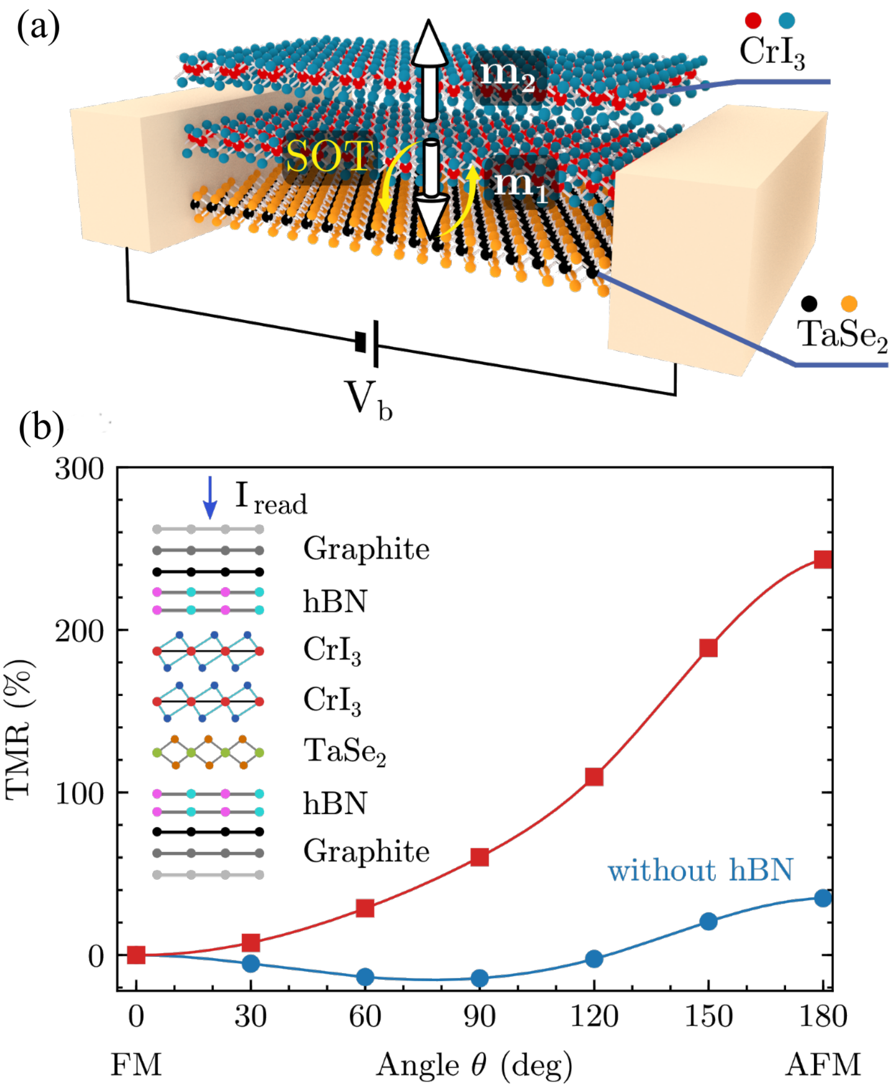

Figure 2.4: (a) Schematic view of a CrI$_3$/TaSe$_2$ vdW heterostructure consisting of an insulating antiferromagnetic bilayer-CrI$_3$ and a nonmagnetic metallic monolayer TaSe$_2$. The spin-orbit torque (SOT) switches the magnetization $\mathbf{m}_1$ to get an antiferromagnet-to-ferromagnet reversible phase transition. (b) A read-out current I$_{read}$ can be used to probe the TMR$(\theta) = [R(\theta) - R(0)]/R(0)$ of the heterostructure, as function of the angle θ between magnetizations $\mathbf{m}_1$ and $\mathbf{m}_2$ on two monolayers of CrI$_3$. Here, R denotes the resistance of the junction. Figures are from Ref. [98].

For example, highly discussed material combinations are graphene/TMDC heterostructures. Graphene lacks a band gap, has very low optical absorption, nearly no intrinsic SOC, but excellent electronic and spin transport properties. In contrast, TMDCs display excellent optical absorption in the visible range with spin-valley locking, but with poor mobilities. In addition, TMDCs have strong intrinsic SOC. Consequently, graphene/TMDC heterostructures are very well suited for optospintronics devices, where spin polarization is optically generated in the TMDC and subsequently transferred to graphene [88, 99], see Fig. 2.3(a).

Recent experiments have focused also on the proximity-induced SOC in graphene, due to the nearby TMDC, which causes a giant lifetime anisotropy in graphene's spin transport [100]. Remarkably, the intrinsic SOC of graphene can be enhanced by two orders of magnitude, by the proximity effect, while still preserving the characteristic Dirac dispersion. Moreover, interconversion between spin and charge currents in graphene/TMDC heterostructures can be achieved via SHE, see Fig. 2.3(b), and Rashba-Edelstein effect (REE) [89, 101–103]. The conversion can be tuned in sign and magnitude by gating, which offers a route for fully electrical spin generation and manipulation, without further need of ferromagnetic electrodes.

One particular example of an all 2D material vdW heterostructure, especially interesting for novel SOT-based MRAM technologies, is shown in Fig. 2.4(a). In the $CrI_3/TaSe_2$ vdW heterostructure, consisting of an insulating antiferromagnetic bilayer-CrI_3 and a nonmagnetic metallic monolayer $TaSe_2$, an antiferromagnet-to-ferromagnet reversible phase transition can be induced by SOT [98]. The unpolarized charge current is injected parallel to the interface by a small applied bias voltage V_b between the left and right electrodes. The charge current in the strong SOC $TaSe_2$ layer, leads to a transverse spin current across the $CrI_3/TaSe_2$ interface. Due to SOT, a reversible switching of the magnetization $\mathbf{m}_1$ of the lower CrI_3 layer can be achieved, by passing short current pulses. A transverse read-out current I_{read} can be used to probe the TMR ratio of the heterostructure, as function of the angle θ between the magnetizations $\mathbf{m}_1$ and $\mathbf{m}_2$ of the two monolayers of CrI_3, see Fig. 2.4(b). By employing suitable graphene/hBN tunneling electrodes, the magnetic states of the bilayer-CrI_3 can be well distinguished, with a maximum TMR ratio of about 240%.

Another example for applications of vdW heterostructures are TMDC-based p-n junctions as high performance photodetectors [104–106]. By combining two different TMDC layers in a heterobilayer, very efficient charge separation is possible. Depending on the combined TMDC monolayers, a special type-II band alignment is achieved, where the conduction band (CB) is formed by one layer, while the valence band (VB) is formed by the other TMDC layer, such that electrons and holes are located in different layers. The resulting photodetectors can operate with zero bias voltage, due to the built-in field of the heterostructure. Furthermore, they show fast response times, high on/off ratios, and wide wavelength detection ranges. The mentioned application prospects give just an initial impression of what is possible with 2D materials and heterostructures. We are not yet at a stage, where these new 2D-based device developments can drastically outperform the conventional state-of-the-art technology. Nevertheless, 2D materials and their heterostructures offer a rich playground for basic research, and hold promise for novel devices in diverse fields. In the following chapters, we will show our results on proximity effects in 2D material heterostructures and discuss their significance for research and industry.

More specifically, in the next part we will talk about graphene-based structures. After introducing a low energy model Hamiltonian, suitable to describe the proximity-modified Dirac states of graphene, we first focus on graphene/hBN heterostructures. Based on extensive density functional theory (DFT) calculations, we find that graphene's characteristic dispersion is preserved with additional weak proximity SOC in the μeV regime. Subsequent spin lifetime and spin relaxation (SR) anisotropy calculations allow us to discuss the significance of these structures for charge and spin transport experiments. In particular, we will see that spin lifetimes are on the order of few to tens of nanoseconds, while SR anisotropies are gate tunable and can reach giant values. Next, we discuss the proximity SOC in graphene/TI heterostructures. In great contrast to hBN, the TI induces a much larger SOC in graphene on the order of few meV. The magnitude of the induced SOC depends on an external gate voltage, the atomic constituents of the TI, and the interlayer distance, which are tuning knobs to find ideal experimental conditions for, e. g., spin-to-charge conversion efficiencies in graphene/TI stacks. In the last chapter about graphene, we discuss the proximity-induced exchange coupling due to the Ising antiferromagnet $\mathrm{MnPSe_3}$. Surprisingly, antiferromagnetic exchange is induced in graphene, i. e., the effective couplings in the model have opposite sign for the different sublattices in order to fit the DFT dispersion. This behavior has never been reported before and opens new avenues for the design of topologically protected edge states in graphene.

In Ch. 7, we switch gears and introduce the basic properties of bilayer graphene (BLG). Especially its unique gate tunable low energy dispersion, with sublattice- and layer-polarized bands, is important for exotic device concepts where spin interactions can be turned on and off. In particular, we will discuss multiple heterostructures comprising BLG, semiconducting TMDCs, and the ferromagnetic insulator (FMI) CGT. Due to the short-range proximity effects, only adjacent layers influence each other. Consequently, spin-orbit and exchange couplings can be fully electrically turned on and off or swapped in the conduction electrons of BLG. Our results provide a basis for unique multifunctional device architectures, employing the full potential of vdW heterostructures and related proximity-induced phenomena.

In the last part of this thesis, we will discuss TMDCs. One important key ingredient for flexible electronics are 2D materials because of their mechanical strength. In this context, especially the semiconducting TMDCs are attractive and this is why we study their strain tunable band structures and optical properties in Ch. 9. Even though these results are not directly related to proximity effects, they are still vital for the interpretation of experiments and heterostructure DFT calculations. In the last main chapter, we consider TMDC/(hBN/$\mathrm{CrI_3}$)/$\mathrm{CrI_3}$ structures. The proximity-induced exchange coupling is short-ranged and originates from the adjacent magnetic $\mathrm{CrI_3}$ layer only. The induced magnetism, combined with the giant intrinsic SOC of the TMDCs, breaks the valley degeneracy in the dispersion. The relevant TMDC band edges at the K and K$'$ points experience a valley splitting on the order of a few meV, which can be tuned by gating and twisting the TMDC/$\mathrm{CrI_3}$ heterostructures. Technologically, this offers a way for persistent valley polarization in TMDCs, and the valley degree-of-freedom could be employed in novel valleytronics heterostructure devices.

PART II

Graphene

CHAPTER 3

The basics of monolayer graphene

In this chapter, we introduce the basic properties of monolayer graphene, such as unit cell, band structure, and low energy Hamiltonian. The Hamiltonian is based on effective p_z orbitals of graphene that can be modified by proximity effects. The modification of the Dirac bands due to proximity of graphene to other materials, such as monolayer transition-metal dichalcogenides (TMDCs) or ferromagnets, can be described by a series of parameters, including orbital, spin-orbit, and exchange effects. The parameters can be determined by fitting the Hamiltonian to a first-principles calculated band structure of a graphene-based heterostructure system. Finally, we briefly analyze the impact of proximity spin-orbit and exchange coupling on the low energy band structure by employing realistic model parameters according to density functional theory (DFT)-calculation examples.

3.1 Unit cell, Brillouin zone, and band structure

The element carbon is very important, especially for life on earth, since all living (organic) compounds contain it. Due to the special electronic configuration [He] $2s^2 2p^2$, with 4 valence electrons, it has the ability to form complex molecules and shows the greatest diversity of chemical combinations among all elements. For example, carbon is found in complex hydrocarbon chains, such as in fossil fuels and plastics which are essential for industry. In great contrast, diamond, one of the hardest and most precious crystals on earth, is also formed by carbon atoms.

A highly discussed material, which exclusively consists of carbon atoms, is graphene. Its prominent properties, like giant electron mobility, optical transparency, and mechanical robustness [77, 107–109], make it very appealing for research, especially in the fields of electronics and spintronics. Monolayers of graphene can be produced via mechanical exfoliation [109] or by chemical vapour deposition (CVD) on metal substrates [110]. The lattice of graphene is shown in Fig. 3.1, which has a lattice constant $a = \sqrt{3}a_0 \approx 2.46$ Å, where $a_0 = 1.42$ Å is the distance between next-nearest carbon atoms [35]. Graphene contains two non-equivalent atoms in the unit cell, thus it is made up from two trigonal sublattices $\mathrm{C_A}$ and $\mathrm{C_B}$. The reciprocal lattice is also hexagonal, containing the non-equivalent high symmetry points Γ, M, K, and K′.

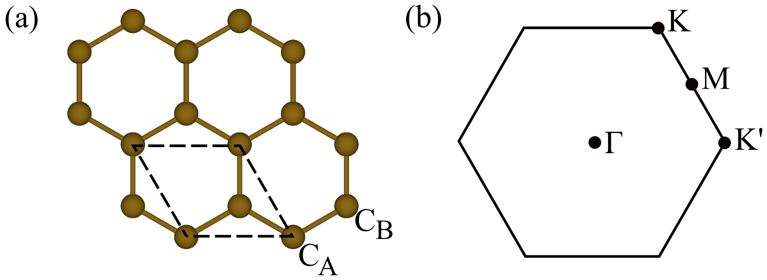

Figure 3.1: Unit cell and Brillouin zone (BZ) of graphene. (a) Real space lattice of graphene with labels for the sublattices C_A and C_B. One unit cell is emphasized by the dashed line. (b) First BZ of the reciprocal lattice, where Γ, M, K, and K′ are non-equivalent high symmetry points.

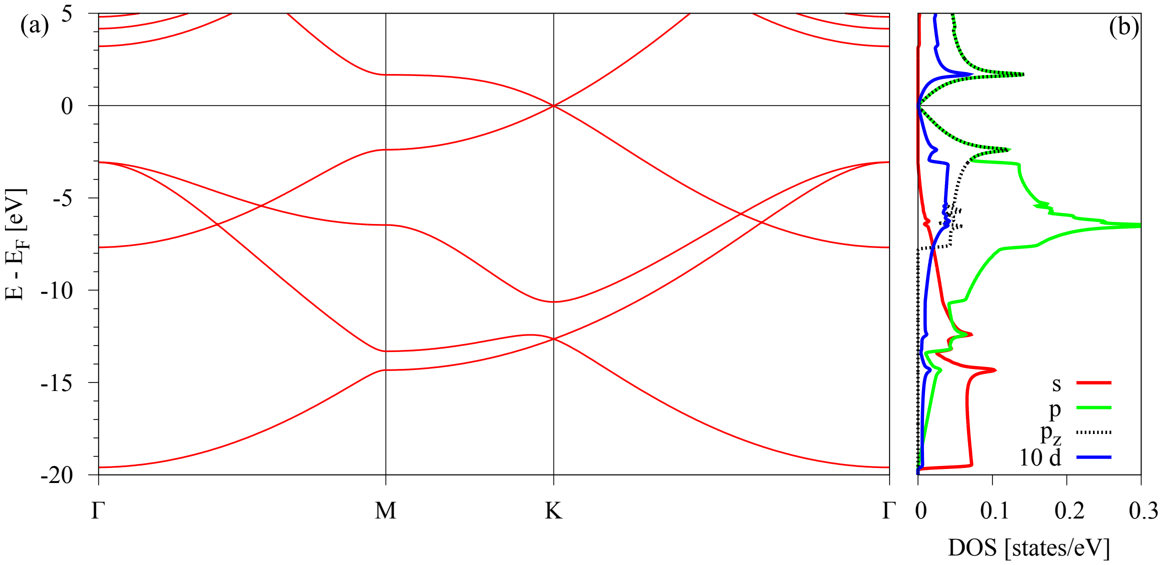

Figure 3.2: Calculated band structure and corresponding orbital resolved density of states (DOS) of graphene. (a) Band structure along the high symmetry path Γ–M–K–Γ. (b) Orbital resolved DOS, where the contribution of d orbitals is multiplied by a factor of 10.

In Fig. 3.2, we show the band structure and the corresponding orbital resolved DOS of graphene, as calculated from DFT. The s, p_x, and p_y orbitals in graphene form sp^2 hybridized covalent σ-bonds in the plane, lying low in energy, which are responsible for the mechanical robustness of graphene. The remaining p_z orbitals, which point out of the graphene plane, are responsible for the π-bands near the Fermi energy and determine the electronic and spin transport properties [35, 111]. At the corners of the BZ (K and K′ points), valence band (VB) and conduction band (CB) touch. The K/K′ points are called Dirac points, since the dispersion is linear in their vicinity and the charge carriers show a similar behavior as massless Dirac fermions, with a Fermi velocity of roughly 10^6 m/s. The bands at the Γ point, for energies larger than 3 eV are parabolic, which is an artifact of the DFT calculation when simulating a monolayer surrounded by vacuum. Tight-binding descriptions [35, 112] and experimental [113] studies of the electronic structure of graphene match well with the

DFT results. Especially tight-binding model descriptions are very useful in exploring the electronic, spin, and transport properties of graphene under several external influences, such as adatoms and substrates [88, 100, 112, 114–117].

Since the first exfoliation, monolayer graphene has attracted a lot of attention due to its theoretically predicted very long spin relaxation (SR) times of $\tau \approx 1$ μs and SR lengths of $l_s \approx 100$ μm, making it the ideal material for spintronics [118–124]. However, first experimental studies found much shorter SR times in the picosecond range [125–135]. From several investigations we now know that adatoms like hydrogen [117, 136] locally enhance the spin-orbit coupling (SOC) strength up to 1 meV, giant compared to graphene's intrinsic SOC of about 10 μeV [111, 137–139]. In addition, DFT studies have shown that also substrates such as TMDCs can strongly enhance the SOC in graphene [88, 140]. All these external sources of SOC significantly reduce the spin lifetimes in graphene.

Still, graphene is one of the most frequently used transport channel materials in spintronics. In principle, the weak intrinsic SOC of graphene is ideal for long-distance spin transport, but detrimental for manipulating (or even generating) spin currents. Thus, we desire to *induce and control* spin interactions in graphene. Because graphene is only one atomic layer thick, it is ideally suited for van der Waals (vdW) heterostructures and short-range proximity effects can be used to manipulate its electronic properties. In the following chapters, we will discuss several examples of vdW heterostructures, where graphene gets proximitized by other (not necessarily two-dimensional (2D)) materials. Proximity-induced spin-orbit and exchange couplings will modify the low energy Dirac bands, but leave the characteristic linear dispersion of graphene intact.

3.2 Hamiltonian of spin-orbit and exchange proximitized graphene

In this part about graphene, our main goal is to answer the question how another material in proximity to graphene modifies the low energy Dirac bands at K/K′.

Several studies of spin-orbit and exchange proximitized graphene, motivate us to introduce the following minimal Hamiltonian [88, 115, 141–144] (as derived from symmetry [112, 145, 146]), which is based on effective p_z orbitals. The basis of the Hamiltonian is $\sigma \otimes s$, where σ denotes the sublattice/pseudospin space ($\mathrm{C_A}$, $\mathrm{C_B}$) and s the spin space ($\uparrow, \downarrow$), resulting in the four basis states $|\mathrm{C_A}\uparrow\rangle$, $|\mathrm{C_A}\downarrow\rangle$, $|\mathrm{C_B}\uparrow\rangle$, and $|\mathrm{C_B}\downarrow\rangle$ with four eigenvalues $\varepsilon_{1/2}^{\mathrm{CB/VB}}$.

As already mentioned, the low energy bands of graphene near the Fermi level display a linear energy-momentum relation and pristine graphene can be described by the massless Dirac Hamiltonian. In the vicinity of K (K′) points,

$$\mathcal{H}_0 = \hbar v_{\mathrm{F}}(\tau k_x \sigma_x - k_y \sigma_y) \otimes s_0, \tag{3.1}$$

where v_F denotes the Fermi velocity, and k_x and k_y are the Cartesian components of the electron wave vector measured from ±K, corresponding to the valley index $\tau = \pm 1$. The Pauli spin matrices are s_i and σ_i are pseudospin matrices, where $i = \{0, x, y, z\}$. The Hamiltonian $\mathcal{H}_0$ describes a gapless linear dispersion near the Dirac points K (K′). The bands are two-fold spin-degenerate.

When graphene is situated above a substrate, the two sublattice atoms C_A and C_B feel different effective surrounding potentials. The Hamiltonian

$$\mathcal{H}_\Delta = \Delta \sigma_z s_0, \tag{3.2}$$

where Δ is the staggered potential gap, describes this difference in the sublattice potentials. The Hamiltonian $\mathcal{H}_\Delta$ essentially describes a mass term, which breaks the pseudospin symmetry. The two terms $\mathcal{H}_0 + \mathcal{H}_\Delta$ describe spin-degenerate parabolic bands near K/K′ points, with an orbital band gap.

Naturally, each carbon atom possesses some amount of intra-atomic SOC λ_I^{atom}. In the case of our effective p_z-based Hamiltonian, this atomic SOC only marginally affects the dispersion near the Dirac points K (K′), in which we are mostly interested in [138]. The parameter we use to model the impact of the atomic SOC on the linear dispersion is λ_I, which we call intrinsic SOC. For freestanding graphene, the two sublattices (C_A and C_B) can be seen as equivalent — there is yet no obvious reason for two carbon atoms to differ. One can translate this into $\lambda_I^A = \lambda_I^B = \lambda_I$ and SOC opens just a tiny gap of about 20 μeV in the spectrum, even though the spin-orbit splitting of p states is on the order of 10 meV [111]. Actually, the value of $\lambda_I \approx 12$ μeV is dominated by the atomic SOC from d orbitals, as they contribute in first order, while p orbitals contribute only in second order, as deduced from perturbation theory [138]. From the DOS, see Fig. 3.2(b), one can actually see that d orbitals contribute in a similar way as p_z orbitals near the Dirac point.

When graphene is located on a substrate, the pseudospin symmetry gets explicitly broken. Furthermore, the substrate can induce some additional amount of SOC by proximity. Thus, the intrinsic SOC values get modified by the proximity effect such that $\lambda_I^A \neq \lambda_I^B$. This can be described by the Hamiltonian

$$\mathcal{H}_I = \tau(\lambda_I^A \sigma_+ + \lambda_I^B \sigma_-) \otimes s_z, \tag{3.3}$$

with λ_I^A and λ_I^B being the sublattice-resolved intrinsic SOC parameters, and $\sigma_\pm = \frac{1}{2}(\sigma_z \pm \sigma_0)$ for shorter notation. Because the SOC is, in most cases, proximity modified, the term "intrinsic" should not be taken too literally.

The presence of a transverse electric field (vertical to the graphene layer) or a substrate breaks all symmetries that would allow to flip the orientation of the transverse z axis (inversion with respect to z or mirror with respect to the xy plane). Two additional terms arise due to this symmetry breaking, namely

$$\mathcal{H}_R = -\lambda_R(\tau \sigma_x \otimes s_y + \sigma_y \otimes s_x) \tag{3.4}$$

and

$$\mathcal{H}_{\text{PIA}} = a(\lambda_{\text{PIA}}^{\text{A}}\sigma_{+} - \lambda_{\text{PIA}}^{\text{B}}\sigma_{-}) \otimes (k_x s_y - k_y s_x). \tag{3.5}$$

The first term is the Rashba SOC Hamiltonian with parameter λ_{R}, which describes the amount of space inversion asymmetry. The second term is the sublattice-resolved pseudospin inversion asymmetry (PIA) SOC Hamiltonian, with parameters $\lambda_{\text{PIA}}^{\text{A}}$ and $\lambda_{\text{PIA}}^{\text{B}}$, which describe the strength of the mirror plane asymmetry. Note that the Rashba and PIA terms, leading to in-plane spin-orbit fields, compete with the intrinsic SOC term, favoring out-of-plane spin textures. This will have important consequences for SR, as we will see in the next chapter.

When graphene is situated above a magnetic substrate, we explicitly break also time-reversal symmetry. In the style of the sublattice-resolved intrinsic SOC Hamiltonian $\mathcal{H}_{\text{I}}$, we introduce a proximity-induced exchange Hamiltonian

$$\mathcal{H}_{\text{ex}} = (-\lambda_{\text{ex}}^{\text{A}}\sigma_{+} + \lambda_{\text{ex}}^{\text{B}}\sigma_{-}) \otimes s_z, \tag{3.6}$$

with $\lambda_{\text{ex}}^{\text{A}}$ and $\lambda_{\text{ex}}^{\text{B}}$ being sublattice-resolved exchange parameters. The impact of the proximity exchange Hamiltonian on the low energy Dirac bands can be seen as an effective magnetic (Zeeman) field that simply shifts spin-up and spin-down bands in energy.

The full low energy graphene Hamiltonian we consider in the following chapters is

$$\mathcal{H}_{\text{GR}} = \mathcal{H}_0 + \mathcal{H}_{\Delta} + \mathcal{H}_{\text{I}} + \mathcal{H}_{\text{R}} + \mathcal{H}_{\text{PIA}} + \mathcal{H}_{\text{ex}}, \tag{3.7}$$

or in matrix form

$$\mathcal{H}_{\text{GR}} = \begin{pmatrix} \Delta + \tau\lambda_{\text{I}}^{\text{A}} - \lambda_{\text{ex}}^{\text{A}} & -\lambda_{\text{PIA}}^{\text{A}}(\mathrm{i}k_x + k_y)a & \hbar v_{\text{F}}(\tau k_x + \mathrm{i}k_y) & 2\mathrm{i}\lambda_{\text{R}}\delta_{\tau\text{K},+\text{K}} \\ -\lambda_{\text{PIA}}^{\text{A}}(-\mathrm{i}k_x + k_y)a & \Delta - \tau\lambda_{\text{I}}^{\text{A}} + \lambda_{\text{ex}}^{\text{A}} & 2\mathrm{i}\lambda_{\text{R}}\delta_{\tau\text{K},-\text{K}} & \hbar v_{\text{F}}(\tau k_x + \mathrm{i}k_y) \\ \hbar v_{\text{F}}(\tau k_x - \mathrm{i}k_y) & -2\mathrm{i}\lambda_{\text{R}}\delta_{\tau\text{K},-\text{K}} & -\Delta - \tau\lambda_{\text{I}}^{\text{B}} - \lambda_{\text{ex}}^{\text{B}} & -\lambda_{\text{PIA}}^{\text{B}}(\mathrm{i}k_x + k_y)a \\ -2\mathrm{i}\lambda_{\text{R}}\delta_{\tau\text{K},+\text{K}} & \hbar v_{\text{F}}(\tau k_x - \mathrm{i}k_y) & -\lambda_{\text{PIA}}^{\text{B}}(-\mathrm{i}k_x + k_y)a & -\Delta + \tau\lambda_{\text{I}}^{\text{B}} + \lambda_{\text{ex}}^{\text{B}} \end{pmatrix}. \tag{3.8}$$

In order to find the parameters, we fit the model Hamiltonian, Eq. (3.7), to DFT-calculated band structures of graphene in proximity to various other materials, which provide either magnetism or strong SOC. Depending on the specific system we consider, some terms can be neglected. Note that the model Hamiltonian, Eq. (3.7), is centered around zero energy Fermi level. For the first-principles calculated band structures, this is not necessarily the case, as charge transfer between the layers can occur, resulting in doping of the graphene. Therefore, we introduce another parameter E_{D}, which shifts the model band structure up (down) in energy, and we call it Dirac point energy, representing the amount of hole (electron) doping of graphene. Consequently, the actual full Hamiltonian is $\mathcal{H}_{\text{GR}} + E_{\text{D}}$.

3.3 Band structure topologies of proximitized graphene

Let us now analyze the different Hamiltonian terms by looking at their individual effects on the band structure. In Fig. 3.3, we show a series of low energy band structures for different parameter sets, without including proximity exchange parameters λ_{ex} such that time-reversal symmetry is preserved.

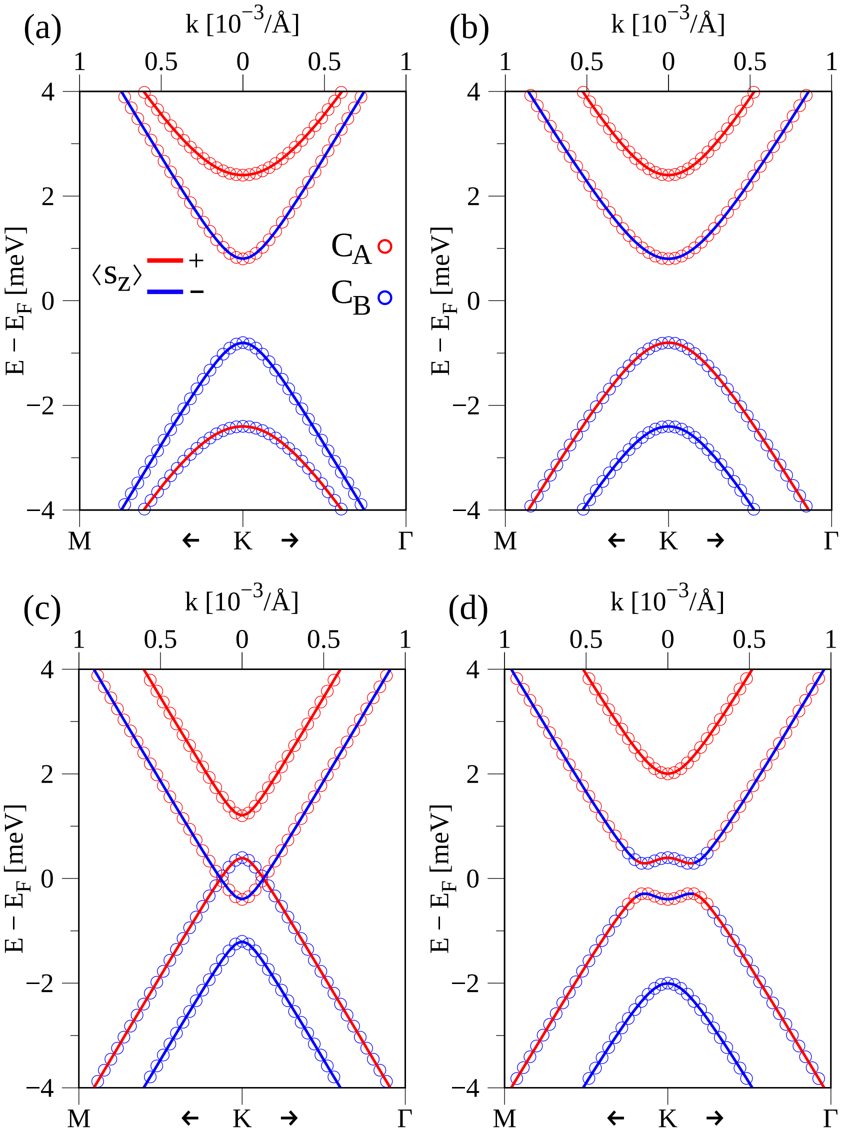

Figure 3.3: Low energy graphene band structures for different parameter sets of the Hamiltonian $\mathcal{H}_{\text{GR}}$. In all subfigures, we use $v_{\text{F}} = 8 \times 10^5 \frac{\text{m}}{\text{s}}$, while unspecified parameters are zero. In these cases, time-reversal symmetry is preserved and we show the bands at the K point only. Color of the lines (symbols) corresponds to the s_z (pseudospin) expectation value. (a) $\Delta = 1.6$ meV, $\lambda_{\text{I}}^{\text{A}} = \lambda_{\text{I}}^{\text{B}} = 0.8$ meV. (b) $\Delta = 1.6$ meV, $\lambda_{\text{I}}^{\text{A}} = -\lambda_{\text{I}}^{\text{B}} = 0.8$ meV. (c) $\Delta = 0.4$ meV, $\lambda_{\text{I}}^{\text{A}} = -\lambda_{\text{I}}^{\text{B}} = 0.8$ meV. (d) $\Delta = 0.4$ meV, $\lambda_{\text{I}}^{\text{A}} = -\lambda_{\text{I}}^{\text{B}} = 0.8$ meV, $\lambda_{\text{R}} = 0.8$ meV.

In the case of $\Delta > (\lambda_{\mathrm{I}}^{\mathrm{A}} = \lambda_{\mathrm{I}}^{\mathrm{B}})$, see Fig. 3.3(a), we find that the CB (VB) is formed by the $\mathrm{C_A}$ ($\mathrm{C_B}$) sublattice. Compared to the case where $\Delta > (\lambda_{\mathrm{I}}^{\mathrm{A}} = -\lambda_{\mathrm{I}}^{\mathrm{B}})$, see Fig. 3.3(b), the VB spin ordering is reversed, while the pseudospin ordering is preserved. Thus, the spin ordering of the bands is determined by the sign of the intrinsic SOC parameters, while the pseudospin order is determined by the sign of the staggered potential parameter Δ. Note that the choice of the sublattices is arbitrary in the geometry, see Fig. 3.1. However, once we have assigned $\mathrm{C_A}$ and $\mathrm{C_B}$ to the lattice, the sign of Δ can be fixed by the pseudospin expectation values, determined from DFT.

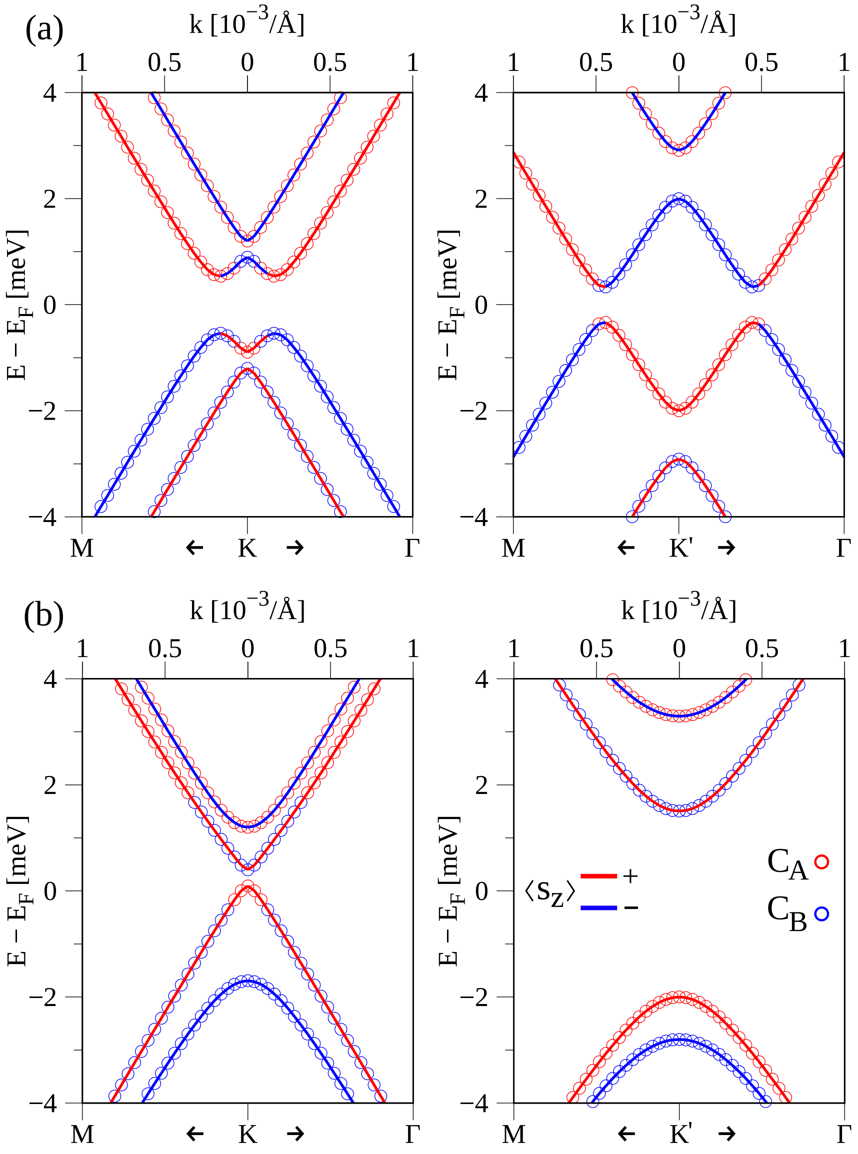

Figure 3.4: Same as Fig. 3.3, but here, time-reversal symmetry is broken and we show the bands at the K (left panels) and K′ (right panels) points. (a) $\Delta = 0.4$ meV, $\lambda_{\mathrm{I}}^{\mathrm{A}} = -\lambda_{\mathrm{I}}^{\mathrm{B}} = 0.8$ meV, $\lambda_{\mathrm{R}} = 0.8$ meV, $\lambda_{\mathrm{ex}}^{\mathrm{A}} = \lambda_{\mathrm{ex}}^{\mathrm{B}} = 1.6$ meV. (b) $\Delta = 0.4$ meV, $\lambda_{\mathrm{I}}^{\mathrm{A}} = \lambda_{\mathrm{I}}^{\mathrm{B}} = 0.8$ meV, $\lambda_{\mathrm{R}} = 0.8$ meV, $\lambda_{\mathrm{ex}}^{\mathrm{A}} = -\lambda_{\mathrm{ex}}^{\mathrm{B}} = 1.6$ meV.

When we decrease the staggered potential parameter Δ, to be smaller than the intrinsic SOC parameters, see Fig. 3.3(c), we allow for crossing of the highest VB with the lowest CB. Including a finite Rashba SOC parameter, see Fig. 3.3(d), the crossing becomes avoided because λ_{R} allows for mixing of the two spin components and opens a band gap. From the topological point of view, we obtain an inverted band structure with respect to both spin and pseudospin. Such a case can be realized in graphene/TMDC heterostructures, such that protected pseudohelical edge states can be present in graphene nanoribbons [140, 147].

Once we introduce a proximity exchange term, originating from a magnetic substrate, we explicitly break time-reversal symmetry and the degeneracy of the K and K′ valleys, see Figs. 3.4(a,b). In the case of uniform exchange and staggered SOC, see Fig. 3.4(a), quantum anomalous Hall (QAH) states can be realized [148–150]. In the case of staggered exchange and uniform SOC, see Fig. 3.4(b), it is possible to address a spin- and sublattice-polarized state only near the K valley, for an energy of about -1 meV below the Fermi level [151].

Note the following similarities when comparing the effects of exchange and intrinsic SOC parameters on the Dirac band splittings. For uniform proximity exchange ($\lambda_{\mathrm{ex}}^{\mathrm{A}} = \lambda_{\mathrm{ex}}^{\mathrm{B}}$), the splitting is reminiscent of the Zeeman splitting from an external magnetic field [152]. Similarly, for staggered intrinsic SOC ($\lambda_{\mathrm{I}}^{\mathrm{A}} = -\lambda_{\mathrm{I}}^{\mathrm{B}}$), the Dirac bands of different valleys (K and K′) are split as if a valley dependent Zeeman field would be present. Hence, staggered intrinsic SOC is also called valley Zeeman SOC. For uniform intrinsic SOC parameters ($\lambda_{\mathrm{I}}^{\mathrm{A}} = \lambda_{\mathrm{I}}^{\mathrm{B}}$), we arrive at the Kane-Mele SOC Hamiltonian [118, 144]. In analogy, staggered exchange parameters ($\lambda_{\mathrm{ex}}^{\mathrm{A}} = -\lambda_{\mathrm{ex}}^{\mathrm{B}}$) would produce a similar dispersion, since the Hamiltonians $\mathcal{H}_{\mathrm{I}}$ and $\mathcal{H}_{\mathrm{ex}}$ are quite similar.

Throughout the following chapters, we will encounter almost all possible situations and various parameter sets, where we have either normal or inverted bands. For example, in the case of graphene on hexagonal boron nitride (hBN), in Ch. 4, we will find that proximity SOC is comparable to the intrinsic SOC in pristine graphene, which will lead to extraordinary long spin lifetimes and giant SR anisotropies. In contrast, when graphene is situated above a topological insulator (TI), see Ch. 5, strong proximity-induced SOC will be imprinted, which is of valley Zeeman type, roughly corresponding to the situation shown in Fig. 3.3(d). Once a ferromagnetic substrate ($\mathrm{CrI_3}$ or $\mathrm{Cr_2Ge_2Te_6}$ (CGT)) is used, we find strong uniform proximity exchange, but also weak (one order of magnitude smaller than exchange) induced SOC in graphene, similarly as shown in Fig. 3.4(a). Such a case is discussed in Ref. [153]. The situation shown in Fig. 3.4(b), can be realized when graphene is in proximity to an Ising antiferromagnet, such as $\mathrm{MnPSe_3}$ [151], where staggered proximity exchange can be induced, as will be discussed in Ch. 6.

CHAPTER 4

Spin relaxation anisotropy in graphene/hBN structures

This chapter is based on the publication: K. Zollner, M. Gmitra, and J. Fabian, Physical Review B **99***, 125151 (2019), "Heterostructures of graphene and hBN: Electronic, spin-orbit, and spin relaxation properties from first principles".*

4.1 Introduction

Graphene encapsulated in hexagonal boron nitride (hBN) is regarded as one of the most important van der Waals (vdW) heterostructures for two-dimensional (2D) spintronics [2, 4, 154]. When experimentalists started to study spin transport in graphene, typical devices were based on SiO_2/Si substrates [125–135]. Unfortunately, spin transport qualities of graphene were tremendously reduced due to the SiO_2 and maximum spin lifetimes of only a few hundreds of picoseconds were obtained. In contrast — and that is why people were puzzled from experimental results — theory predicts only few μeV spin-orbit coupling (SOC) in pristine graphene [111, 137, 138], which should give rise to outstanding spin lifetimes in the nanosecond range [120–124]. This issue has been resolved since then since electron-hole puddles [155, 156], surface roughnesses, defects, and impurities [157, 158] are present in experiments. Consequently, graphene's weak SOC can be significantly increased, substantially influencing charge and spin transport properties. In addition, there is no indication of different lifetimes for out-of-plane and in-plane spins, i. e., a spin relaxation (SR) anisotropy[1], in these devices [159–161]. Due to the presence of magnetic resonant scatterers [114, 162, 163], an efficient SR and spin flip channel is present, randomizing the directions of the spins, which leads to the absence of a SR anisotropy.

In the context of SR, graphene/TMDC heterostructures are found to be important. Graphene in proximity to a TMDC acquires large Rashba and valley Zeeman SOC (1 meV) [88], leading to giant SR anisotropies [100, 164, 165], see Fig. 4.1. In general, the SOC induced by the TMDC substrate strongly reduces spin lifetimes to the picosecond range. However, as theoretically predicted [100] and experimentally confirmed [164, 165], in-plane spins relax

---

[1] The SR anisotropy is defined via the ratio $\xi = \tau_{s,z}/\tau_{s,x}$. In 2D electron gases, the out-of-plane electron spins have lifetimes ($\tau_{s,z}$) smaller than in-plane spins ($\tau_{s,x}$) because of the strong interfacial Rashba SOC [2], which typically leads to $\xi = 1/2$.

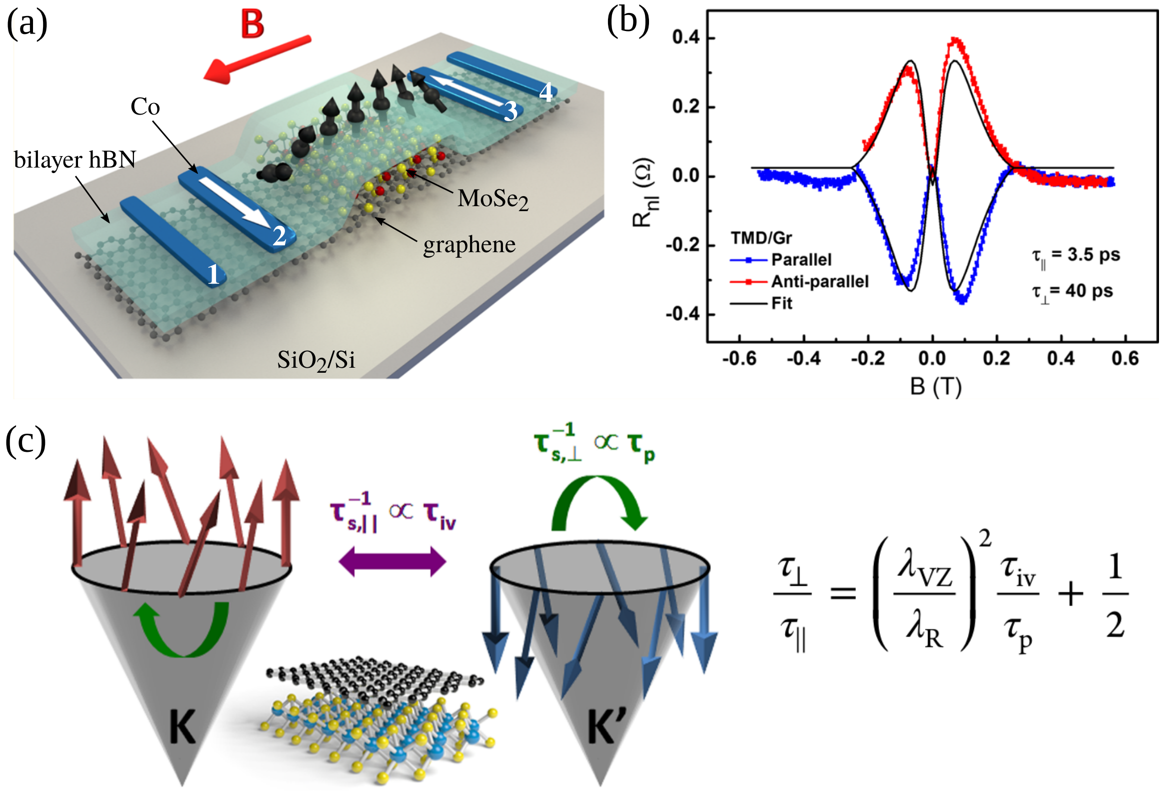

Figure 4.1: Spin lifetime anisotropy in graphene/transition-metal dichalcogenide (TMDC) heterostructures. (a) Sketch of the graphene/$MoSe_2$ structure on a SiO_2/Si substrate with top hBN as tunneling barrier and Co spin injection and detection contacts. White arrows are the Co magnetizations and black arrows depict the spins. (b) The non-local resistance R_{nl} as function of the applied in-plane magnetic field B_x. The spins are injected from Co contact 2 and the non-local voltage V_{nl} is measured between contacts 3 and 4 for parallel (blue) and antiparallel (red) magnetizations of contacts 2 and 3. By fitting these so-called Hanle curves, the spin lifetimes for out-of-plane ($\tau_{\perp}$) and in-plane ($\tau_{||}$) spins can be obtained. Due to the proximity-induced giant valley Zeeman SOC in graphene, the lifetimes are short (picoseconds) and out-of-plane spins live much longer than in-plane spins ($\tau_{\perp} \approx 10 \cdot \tau_{||}$). (c) The formula represents the ratio of spin lifetimes, i. e., the SR anisotropy as deduced from spin dynamics model considerations, taking into account valley Zeeman (λ_{VZ}) and Rashba (λ_{R}) SOC, as well as the momentum relaxation (τ_p) and intervalley scattering (τ_{iv}) times. The figure schematically illustrates SR in graphene/TMDC heterostructures. The tall arrows depict the effective spin-orbit fields for the Dirac bands at K and K′ valleys. The spin dynamics model in Ref. [100] reveals that in-plane spins predominantly relax due to intervalley scattering, while out-of-plane spins relax due to momentum scattering. Figures (a,b) are from Ref. [164] and (c) from Ref. [100].

much faster than out-of-plane spins. Regarding spin lifetimes, one possibility to counteract the influence from the substrate is to suspend graphene [166–168]. Indeed, recent resonance microwave measurements of suspended graphene on SiO_2 were used to experimentally determine the intrinsic spin-orbit gap of graphene to be 42 μeV [139], in agreement with theory [111]. Even though suspended samples can have high mobilities, one major drawback is that their spin transport qualities are limited. The search for new substrates revealed that hBN, the 2D insulating graphene analog, is the material of interest. It cannot only efficiently protect graphene from environmental influences, but also serve as a tunnel barrier for spin injection [141]. In addition and most important, the outstanding spin transport properties of graphene will be preserved, due to the chemical inertness of hBN.

The current generation of graphene spintronics devices relies on hBN as substrate or encapsulation material [38, 169–180]. These (hBN)/graphene/hBN heterostructures show outstanding spin and charge transport qualities. The mobilities can be giant, up to 10^6 cm^2/Vs [77, 107, 108], and go beyond the values reported for III-V semiconductors in state-of-the-art field-effect transistor (FET) technology [75, 76]. Also record spin lifetimes have been achieved. In early experiments, only a few nanoseconds, but recently pushed beyond the value of 10 ns [174] because of the improved growth techniques. We are now at a stage, where large scale, defect free, and smooth interfaces of graphene and hBN [155, 181–185] can be easily produced, which is certainly helpful for mass market applications. The mentioned experimental findings about the spin and charge transport properties of graphene/hBN heterostructures demonstrate their importance and potential for the future generation of spintronics and spin-logic devices [2, 3, 154, 170, 171, 186–197].

In this chapter, we will discuss (hBN)/graphene/hBN heterostructures, in the context of spin lifetime limits and SR anisotropies. By combining first-principles calculations and the low energy graphene model Hamiltonian, introduced in Sec. 3.2, we describe the Dirac states of graphene in a variety of important structures. We present the extracted SOC parameters for proximitized graphene, which are in the μeV-range. The fitted model parameters, including SOC and also orbital ones, are very sensitive to the actual atomic arrangement in the heterostructure. Moreover, the parameters depend on the interlayer distance and especially the Rashba SOC can be precisely tuned by applying a transverse electric field. Armed with the fitted model parameters, we employ the Dyakonov-Perel formalism to calculate spin lifetimes for graphene in the nanosecond range, in agreement with recent experimental measurements. The values of the SR anisotropy $\xi = \tau_{s,z}/\tau_{s,x}$ are giant and maximal close to the charge neutrality point, decreasing with the doping level. Most important, we find that the anisotropy can be tuned within a few orders of magnitude by applying an external electric field, which controls the magnitude of the Rashba SOC.

4.2 Geometry, computational details, and band structure

In order to calculate the electronic band structure of (hBN)/graphene/hBN heterostructures from first-principles, we have to use a common unit cell for graphene and hBN. Therefore, we fixed the lattice constant of graphene [35] to $a = 2.46$ Å and changeed the hBN lattice constant from its experimental value [198] of $a = 2.504$ Å to the graphene one. The lattice constants of graphene and hBN differ by less than 2%, which justifies our assumption of commensurate geometries. Typically, only three high-symmetry stacking configurations are usually considered when graphene is placed above hBN, see Fig. 4.2. From previous density functional theory (DFT) studies, we also already know the configuration with the lowest energy, with one C atom over the B atom and the other C atom over the hollow site of

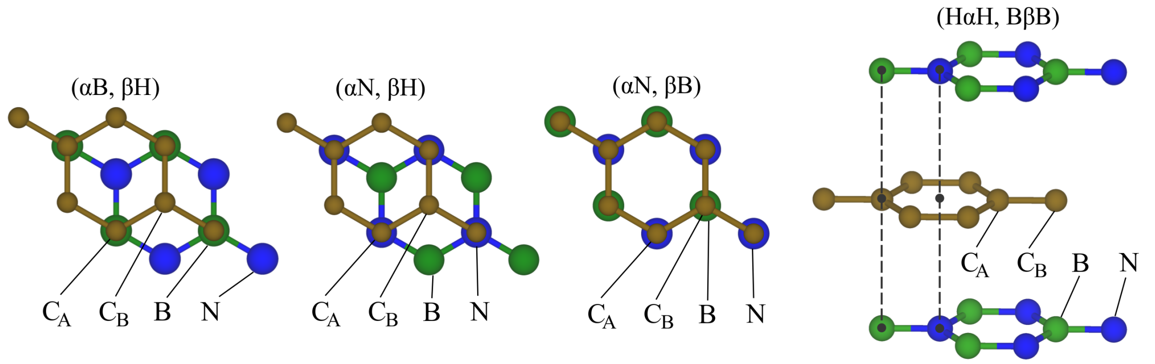

Figure 4.2: Three high-symmetry commensurate stacking configurations of graphene on hBN, i. e., the (αB, βH), (αN, βH), and (αN, βB) geometries. The (HαH, BβB) stacking is an example of hBN encapsulated graphene. The stacking terminology is described in the text.

hBN [199]. However, in real samples, the small lattice mismatch leads to the observation of a moiré-pattern, which consists of several local stacking geometries [200–202]. Even though the low energy bands of graphene differ among various stackings, the global band structure remains qualitatively the same [199, 203]. By considering all structural arrangements of graphene on hBN, we can get a more quantitative feeling for SOC in a realistic experimental setup.

The stacking of graphene on hBN is a crucial point and we first have to define a common terminology to distinguish them. We label the three relevant sites in hBN as the B site (Boron), the N site (Nitrogen), and the H site (hollow position in the center of the hexagon). Similarly, we have two graphene sublattices α (C_A) and β (C_B). We call the energetically most favorable configuration (αB, βH), where C_A is located above Boron, and C_B is above the hollow site. According to this definition, we define the other configurations as (αN, βH) and (αN, βB). Due to symmetry, the configurations with interchanged C_A and C_B sublattices give the same results. Not only the stacking is an important point, but also the interlayer distance between graphene and the hBN. A previous study has shown that the energetically most favorable interlayer distance slightly varies between the stackings [199]. We include a distance study for all three configurations in order to cross-check what the corresponding lowest energy distances are and to obtain a qualitative and quantitative feeling about how the proximity SOC depends on the interlayer distance.

In analogy to the graphene/hBN structures, a stacking sequence of hBN encapsulated graphene is then abbreviated as (UαV, XβY), indicating that the α (β) sublattice of graphene is sandwiched between the U and V (X and Y) sites of top and bottom hBN, each of which can take the values {B, N, H}. It has been shown [203] that the energetically most favorable sandwich structure is (HαH, BβB), which agrees with our findings, as we will see later. This means that the graphene α (β) sublattice is sandwiched between the two H sites (B sites) of top and bottom hBN. For a very accurate description of the encapsulated structures, one would have to vary both interlayer distances and check for the energetically most favorable situation. However, this is computationally very demanding and, for simplicity, we use the distances determined from the non-encapsulated structures. Of course, we respect the stackings between graphene and the top and bottom hBN layer individually, which can

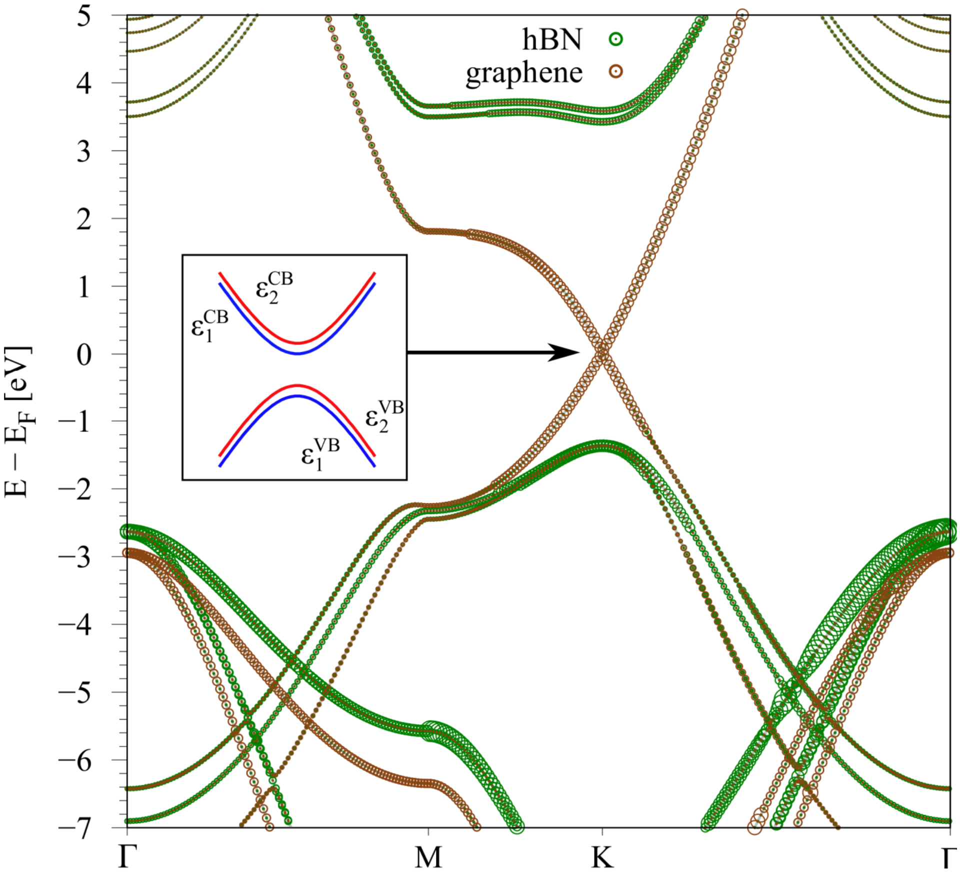

Figure 4.3: Calculated electronic band structure of the (HαH, BβB) geometry, see Fig. 4.2. The bands of graphene (hBN) are plotted in brown (green). The left inset shows a sketch of the low energy dispersion close to the K point. Due to the presence of the hBN layer(s), graphene's low energy bands are split into four states $\varepsilon_{1/2}^{CB/VB}$, separated by a band gap.

have different interlayer distances. In Fig. 4.2, we show the three commensurate stacking configurations of graphene on hBN, as well as the (HαH, BβB) geometry, as an example of hBN encapsulated graphene.

The following first-principles calculated results were obtained with a full potential linearized augmented plane wave (FLAPW) code based on DFT [204] and implemented in WIEN2k [205]. Exchange-correlation effects were treated with the generalized gradient approximation (GGA) [206], including a long-range vdW dispersion correction [207] and using a k-point grid of $42 \times 42 \times 1$ in the hexagonal Brillouin zone (BZ) if not specified otherwise. The values of the Muffin-tin radii we used are $R_C = 1.34$ for C atoms, $R_B = 1.27$ for B atoms, and $R_N = 1.40$ for N atoms. The Muffin-tin radius R in WIEN2k is defined in atomic units, i. e., $R = 1$ equals the Bohr radius a_0. We used the plane wave cutoff parameter $RK_{MAX} = 9.5$. In order to avoid interactions between periodic images of our slab geometry, we added a vacuum of at least 20 Å in z direction.

The calculated band structure of encapsulated graphene in the (HαH, BβB) configuration is shown in Fig. 4.3, as a representative example for all considered geometries. The other encapsulated stacking geometries, as well as graphene on hBN, exhibit a similar global band structure. The Dirac bands of graphene are located within the hBN band gap. In general, all geometries we consider in the following break the pseudospin symmetry, and open a band gap in graphenes spectrum. Then, for example, the orbitals from the $\mathrm{C_A}$ sublattice form the conduction band (CB), while orbitals from the $\mathrm{C_B}$ sublattice form the valence band (VB). In addition, the low energy bands split into four states $\varepsilon_{1/2}^{\mathrm{CB/VB}}$, see left inset in Fig. 4.3. The splitting of the bands originates from a combination of (proximity-induced) intrinsic and Rashba SOCs. In the following, we focus on the graphene Dirac bands in such (hBN)/graphene/hBN geometries. The DFT-computed low energy bands, which roughly look like the ones from the left inset of Fig. 4.3, are fitted to the model Hamiltonian, Eq. (3.7), introduced in Sec. 3.2. The fitted model parameters are extremely valuable for subsequent spin and charge transport simulations. Here, we finally use them to calculate spin lifetimes and SR anisotropies.

4.3 Graphene on hBN

In this section, we first discuss the non-encapsulated graphene/hBN heterostructures. For one exemplary case, we explicitly show a comparison between the DFT-calculated and model band structures. For all other stacking configurations, we only summarize the fitted model parameters in a tabular form. In addition, we analyze the influence of the interlayer distance between graphene and hBN on the extracted orbital and SOC model parameters. Moreover, we show the tunability of the parameters by applying a transverse electric field for one specific stacking configuration. We then introduce the Dyakonov-Perel formalism, from which we calculate spin lifetimes. Finally, we discuss the SR anisotropy and its electric field tunability.

4.3.1 Low energy bands

In Fig. 4.4, we show the calculated low energy Dirac bands of graphene in the vicinity of the K point, together with a fit to our minimal Hamiltonian $\mathcal{H}_{\mathrm{GR}}$ for the (αB, βH) configuration of graphene on hBN. We can see that the orbital band structure is perfectly reproduced by our model, see Fig. 4.4(a), in quite a large energy window of about ±100 meV around the Fermi level. The splittings of the bands are shown in Figure 4.4(b), which are in the μeV range and are defined as $\Delta\mathrm{E_{CB}} = \varepsilon_2^{\mathrm{CB}} - \varepsilon_1^{\mathrm{CB}}$ and $\Delta\mathrm{E_{VB}} = \varepsilon_2^{\mathrm{VB}} - \varepsilon_1^{\mathrm{VB}}$. Also the band splittings can be reproduced by the model, with a maximum discrepancy of about 10% compared to the first-principles data. More specifically, the model overestimates (underestimates) the splittings along the K-M (K-Γ) path. The reason for the discrepancy of the fit is the influence of the hBN substrate. Our model Hamiltonian is based on effective p_z orbitals of graphene only. However, in the presented case, the states forming the Dirac bands have an additional small contribution of p orbitals of hBN, as we find from the DFT-calculation. In particular, Boron p_z orbitals and Nitrogen ($p_x + p_y$) orbitals are contributing close to the charge neutrality point and are the origin of this difference [142]. However, the overall fit results are still very accurate and sufficient for our needs.

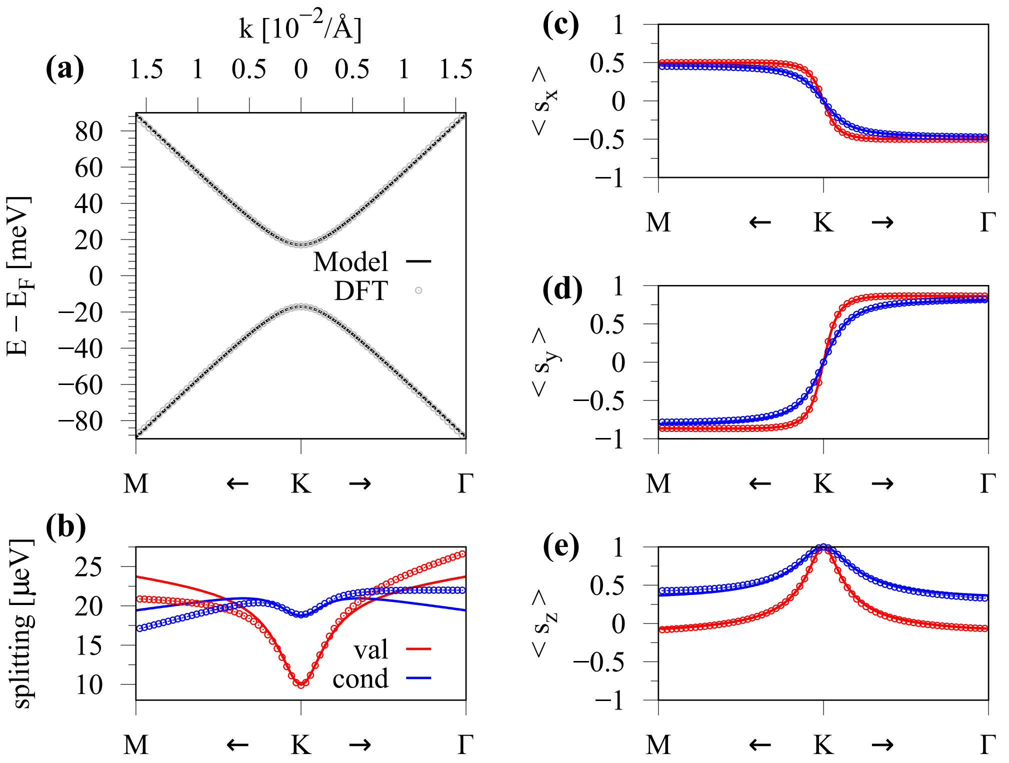

Figure 4.4: Calculated band properties of graphene on hBN in the vicinity of the K point for the (αB, βH) configuration and an interlayer distance of 3.35 Å. (a) DFT-calculated band structure (symbols) with a fit to the model Hamiltonian (solid line). (b) The splitting of the CB ΔE_{CB} (blue) and the VB ΔE_{VB} (red) close to the K point and calculated model results. (c)-(e) The spin expectation values of the bands ε_2^{VB} and ε_1^{CB} with a comparison to the model results. The fit parameters are given in Tab. 4.1.

Table 4.1: Fit parameters for the three graphene/hBN stacks for their energetically most favorable interlayer distances, employing the Hamiltonian $\mathcal{H}_{GR}$, Eq. (3.7). The Fermi velocity v_F, the gap parameter Δ, Rashba SOC parameter λ_R, intrinsic SOC parameters λ_I^A and λ_I^B, and pseudospin inversion asymmetry (PIA) SOC parameters λ_{PIA}^A and λ_{PIA}^B are summarized. In the last row we average over the configurations for each parameter.

Configuration	distance [Å]	v_F [$10^5 \frac{m}{s}$]	Δ [meV]	λ_R [μeV]	λ_I^A [μeV]	λ_I^B [μeV]	λ_{PIA}^A [μeV]	λ_{PIA}^B [μeV]
(αB, βH)	3.35	8.308	−17.08	10.65	5.00	9.37	33.58	37.57
(αN, βH)	3.50	8.197	16.31	12.67	11.78	13.96	4.431	26.68
(αN, βB)	3.55	8.128	23.50	17.89	12.21	15.82	12.91	29.73
average	3.47	8.211	7.577	13.74	9.66	13.05	16.97	31.33

Finally, Figs. 4.4(c)-(e) display the spin expectation values of the bands ε_2^{VB} and ε_1^{CB}, which are in perfect agreement with the model. The s_x and s_y spin expectation values show a pronounced signature of Rashba SOC, with a sign change around the K point. The s_z expectation values have a maximum at the K point, and slowly decay towards the M and Γ points, as we go to higher energies in the dispersion.

The model parameters are summarized in Tab. 4.1 for the three non-encapsulated graphene/hBN structures, considering their individual lowest energy interlayer distances. The interlayer distance results are discussed in the following section. All of the stacking configurations can be fitted with the same Hamiltonian $\mathcal{H}_{\mathrm{GR}}$, Eq. (3.7), just using different parameter sets. In general, the proximity-modified graphene Dirac spectrum is dominated by the pseudospin symmetry breaking (Δ), introducing a mass gap of tens of meV. Nevertheless, the band splittings and the SOC parameters, which will dominate spin lifetimes and SR, are small and in the μeV range.

4.3.2 Distance study

As already mentioned, different stacking configurations lead to different interlayer distances between graphene and hBN when minimizing the total energy of the individual geometries. In this regard, DFT-predicted results can, sometimes significantly, differ from reality because the energetically most favorable interlayer distance varies between the employed methods, which use different vdW interactions [208]. Therefore, it is important to know how the proximity SOC parameters evolve with distance. In Fig. 4.5, we show the fit parameters of $\mathcal{H}_{\mathrm{GR}}$ as a function of the distance between graphene and hBN and for the different stacking configurations. Overall, the lowest energy is obtained for the (αB, βH) configuration with an interlayer distance of 3.35 Å, see Fig. 4.5(a). The energetically most favorable interlayer distances for the (αN, βH) and (αN, βB) configurations are obtained at distances of 3.50 Å and 3.55 Å. Translating this into real samples, where a moiré-pattern is present, leads to a wave-like graphene sheet above hBN [209–211].

The Fermi velocity v_{F}, see Fig. 4.5(b), which reflects the nearest neighbor hopping strength via $t = \frac{2\hbar v_{\mathrm{F}}}{\sqrt{3}a}$ [112], grows as a function of distance, especially for the (αN, βH) and (αN, βB) configurations. For all three structures, v_{F} converges to a common value of about $8.3 \times 10^5 \, \frac{\mathrm{m}}{\mathrm{s}}$. Once, the interlayer distance approaches infinity, we recover the band structure properties of a freestanding graphene sheet. Thus, it is not surprising that the Fermi velocity converges to a common value for all geometries. In contrast to that, the gap parameter Δ decreases with distance, in agreement with literature [199]. Once we spatially separate graphene and hBN, the sublattice (pseudospin) symmetry breaking reduces, the staggered potential parameter Δ decreases, and the mass gap in the Dirac spectrum diminishes.

One at first glance illogical observation is that the gap parameter Δ of the (αB, βH) configuration is opposite in sign compared to the other two stackings, as seen in moiré-pattern geometries [209–211]. An issue which can be easily resolved, remembering that the parameter Δ determines the pseudospin ordering of the bands, as already discussed in Sec. 3.3. In the (αB, βH) configuration, the $\mathrm{C_A}$ sublattice is located above the Boron. By projecting onto the basis states of the two carbon atoms in the DFT calculation, we find that the orbitals from sublattice $\mathrm{C_A}$ form the VB. Consequently, we need a negative value of Δ in the model to match the sublattice character of the DFT results. In contrast, the other two stackings we consider have the $\mathrm{C_A}$ sublattice above the Nitrogen. Then, $\mathrm{C_A}$ orbitals form the CB leading to a positive value of Δ. In experiments, typically micrometer size flakes of graphene and hBN are considered. As already mentioned, all of our stacking configurations

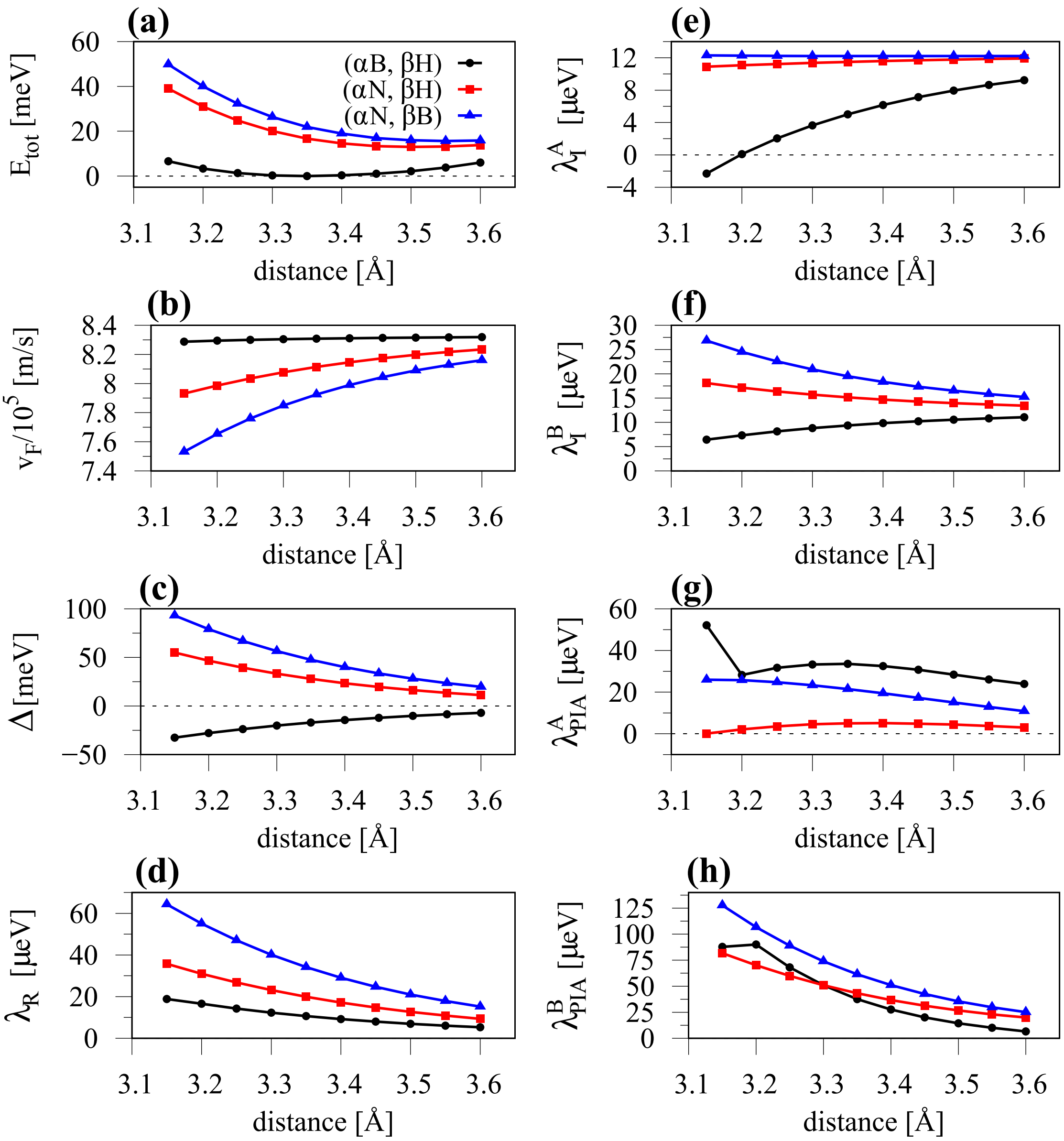

Figure 4.5: Fit parameters as a function of interlayer distance between graphene and hBN for the three different stacking configurations. (a) The total energy, (b) the Fermi velocity v_F, (c) the gap parameter Δ, (d) the Rashba SOC parameter λ_R, (e) the intrinsic SOC parameter λ_I^A for sublattice A, (f) the intrinsic SOC parameter λ_I^B for sublattice B, (g) the PIA SOC parameter λ_{PIA}^A for sublattice A, and (h) the PIA SOC parameter λ_{PIA}^B for sublattice B.

appear simultaneously in a moiré-pattern geometry. With that in mind, there can be a region with $\Delta < 0$, spatially separated from a region with $\Delta > 0$. Consequently, there must be local regions, where the orbital gap closes when the two sublattices feel the same surrounding potential, and the low energy dispersion is solely dominated by SOC.

The Rashba SOC parameter, see Fig. 4.5(d), also decreases with distance. By varying the interlayer distance within our considered range of about 3.1–3.6 Å, the Rashba parameter can be significantly tuned by about a factor of 2–3. When the distance between graphene and hBN approaches infinity, we practically recover the properties of pristine graphene and the Rashba SOC parameter vanishes. The two intrinsic SOC parameters $\lambda_{\mathrm{I}}^{\mathrm{A}}$ and $\lambda_{\mathrm{I}}^{\mathrm{B}}$ approach the intrinsic SOC of 12 μeV of pristine graphene [111] as we increase the distance, see Figs. 4.5(e,f). However, for small interlayer distances the hBN substrate induces quite a significant contribution to graphene's SOC, as can be seen for the (αB, βH) geometry, where negative values of $\lambda_{\mathrm{I}}^{\mathrm{A}}$ can be achieved. Especially the $\lambda_{\mathrm{I}}^{\mathrm{B}}$ parameter shows a giant relative tunability with respect to the interlayer distance.

Finally, we find that the two PIA SOC parameters $\lambda_{\mathrm{PIA}}^{\mathrm{A}}$ and $\lambda_{\mathrm{PIA}}^{\mathrm{B}}$, see Figs. 4.5(g,h), also decrease with distance. Overall, as expected, we restore the pristine graphene properties as the interlayer distance gradually increases. However, by pushing the graphene towards the hBN, one could open a large mass gap and induce a significant amount of proximity SOC in graphene. A recent experiment [212] could demonstrate the band gap opening due to external hydrostatic pressure, which diminishes the interlayer distance in a graphene/hBN moiré-structure, confirming the presented findings. What remains to be proven is the distance-tunability of SOC.

4.3.3 Transverse electric field

For such heterostructures, transverse electric fields can be used in experiments to control the Fermi level. With the help of top and back gate electrodes, one can tune the doping level and simultaneously apply an electric displacement field across (hBN)/graphene/hBN structures. How does the electric field influence the low energy Dirac states? To answer this question, we consider our lowest energy configuration (αB, βH) for graphene on hBN, as an exemplary case. Similar observations hold for the other geometries. In a similar way, DFT calculations have revealed that the Rashba SOC in pristine graphene can be tuned with an electric field [111]. In the DFT-code WIEN2K, that we employ here, the electric field is modeled by a zig-zag potential along the z direction (transverse to the heterostructure).

For every magnitude of the electric field we extract the DFT-calculated low energy band structure of graphene and employ the model Hamiltonian to find the best-fitting parameters. In Fig. 4.6 we summarize the fit parameters for the (αB, βH) configuration as a function of the external electric field. Indeed, most of the parameters can be influenced by the field. In Fig. 4.6(a), we display the evolution of the VB edge with respect to the Fermi level, which is negative and independent of the electric field. Consequently, the Fermi level will always be located within the orbital gap of the Dirac states and no doping occurs for our DFT-calculated results.

The Fermi velocity v_{F}, as well as intrinsic SOC parameters $\lambda_{\mathrm{I}}^{\mathrm{A}}$ and $\lambda_{\mathrm{I}}^{\mathrm{B}}$, are barely affected. Within the used field range of ±5 V/nm, which are experimentally accessible, we find that the intrinsic SOC parameters can be changed by only about 1 μeV. However, the field tunes the orbital gap parameter Δ quite significantly. The built-in sublattice asymmetry can be increased (decreased) with a negative (positive) electric field. Since the orbital gap in the Dirac spectrum is roughly calculated as 2Δ, it can be tuned by nearly 100% in magnitude when switching the field from 5 V/nm to -5 V/nm.

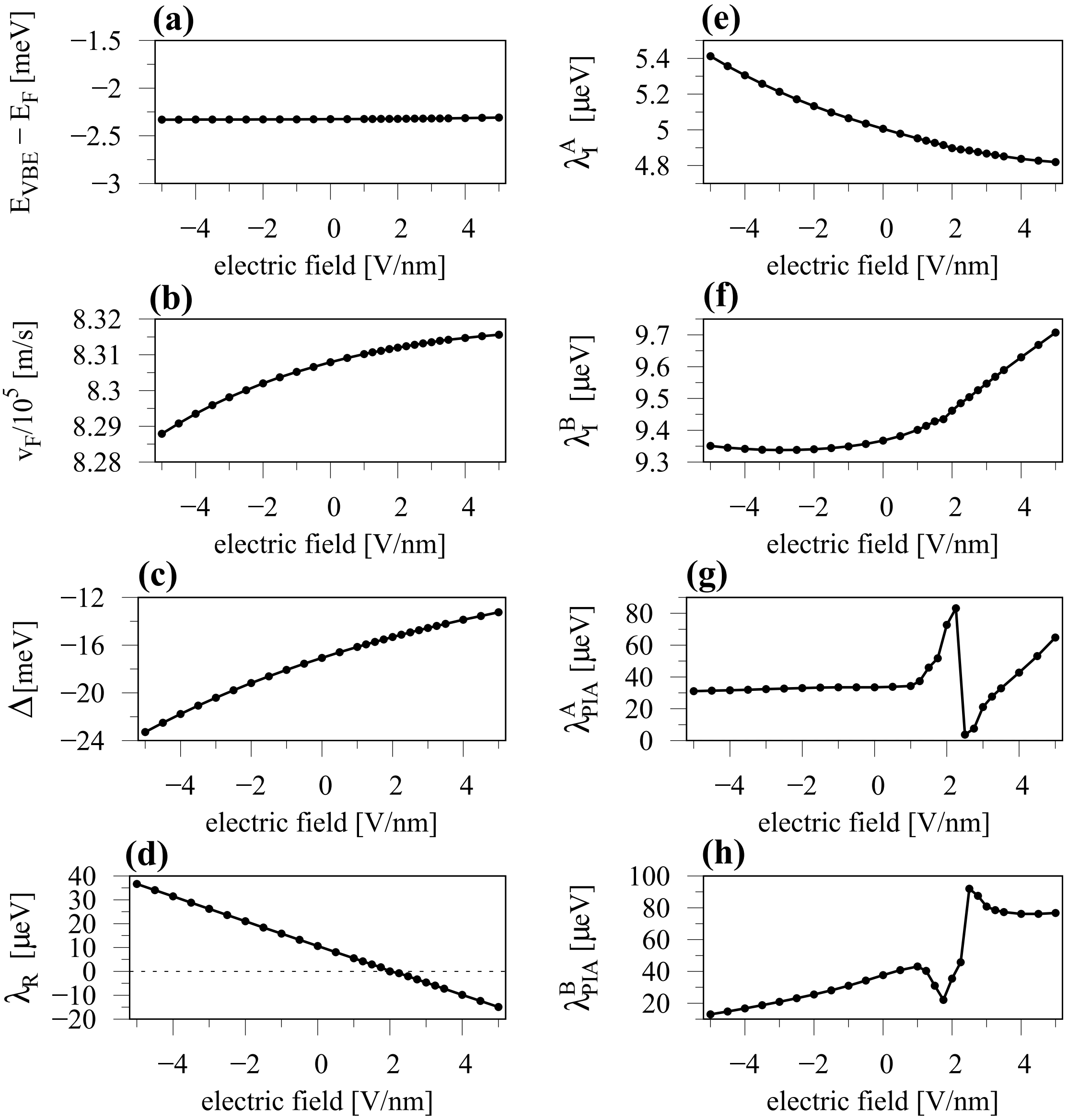

Figure 4.6: Fit parameters as a function of the applied transverse electric field for the (αB, βH) configuration. (a) The VB edge with respect to the Fermi level, (b) the Fermi velocity v_F, (c) the gap parameter Δ, (d) the Rashba SOC parameter λ_R, (e,f) the two intrinsic SOC parameters λ_I^A and λ_I^B, and (g) the PIA SOC parameters λ_{PIA}^A and λ_{PIA}^B.

Even more fascinating, and this will have significant impact on the spin lifetimes, is that the Rashba and PIA SOC parameters drastically change with the field. As we know from theory, the Rashba SOC dictates the in-plane spin lifetimes [2, 3]. In Fig. 4.6(d), we show that the Rashba parameter changes linearly from about 40 μeV to -20 μeV with the field, translating into a giant tunability that includes a zero transition at about 2 V/nm. Remarkably, one can precisely control the Rashba SOC and even tune it to zero. We notice that near 2 V/nm, where the Rashba parameter is zero, the PIA SOC parameters show a huge jump in their electric field behavior. We were not able to find an intuitive explanation for this, but believe that it is connected with the zero transition of the Rashba SOC.

4.3.4 Spin relaxation anisotropy

Measuring the SR anisotropy is gaining strong attention at the moment [159–161], because spin lifetimes depend on the actual spin orientation. Experiments could show that in hBN encapsulated bilayer graphene (BLG), there is evidence for strong and gate tunable spin lifetime anisotropy, which is solely due to SOC [213, 214]. In these encapsulated BLG heterostructures, out-of-plane spins show a long lifetime of nearly 10 ns, similarly to monolayer graphene samples. In addition, a marked SR anisotropy of $\xi \approx 10$ is observed near the charge neutrality point. The resolution lies in the intrinsic SOC of BLG, being now strong enough to play the dominant role for spin manipulation due to encapsulation with hBN. Analogously to hBN encapsulated BLG, graphene on TMDCs also shows $\xi \approx 10$. In contrast, the origin is not the weak intrinsic SOC (10 μeV [111, 139]), but graphene acquires strong valley Zeeman SOC (1 meV [88, 140]), being induced from the TMDC. However, these giant spin-orbit fields detrimentally influence the spin lifetimes, reducing them to the tens of picosecond range. Moreover, heterostructures of BLG on a TMDC show even larger anisotropies $\xi \approx 40 - 70$ [215], with intermediate out-of-plane spin lifetimes of about 1 ns.

Theory predicted [100], and experiments confirmed [165, 213, 214, 216], that 2D materials can give unique control over ξ. For example, the SR anisotropy ξ in encapsulated BLG can be tuned by two orders of magnitude by a transverse electric field [214] at a fixed doping level. Remarkably, near the charge neutrality point, ξ increases with the field. This is in contrast to the expectation of increasing the Rashba SOC and reducing the out-of-plane spin lifetime. Fortunately, we know from DFT studies that the BLG low energy band splittings are not sensitive to moderate electric fields [217] and keep their intrinsic value of about 24 μeV. Under this condition, only the out-of-plane spin polarization s_z controls the anisotropy, which indeed increases with moderate applied fields [214]. From recent theoretical considerations, giant SR anisotropies can be also expected in graphene/topological insulator (TI) heterostructures [218]. Similar to graphene/TMDC structures, the valley Zeeman SOC is the origin. In addition, a marked electron-hole asymmetry in the anisotropy can be present, which is due to a significant contribution from the PIA SOC. Given all these results, measuring the SR anisotropy can be a tool to determine the strength and type of the induced SOC in graphene.

What about the spin lifetime limits and SR anisotropies in our graphene/hBN structures? We have seen that the model Hamiltonian $\mathcal{H}_{\mathrm{GR}}$, Eq. 3.7, is capable of reproducing the orbital band structure, band splittings, as well as spin expectation values near the K point, see Fig. 4.4. In the following, we employ the model in combination with our fit parameters for different geometries summarized in Tab. 4.1 and for an electric field shown in Fig. 4.6, to calculate spin lifetimes and SR ratios. We set up a dense mesh near the K point and calculate for each k point the eigenvalues, as well as the corresponding spin expectation values, of the four Dirac bands. To calculate the SR times, we define the spin-orbit field components $\omega_{k,\mathrm{i}}$ as [3]

$$\omega_{k,\mathrm{i}} = \frac{\Delta \mathrm{E}_k}{\hbar} \cdot \frac{s_{k,\mathrm{i}}}{s_k}, \tag{4.1}$$

where k is the momentum and $s_{k,\mathrm{i}}$ are the spin expectation values along the direction $\mathrm{i} = \{\mathrm{x}, \mathrm{y}, \mathrm{z}\}$. The energy splitting of the Dirac bands is $\Delta \mathrm{E}_k$ (either CB or VB) and $s_k = \sqrt{s_{k,\mathrm{x}}^2 + s_{k,\mathrm{y}}^2 + s_{k,\mathrm{z}}^2}$ is the absolute value of the spin. By that, we obtain at each k point the spin-orbit vector fields, for the CB and VB. Following the derivation in Refs. [100, 219], we then calculate the SR times as follows

$$\tau_{s,\mathrm{x}}^{-1}(\mathrm{E}) = \tau_p \cdot \langle \omega_{k,\mathrm{y}}^2 \rangle + \tau_{iv} \cdot \langle \omega_{k,\mathrm{z}}^2 \rangle, \tag{4.2}$$

$$\tau_{s,\mathrm{y}}^{-1}(\mathrm{E}) = \tau_p \cdot \langle \omega_{k,\mathrm{x}}^2 \rangle + \tau_{iv} \cdot \langle \omega_{k,\mathrm{z}}^2 \rangle, \tag{4.3}$$

$$\tau_{s,\mathrm{z}}^{-1}(\mathrm{E}) = \tau_p \cdot \langle \omega_{k,\mathrm{x}}^2 + \omega_{k,\mathrm{y}}^2 \rangle. \tag{4.4}$$

The average $\langle \cdot \rangle$ is performed over all k-points that have the same constant energy E, either belonging to the CB or VB. For the calculation of the averages $\langle \cdot \rangle$, we use energy steps of 100 μeV with a smearing of ± 50 μeV, corresponding to a temperature of 0.58 K. In the energy region of the orbital gap, no states are available and spin lifetimes cannot be calculated. The momentum relaxation time is τ_p and τ_{iv} is the intervalley scattering time. Measurements [171–174] provide SR lengths of $\lambda_s \approx 20$ μm, SR times of $\tau_s \approx 8$ ns, and spin diffusion constants of $D_s \approx 0.04$ $\frac{\mathrm{m}^2}{\mathrm{s}}$. With the relation $\lambda_s = \sqrt{\tau_s D_s}$ and using that the spin diffusion constant is roughly equal to the charge diffusion constant $D_s \approx D_c = \frac{1}{2} v_\mathrm{F}^2 \tau_p$ and $v_\mathrm{F} \approx 8 \times 10^5$ $\frac{\mathrm{m}}{\mathrm{s}}$, we get $\tau_p = 125$ fs, which we use in the calculations. The value for τ_p is reasonable, assuming ultraclean samples. Since intervalley scattering times are hard to estimate from experiments, we consider it as a tunable variable, $\tau_{iv} = N \cdot \tau_p$ with $N = \{1, ..., 15\}$, for our calculations. By that, we obtain the SR time as a function of the energy, for spins along x, y, and z directions and for each ratio $N = \tau_{iv}/\tau_p$. More interesting than the individual SR times is the SR anisotropy $\xi = \tau_{s,\mathrm{z}}/\tau_{s,\mathrm{x}}$, because this can be experimentally detected and gives information about the SOC of the system.

As we have discussed above, it is most likely that one deals with a moiré-structure in experiments, containing all different stacking configurations. One can expect that electron spins will feel all kinds of local spin-orbit fields while *traveling* through graphene in proximity to hBN. Therefore, we consider directly the averaged parameters of graphene on hBN given in Tab. 4.1, for the calculation of spin lifetimes. In Fig. 4.7(a), we show a colormap of the calculated anisotropy ξ as a function of N (the intervalley scattering time) and the energy using the averaged parameters. We find that electrons have an anisotropy ratio $\xi \approx \frac{1}{2}$ almost independent of N and the energy, see Fig. 4.7(b). The out-of-plane (in-plane) spin lifetimes are about 10 (5) nanoseconds for electrons, in good agreement with experiments [171–174]. Note that for our isotropic model Hamiltonian, in-plane spin lifetimes for x and y direction are the same.

Close to the band edges, which would correspond to the charge neutrality point in experiment, the anisotropy can reach very large values. The explanation is that at the band edges (directly at the K point), the s_z spin expectation value is maximal, while in-plane spin expectation values are zero, see for example Fig. 4.4. Consequently, the in-plane spin-orbit field components are zero, leading to infinite out-of-plane spin lifetimes and a giant anisotropy. The more we move away from the band edges, the greater will be the contribution from in-plane spin-orbit field components and the anisotropy shrinks. In

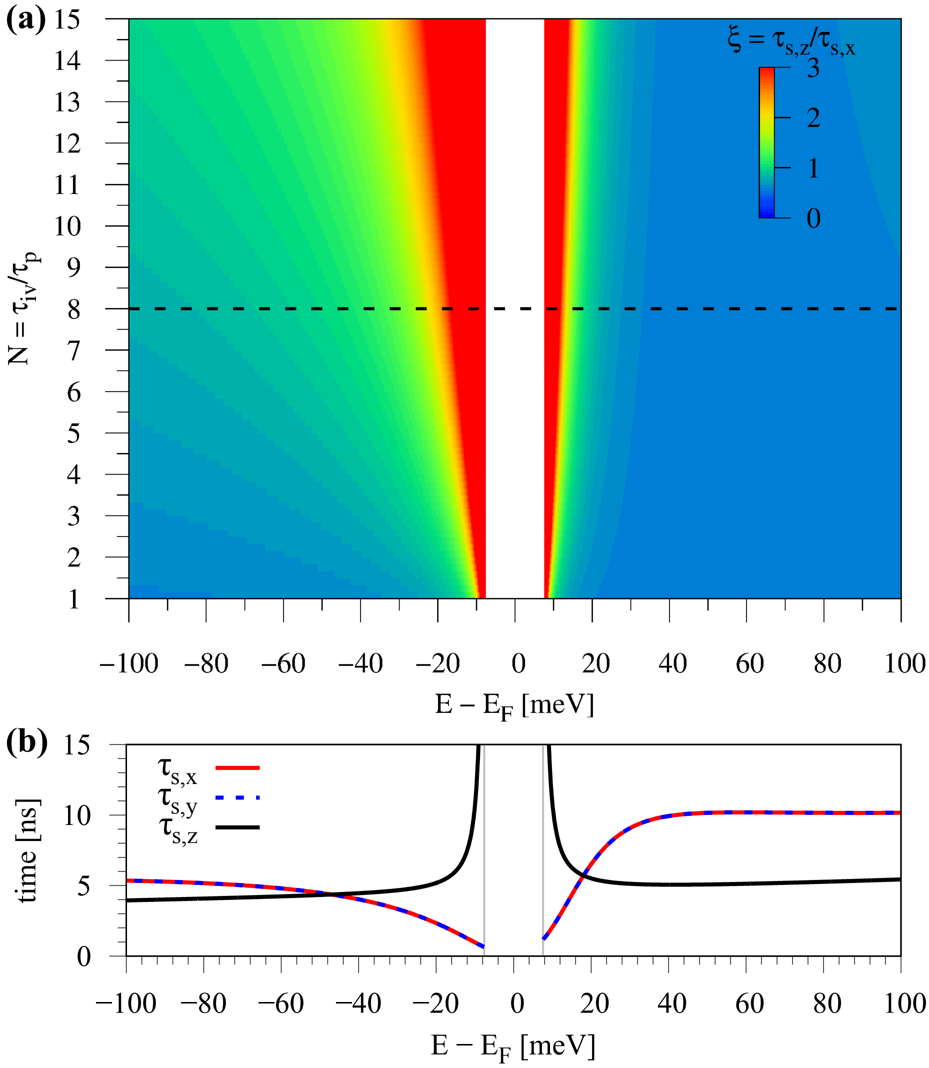

Figure 4.7: Calculated SR times and anisotropies for graphene on hBN. Here, we use the averaged parameters of the graphene/hBN heterostructures given in Tab. 4.1 (a) Colormap of the SR anisotropy $\xi = \tau_{s,z}/\tau_{s,x}$ as a function of $N = \tau_{iv}/\tau_p$ and the energy. (b) Individual SR times as a function of energy, corresponding to the dashed line in (a) with $\tau_p = 125$ fs and $\tau_{iv} = 8 \cdot \tau_p$. The grey lines indicate the band edges.

contrast to electron doping ($\xi \approx 1/2$), the anisotropy varies around $\xi \approx 1$ for holes and moderate doping densities. The energy range for which one can observe the giant anisotropy depends weakly on the intervalley scattering time. Comparing our model calculations with measured values for graphene on hBN and SiO_2 [159, 160, 172, 220, 221], yielding $\xi \approx 1$, we find good agreement to the presented case of the averaged parameters. Always keep in mind that in real experiments, spin lifetimes can locally drastically vary, but individual regions in macroscopic samples are not accessible.

We have seen now how the anisotropy depends on the doping level and intervalley scattering time. What about the electric field dependence? By employing top and back gate electrodes, one can individually tune the doping level and the displacement field across

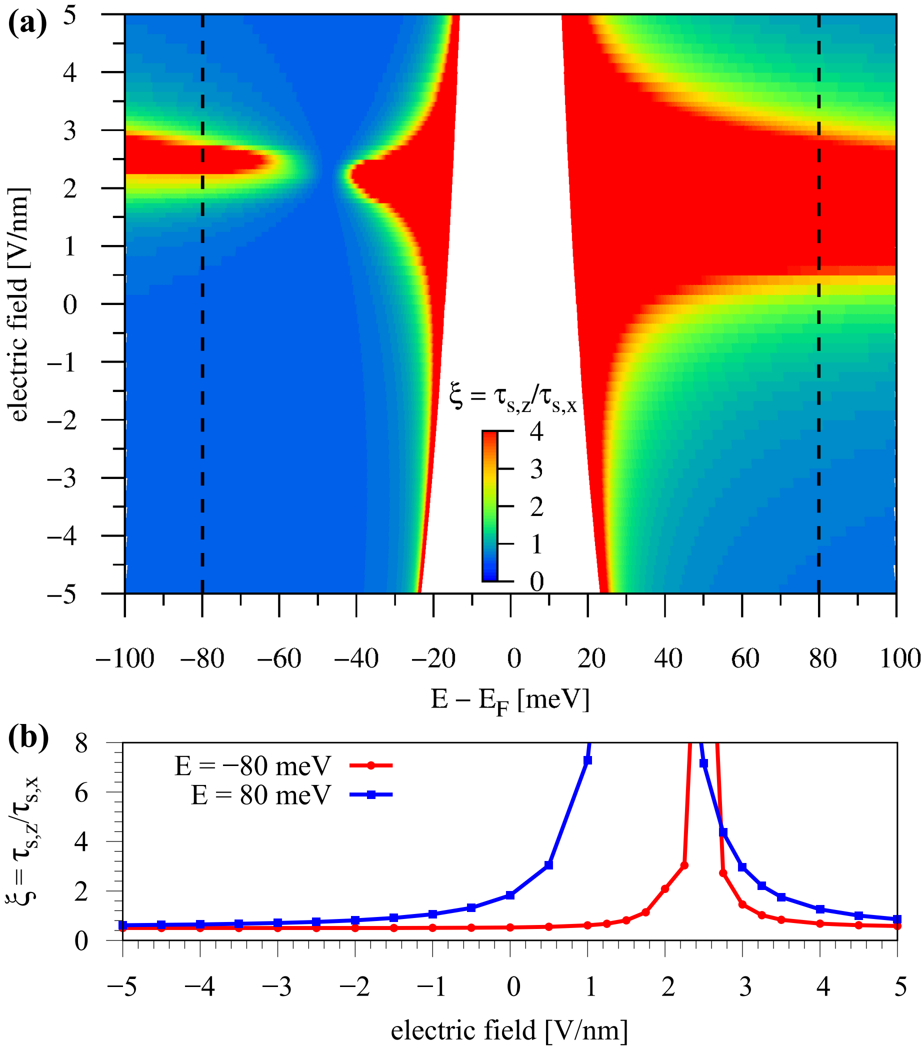

Figure 4.8: (a) Calculated SR anisotropy $\xi = \tau_{s,z}/\tau_{s,x}$ as a function of energy and applied transverse electric field for the (αB, βH) configuration, using $\tau_p = 125$ fs and $\tau_{iv} = 8 \cdot \tau_p$. (b) Anisotropy ξ at energies E $= \pm 80$ meV, corresponding to the dashed lines in (a).

the graphene/hBN interface. In Fig. 4.8 we show the SR anisotropy ξ specifically for the (αB, βH) configuration as a function of energy and electric field. For the calculation, we have employed the model parameters summarized in Fig. 4.6. For every value of the electric field, the individual parameter sets were used to calculate the spin lifetimes and anisotropy as functions of the energy, assuming an intermediate (but fixed) intervalley scattering time $\tau_{iv} = 8 \cdot \tau_p$. The result is plotted as a colormap in Fig. 4.8.

For all electric field values the anisotropy is giant near the charge neutrality point (the band edges), as explained above. Overall, one can see that the anisotropy is strongly tunable by means of external gating. Let us focus on the dashed line at E = 80 meV in Fig. 4.8(a). The corresponding evolution of the anisotropy, as a function of the field, is plotted in Fig. 4.8(b). At a strongly negative field value (-5 V/nm), $\xi \approx 1/2$, i. e., in-plane spin-orbit fields dominate the spectrum, which is consistent with our picture of a large Rashba SOC parameter, as seen in Fig. 4.6(d). By increasing the field to more positive values, the

Rashba parameter decreases, while ξ increases due to the competition between the different spin-orbit field components. Once $\lambda_{\mathrm{R}} \approx 0$, at around 2 V/nm, the Dirac bands are mainly s_z-polarized, leading to giant values of $\tau_{s,z}$ and to anisotropy ratios $\xi \gg 1$. Further increasing the electric field again increases the magnitude of the Rashba SOC and in-plane spin-orbit fields once more start to play a significant role until they dominate the spectrum for large enough positive electric fields. In Fig. 4.8(b), we explicitly show that an electric field can tune the anisotropy by two orders of magnitude at a fixed doping level. The presented gate-tunability of the anisotropy should be also valid for the other geometries and especially in graphene/hBN moiré-structures. Due to the high computational efforts, we restricted ourselves to the presented (αB, βH) configuration.

Why is the tunability of the SR anisotropy important? Experimentally, one can manipulate the "survival" of injected in-plane and out-of-plane spins by their different lifetimes. In the case of a large (small) anisotropy, out-of-plane (in-plane) spins will survive for a longer time than in-plane (out-of-plane) spins. As we have demonstrated, the electrical tunability of the anisotropy is giant and can be employed in novel dual-gated hybrid spintronics devices.

4.4 hBN encapsulated graphene

Similarly to the previous section, we now discuss the encapsulated (hBN)/graphene/hBN heterostructures. Again, we focus on the results for one specific geometry only, for which we show the model band structure fit, as well as the tunability of the orbital and spin-orbit parameters by applying a transverse electric field. Finally, we calculate spin lifetimes and SR anisotropies, and briefly discuss the obtained results.

4.4.1 Low energy bands

In the last section about graphene on hBN, we have found the energetically most favorable interlayer distance for each stacking geometry. Note that for the encapsulated geometries, depending on the relative stacking of the top and bottom hBN with respect to graphene, different interlayer distances can be present. For the encapsulated structures, we use the lowest energy distances from the non-encapsulated structures, respectively. In the very beginning of this chapter, when we have discussed the geometrical setup, the stacking sequences have been already defined. Just to remind the reader, the general notation is (UαV, XβY), indicating that the α (β) sublattice of graphene is sandwiched between the U and V (X and Y) sites of top and bottom hBN. The sites of hBN are labeled as {B, N, H}.

In Fig. 4.9, we show the low energy band properties of the (HαH, BβB) configuration, along with a fit to our model Hamiltonian. In the following, we denote the stacking (HαH, BβB) as the C1 configuration for shorter notation. For the C1 structure, the model is in perfect agreement with the DFT-computed data. Especially for the C1 configuration, the structure recovers the z-mirror symmetry of graphene, see Fig. 4.2. The model reduces to the D_{3h} symmetric version of the Hamiltonian with vanishing Rashba and PIA terms [112]. Indeed, it is enough to include just the four parameters v_{F}, Δ, $\lambda_{\mathrm{I}}^{\mathrm{A}}$, and $\lambda_{\mathrm{I}}^{\mathrm{B}}$, summarized in Tab. 4.2, for

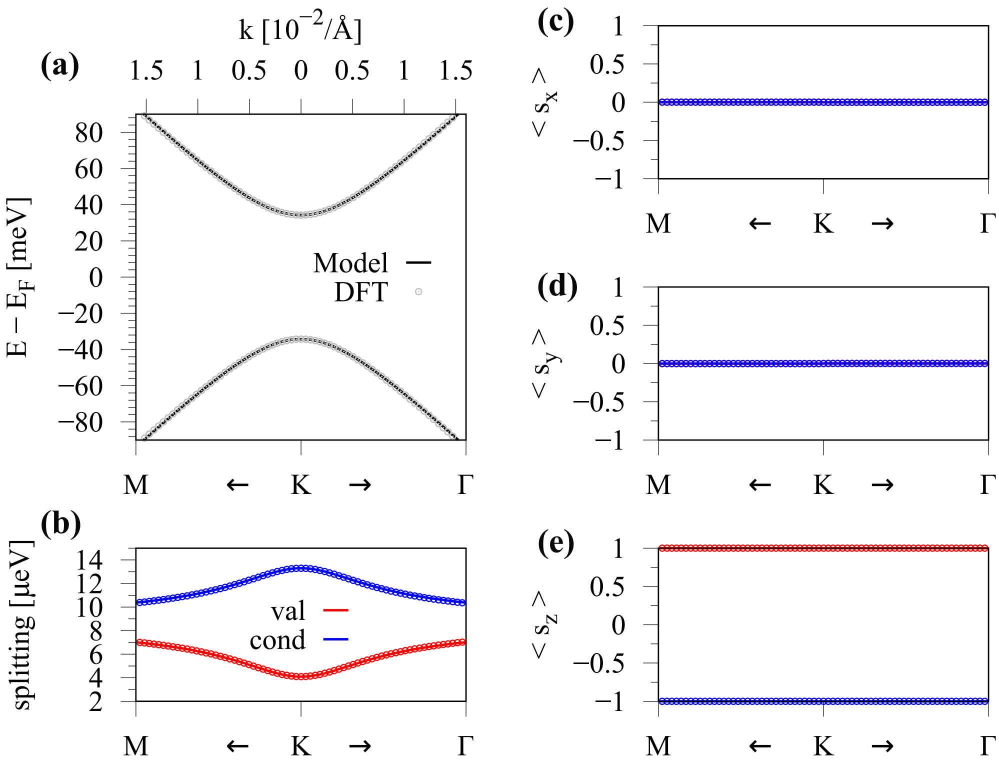

Figure 4.9: Calculated band properties of hBN encapsulated graphene in the vicinity of the K point for the (HαH, BβB) = C1 configuration and interlayer distances of 3.35 Å between graphene and the hBN layers. (a) DFT-calculated band structure (symbols) with a fit to the model Hamiltonian (solid line). (b) The splitting of the CB ΔE_{CB} (blue) and the VB ΔE_{VB} (red) close to the K point and calculated model results. (c)-(e) The spin expectation values of the bands ε_2^{VB} and ε_1^{CB} with a comparison to the model. The fit parameters are given in Tab. 4.2.

the fitting, Rashba and PIA SOC parameters are not necessary. As a consequence, the bands are purely s_z-polarized and we expect to get giant out-of-plane spin lifetimes and anisotropy ratios for this structure.

For all of the investigated structures, the low energy bands are somewhat similar, but each configuration has a very individual parameter set, as can be seen in Tab. 4.2. Overall, the magnitudes of the SOC parameters are tens of μeV, while the parameters can differ (also in sign) from structure to structure. For configurations, where the surrounding potentials for the two graphene sublattices become equal, the orbital gap parameter Δ vanishes. For configurations, which belong to the D_{3d} subgroup, the only allowed SOC parameters are $\lambda_I^A = \lambda_I^B = \lambda_I$ [112]. For z-mirror symmetric structures, also Rashba and PIA SOC parameters vanish. We see that symmetry plays an important role for encapsulated heterostructures and the obtained parameter space is an interesting playground for spin physics.

Keep in mind that, as a consequence of the slightly different lattice constants of graphene and hBN, a moiré-pattern is formed between graphene and the surrounding hBN layers. Experimentally, one can therefore expect local regions where no symmetry is present and our simple model, which is based on symmetry, would fail to describe the dispersion there.

Table 4.2: Fit parameters for the different hBN encapsulated graphene geometries, using the energetically most favorable graphene-hBN interlayer distances. The energy difference ΔE with respect to the C1 configuration, the Fermi velocity v_F, the gap parameter Δ, the Rashba SOC parameter λ_R, the two intrinsic SOC parameters $\lambda_\mathrm{I}^\mathrm{A}$ and $\lambda_\mathrm{I}^\mathrm{B}$, and the PIA SOC parameters $\lambda_\mathrm{PIA}^\mathrm{A}$ and $\lambda_\mathrm{PIA}^\mathrm{B}$. In the case of hBN/graphene/2hBN, the energy difference is with respect to the (BαBN, HβHH) configuration.

Configuration	ΔE [meV]	v_F [$10^5 \frac{\mathrm{m}}{\mathrm{s}}$]	Δ [meV]	λ_R [μeV]	$\lambda_\mathrm{I}^\mathrm{A}$ [μeV]	$\lambda_\mathrm{I}^\mathrm{B}$ [μeV]	$\lambda_\mathrm{PIA}^\mathrm{A}$ [μeV]	$\lambda_\mathrm{PIA}^\mathrm{B}$ [μeV]
(HαB, BβH)	0.01	8.296	0	0	2.19	2.19	0	0
(HαN, NβH)	26.60	8.068	0	0	13.31	13.31	0	0
(NαB, BβN)	32.05	7.931	0	0	15.76	15.76	0	0
(HαH, BβB) = C1	0	8.294	34.24	0	6.65	−2.05	0	0
(NαN, HβH)	26.09	8.070	34.10	0	11.38	15.47	0	0
(BαB, NβN)	31.76	7.932	−48.00	0	18.95	12.34	0	0
(HαB, NβH)	13.12	8.175	−34.85	−1.97	6.51	9.05	3.15	31.35
(NαB, BβH)	15.89	8.110	6.29	−7.75	5.09	12.84	1.26	22.72
(BαN, NβH)	29.20	7.998	−6.50	−4.97	15.23	13.92	−61.34	49.22
(NαB, HβH)	13.16	8.176	−0.069	−2.58	4.76	11.01	16.02	15.98
(BαB, NβH)	15.85	8.108	−41.50	−7.37	8.31	9.55	6.71	16.36
(NαN, BβH)	28.82	8.000	41.14	−3.29	11.89	17.26	94.83	−106.79
(HαBN, BβHH)	0.07	8.296	0.093	0.40	2.06	2.22	0	0
(BαBN, HβHH)	0	8.298	−34.06	0.31	−2.23	6.66	0	0

Still, by considering several geometries, one can get a very good qualitative and quantitative feeling for spin-orbit phenomena in these structures. Of course, experimentalists may also consider asymmetric hBN encapsulated graphene structures, say with two hBN layers below graphene and one hBN layer above it. The fit parameters for some asymmetric configurations are also summarized in Tab. 4.2, considering hBN to be AA′ stacked[2] with an interlayer distance of 3.35 Å. Comparing, for example, the (HαH, BβB) and (BαBN, HβHH) structures, one sees that the fitted parameters do not differ much, except that the graphene sublattices are interchanged.

We have seen earlier in this chapter, that SR is due to the interplay of the competing intrinsic and Rashba SOC parameters. Due to the hBN encapsulation, the average Rashba SOC can be significantly reduced, while intrinsic SOCs show similar magnitudes, when compared to the non-encapsulated structures. With regard to spin transport, hBN encapsulated graphene should therefore display much longer lifetimes for out-of-plane spins.

---

[2] AA′ stacking corresponds to the situation when the upper layer Boron (Nitrogen) atom is above the lower layer Nitrogen (Boron) atom.

4.4.2 Transverse electric field

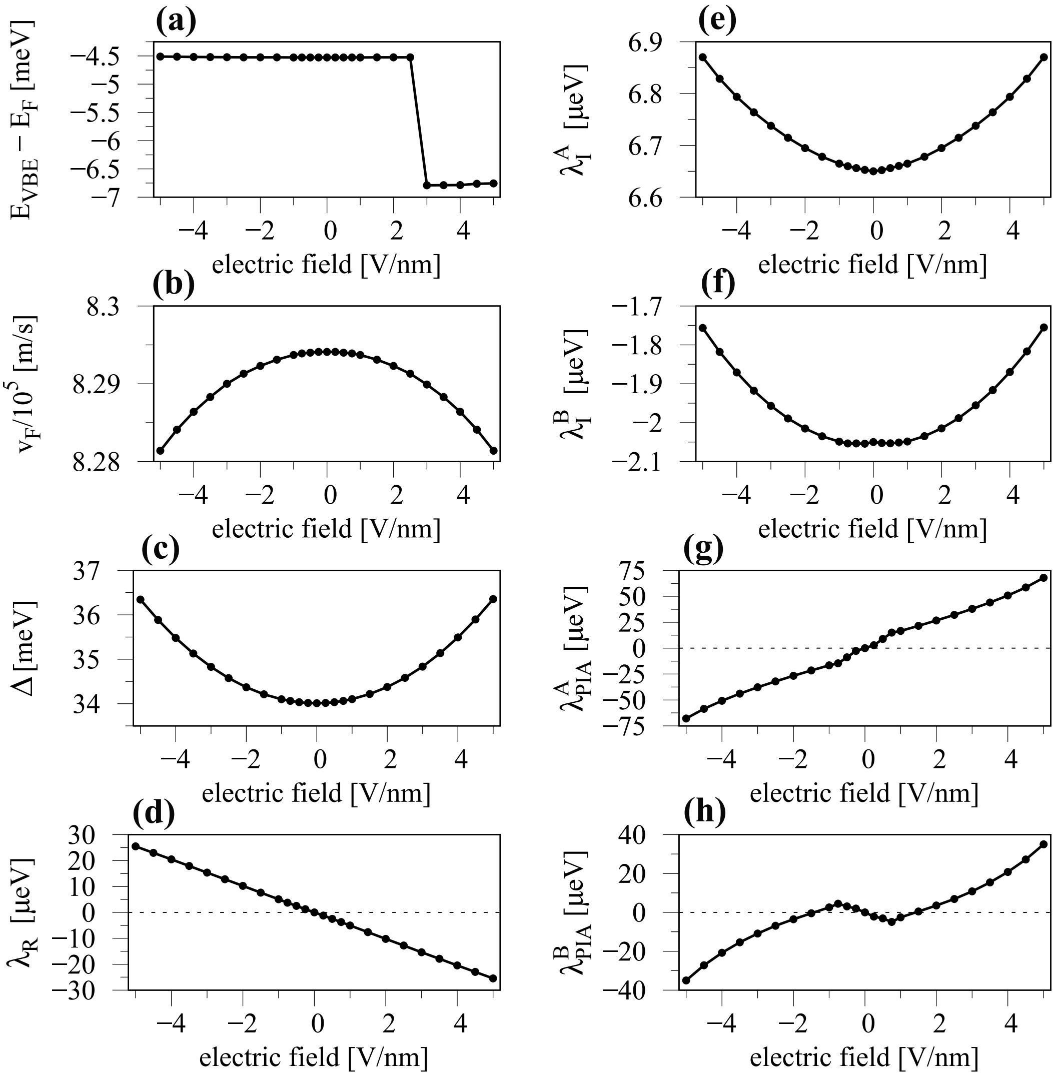

Figure 4.10: Fit parameters as a function of the applied transverse electric field for the C1 configuration. (a) The VB edge with respect to the Fermi level, (b) the Fermi velocity v_F, (c) the gap parameter Δ, (d) the Rashba SOC parameter λ_R, (e,f) the two intrinsic SOC parameters λ_I^A and λ_I^B, and (g,h) the PIA SOC parameters λ_{PIA}^A and λ_{PIA}^B.

Analogously to before, we study the effects of a transverse electric field on the low energy Dirac bands and the fit parameters for the C1 configuration of hBN encapsulated graphene. The obtained results of the tunability of the orbital and SOC parameters are summarized in Fig. 4.10. The VB edge is again lower in energy than the Fermi level for every field value we consider, i. e., no doping occurs in the structure. The sudden jump of the VB edge energy at about 2.5 V/nm can be attributed to the assigned Fermi levels in the DFT calculations, but has no consequences for the relevant results. The orbital parameters v_F and Δ depend in a symmetric fashion on the applied field, see Figs. 4.10(b,c), in contrast to the non-encapsulated case presented in Figs. 4.6(b,c). We also observe that the parameter Δ of the C1 configuration is roughly twice as large as compared to the non-encapsulated (αB, βH) structure because of the enhanced sublattice potential asymmetry. However, the absolute tunability in magnitude of v_{F} and Δ is larger in the non-encapsulated case.

Let us now discuss the SOC parameters. Similarly to the orbital parameters, also the intrinsic SOC parameters $\lambda_{\mathrm{I}}^{\mathrm{A}}$ and $\lambda_{\mathrm{I}}^{\mathrm{B}}$ are even functions and only weakly affected by the applied transverse electric field. Their functional behavior with respect to the field is again different, but the tunability in magnitude is roughly the same compared to the non-encapsulated case. In contrast to the already discussed parameters, the Rashba and PIA ones are odd functions, depend almost linearly on the electric field, and are strongly tunable. By applying an external field, we find a linear tunability of roughly 5 μeV per V/nm of λ_{R}, analogously to freestanding graphene [111]. By tuning the field amplitude within the considered electric field limits of ± 5 V/nm, we can precisely control the Rashba parameter within the range of ± 25 μeV. The two PIA parameters can be tuned even more drastically within the considered field range since $\lambda_{\mathrm{PIA}}^{\mathrm{A}}$ ($\lambda_{\mathrm{PIA}}^{\mathrm{B}}$) changes in between ± 75 μeV (± 40 μeV).

In summary, we observe a strong electric field tunability of the SOC parameters, which is related to the band splittings and, consequently, will have an impact on the spin lifetimes. As we have seen before for the non-encapsulated structure, this tunability can be used as an experimental control knob for varying the SR anisotropy ratio.

4.4.3 Spin relaxation anisotropy

In analogy to the previous section, we calculate the spin lifetimes and SR anisotropies for the considered C1 configuration as an example of hBN encapsulated graphene. In Fig. 4.11, we show the SR anisotropy $\xi = \tau_{\mathrm{s,z}}/\tau_{\mathrm{s,x}}$ as a function of energy and transverse electric field, fixing the intervalley scattering time. We find that ξ exhibits a giant maximum around zero field amplitude, which is connected to $\lambda_{\mathrm{R}} = 0$ for this symmetric geometry. For other structures, where a finite Rashba SOC is already present at zero field, we expect ξ to be giant for finite electric field amplitudes, as demonstrated above for the non-encapsulated (αB, βH) structure. If we increase the field amplitude at a fixed doping level, the anisotropy sharply decreases and converges to the Rashba limit $\xi = 1/2$. Again, this is connected to the strongly field-tunable Rashba parameter, while intrinsic SOCs stay nearly constant in value. Since the fitted parameters, see Fig. 4.10, have already shown symmetric behavior with respect to the applied field, this is manifested also in ξ. This can be seen best by looking at the evolution of ξ for fixed doping levels, shown in Fig. 4.11(b). Independent of the sign of the electric field, the anisotropy can be strongly tuned in this case of a symmetric geometry. Once again, we want to emphasize that the Rashba parameter dictates this behavior. If λ_{R} is large, in-plane spin-orbit fields dominate the spectrum and the anisotropy becomes $\xi = 1/2$. In contrast, when $\lambda_{\mathrm{R}} \approx 0$, out-of-plane spins have a giant lifetime and $\xi \gg 1$.

The overall tunability of ξ in our monolayer graphene heterostructures is comparable to recent experiments in dual-gated BLG [214]. Similarly, the anisotropy can be tuned within two orders of magnitude by applying an electric field for a fixed doping level. However, in encapsulated BLG, the SR anisotropy increases with increasing the electric field amplitude,

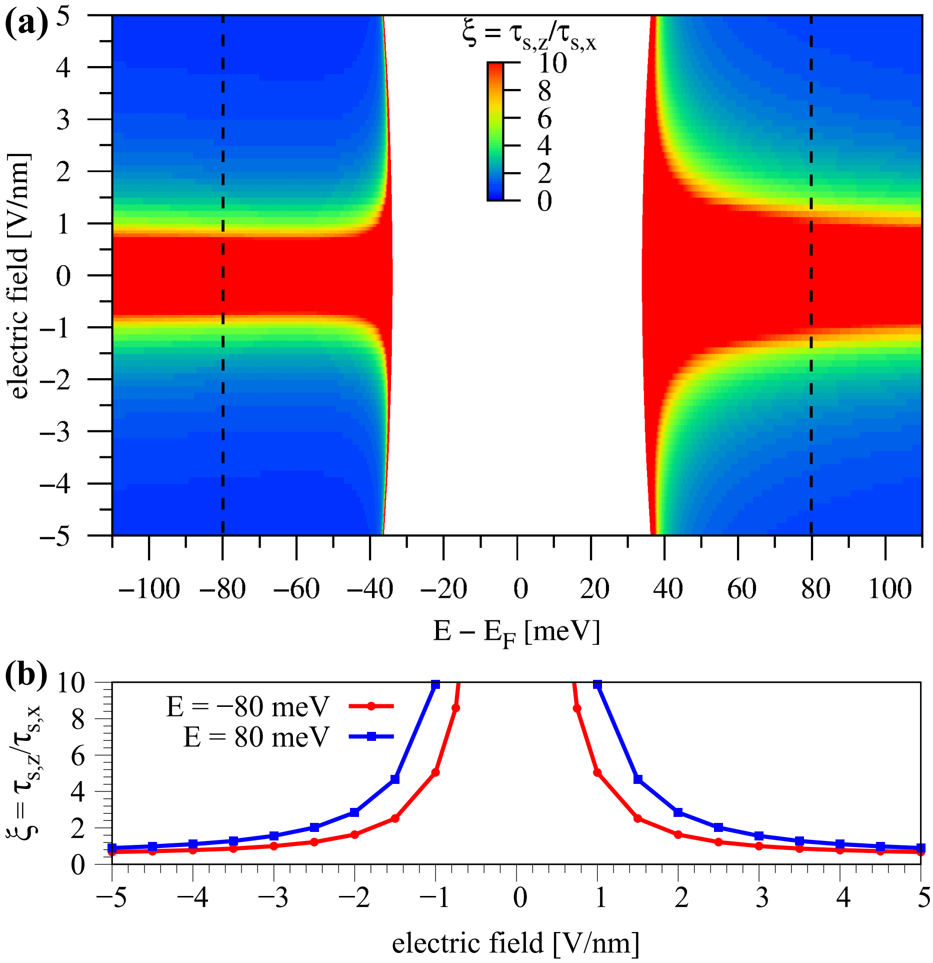

Figure 4.11: (a) Calculated SR anisotropy $\xi = \tau_{s,z}/\tau_{s,x}$ as a function of energy and applied transverse electric field for the C1 configuration of hBN encapsulated graphene, using $\tau_p = 125$ fs and $\tau_{iv} = 8 \cdot \tau_p$. (b) Anisotropy ξ at energies E $= \pm 80$ meV, corresponding to the dashed lines in (a).

opposite to the behavior that we found. The reason is that in BLG, it is not the spin splitting that is primarily affected by the field [217], but rather the out-of-plane spin expectation values of the relevant bands [214].

4.5 Summary and conclusion

In summary, we have performed extensive DFT calculations for several encapsulated and non-encapsulated (hBN)/graphene/hBN heterostructures. In combination with our low energy tight-binding model Hamiltonian ($\mathcal{H}_{\mathrm{GR}}$) we were able to extract valuable orbital and SOC parameters of graphene in contact to hBN. The extracted parameters depend on the actual stacking configuration, each having its own energetically most favorable interlayer distance. These observation are important for the understanding of realistic moiré-pattern geometries. In addition, a transverse electric field can be used to tune the SOCs and band splittings. As a consequence, spin-orbit fields, spin lifetimes, and most importantly spin transport properties can be controlled in dual gated structures, where the doping level, as well as the displacement field, can be tuned. From the calculation of spin lifetimes, we predict that the SR anisotropy $\xi = \tau_{s,z}/\tau_{s,x}$ can reach giant values ($\xi \gg 1$) and is strongly tunable by the field due to the precise control of the Rashba SOC in graphene/hBN heterostructures.

Recent experiments, reporting on the spin-orbit gap in mono- and bilayer graphene have found that a few tens of μeV can now be spectrally resolved [139, 222]. Thus, we believe that also our obtained results, which are precisely in this energy regime, can be experimentally verified. Based on our observations, we expect the most striking impact to be in SR anisotropy measurements, as we have shown a wide tunability of the relevant SOC parameters.

CHAPTER 5

Proximity spin-orbit coupling in graphene on Bi_2Se_3

This chapter is based on the publications: K. Zollner and J. Fabian, Physical Review B ***100****, 165141 (2019), "Single- and bilayer graphene on the topological insulator* Bi_2Se_3*: Electronic and spin-orbit properties from first principles", and K. Zollner and J. Fabian, Physica Status Solidi (b)* ***258****, 2000081 (2020), "Heterostructures of graphene and topological insulators* Bi_2Se_3*,* Bi_2Te_3*, and* Sb_2Te_3*".*

5.1 Introduction

Proximity effects [30] enable us to induce custom-made properties in two-dimensional (2D) materials within van der Waals (vdW) heterostructures [34, 223, 224]. In this context, also three-dimensional (3D) topological insulators (TIs) [225], such as Bi_2Se_3, Bi_2Te_3, and Sb_2Te_3, are important because of their strong spin-orbit coupling (SOC) and protected Dirac surface states with spin-momentum locking [226–229], which can couple to other materials. As demonstrated by angle resolved photoemission spectroscopy (ARPES) [230] and density functional theory (DFT) calculations [231–233], about 5–6 quintuple layers (QLs) are necessary to decouple the surfaces of the TI such that the topologically protected Dirac states emerge.

First approaches to manipulate the surface states have focused on magnetically doping the TI, which breaks time-reversal symmetry and opens a mass gap [234, 235]. The combination of magnetism, strong SOC, and the gap opening leads to the observation of the quantum anomalous Hall (QAH) effect in magnetic TIs [236, 237] if the Fermi energy is located in the magnetization gap. Similarly, the topologically protected surface states can be manipulated by magnetic materials via proximity effects. For example, when Bi_2Se_3 is in proximity to the magnetic insulators MnSe [238] or EuS [239], also a gapped Dirac state emerges. Such TI/ferromagnetic insulator (FMI) hybrids are also a playground for new physical phenomena, such as the axion insulator state [240], where the topological magnetoelectric effect occurs [241]. The axionic state can be realized when all surface states are gapped, i. e., the magnetization is perpendicular to all surfaces of the TI [242]. Also other novel states can be potentially realized in TI hybrids. For example, (ferromagnet)/TI/superconductor structures show indications for Majorana fermions [227, 243, 244], which are seen as vital ingredients for quantum computing [245, 246].

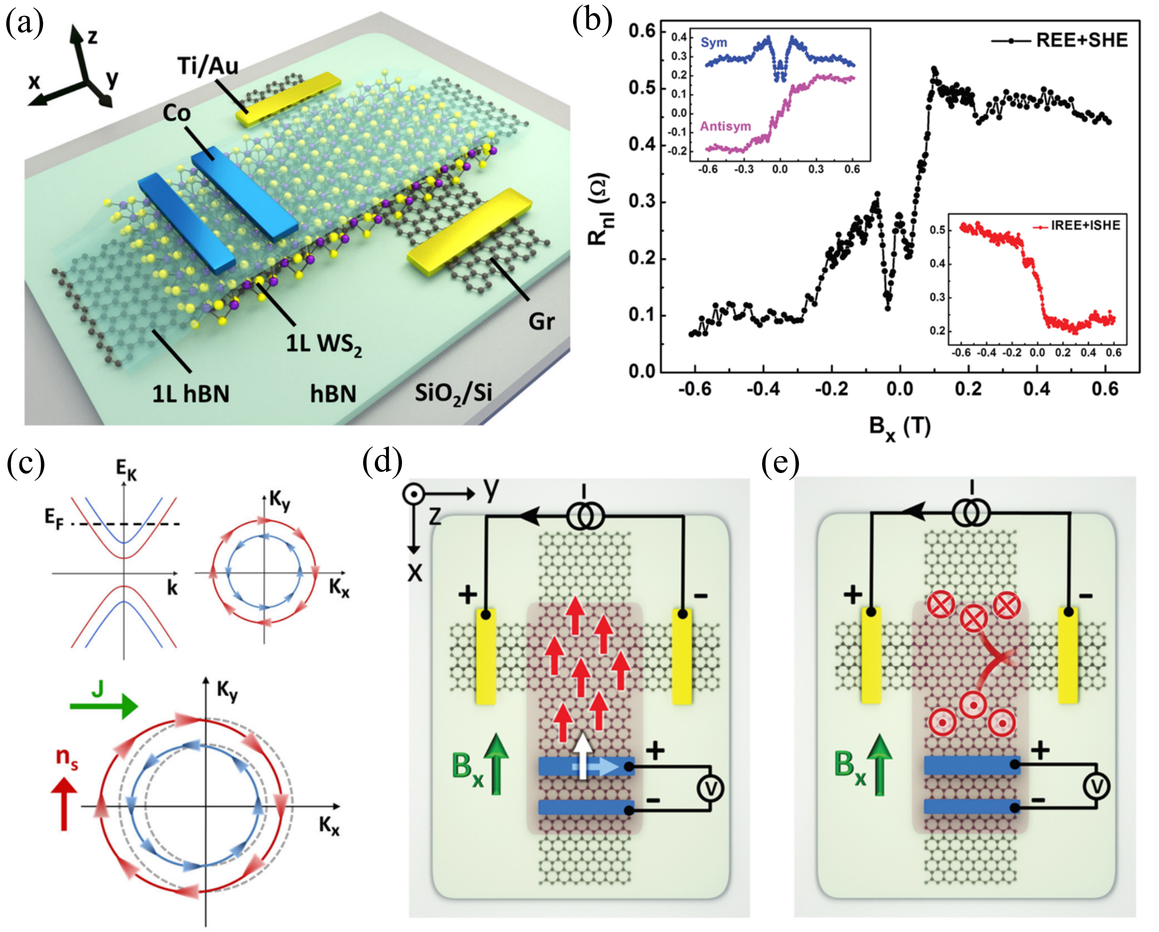

Figure 5.1: Spin-to-charge interconversion in a graphene/transition-metal dichalcogenide (TMDC) heterostructure. (a) Sketch of the graphene/WS$_2$ heterostructure encapsulated by top monolayer hexagonal boron nitride (hBN) and bottom bulk hBN with Ti/Au and Co electrodes and on a SiO$_2$/doped-Si substrate. (b) The measured non-local resistance (R_{nl}) as function of the applied in-plane magnetic field B_x. The non-local voltage (V_{nl}) is measured at the Co when charge current is injected at the Ti/Au electrodes. Due to Rashba-Edelstein effect (REE) and spin Hall effect (SHE), a charge-to-spin conversion happens in the proximitized graphene region. The right lower inset shows the inverse measurement result, i. e., spin-to-charge conversion when spins are injected from the Co and the voltage is measured at the Ti/Au electrodes. The upper left inset shows the decomposition of the signal into symmetric and antisymmetric components, in order to discriminate the contributions dominated by SHE and REE, respectively. (c) Schematic band structure diagram of the proximity spin-orbit split graphene Dirac bands. A charge current (J), shifts the Fermi contours and leads to a non-equilibrium spin density (n_s) due to REE, with a spin polarization perpendicular to the current direction. (d,e) Measurement schematics and corresponding spin accumulations for the REE and SHE, respectively. Red arrows represent the generated spin density, with in-plane (out-of-plane) spins for REE in (d) (SHE in (e)). The white arrow in (d) represents the Co magnetization. Figures are from Ref. [101].

Not only the TI itself can be subject to proximity effects, but it can also provide them. Especially graphene/TI bilayers have been investigated in several studies [218, 247–262]. One cannot only epitaxially grow high-quality Bi$_2$Se$_3$ on graphene [252, 253], but also a significant amount of proximity SOC is induced. Moreover, graphene on a 3D TI can exhibit quantum spin Hall states [254, 258] and spin transport experiments have demonstrated spin-to-charge conversion in such bilayers [261, 263]. Remarkably, the proximity SOC can be tuned in type and magnitude by twisting the layers [218, 249]. By comparing recent studies of graphene/TI [218, 247, 248, 264] and graphene/TMDC heterostructures [88, 140], one can certainly find similarities. For example, in both cases the Dirac bands of graphene are preserved, giant SOC is induced by the proximity effect, and spin-to-charge conversion has been demonstrated [89, 101, 102, 263]. In Fig. 5.1, we summarize the main results from Ref. [101], where the spin-to-charge conversion in the graphene/WS_2 heterostructure is due to both SHE and REE. Similar results can be obtained in graphene/TI structures. However, for example, in Ref. [263] only an antisymmetric signal due to REE was measured in graphene on $(Bi_{0.15}Sb_{0.85})_2Te_3$. In contrast, recent measurements in graphene on WSe_2 have shown only a symmetric signal due to SHE [89]. These different results originate from the different relative strengths of proximity-induced valley Zeeman and Rashba SOCs in graphene, as pointed out in Ref. [89]. Nevertheless, these heterostructures are important for the generation and detection of spin currents.

In transport experiments, one does not directly notice the presence of the semiconducting TMDC, but only indirectly via the signatures of the proximitized graphene [102]. When a TI is used, with topologically protected surface states at the Fermi level, it is much harder to disentangle the signatures from both materials [263] and experimental studies need to rely on the help of theory. In this chapter, we investigate graphene on the TI Bi_2Se_3, using first-principles calculations. The SOC proximity effects are quantified by the previously introduced model Hamiltonian $\mathcal{H}_{GR}$, Eq. (3.7). From our studies, we find that valley Zeeman (staggered) SOC of about 1–2 meV is induced in graphene, in agreement with Ref. [218]. Moreover, graphene gets strongly hole doped due to the significant amount of charge transfer to the TI. Adding more QLs to the TI has a negligible effect on the spin splitting of the graphene Dirac states, while topological surface states emerge. Most important are the three potential tunability knobs that we investigate here: i) gating, ii) the interlayer distance, and iii) the atomic constituents of the TI. In the case of a transverse electric field, the band alignment and SOC parameters can be tuned, affecting spin lifetimes and spin relaxation (SR) anisotropies. In addition, external pressure can be used to reduce the interlayer distance between graphene and the TI surface, thereby dramatically increasing band splittings and the corresponding SOC parameters. Moreover, by tuning x and y of a generic 3D TI substrate $Bi_{2-x}Sb_xTe_{3-y}Se_y$, also band alignment and proximity SOC can be controlled. Experimentally, such graphene/TI hybrids are promising for the simultaneous study of two kinds of Dirac electrons. The following results should be certainly helpful to interpret experimental transport and spin-to-charge conversion data of such bilayers.

5.2 Geometry and computational details

For the calculation of graphene on the family of 3D TI materials, we considered a 5×5 supercell of graphene on top of a 3×3 supercell of Bi_2Se_3. Initial atomic structures were set up with the atomic simulation environment (ASE) [265]. We strained the lattice constant

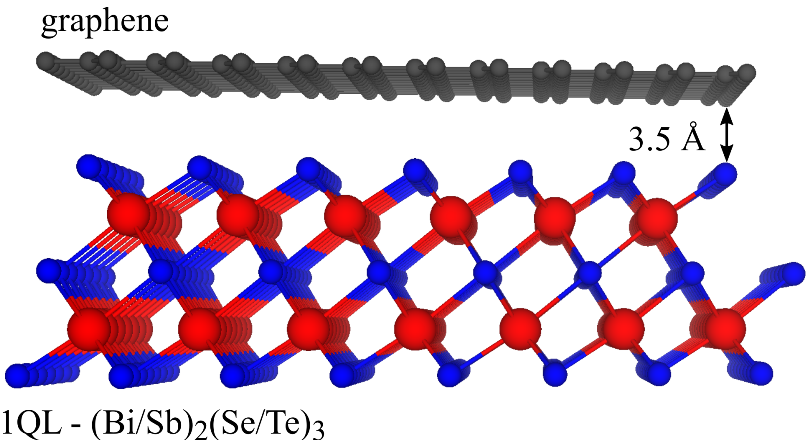

Figure 5.2: Geometry of graphene above 1 QL of (Bi/Sb)$_2$(Se/Te)$_3$. Different colors correspond to different atomic species (gray = C, red = Bi/Sb, blue = Se/Te).

of graphene by about 1% [35] to $a = 2.486$ Å and left the Bi$_2$Se$_3$ lattice constants [266] unchanged, with $a = 4.143$ Å and $c = 28.636$ Å, using the atomic parameters $(u, v) = (0.4008, 0.2117)$. According to Ref. [266], Bi$_2$Se$_3$ crystallizes in the space group $R\bar{3}m$ with atomic positions of Bi at $\pm(u, u, u)$ and Se at $(0, 0, 0)$ and $\pm(v, v, v)$. In general, the TI materials consist of vdW-bonded QLs, made up from alternating chalcogen (Se, Te) and pnictogen (Bi, Sb) atoms. If nothing else is specified, we considered only geometries without relaxation, using interlayer distances of 3.5 Å between the graphene layer and the topmost QL of Bi$_2$Se$_3$, according to recent studies [218]. In Fig. 5.2, we show the geometry of graphene on top of 1 QL of (Bi/Sb)$_2$(Se/Te)$_3$, representing a generic case of graphene on a 3D TI. The heterostructures we consider here have C_{3v} symmetry.

The electronic structure calculations were performed by DFT [204] with QUANTUM ESPRESSO [267]. Self-consistent calculations were performed with the k-point sampling of $9 \times 9 \times 1$. Only for the largest heterostructures, when 3QLs of the TI are considered, a smaller k-point sampling of $6 \times 6 \times 1$ was used due to computational limitations. We used an energy cutoff for charge density of 500 Ry and the kinetic energy cutoff for wavefunctions was 60 Ry for the relativistic pseudopotentials within the projector augmented wave (PAW) method [268] employing the Perdew-Burke-Ernzerhof (PBE) exchange correlation functional [206]. We also added vdW corrections [269, 270], and dipole corrections [271] were included to get correct band offsets and internal electric fields. In order to simulate quasi-2D systems, we added a vacuum layer of 24 Å to avoid interactions between periodic images in our slab geometry.

5.3 Band structures and fit results

How does the TI Bi$_2$Se$_3$ affect the low energy bands of graphene? This question has already been partially answered in Ref. [218], where two interface configurations have been discussed. In the "small unit cell" case, a so-called Kekulé lattice distortion [218, 272–275] is present, leading to a nearest neighbor hopping asymmetry [276] and opening the orbital band gap

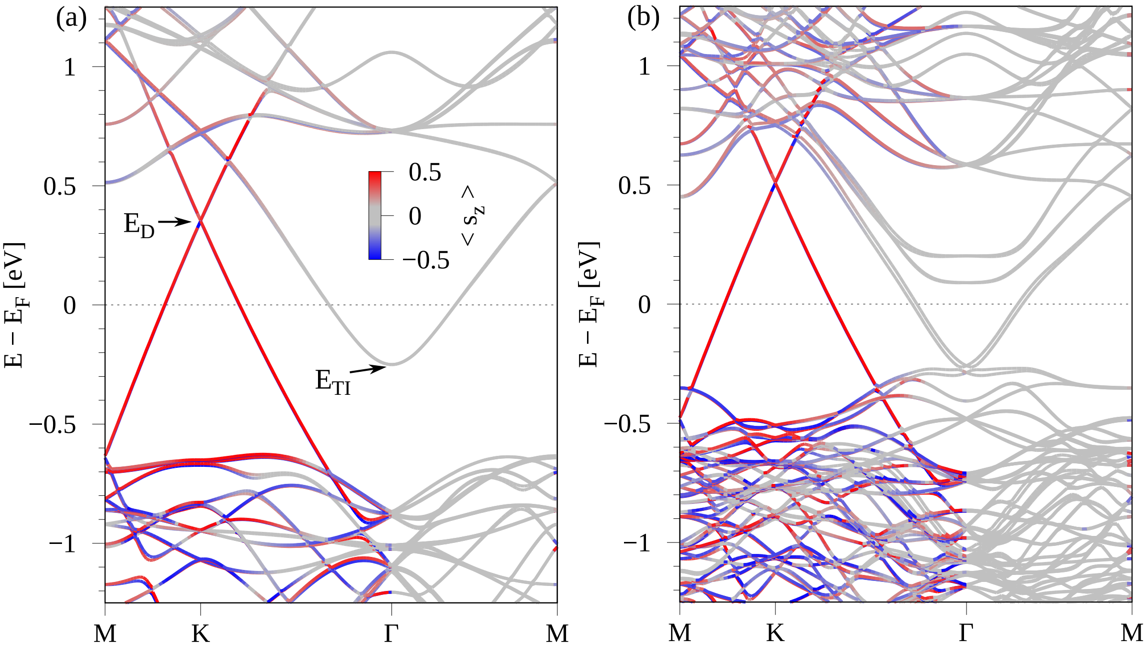

Figure 5.3: DFT-calculated band structures of graphene on (a) one and (b) three QLs of Bi_2Se_3. The color corresponds to the s_z expectation value. In (a), we define the Dirac point energy E_D and the *doping energy* of the TI E_{TI}.

of graphene. In addition, uniform proximity-induced SOC is present. In contrast, for the "large unit cell" case, staggered (valley Zeeman) SOC is induced in graphene. According to our geometry definition, we focus on the "large unit cell" case and want to address some outstanding questions. How do additional QLs, i. e., a thicker TI, influence the results of the induced valley Zeeman SOC? Can a transverse electric field tune the magnitude of the induced SOC? How does the interlayer distance affect the proximity SOC?

In Fig. 5.3, we show the full band structures of graphene above one and three QLs of Bi_2Se_3. The two QL case does not provide us with additional information and is thus not shown. At the K point, one finds the linearly dispersing bands from graphene. Due to the significant amount of charge transfer between graphene and the TI, the Dirac point is shifted to higher energies, about 350 meV above the heterostructure Fermi level, i. e., graphene is hole doped. At the Γ point, we can already recognize the precursor surface states from the TI. Since we consider only 1QL of Bi_2Se_3, the *true* topologically protected surface states have not yet formed [230, 232, 233]. Still, in Fig. 5.3(a), we define the Dirac point energy, E_D, and the *doping energy* of the TI, E_{TI}, for comparative reasons that will be useful later. For the 1QL structure, the TI is electron doped and $E_{TI} \approx -250$ meV. By considering a 3QL thick TI, see Fig. 5.3(b), we notice two differences in the heterostructure dispersion. First, graphene gets even more hole doped, with the Dirac point now at about 500 meV above the Fermi level. Second, the topological surface states have nearly[1] formed since top and bottom surface of the TI are now almost decoupled, i. e., the wavefunction overlap is minimized. Since the surface states feature in-plane spin-momentum locking [226, 277], they appear gray in the

---

[1] If one would zoom in to the Γ point, one would still see a tiny hybridization gap.

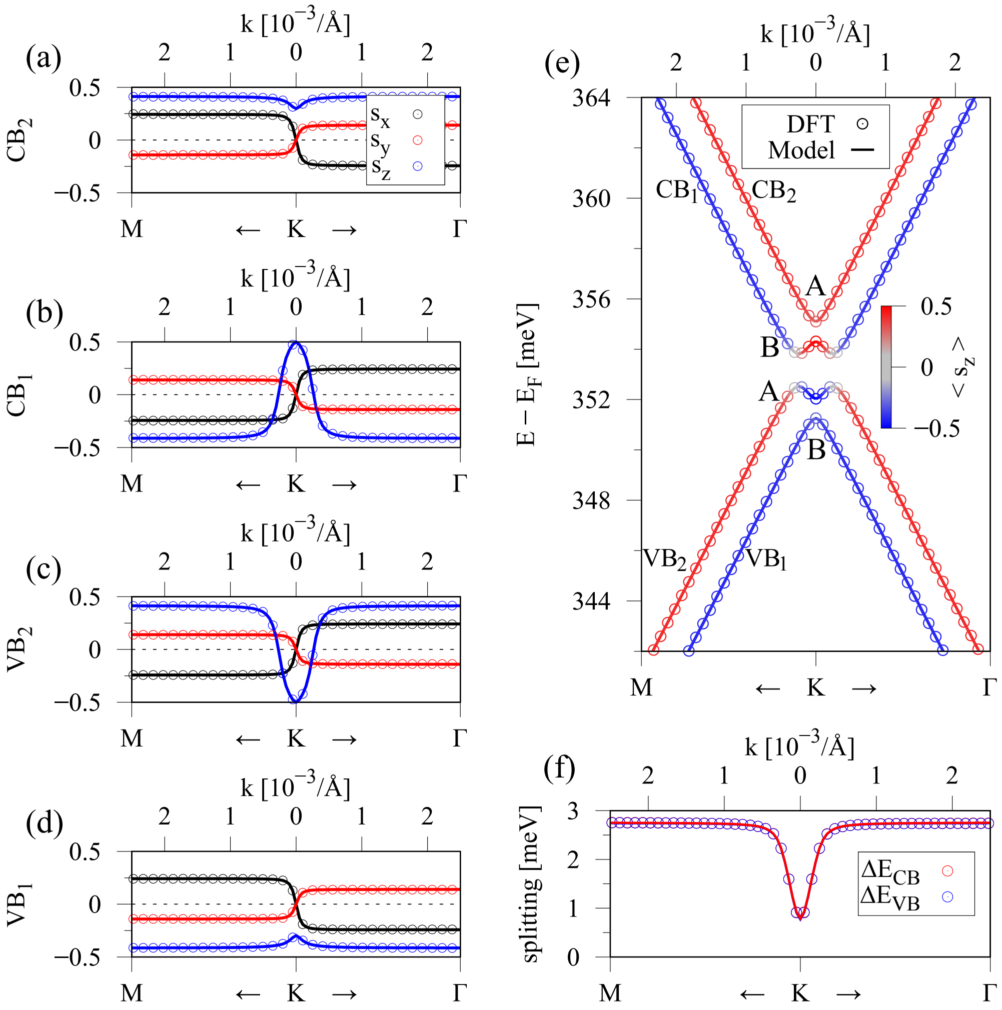

Figure 5.4: Calculated low energy band properties (symbols) for the graphene/1QL-Bi$_2$Se$_3$ heterostructure, with a fit to the model Hamiltonian $\mathcal{H}_{\mathrm{GR}}$ (solid lines). (a)-(d) The spin expectation values of the four low energy bands, as labeled in (e). (e) The low energy band structure of proximitzed graphene. The color corresponds to the s_z expectation value. Labels A/B denote the sublattice character of the four bands at the K point. (f) The splitting of the valence band (VB) (conduction band (CB)) in blue (red).

band structure, as the color denotes the s_z expectation value. Moreover, the topological states at the Γ point from opposite surfaces are split in energy, see Fig. 5.3(b). The origin is the heterostructure itself, having a built-in dipole that causes a potential asymmetry between the top and bottom QL of the TI. Anyway, we are mainly interested in the proximity-induced SOC in graphene, which we analyze in more detail now.

In Fig. 5.4(e), we show a zoom to the low energy Dirac bands for graphene on 1QL of Bi$_2$Se$_3$, with a fit to the model Hamiltonian $\mathcal{H}_{\mathrm{GR}}$, Eq. (3.7). The model dispersion perfectly agrees with the DFT data, using the fit parameters summarized in Tab. 5.1. In the dispersion, the two inner bands (CB$_1$ and VB$_2$) are inverted near the K point, i. e., the spin and sublattice characters are flipped, as recently observed also for graphene on WSe$_2$ [140]. As a consequence, graphene proximitzed by the TI could host protected pseudohelical

Table 5.1: Fit parameters of the Hamiltonian $\mathcal{H}_{GR}$, Eq. (3.7), for the graphene/Bi_2Se_3 stacks for different number of QLs. The Fermi velocity v_F, gap parameter Δ, Rashba SOC parameter λ_R, intrinsic SOC parameters λ_I^A and λ_I^B, and pseudospin inversion asymmetry (PIA) SOC parameters λ_{PIA}^A and λ_{PIA}^B. The Dirac point energy E_D, as defined in Fig. 5.3(a).

QLs	v_F [$10^5\frac{m}{s}$]	Δ [μeV]	λ_R [meV]	λ_I^A [meV]	λ_I^B [meV]	λ_{PIA}^A [meV]	λ_{PIA}^B [meV]	E_D [meV]
1	8.134	0.6	−0.771	1.142	−1.135	0.465	0.565	353.2
2	8.131	1.1	−0.691	1.221	−1.211	1.834	1.733	352.1
3	8.126	0.4	−0.827	1.343	−1.330	2.904	2.976	509.1
1 [1]	8.110	21.32	−0.799	1.638	−1.517	2.708	2.433	341.2

[1] In this case, we considered a hBN/graphene/Bi_2Se_3 trilayer structure. The parameter Δ is given in meV.

states [147]. In addition, the SOC-induced spin splittings are giant, up to 3 meV near the K point, see Fig. 5.4(f), and much larger than for pristine graphene [111, 139]. The spin-expectation values of the four bands, see Fig. 5.4(a-d), are predominantly out-of-plane (s_z) with additional Rashba SOC in-plane (s_x and s_y) contributions. Not only the dispersion is in perfect agreement with the model, but also the spin splittings of the CB and VB, as well as their spin expectation values.

From the parameters in Tab. 5.1, we find that the sublattice potential asymmetry, encoded in the parameter Δ, is tiny and in the μeV range. Apparently, due to our supercell approach, the sublattice symmetry breaking in graphene is negligible. In addition, we find significantly large Rashba and PIA SOC parameters, consistent with the deduced in-plane spin expectation values. Most interesting are the intrinsic SOC parameters, λ_I^A and λ_I^B, which are about 1 meV in magnitude and opposite in sign, i. e., they are of valley Zeeman type. By adding a second and a third QL to Bi_2Se_3, the overall band structure picture and the fitted parameters remain nearly the same, see Tab. 5.1. In conclusion, proximity-induced SOC is mainly due to adjacent layers. Still, we want to be precise in our analysis, where we find: 1) The intrinsic SOC parameters increase from about 1.1 meV to 1.3 meV in magnitude, keeping the opposite sign, 2) the sublattice potential asymmetry (Δ) and the Rashba SOC are unaffected, and 3) surprisingly, the PIA SOC parameters[2] increase from 0.5 meV to 3 meV by increasing the number of QLs from one to three. The strong valley Zeeman SOC significantly reduces spin lifetimes in graphene, but leads to a giant SR anisotropy, as recently demonstrated [100, 215, 218]. The large PIA couplings lead to a marked electron-hole asymmetry in the SR anisotropy [218], i. e., an experimental tool to verify their magnitude and increasing behavior with additional QLs.

For experimental studies, it may also be interesting to consider a hBN/graphene/Bi_2Se_3 structure. The hBN layer protects graphene from the environment and significantly boosts its spin and charge transport qualities, while not inducing much additional proximity SOC, as we have seen in Ch. 4. The fitted parameters of the hBN/graphene/Bi_2Se_3 structure, when using 1QL of the TI, are also summarized in Tab. 5.1. At first glance, we immediately notice that the parameter Δ is much larger, about 20 meV, in agreement with the relatively strong sublattice potential asymmetry, found in commensurate graphene/hBN structures [142]. Including the hBN layer, the Dirac point energy E_D is nearly unchanged, while $E_\mathrm{TI} \approx -110$ meV. In addition, the intrinsic SOC parameters are strongly enhanced by about 0.5 meV, comparing the cases with and without hBN. As we have seen in the last chapter, SOC induced by hBN is in the μeV range and cannot be the origin. Also the PIA parameters are enhanced, now similarly in magnitude to the case of graphene on 3QLs of $\mathrm{Bi_2Se_3}$. From where does the SOC come from? One possibility could be the built-in dipole field. As we will see in the next section, a transverse electric field can tune the band alignment and SOC. Similarly, additional hBN or $\mathrm{Bi_2Se_3}$ layers change the electrostatics and the band alignment, which would explain the increase of SOC in our scenarios.

---

[2] The PIA SOC parameters represent spin-flipping next nearest neighbor matrix elements [112].

5.4 Transverse electric field

For the electric field study, we focus on our smallest possible geometry — graphene on 1QL of $\mathrm{Bi_2Se_3}$. In Fig. 5.5, we show the evolution of the fit parameters of $\mathcal{H}_\mathrm{GR}$ as functions of the transverse electric field. As mentioned before, the field tunes the full dipole of the structure, i. e., built-in plus external field. For zero electric field, our structure already possesses an intrinsic electric field of about 2.5 debye. Within our applied field range of ±2.5 V/nm, the full dipole can be significantly tuned, see Fig. 5.5(c). Certainly, this affects the band alignment. The Dirac point energy E_D stays nearly unchanged with respect to the Fermi level. In contrast, the doping level of 1QL of $\mathrm{Bi_2Se_3}$, E_TI, diminishes for negative field amplitudes, see Fig. 5.5(f). The orbital parameters v_F and Δ, are nearly unaffected by the field. The Fermi velocity changes by less than 0.1%, but with a linear trend. The sublattice symmetry breaking, represented by Δ, does not show a noticeable behavior with respect to the field. Nevertheless, it stays in the μeV regime.

Most important for the control of spin interactions are the field tunable SOC parameters, see Figs. 5.5(d,e). By tuning the field from −2.5 V/nm to 2.5 V/nm, the intrinsic SOC parameters $\lambda_\mathrm{I}^\mathrm{A}$ and $\lambda_\mathrm{I}^\mathrm{B}$ can be increased from 1 meV to 1.2 meV, a giant relative enhancement of 20%. In addition, they remain opposite in sign, independent of the field. Especially important for SR properties is the relative strength of the Rashba SOC compared to the intrinsic ones. Here, λ_R can be tuned in magnitude from 0.6 meV to 0.9 meV within our field range, an even larger relative enhancement of 50%. As a consequence, $\lambda_\mathrm{I}/\lambda_\mathrm{R}$, which more or less represents the ratio between out-of-plane and in-plane spin-orbit fields, and which also affects the spin lifetimes, can be tuned by gating. In SR anisotropy measurements, the gate tunability should be detectable [142, 218]. In addition, the spin-to-charge interconversion efficiency depends on the overall strength of the induced SOC and is therefore gate-tunable, as for example demonstrated in Ref. [263]. Moreover, the PIA parameters can be tuned from about 0.2 meV to 0.8 meV. According to our previous explanations, one could experimentally control the electron-hole asymmetry of the SR anisotropy by gating.

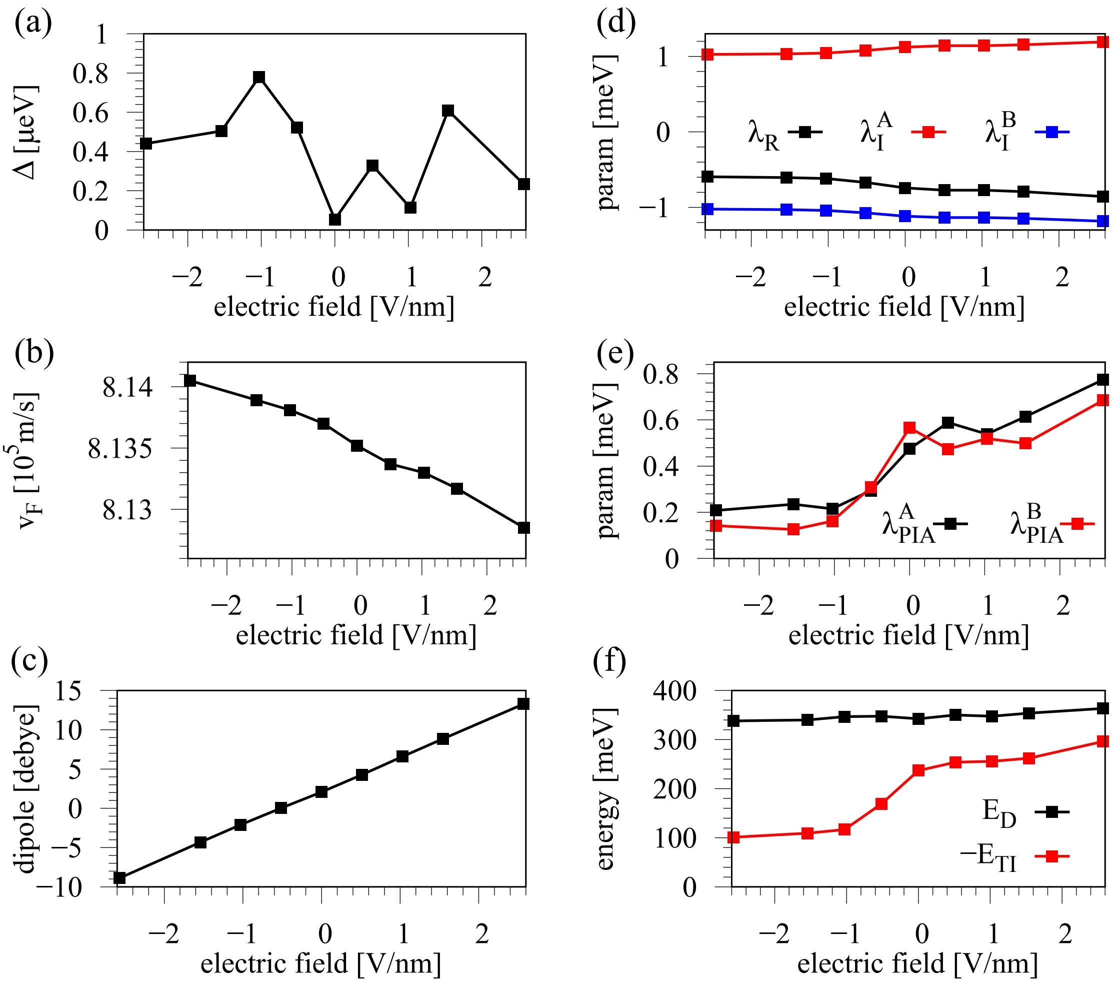

Figure 5.5: Fit parameters of the Hamiltonian $\mathcal{H}_{\mathrm{GR}}$ for the graphene/1QL-Bi$_2$Se$_3$ stack as a function of the transverse electric field. (a) The gap parameter Δ, (b) the Fermi velocity v_{F}, (c) the dipole of the structure, (d) Rashba SOC parameter λ_{R}, intrinsic SOC parameters $\lambda_{\mathrm{I}}^{\mathrm{A}}$ and $\lambda_{\mathrm{I}}^{\mathrm{B}}$, (e) PIA SOC parameters $\lambda_{\mathrm{PIA}}^{\mathrm{A}}$ and $\lambda_{\mathrm{PIA}}^{\mathrm{B}}$, and (f) the Dirac point energy E_{D} and the doping energy of the TI E_{TI}, as defined in Fig. 5.3(a).

5.5 Distance study

As we have seen in the previous chapter for graphene/hBN structures, the interlayer distance between graphene and the TI should also significantly influence the magnitude of the induced SOC. So far, we have considered only a distance of 3.5 Å. What happens to the proximity SOC if we go to larger or smaller interlayer distances?

In Fig. 5.6, we summarize the parameters of the Hamiltonian $\mathcal{H}_{\mathrm{GR}}$, matching the DFT calculated low energy graphene Dirac bands for a series of interlayer distances. From the total energy, we find the equilibrium at a distance of 3.4 Å, in good agreement with literature [218]. Note that the energetically most favorable interlayer distance depends on the specific DFT methodology, e. g., as shown for graphene on metal surfaces [278]. The sublattice potential asymmetry (Δ) diminishes with increasing distance, but it is still in the μeV range, which is small compared to the SOC parameters. The Fermi velocity, representing

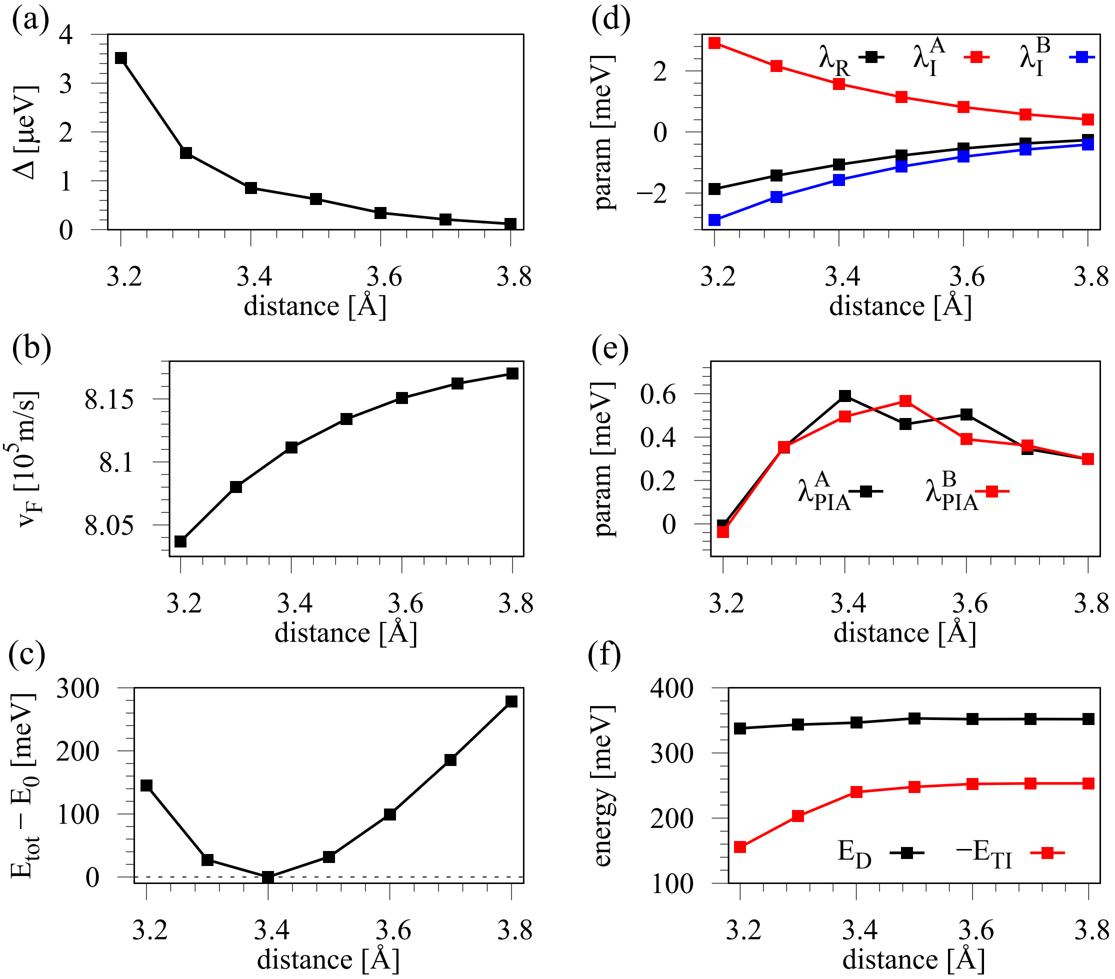

Figure 5.6: Fit parameters of the Hamiltonian $\mathcal{H}_{\mathrm{GR}}$ for the graphene/1QL-$\mathrm{Bi_2Se_3}$ stack as a function of the interlayer distance. (a) The gap parameter Δ, (b) the Fermi velocity v_{F}, (c) the total energy with respect to the minimal energy E_0, (d) Rashba SOC parameter λ_{R} and intrinsic SOC parameters $\lambda_{\mathrm{I}}^{\mathrm{A}}$ and $\lambda_{\mathrm{I}}^{\mathrm{B}}$, (e) PIA SOC parameters $\lambda_{\mathrm{PIA}}^{\mathrm{A}}$ and $\lambda_{\mathrm{PIA}}^{\mathrm{B}}$, and (f) the Dirac point energy E_{D} and the doping energy of the TI E_{TI}, as defined in Fig. 5.3(a).

the nearest neighbor hopping amplitude via $t = \frac{2\hbar v_{\mathrm{F}}}{\sqrt{3}a}$ [112], is quite strongly affected by the interlayer distance, see Fig. 5.6(b). The closer graphene and the TI get, the stronger the p_z orbitals of graphene are influenced, which is not only reflected in v_{F}, but also in the induced SOC. Especially the two intrinsic and the Rashba SOC parameters show a giant relative change, well above 100% within our considered distance limits. For example, λ_{R} can be increased from about 0.2 meV at 3.8 Å to nearly 2 meV at 3.2 Å, an enormous tunability by one order of magnitude. Similarly, $\lambda_{\mathrm{I}}^{\mathrm{A}}$ and $\lambda_{\mathrm{I}}^{\mathrm{B}}$ can be drastically enhanced to about 3 meV at our lowest interlayer distance, while simultaneously keeping their opposite sign.

The distance between vdW materials, and consequently their interactions, can be (easily) reduced by external pressure. As spectacularly demonstrated in graphene/hBN moiré-structures [212], hydrostatic pressure could reduce the interlayer distance by more than 5%, thereby doubling the induced band gap of graphene. In combination with our predictions, a change in the interlayer distance should be accompanied by tuning the proximity-induced

SOCs, see Figs. 5.6(d,e). Of course, also the band alignment changes with the distance, as can be seen from the Dirac point energy, E_D, and the doping energy of the TI, E_TI, see Fig. 5.6(f).

Note that the PIA couplings roughly follow the trend of $-E_\mathrm{TI}$ in both cases, electric field (Fig. 5.5) and distance (Fig. 5.6) study. We believe that the PIA parameters, which give a linearly increasing contribution to the band splittings away from the K point, are sensitive to the band alignment. Since the Dirac bands anti-cross with states from the TI at higher energies, see Fig. 5.3, the band splittings are affected by hybridization, which should directly influence the PIA parameters.

5.6 Different topological insulators

From the experimental perspective, 3D TIs typically have some unintentional intrinsic defect doping. In order to compensate this, artificial TI crystals like $Bi_{2-x}Sb_xTe_{3-y}Se_y$ are considered to push the topological surface states towards the Fermi level and suppress bulk transport [279, 280]. How does the proximity SOC and band alignment depend on the TI itself? To answer this, we take our heterostructure of graphene on 1QL of Bi_2Se_3 and replace the atomic constituents without changing the interlayer distance of 3.5 Å and the overall geometry. We replace full atomic layers of the 1QL structure such that the C_{3v} symmetry of the graphene/TI heterostructure remains[3]. For each of them, we calculate the low energy dispersion of graphene and employ our model Hamiltonian to obtain the relevant orbital and SOC paramaters. Of course, different TI materials have different in-plane lattice constants [266], so this is just a simple approximation to obtain qualitative differences.

Table 5.2: Fit parameters of the Hamiltonian $\mathcal{H}_\mathrm{GR}$ for the different graphene/1QL-TI bilayers. The Fermi velocity v_F, gap parameter Δ, Rashba SOC parameter λ_R, intrinsic SOC parameters $\lambda_\mathrm{I}^\mathrm{A}$ and $\lambda_\mathrm{I}^\mathrm{B}$, and PIA SOC parameters $\lambda_\mathrm{PIA}^\mathrm{A}$ and $\lambda_\mathrm{PIA}^\mathrm{B}$. The Dirac point energy E_D and the doping energy of the TI E_TI, as defined in Fig. 5.3(a).

TI	v_F $[10^5 \frac{\mathrm{m}}{\mathrm{s}}]$	Δ [μeV]	λ_R [meV]	$\lambda_\mathrm{I}^\mathrm{A}$ [meV]	$\lambda_\mathrm{I}^\mathrm{B}$ [meV]	$\lambda_\mathrm{PIA}^\mathrm{A}$ [meV]	$\lambda_\mathrm{PIA}^\mathrm{B}$ [meV]	E_D [meV]	E_TI [meV]
Bi_2Se_3	8.134	0.6	−0.771	1.142	−1.135	0.465	0.565	353.2	−250.2
Bi_2Te_3	8.120	0.6	−0.882	1.243	−1.234	1.247	0.527	−1.5	13.7
Sb_2Te_3	8.119	0.2	−0.221	0.147	−0.139	2.623	1.177	−2.0	416.5
Bi_2Te_2Se	8.123	0.3	−0.669	1.353	−1.351	−1.091	−1.209	4.0	1.2
$BiSbTeSe_2$	8.095	2.3	−1.050	0.343	−0.316	3.240	2.805	338.7	−71.4

In Tab. 5.2, we summarize the fit parameters of the Hamiltonian $\mathcal{H}_\mathrm{GR}$ for graphene on 1QL of different TIs. Even though the results are somewhat similar, i. e., all of them lead to valley Zeeman and Rashba SOC, there are huge variations in magnitude. For example, the intrinsic SOC values from Sb_2Te_3 are only about 0.15 meV, compared to the 1.2 meV provided by

---

[3] For Bi_2Te_2Se, the middle layer of the 1QL is formed by Se atoms. For $BiSbTeSe_2$, the layer sequence of the full heterostructure is Se-Bi-Te-Sb-Se-C.

Bi_2Se_3 or Bi_2Te_3. In the case of $BiSbTeSe_2$, the Rashba SOC is much larger than the intrinsic ones, while for Bi_2Se_3, they are of similar magnitude. Based on the results from Tab. 5.2, we suggest that for different TI materials the charge-to-spin conversion efficiency and its origin might vary. The measured non-local voltage in experiment — either being symmetric due to SHE, antisymmetric due to REE, or a mixture of both, with respect to an external in-plane magnetic field — depends on the relative strengths of the induced valley Zeeman and Rashba SOCs [89]. In addition, the band alignments are very different. For Sb_2Te_3, the Dirac point is located at the Fermi level, while it is at about 350 meV above E_F for Bi_2Se_3. Also the TI doping energies E_{TI} differ by more than 600 meV. In contrast, for Bi_2Te_2Se, both energies, E_D and E_{TI}, are located at the Fermi level, while the SOC parameters are similar to Bi_2Se_3. By explicitly comparing the results of Bi_2Te_3 and Sb_2Te_3, we find that the Sb content pushes E_{TI} to higher energies, in agreement to ARPES observations [279, 280], while E_D stays nearly unchanged. From the comparison of Bi_2Se_3 and Bi_2Te_2Se, we find that the Se content pushes E_{TI} (E_D) to lower (higher) energies.

Recent transport measurements of graphene on $Bi_{1.5}Sb_{0.5}Te_{1.7}Se_{1.3}$, which has suppressed bulk transport, have found proximity SOC of at minimum 2.5 meV [248]. How does this compare to our results? As we have seen, the interlayer distance plays a significant role and the experimental one could be slightly smaller than our predicted energetically favorable value of 3.4 Å for Bi_2Se_3. Furthermore, the overall electrostatics and band alignment can be different, since experimentally additional hBN encapsulation layers and a Si/SiO_2 substrate are present. Finally, also the atomic constituents of the TI play a role for the band alignment and the magnitude of proximity-induced SOC.

5.7 Summary and conclusion

We have shown that graphene in proximity to the TI Bi_2Se_3 experiences giant valley Zeeman SOC of about 1–2 meV. By increasing the number of QLs of the TI, the proximity effect is marginally influenced, because of its short rangeness. A transverse electric field, i. e., gating, can be used as an experimental control knob to significantly tune the intrinsic, Rashba, and PIA SOCs, which will strongly affect spin transport properties, where giant electron-hole asymmetric SR anisotropies are expected [218]. Recent experiments could even demonstrate that spin-to-charge conversion in graphene/TI heterostructures, which is due to proximity SOC, can be tuned in sign and magnitude by gating [263]. Our electric field results can definitely provide further insights for experimental interpretations. Another tunability knob that we investigated is the interlayer distance. We have found that one can strongly enhance the induced SOC by one order of magnitude with external pressure, tuning the interlayer distance by about 10%, which is within the experimental possibilities for graphene-based structures [212, 281, 282] . Finally, the band alignment and the proximity SOC depends on the atomic constituents of the TI, as we have found by considering a variety of compositions (x and y) of the more generic $Bi_{2-x}Sb_xTe_{3-y}Se_y$ substrate below graphene. At least in theory, our results reveal the ingredients to tune both Dirac states towards the Fermi level and simultaneously maximize the induced SOC.

CHAPTER 6

Proximity exchange in graphene on $MnPSe_3$

This chapter discusses the first-principles results presented in the publication: P. Högl, T. Frank, K. Zollner, D. Kochan, M. Gmitra, and J. Fabian, Physical Review Letters ***124****, 136403 (2020), "Quantum Anomalous Hall Effects in Graphene from Proximity-Induced Uniform and Staggered Spin-Orbit and Exchange Coupling".*

6.1 Introduction

A major breakthrough in condensed matter physics has been the recent discovery of atomically thin magnets [283, 284], which has opened new avenues for basic research [51, 285] on magnetism in the two-dimensional (2D) limit, as well as for applications in spintronics [52, 95, 286–288]. The family of van der Waals (vdW) layered magnetic materials is continually growing and already includes conductors (such as Fe_3GeTe_2) and insulators (such as $Cr_2Ge_2Te_6$ (CGT) and CrI_3), as well as ferromagnets (such as Fe_3GeTe_2 and CGT) and antiferromagnets (such as few layer CrI_3 and $MnPSe_3$) [51]. In addition, the available 2D material family covers also semimetallic graphene, semiconductors [289–293] (such as MoS_2 and WSe_2), superconductors [294–296] ($NbSe_2$), and topological insulators [297] (WTe_2), which offer unforeseen potential for novel device architectures [2, 3].

Due to their sensitivity to external manipulations, such as gating, straining, and coupling to other materials within vdW heterostructures, we can dramatically change the electronic structure of mono- and few-layer 2D materials. The commonly considered prototype material is graphene, which is neither magnetic nor has a strong spin-orbit coupling (SOC) [111] relevant for spin manipulation. With the whole 2D material repertoire as a playground, proximity effects can be used to change this. For example, recent theoretical studies have shown that a transition-metal dichalcogenide (TMDC) in proximity to graphene can induce giant SOC (1 meV) in graphene [88, 140], which was quickly confirmed by experiments [99, 165, 194, 216, 298, 299]. Interestingly, the induced SOC is of valley Zeeman type, i. e., $\lambda_I^A \approx -\lambda_I^B$, in agreement with spin relaxation (SR) anisotropy measurements [100, 164, 300]. In contrast, graphene on a topological insulator (TI) can experience proximity SOC of both

Kane-Mele [118, 144] (uniform) or valley Zeeman (staggered) type, depending on the twist angle [218, 301]. This valley Zeeman type SOC leads to protected pseudohelical edge states with a trivial $\mathcal{Z}_2$ invariant [147].

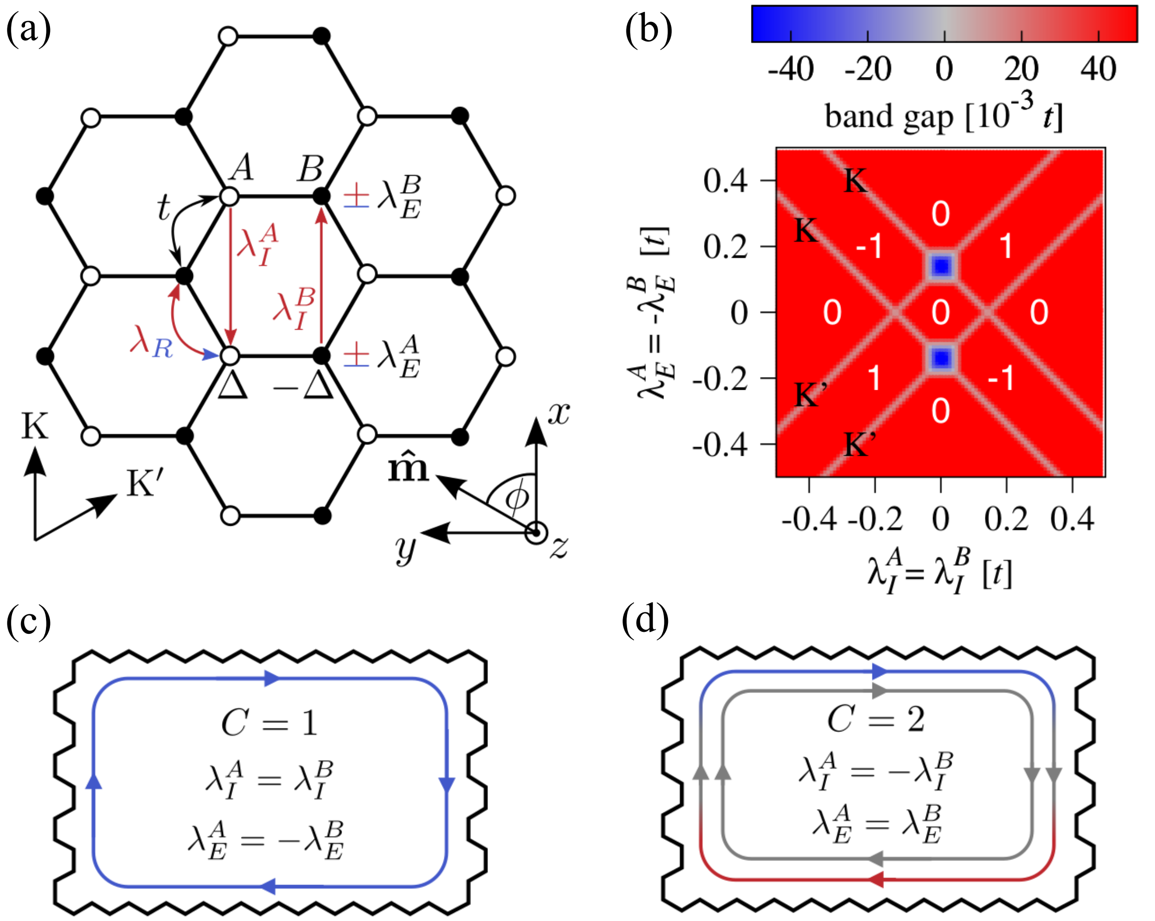
(a)
A
B
t
$\pm\lambda_E^B$
λ_I^A
λ_I^B
λ_R
$\pm\lambda_E^A$
Δ
$-\Delta$
K
K′
$\hat{\mathbf{m}}$
x
y
z
ϕ
(b)
-40
-20
0
20
40
band gap [10^{-3} t]
$\lambda_E^A = -\lambda_E^B$ [t]
0.4
0.2
0
-0.2
-0.4
K
K
0
-1
1
0
0
0
1
-1
0
K'
K'
-0.4
-0.2
0
0.2
0.4
$\lambda_I^A = \lambda_I^B$ [t]
(c)
$C = 1$
$\lambda_I^A = \lambda_I^B$
$\lambda_E^A = -\lambda_E^B$
(d)
$C = 2$
$\lambda_I^A = -\lambda_I^B$
$\lambda_E^A = \lambda_E^B$

Figure 6.1: Topological states in proximity-modified graphene. (a) Schematic graphene lattice with proximity-induced hopping parameters. Empty (full) dots denote sublattice A (B), while the color of the hoppings indicates the action on spin. The minimal model Hamiltonian in Ref. [151] is similar to $\mathcal{H}_{\mathrm{GR}}$, Eq. (3.7), containing the spin neutral nearest-neighbor hopping t, staggered on-site potential Δ, spin-flipping nearest-neighbor Rashba SOC λ_{R}, spin and sublattice resolved next nearest-neighbor intrinsic SOCs $\lambda_{\mathrm{I}}^{\mathrm{A}}$ and $\lambda_{\mathrm{I}}^{\mathrm{B}}$, and on-site sublattice resolved proximity exchange couplings $\lambda_{\mathrm{E}}^{\mathrm{A}}$ and $\lambda_{\mathrm{E}}^{\mathrm{B}}$. In this thesis, specifically in $\mathcal{H}_{\mathrm{GR}}$, Eq. (3.7), the exchange couplings are denoted as $\lambda_{\mathrm{ex}}^{\mathrm{A}}$ and $\lambda_{\mathrm{ex}}^{\mathrm{B}}$. The orientation of the reciprocal lattice is indicated by K and K′ and the magnetization orientation in real space is specified by $\hat{\mathbf{m}}$. (b) Topological phase diagram of proximitized graphene for staggered exchange and uniform intrinsic SOCs and out-of-plane magnetization $\hat{\mathbf{m}} = \hat{z}$. The calculated Chern number C is indicated in white, while the bulk band gap is color-coded. (c,d) Sketch of the quantum anomalous Hall (QAH) states along zigzag and armchair edges, corresponding to different exchange and spin-orbit parameters. Color indicates the s_z spin expectation value (red = spin-up, blue = spin-down, gray = unpolarized). Figures are from Ref. [151].

However, by adding the proper ingredients, graphene can also host topological states [147, 151], see Fig. 6.1, which do not only display intriguing physics, but they are also relevant for applications in dissipationless electronics and spintronics [2, 154]. One limiting issue is the absence of magnetism in graphene. By combining magnetic exchange coupling with SOC, one would enter the QAH regime, where time-reversal symmetry is broken. For example, the monolayer ferromagnetic insulator (FMI) CGT with perpendicular magnetic anisotropy (PMA) induces significant proximity exchange (5 meV) in graphene with additional small (0.1 meV) valley Zeeman SOC [148, 153, 264]. In the case of doubly proximitized graphene — by a top layer TMDC and bottom layer CGT — significant amounts of both couplings, exchange and spin-orbit, can be induced [153]. Nevertheless, so far only uniform (ferromagnetic), $\lambda_{\text{ex}}^{\text{A}} \approx \lambda_{\text{ex}}^{\text{B}}$, proximity-induced exchange coupling was observed in graphene [141, 152, 264, 302–311], even when an antiferromagnetic substrate was considered [149].

A detailed analysis of the role of uniform and staggered proximity-induced spin-orbit and exchange couplings in graphene for possible topological phases is given in Ref. [151]. One of the main results is shown in Fig. 6.1(b) — the topological phase diagram for proximity-induced staggered exchange and uniform intrinsic SOC in graphene — showing that a QAH phase with Chern number of 1 can be realized, see Fig. 6.1(c). Can we actually realize staggered (antiferromagnetic), $\lambda_{\text{ex}}^{\text{A}} \approx -\lambda_{\text{ex}}^{\text{B}}$, proximity exchange in graphene? Suitable material candidates would have to be layered semiconducting Ising antiferromagnets, which could eventually induce staggered exchange. Fortunately, there is a whole bunch of them available. Metal phosphorous trichalcogenides (MPX_3) are vdW magnets [312, 313], each of which shows a different antiferromagnetic ground state. In this chapter, we propose a material platform that induces staggered exchange in graphene. By combining density functional theory (DFT) calculations with our model Hamiltonian from Sec. 3.2, we extract the proximity exchange coupling in graphene induced by a monolayer $MnPSe_3$, which is an Ising-type antiferromagnetic semiconductor. The Dirac states of graphene are well preserved and located within the band gap of $MnPSe_3$. Surprisingly, but fortunately, we find staggered proximity exchange parameters on the order of 100 μeV. By decreasing the vdW gap (interlayer distance) between the materials, the magnitude of the staggered exchange can be further enhanced.

6.2 Computational details and geometry

The electronic structure calculations and structural relaxation of graphene on $MnPSe_3$, were performed by DFT [204] with QUANTUM ESPRESSO [267]. Self-consistent calculations were performed with the k-point sampling of $30 \times 30 \times 1$ to get converged results for the proximity exchange splittings. We performed open shell calculations that provide the spin polarized antiferromagnetic ground state of $MnPSe_3$. A Hubbard parameter[1] of $U = 5$ eV was employed for Mn d orbitals, similar to recent calculations [316, 317]. We used an energy cutoff for charge density of 700 Ry and the kinetic energy cutoff for wavefunctions was

---

[1] In the Hubbard model, interactions of localized electrons are modeled by an on-site Coulomb repulsion. A similar approach is used in the so-called DFT+U method, typically employed for strongly correlated materials [314, 315], e. g., Mott insulators.

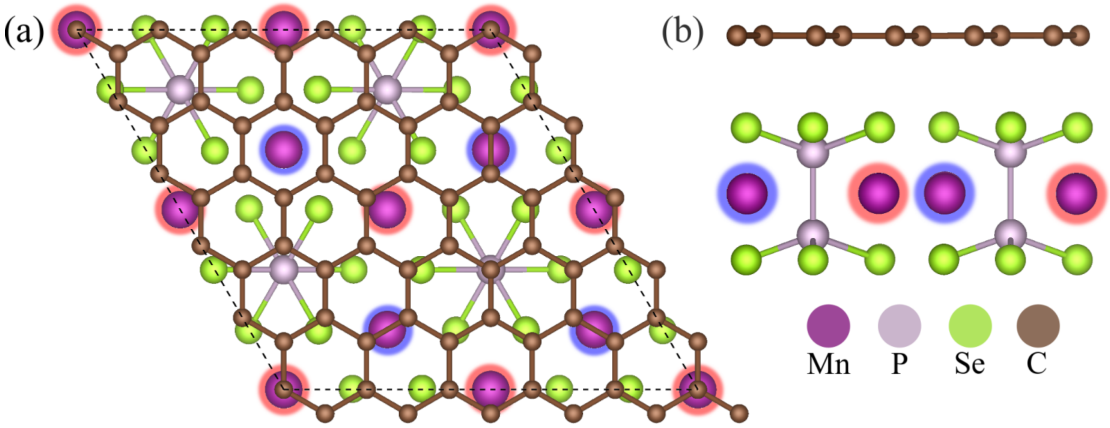

Figure 6.2: (a) Top and (b) side view of the graphene/$MnPSe_3$ heterostructure geometry. The colored spheres around the Mn atoms indicate the magnetization direction (red $=\uparrow$, blue $=\downarrow$) with antiferromagnetic Ising-type magnetic ordering.

65 Ry for the scalar relativistic pseudopotential within the projector augmented wave (PAW) method [268] with the Perdew-Burke-Ernzerhof (PBE) exchange correlation functional [206]. For the relaxation of the heterostructures, we added van der Waals corrections [269, 270] and used the quasi-Newton algorithm based on trust radius procedure. In order to simulate quasi-2D systems, we added a vacuum of 20 Å to avoid interactions between periodic images in our slab geometry. To determine the interlayer distances, the atoms of graphene were allowed to relax only in their z positions (vertical to the layers) and the atoms of $MnPSe_3$ were allowed to move in all directions until all components of all forces were reduced below 10^{-3} [Ry/a_0], where a_0 is the Bohr radius.

We place graphene on the Ising antiferromagnet $MnPSe_3$ [318, 319]. $MnPSe_3$ is an antiferromagnetic semiconductor with an optical gap of about 2.3 eV [320] and a Néel temperature of 74 K [319]. The heterostructure of graphene/$MnPSe_3$ contains a 5×5 supercell of graphene on a 2×2 $MnPSe_3$ supercell. We stretched the lattice constant of graphene [321] from 2.46 Å to 2.48 Å and compressed the lattice constant of $MnPSe_3$ by roughly 3% from 6.387 Å [319] to 6.20 Å. The considered heterostructure model has a lattice constant of 12.4 Å and contains 90 atoms in the unit cell. The average interlayer distance was relaxed to 3.46 Å, but we performed an interlayer distance study of the proximity effects. In Figs. 6.2(a,b), we show the geometry of the graphene/$MnPSe_3$ stack. The Mn atoms of $MnPSe_3$ form a hexagonal lattice with alternating magnetization within a monolayer, which is the experimentally predicted ground state [319].

6.3 Band structure and fit results

The first-principles calculated band structure of the graphene/$MnPSe_3$ stack is shown in Fig. 6.3, where we use a decreased interlayer distance of 3.16 Å compared to the DFT-relaxed one. The reduced distance allows for a more clear analysis of the low energy band structure features, as proximity effects are enhanced. The Dirac states of graphene are nicely preserved

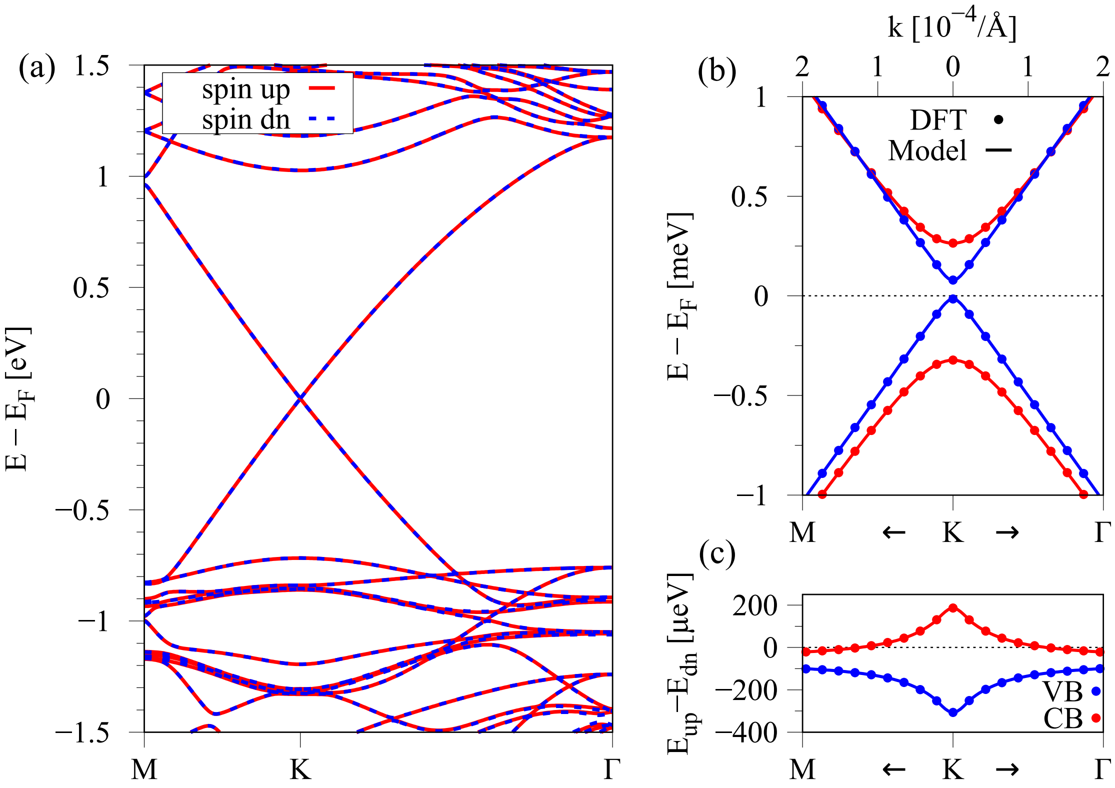

Figure 6.3: (a) Calculated electronic band structure of the graphene/MnPSe$_3$ heterostructure without SOC for an interlayer distance of 3.16 Å. Bands in red (blue) correspond to spin up (down). (b) Zoom to the calculated low energy bands (symbols) with a fit to the model Hamiltonian (solid line). (c) The splitting between spin-up and spin-down bands, $E_{\text{up}} - E_{\text{dn}}$, for the valence band (VB) and conduction band (CB).

and reside within the band gap of MnPSe$_3$. A zoom to the low energy bands around the K point reveals the proximity-induced exchange splitting of the bands. Our model Hamiltonian clearly reproduces the low energy dispersion and spin splittings, see Figs. 6.3(b,c), of our DFT calculation without including SOC effects. From the low energy dispersion at the K point, we find that spin-down bands from both CB and VB reside near the zero energy Fermi level, while spin-up bands are shifted to higher energies.

So far, only cases of uniform (ferromagnetic) exchange are known in literature where sublattice resolved exchange parameters have the same sign [148–150, 153]. The reason is, that in all these cases, the effective underlying substrate is a ferromagnet, even in the case of the antiferromagnet BiFeO$_3$(111) [149], where the ferromagnetic Fe(111)-plane proximitizes graphene. To induce antiferromagnetic exchange by proximity (sublattice resolved exchange parameters with opposite sign), the substrate has to have antiferromagnetic ordering within the underlying monolayer and must optimally be commensurate with the graphene lattice. For our heterostructure, the splitting between spin-up and spin-down bands, $E_{\text{up}} - E_{\text{dn}}$, for the VB is negative, while the one for the CB is positive at the K point, see Figs. 6.3(b,c). Even though, the antiferromagnetic hexagonal Mn-lattice is not commensurate with the graphene lattice, we effectively get different spin splittings (opposite in sign) for the VB and CB.

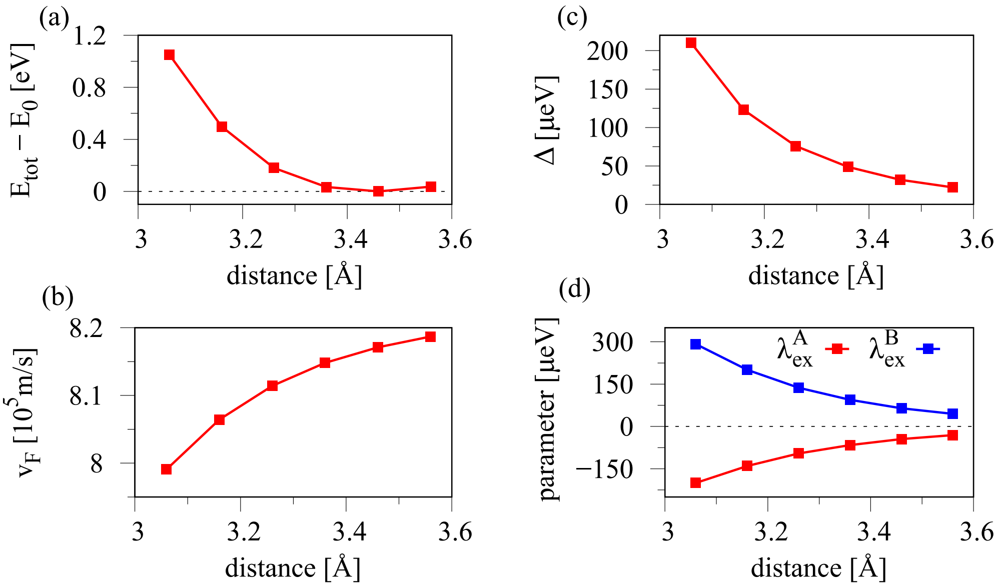

Figure 6.4: Fit parameters as a function of the interlayer distance for the graphene/MnPSe$_3$ heterostructure. (a) Total energy of the system, (b) the Fermi velocity v_F, (c) the staggered potential Δ, and (d) the two proximity exchange parameters λ_{ex}^A and λ_{ex}^B.

The fit parameters of the low energy model Hamiltonian for several interlayer distances, see Fig. 6.4, show that the sublattice resolved proximity exchange couplings are opposite in sign. Therefore, our first-principles results indeed show that graphene on MnPSe$_3$ displays staggered proximity exchange with spin splittings on the order of 100 μeV. Decreasing the interlayer distance, the staggered potential, and most importantly the proximity exchange parameters, can be increased, while the Fermi velocity decreases. The exact values of the parameters as functions of the interlayer distance are summarized in Tab. A.1. This behavior has never been reported so far in the literature and paves the way for the realization of a new Hamiltonian term. Reminding ourselves about the exchange Hamiltonian $\mathcal{H}_{ex}$ from Sec. 3.2 and employing the condition of staggered exchange parameters, i. e., $\lambda_{ex}^A = -\lambda_{ex}^B = \lambda_{ex}$, we find $\mathcal{H}_{ex} = -\lambda_{ex}\sigma_z \otimes s_z$, which is reminiscent of the Kane-Mele SOC Hamiltonian [118, 144].

We also compare the results of the DFT calculations and model fitting to the case when the MnPSe$_3$ is in the ferromagnetic state, i. e., all Mn atoms have magnetization pointing towards graphene. The total energies of the graphene/MnPSe$_3$ heterostructure, see Tab. A.1, show that the antiferromagnetic state is about 200 meV lower in energy than the ferromagnetic one (for one specific interlayer distance of 3.36 Å). This confirms that the antiferromagnetic state is the ground state of the MnPSe$_3$ monolayer, consistent with experiments [319]. In the ferromagnetic case, we should induce uniform proximity exchange in graphene. The band structure, see Fig. 6.5, shows again that the graphene Dirac cone is located within the band gap of the ferromagnetic MnPSe$_3$. Surprisingly, the MnPSe$_3$ remains semiconducting even in the ferromagnetic phase, but with a reduced band gap compared to the antiferromagnetic phase. The zoom to the low energy Dirac bands in Fig. 6.5(b) shows that spin-down bands are shifted towards lower energies, while spin-up bands are shifted to higher energies. The

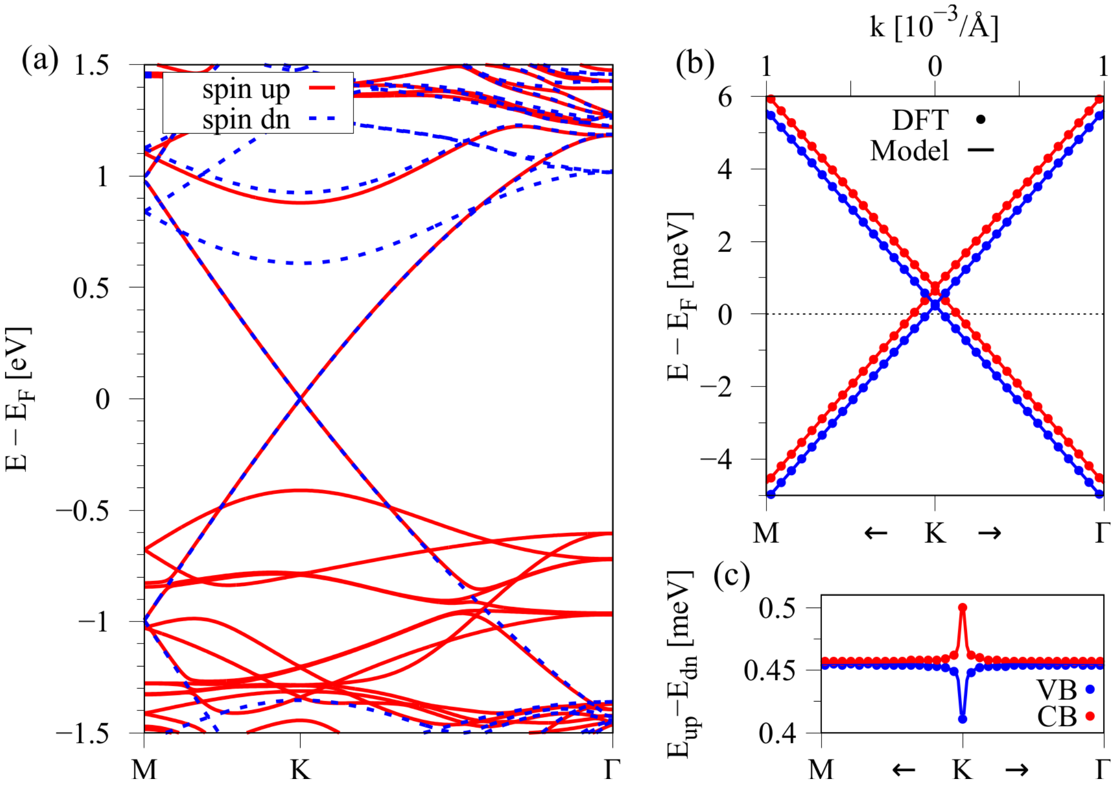

Figure 6.5: (a) Calculated electronic band structure of the graphene/MnPSe$_3$ heterostructure without SOC for an interlayer distance of 3.36 Å and when the MnPSe$_3$ is in the ferromagnetic state. Bands in red (blue) correspond to spin up (down). (b) Zoom to the calculated low energy bands (symbols) with a fit to the model Hamiltonian (solid line). (c) The splitting between spin-up and spin-down bands, $E_{\text{up}} - E_{\text{dn}}$, for the VB and CB.

spin splittings for VB and CB have the same sign, see Fig. 6.5(c). The full model Hamiltonian $\mathcal{H}_{\text{GR}}$, Eq. (3.7), is again in very good agreement with the first-principles results, see Fig. 6.5, with proximity exchange parameters of about -200 μeV. The fitted parameters are also summarized in Tab. A.1. In the ferromagnetic phase, we find roughly uniform exchange parameters, i. e., $\lambda_{\text{ex}}^{\text{A}} = \lambda_{\text{ex}}^{\text{B}} = \lambda_{\text{ex}}$. The Hamiltonian reduces to $\mathcal{H}_{\text{ex}} = -\lambda_{\text{ex}}\, \sigma_0 \otimes s_z$, and proximity exchange is similar to the Zeeman splitting from an external magnetic field [152].

Which orbitals take part in the hybridization causing the proximity exchange? In Fig. 6.6, we show the atom resolved DOS of the graphene/MnPSe$_3$ heterostructure with MnPSe$_3$ in the antiferromagnetic phase, as depicted in Fig. 6.2. For the DOS, we considered the energetically favorable interlayer distance of 3.46 Å. We find that, as expected, the C atoms of graphene form the low energy Dirac states, linearly dispersing near the Fermi level. The band edges originating from the MnPSe$_3$, which are about ±0.8 eV away from the Fermi level, are mainly formed by the Se atoms. In addition, the CB edge has a significant contribution from P atoms, while the DOS from Mn atoms is the smallest. Both Mn atom species, Mn$_\uparrow$ and Mn$_\downarrow$, give the same contributions to the DOS, but majority and minority spins are interchanged because of their opposite magnetization directions in the antiferromagnetic phase. The hybridization can be best seen in the band structure, Fig. 6.3, at energies of about -1 eV along the K-Γ line, where the graphene Dirac states and the MnPSe$_3$ bands

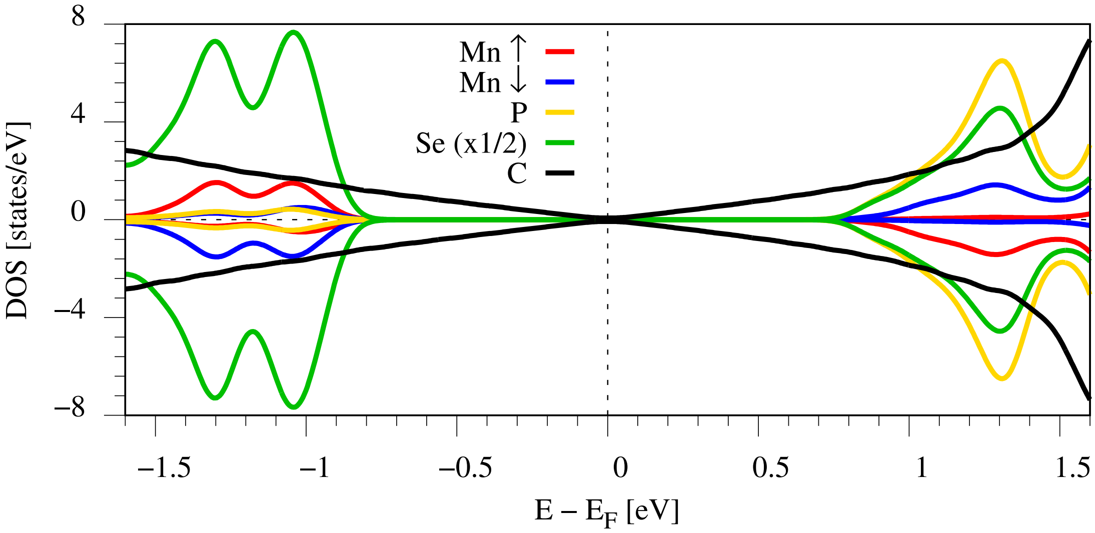

Figure 6.6: The atom resolved density of states (DOS). The contribution from the Se atoms is multiplied by a factor of 1/2. We differentiate into $\text{Mn}_\uparrow$ and $\text{Mn}_\downarrow$, corresponding to the Mn atoms with different magnetization, as shown in Fig. 6.2.

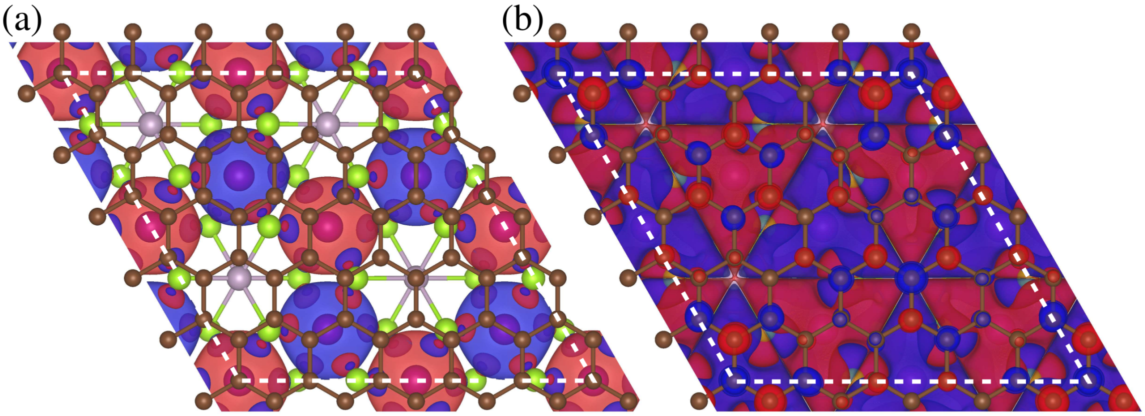

Figure 6.7: The calculated spin polarization $\Delta\rho = \rho_\uparrow - \rho_\downarrow$ of the graphene/MnPSe$_3$ heterostructure, where $\rho_{\uparrow/\downarrow}$ are the electronic charge densities for spin-up/spin-down. The color red (blue) corresponds to $\Delta\rho > 0$ ($\Delta\rho < 0$). In (a), we show the isosurfaces corresponding to the isovalues of $\Delta\rho = \pm 10^{-3}\text{Å}^{-3}$. In (b), the isovalues are $\Delta\rho = \pm 10^{-5}\text{Å}^{-3}$. The white dashed line emphasizes the unit cell.

anticross. From the atom resolved DOS, we find that mainly Se p orbitals are responsible for the hybridization with the C p_z orbitals. We conclude that the magnetization of the MnPSe$_3$, which is due to the partially filled Mn d orbitals, is mediated via the Se p orbitals over the vdW gap that in turn proximity magnetize the C atoms.

Another way to visualize the proximity effect is by looking at the spin polarization, $\Delta\rho = \rho_\uparrow - \rho_\downarrow$, in real space. The spin densities $\rho_{\uparrow/\downarrow}(\boldsymbol{r}) = \sum_{n,\boldsymbol{k}} |\phi^{\boldsymbol{k}}_{n,\uparrow/\downarrow}(\boldsymbol{r})|^2$ are sums over the eigenstates with the corresponding spin and energy below the Fermi level. In Fig. 6.7(a), one can see the alternating spin polarizations around the Mn atoms, in agreement with the structural setup in Fig. 6.2. The P and C atoms display no polarization for the chosen isovalues, while around the Se atoms there is a spin polarization in the shape of p orbitals. From there it is evident that the Se atoms (p orbitals) couple to the magnetic Mn atoms (d orbitals) and get spin polarized. For smaller isovalues, see Fig. 6.7(b), the spin polarizations around the C atoms, which are of p_z orbital shape, can be visualized. We find that neighboring C atoms have nearly always alternating polarizations, which, on average, lead to an effectively "antiferromagnetic graphene". These findings are in agreement with the band structure and model Hamiltonian analysis, where we have found staggered exchange couplings.

At the end of this chapter, we would like to add a few words of precaution. Note that the effects of SOC have been neglected in the presented results. In reality, we believe that SOC plays an important role and the graphene Dirac states will additionally experience some amount of proximity SOC, given the structural similarities of MnPSe$_3$ and TMDCs. Without any calculations and experimental data, we can only speculate about the values, but we expect that the induced SOC is at least of similar magnitude than proximity exchange. Moreover, the calculated proximity exchange parameters are only about 50 μeV in magnitude for our predicted energetically most favorable interlayer distance, see Tab. A.1. In this regard, one can ask the questions whether the staggered exchange coupling survives if 1) we tune the Hubbard U for the Mn d orbitals, which is a parameter in the DFT calculation, 2) the lattice constant of MnPSe$_3$ is not compressed, as we considered in our commensurate geometry, and 3) one uses a different DFT implementation to describe the heterostructure dispersion like in the full potential linearized augmented plane wave (FLAPW) code WIEN2K [205]. We also want to note that maybe a different material in the MPX$_3$ family [312, 313] might be even more suitable to achieve staggered proximity exchange coupling in graphene. Certainly, not only the presented case, but all graphene/MPX$_3$ structures deserve a more extended theoretical and experimental analysis. We leave this as an exercise for the reader and hope that the presented findings will be confirmed in the near future.

6.4 Summary and conclusion

In summary, we have shown that the antiferromagnetic Ising semiconductor MnPSe$_3$ is a material platform for inducing staggered exchange coupling in graphene. Our calculations and model fitting study has shown $\lambda_{\mathrm{ex}}^{\mathrm{A}} \approx -0.7\lambda_{\mathrm{ex}}^{\mathrm{B}}$, which is already a good basis on realizing exact staggered exchange coupling in graphene. We have also seen that diminishing the interlayer distance enhances the strength of the exchange coupling in graphene due to stronger hybridization with the magnetic substrate. By switching from the antiferromagnetic, which is the ground state, to the ferromagnetic phase of MnPSe$_3$, which can be experimentally achieved by an external magnetic field, we can swap from staggered to uniform proximity exchange in graphene. Our fitted parameters, together with the model Hamiltonian, can be used to study electronic and spin transport properties in proximity magnetized graphene.

PART III

Bilayer graphene

CHAPTER 7

The basics of bilayer graphene

In this chapter, we introduce the basic properties of bilayer graphene (BLG), such as its unit cell, band structure, and low energy Hamiltonian. The Hamiltonian is based on effective p_z orbitals of two monolayer graphene sheets. In contrast to the monolayer scenario, additional interlayer couplings are present in BLG. The modification of the low energy band structure, due to proximity of BLG to other materials, can be described by a series of parameters that include orbital, spin-orbit, and exchange effects. The parameters can be determined by fitting the Hamiltonian to a realistic density functional theory (DFT)-calculated band structure of a BLG-based system. Due to the short-rangeness of proximity effects, only the graphene layer that is adjacent to the proximitizing material gets modified. Here, we also briefly analyze the low energy band structure, employing different parameter sets obtained from DFT-calculations.

7.1 Unit cell, Brillouin zone, and band structure

BLG is formed by two monolayer graphene sheets that are stacked on top of each other. The most natural form of the stacking is the AB one, shown in Fig. 7.1(a), which is also termed Bernal stacking. In the Bernal stacking case, the sublattice atom C_{A1} of the lower layer is directly underneath the sublattice atom C_{B2} of the upper layer. Because of their direct connection via interlayer hoppings, we name this pair of atoms the *dimer* ones, while the other two atoms C_{B1} and C_{A2} are the *non-dimer* ones. The non-dimer atom C_{A2} (C_{B1}) is located above (below) the center of the hexagon of the lower (upper) graphene layer. Since BLG has a hexagonal lattice structure, also its Brillouin zone (BZ) is hexagonal, see Fig. 7.1(b), similarly to monolayer graphene. The stacking of the two graphene layers can have significant ramifications for its band structure and related physical properties. For example, recent studies have shown that even superconductivity can arise in twisted BLG[1] for twist angles of about 1.1° [322, 323]. In the following chapters, we will only consider BLG in Bernal stacking due to its idiosyncratic low energy band structure.

---

[1] Due to the small twist angle of the two graphene sheets, a moiré-pattern arises and strong electron confinement and correlation is present in regions of AA stacking.

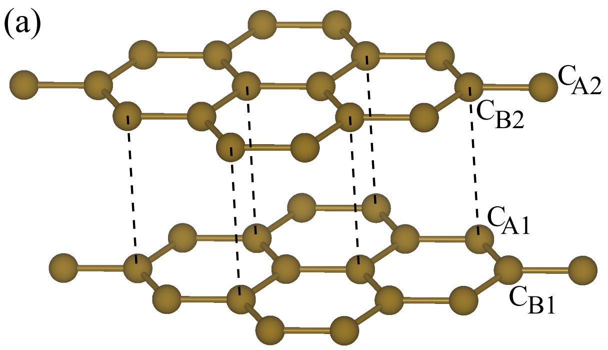

Figure 7.1: Unit cell and BZ of BLG. (a) Lattice of BLG with labels C_{A1} and C_{B1} (C_{A2} and C_{B2}) for the sublattice atoms of the lower (upper) layer. The dimer atoms are vertically connected (dashed lines) via direct interlayer couplings. (b) First BZ of the reciprocal lattice, where Γ, M, K, and K′ are non-equivalent high symmetry points.

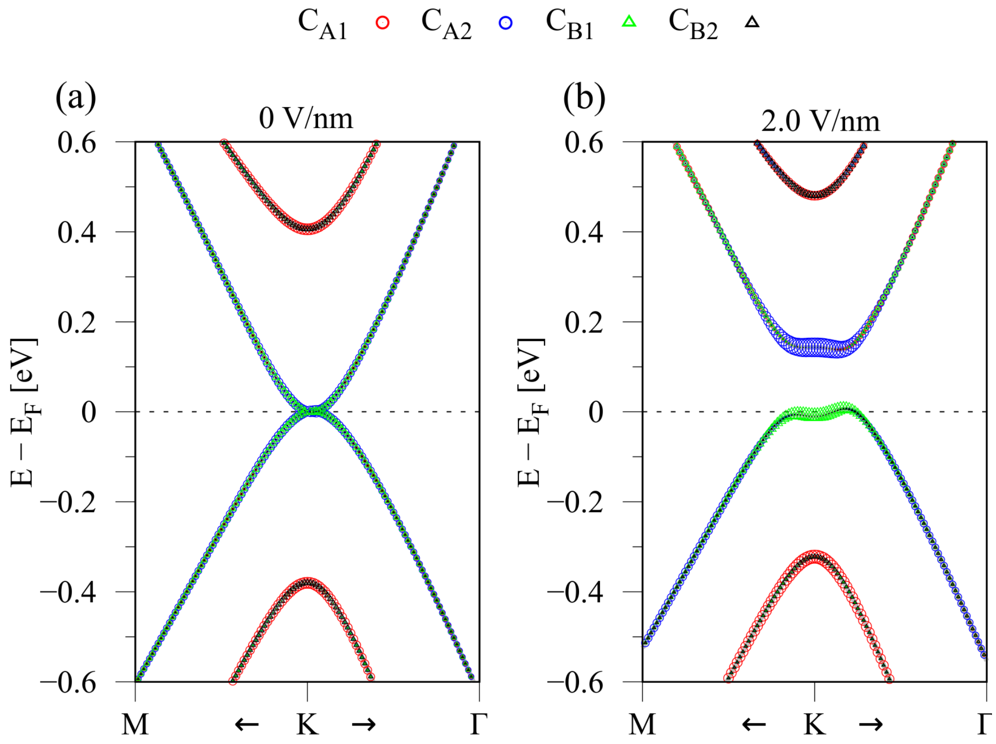

Figure 7.2: (a) Zoom to the low energy bands of BLG near the K point for a transverse electric field of 0 V/nm. Different colors correspond to projections onto different atoms of the unit cell. (b) Same as (a), but for a field of 2 V/nm.

The band structure of BLG near the Fermi level is shown in Fig. 7.2(a) and consists of four parabolic bands. We find two low energy bands, touching at the Fermi level, which are formed by the non-dimer atoms. In addition, there are two high-lying energy bands, at about ±400 meV in the vicinity of the K point, which are formed by the dimer atoms. Since the dimer atoms are connected by direct interlayer hoppings, see Fig. 7.1(a), the corresponding bands are split off in energy.

A pecularity of the low energy bands of BLG is the tunability of the band gap by an external electric field that is applied transverse to the graphene sheets [217, 324–328]. In Fig. 7.2(b), we show the low energy bands when a transverse electric field of 2 V/nm is applied across the BLG. We find that we can open a significantly large band gap of about 100 meV. At the K point, each band is now primarily formed by a specific layer and sublattice atom. The reason is that, once a field is applied, each graphene layer is situated in a different potential energy V. Since the low energy bands are formed by the non-dimer atoms, from two different layers, a band gap opens where each band reveals a specific sublattice and layer character. In reality, already a substrate below BLG is enough to introduce a band gap, since an intrinsic dipole will then be present in heterostructures with BLG, as we will see later. The continuous electrically tunable band gap of BLG is an ideal control knob for device applications. Similarly to monolayer graphene, the intrinsic spin-orbit coupling (SOC) of BLG is nearly negligible for the description of the low energy bands near the K and K′ valleys. Recent transport experiments have found an intrinsic spin-orbit gap of about 40 μeV [222], in agreement with DFT calculation predictions [217].

7.2 Hamiltonian of spin-orbit and exchange proximitized bilayer graphene

In what follows, we want to describe the low energy band structure of BLG in the vicinity of the K and K′ valleys, when proximity effects, due to other two-dimensional (2D) materials, are present. Therefore, we introduce the following Hamiltonian derived from symmetry [217],

$$\mathcal{H}_{\mathrm{BLG}} = \mathcal{H}_{\mathrm{orb}} + \mathcal{H}_{\mathrm{soc}} + \mathcal{H}_{\mathrm{ex}} + E_D, \tag{7.1}$$

$$\mathcal{H}_{\mathrm{orb}} = \begin{pmatrix} \Delta + V & \gamma_0 f(\boldsymbol{k}) & \gamma_4 f^*(\boldsymbol{k}) & \gamma_1 \\ \gamma_0 f^*(\boldsymbol{k}) & V & \gamma_3 f(\boldsymbol{k}) & \gamma_4 f^*(\boldsymbol{k}) \\ \gamma_4 f(\boldsymbol{k}) & \gamma_3 f^*(\boldsymbol{k}) & -V & \gamma_0 f(\boldsymbol{k}) \\ \gamma_1 & \gamma_4 f(\boldsymbol{k}) & \gamma_0 f^*(\boldsymbol{k}) & \Delta - V \end{pmatrix} \otimes s_0, \tag{7.2}$$

$$\mathcal{H}_{\mathrm{soc}} + \mathcal{H}_{\mathrm{ex}} = \begin{pmatrix} (\tau\lambda_{\mathrm{I}}^{\mathrm{A1}} - \lambda_{\mathrm{ex}}^{\mathrm{A1}})s_z & \mathrm{i}(\lambda_0 + 2\lambda_{\mathrm{R}})s_-^\tau & 0 & 0 \\ -\mathrm{i}(\lambda_0 + 2\lambda_{\mathrm{R}})s_+^\tau & (-\tau\lambda_{\mathrm{I}}^{\mathrm{B1}} - \lambda_{\mathrm{ex}}^{\mathrm{B1}})s_z & 0 & 0 \\ 0 & 0 & (\tau\lambda_{\mathrm{I}}^{\mathrm{A2}} - \lambda_{\mathrm{ex}}^{\mathrm{A2}})s_z & -\mathrm{i}(\lambda_0 - 2\lambda_{\mathrm{R}})s_-^\tau \\ 0 & 0 & \mathrm{i}(\lambda_0 - 2\lambda_{\mathrm{R}})s_+^\tau & (-\tau\lambda_{\mathrm{I}}^{\mathrm{B2}} - \lambda_{\mathrm{ex}}^{\mathrm{B2}})s_z \end{pmatrix}, \tag{7.3}$$

where we keep only the most relevant terms. For simplicity, we use the linearized version of the nearest-neighbor structural function $f(\boldsymbol{k}) = -\frac{\sqrt{3}a}{2}(\tau k_x - \mathrm{i}k_y)$, with the graphene lattice constant a and the Cartesian wave vector components k_x and k_y measured from $\pm$K for the valley indices $\tau = \pm 1$. The Pauli spin matrices are s_i, with $i = \{0, x, y, z\}$, and $s_\pm^\tau = \frac{1}{2}(s_x \pm \mathrm{i}\tau s_y)$. Here, γ_j, $j = \{0, 1, 3, 4\}$, describe intra- and interlayer hoppings in BLG when the lower (upper) graphene layer is placed in the potential V $(-V)$. The parameter Δ describes the asymmetry in the energy shift of the bonding and antibonding states. The parameters λ_{I} (λ_{ex}) describe the intrinsic SOC (proximity-induced exchange) of the corresponding layer and sublattice atoms ($\mathrm{C_{A1}}, \mathrm{C_{B1}}, \mathrm{C_{A2}}, \mathrm{C_{B2}}$). The combination of λ_0 and λ_{R} describe the global and local breaking of space inversion symmetry, similarly to the Rashba term in graphene.

For a more detailed description of the parameters, we refer the reader to Ref. [217]. We use the basis $|\mathrm{C_{A1}}, \uparrow\rangle$, $|\mathrm{C_{A1}}, \downarrow\rangle$, $|\mathrm{C_{B1}}, \uparrow\rangle$, $|\mathrm{C_{B1}}, \downarrow\rangle$, $|\mathrm{C_{A2}}, \uparrow\rangle$, $|\mathrm{C_{A2}}, \downarrow\rangle$, $|\mathrm{C_{B2}}, \uparrow\rangle$, and $|\mathrm{C_{B2}}, \downarrow\rangle$. Note that the model Hamiltonian is centered around zero energy Fermi level. This is not necessarily the case for the first-principles results as doping can occur. Therefore, we introduce another parameter E_D, which introduces an energy shift on the global model band structure and we call it the Dirac point energy, similarly to the monolayer graphene case. Depending on the investigated heterostructure system, some terms in the Hamiltonian can be further neglected. For example, when there is no magnetism in the game we set the proximity-induced exchange couplings (λ_{ex}) to zero.

7.3 Band structure topologies of proximitized bilayer graphene

Similarly to the graphene chapter, let us now especially analyze the effects of proximity spin-orbit and exchange parameters on the band structure. The parameters γ_j, describing intra- and interlayer hoppings, are more or less fixed by the BLG structure itself. As we have already seen, the parameter V can be tuned by a transverse electric field and is responsible for the orbital band gap. The exchange and SOC terms are influenced by proximity effects. Consequently, the impact of other 2D materials in proximity to BLG will be mainly on the parameters V, λ_{I}, and λ_{ex}. In Fig. 7.3, we summarize some important low energy band structure cases for different parameter sets. In Fig. 7.3(a), we show the case when there would be, for example, a transition-metal dichalcogenide (TMDC) above BLG [31] such that strong SOC is induced only in the top graphene layer due to short-rangeness of proximity effects. In other words, only the intrinsic SOC parameters of the top layer, $\lambda_{\mathrm{I}}^{\mathrm{A2}}$ and $\lambda_{\mathrm{I}}^{\mathrm{B2}}$, are proximity enhanced to the meV range. We can see that the low energy valence band (VB) is formed by $\mathrm{C_A}$ orbitals, especially by the $\mathrm{C_{A2}}$ atom, because as previously explained, the non-dimer atoms form the low energy bands. The low energy conduction band (CB) is then formed by the non-dimer atom $\mathrm{C_{B1}}$. As we have set $V > 0$ in this case, bands formed by orbitals from the upper layer are at a lower potential energy, as reflected in the band structure. In a realistic DFT calculation, the parameter V reflects the built-in electric field of the heterostructure. Once a transverse external field is applied, V can be tuned. The short-range proximity-induced SOC affects only bands of the upper layer — in our case just the VB, which displays a finite spin splitting.

Now, we exploit the field tunability of the low energy bands of BLG. Similarly to Fig. 7.3(a), we still imagine a TMDC on top of BLG. In Fig. 7.3(b), we show the case for $V < 0$ such that bands formed by orbitals from the lower layer are situated in a lower potential energy. We effectively *invert* the band structure and it is now the CB that is spin-split because proximity SOC still affects only this graphene layer that is adjacent to the TMDC. In experiments,

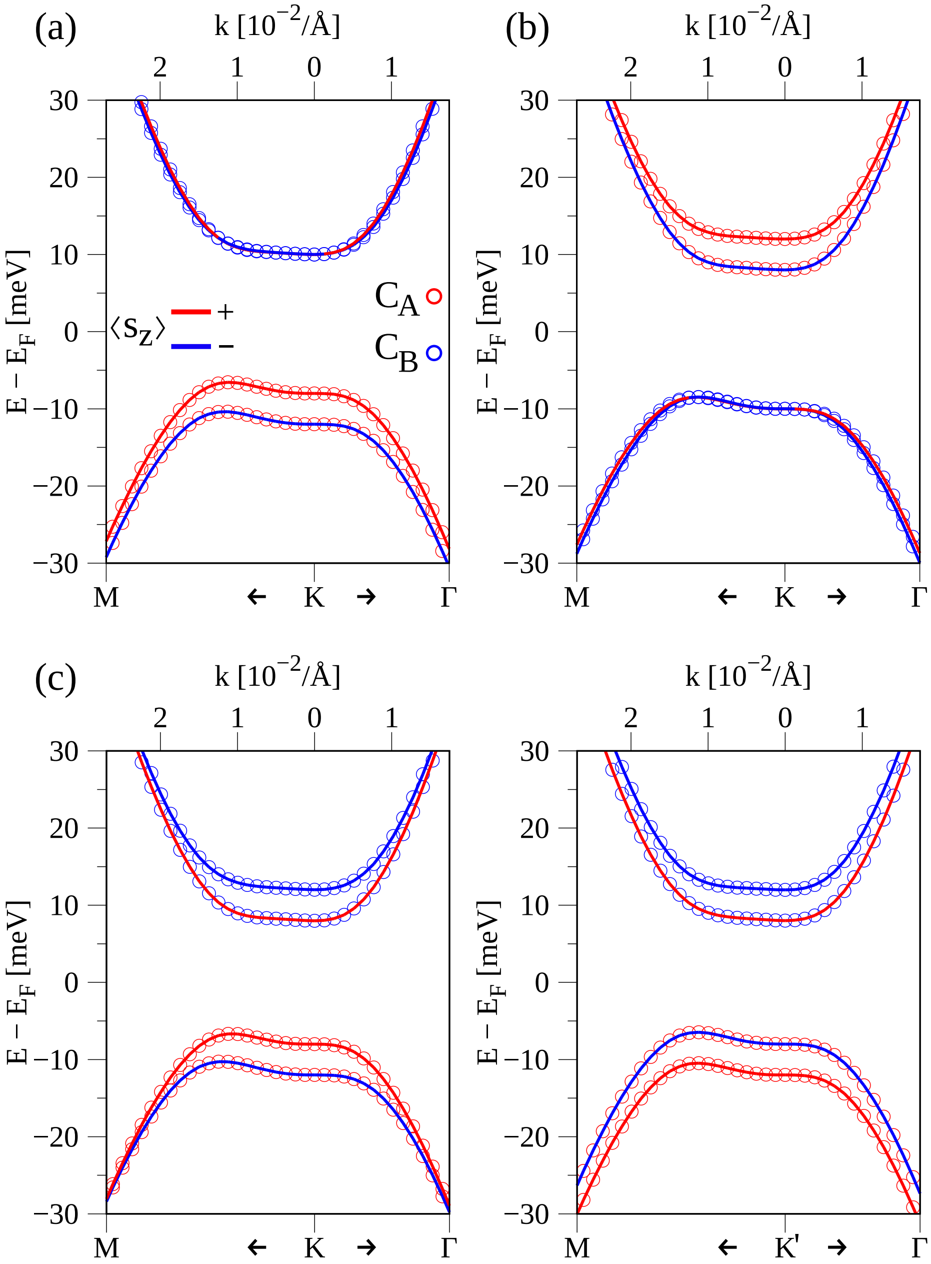

Figure 7.3: Low energy BLG band structures for different parameter sets of the Hamiltonian $\mathcal{H}_{\mathrm{BLG}}$. For all of the subfigures, we use $\gamma_0 = 2.45$ eV, $\gamma_1 = 365$ meV, $\gamma_3 = -270$ meV, $\gamma_4 = -165$ meV, and $\Delta = 10$ meV, while unspecified parameters are zero. Color of the lines (symbols) corresponds to the s_z (pseudospin) expectation value. In the case, in which time-reversal symmetry is preserved (broken), we show the bands at K (K and K′). (a) $V = 10$ meV, $\lambda_{\mathrm{I}}^{\mathrm{A2}} = \lambda_{\mathrm{I}}^{\mathrm{B2}} = 2$ meV. (b) Same as (a), but $V = -10$ meV. (c) Same as (a), but with additional $\lambda_{\mathrm{ex}}^{\mathrm{A1}} = \lambda_{\mathrm{ex}}^{\mathrm{B1}} = 2$ meV.

one would have to apply a transverse electric field that counters the built-in dipole of the mentioned BLG/TMDC heterostructure, in order to close the orbital band gap. By further increasing the amplitude of the external field, the gap reopens with switched band characters. The tuning of the SOC from the VB to the CB is a crucial knob to control the spin relaxation (SR) of conduction electrons in BLG, as recently shown in Ref. [31]. A similar effect, but with proximity exchange coupling, can be achieved in BLG/ferromagnetic insulator (FMI) heterostructures [311]. We will explicitly discuss these scenarios in the next chapter.

Finally, Fig. 7.3(c) illustrates the case of BLG sandwiched between a strong SOC and a magnetic material, as for example realized in TMDC/BLG/$Cr_2Ge_2Te_6$ (CGT) heterostructures. Such a case is interesting since we simultaneously create proximity magnetism and SOC in BLG, where the individual proximity effects are limited to one of the graphene layers. In Fig. 7.3(c), we show the band structure around the K and K′ valleys. The VB, which is split by proximity SOC, displays time-reversal symmetry, while the CB, which is split by proximity exchange, does not. The band structure can be tuned fully electrically as previously shown, thus yielding on-demand exchange and SOC of conduction electrons in BLG. In the next chapter, we will explicitly discuss realistic examples of proximity effects in BLG on the basis of DFT-calculation results. With the help of our Hamiltonian, we can extract valuable parameter sets, describing the proximitized BLG bands. In addition, we also elaborate on some potential spintronics device proposals due to the unique tunable band structure of proximitized BLG.

CHAPTER 8

Heterostructures of bilayer graphene, WS_2, and $Cr_2Ge_2Te_6$

This chapter is based on the publications: K. Zollner, M. Gmitra, and J. Fabian, New Journal of Physics ***20****, 073007 (2018), "Electrically tunable exchange splitting in bilayer graphene on monolayer* $Cr_2X_2Te_6$ *with X = Ge, Si, and Sn", and K. Zollner, M. Gmitra, and J. Fabian, Physical Review Letters* ***125****, 196402 (2020) "Swapping Exchange and Spin-Orbit Coupling in 2D van der Waals Heterostructures".*

8.1 Introduction

Since the first successful exfoliation of graphene, two-dimensional (2D) van der Waals (vdW) materials have become indispensable for spintronics [4, 154]. Because adjacent materials mutually influence each other via proximity effects [30], several interactions, such as superconductivity, magnetism, and spin-orbit coupling (SOC), can be induced on demand, while simultaneously each individual layer maintains its characteristic properties. Moreover, and this is a key ingredient, gating is a tool to control these proximity-induced spin interactions, as impressively demonstrated in several studies [99, 101, 102, 164, 194, 264, 329–333]. Especially the recently discovered vdW layered magnets [283, 284] have opened new avenues for basic research [51, 285] on magnetism in the 2D limit, as well as for applications [52, 95, 286–288]. The family of 2D magnetic materials includes conductors, insulators, ferromagnets, and antiferromagnets. Prominent examples, which are frequently considered now are Fe_3GeTe_2, $Cr_2Ge_2Te_6$ (CGT), CrI_3, and $MnPSe_3$ [51, 334]. In addition, the available 2D material family includes also the semiconducting transition-metal dichalcogenides (TMDCs), such as MoS_2 and WSe_2, which provide giant SOC, spin-valley locking, and are a favorite platform for optical experiments [289–293, 335].

Another particularly high-ranking material in this context is bilayer graphene (BLG), which features an idiosyncratic[1] low energy band structure [217], as we have seen in the last chapter. BLG itself is already full of surprises as it provides a playground for strongly correlated physics, given the right twist of its layers [322, 323]. However, and this is a major drawback for spin manipulation, it has negligible intrinsic SOC [217] and additionally lacks magnetism. Fortunately, we can add all the necessary ingredients via proximity coupling [31, 88, 140, 153, 264, 311]. For AB-stacked BLG in proximity to a TMDC, recent capacitance measurements [336] demonstrated that SOC of conduction electrons can be turned on and off by gating, see Fig. 8.1, in accordance to previous predictions [31, 337]. In the experiment, they measured the so-called penetration field capacitance C_p, as function of the displacement field and the electron density in a dual-gated structure. Since the measured capacitance C_p is essentially inversely proportional to the density of states (DOS) [338] of the proximitized BLG, electronic gaps will manifest as C_p maxima. With the help of hexagonal boron nitride (hBN)/graphite junctions as top and bottom gate electrodes, the low energy band structure of the proximitized BLG can be tuned and the doping density can be controlled. The measured capacitance, see Fig. 8.1(b), suggests that proximity-induced SOC in BLG is layer resolved and thus can be switched from valence band (VB) to conduction band (CB) and vice versa. Similarly, when BLG is in proximity to a magnetic material, exchange coupling can be switched on and off [311, 339, 340].

---

[1] The low energy bands are layer- and sublattice-polarized, and an external electric field can tune the band gap.

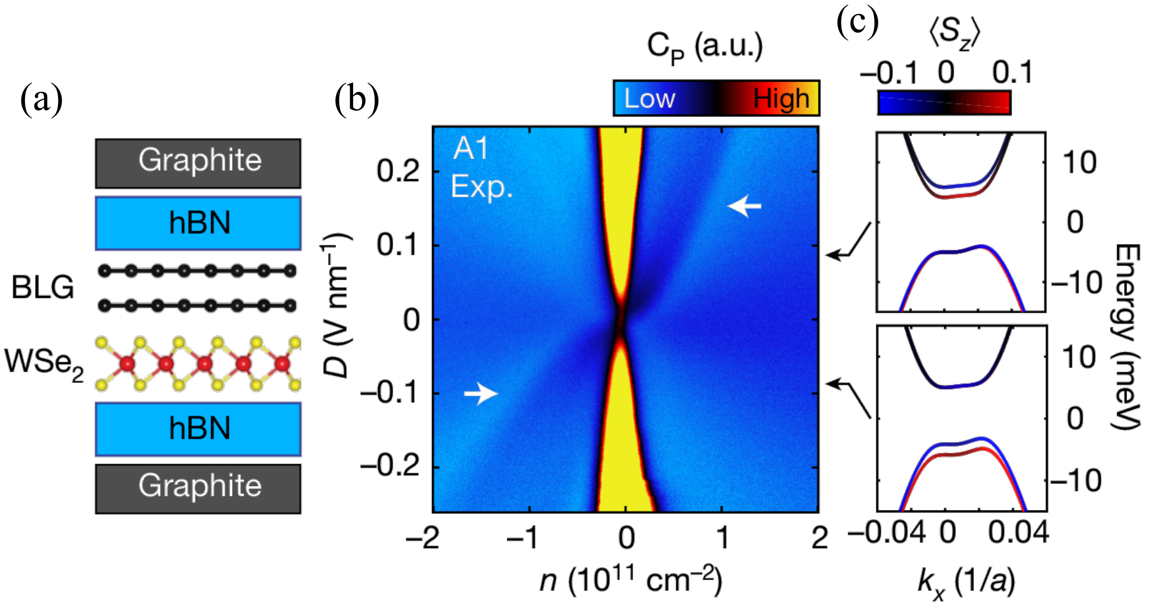

Figure 8.1: Measurement of the layer resolved SOC in BLG. (a) Schematic view of the geometry of the BLG/WSe$_2$ heterostructure, with hBN/graphite junctions as top and bottom gate electrodes. (b) Colormap of the measured penetration field capacitance, C_p, as function of the displacement (transverse electric) field D and the doping density n. The measured capacitance $C_p = c^2/(2c + \partial n/\partial \mu)$ depends on the geometric capacitance c and the electronic compressibility $\partial n/\partial \mu$, so that gaps in the band structure manifest as maxima in C_p. The white arrows in (b) indicate the proximity spin-orbit split bands of BLG. (c) The low energy model band structures of proximitized BLG that would correspond to fixed values of positive (top) and negative (bottom) displacement fields. Figures are from Ref. [336].

In this chapter, we investigate the mentioned BLG vdW heterostructures in detail by combining first-principles calculations with our model Hamiltonian, and provide a well founded basis for further considerations. First, we discuss BLG in proximity to CGT and explicitly show that an external transverse electric field can switch the exchange splitting from the VB to the CB. An additionally important case is that of CGT encapsulated BLG, where the in-plane conductance can be turned on and off via switching the magnetization direction in one of the CGT layers. Second, we investigate BLG in proximity to the strong SOC TMDC WS_2 and explain the most important band structure features. The gate tunability is similar as for the CGT case. For the singly proximitized structures, we briefly discuss some application prospects. Finally, we come to the case of the doubly proximitized CGT/BLG/WS_2 sandwich structure, providing both spin interactions simultaneously, SOC and exchange. *We demonstrate the fully electrical swapping of two different spin interactions in a single heterostructure device.*

8.2 Computational details

The electronic band structure calculations and structural relaxation of the BLG-based heterostructures were performed by density functional theory (DFT) [204] with QUANTUM ESPRESSO [267]. Self-consistent calculations were performed with the k-point sampling of $12 \times 12 \times 1$ to get converged results for the proximity exchange and SOC. Only for the CGT/BLG/WS_2 sandwich structure, when SOC is included, a smaller k-point sampling of $6 \times 6 \times 1$ was used due to computational limitations. We performed open shell calculations that provide the spin polarized ground state of CGT. A Hubbard parameter of $U = 1$ eV was used for Cr d-orbitals, being in the range of proposed values for CGT [283, 311]. We used an energy cutoff for charge density of 500 Ry and the kinetic energy cutoff for wavefunctions was 60 Ry for the scalar relativistic pseudopotential within the projector augmented wave (PAW) method [268] with the Perdew-Burke-Ernzerhof (PBE) exchange correlation functional [206]. When SOC was included, we used the relativistic versions of the pseudopotentials. For the relaxation of the heterostructures, we added vdW corrections [269, 270] and used quasi-Newton algorithm based on trust radius procedure. Dipole corrections [271] were also included to get correct band offsets and internal electric fields. In order to simulate quasi-2D systems, we added a vacuum of 20 Å to avoid interactions between periodic images in our slab geometry. To determine the interlayer distances, the atoms of BLG and WS_2 were allowed to relax only in their z positions (vertical to the layers), and the atoms of CGT were allowed to move in all directions until all components of all forces are reduced below 10^{-3} [Ry/a_0], where a_0 is the Bohr radius. The obtained interlayer distances are of typical vdW size and summarized in Fig. 8.7(b).

8.3 Exchange valve in bilayer graphene on $Cr_2Ge_2Te_6$

For the BLG/CGT heterostructure, we used a 5×5 supercell of BLG in Bernal stacking and a $\sqrt{3} \times \sqrt{3}$ CGT supercell, i. e., the CGT substrate is twisted by an angle of 30° with respect to BLG. We kept the lattice constant of graphene unchanged at $a = 2.46$ Å and stretched the CGT lattice constant by roughly 4% from 6.8275 Å [341] to 7.1014 Å. The supercell of BLG on CGT has a lattice constant of 12.3 Å and contains 130 atoms in the unit cell. The average calculated magnetic moments are: Cr ($+3.217\ \mu_B$), Ge ($+0.032\ \mu_B$), Te ($-0.104\ \mu_B$), G_1 ($-0.0002\ \mu_B$), and G_2 ($0.0\ \mu_B$), where $G_{1/2}$ denotes the bottom/top graphene layer. The bottom graphene layer displays a proximity-induced magnetization along the $-z$ direction

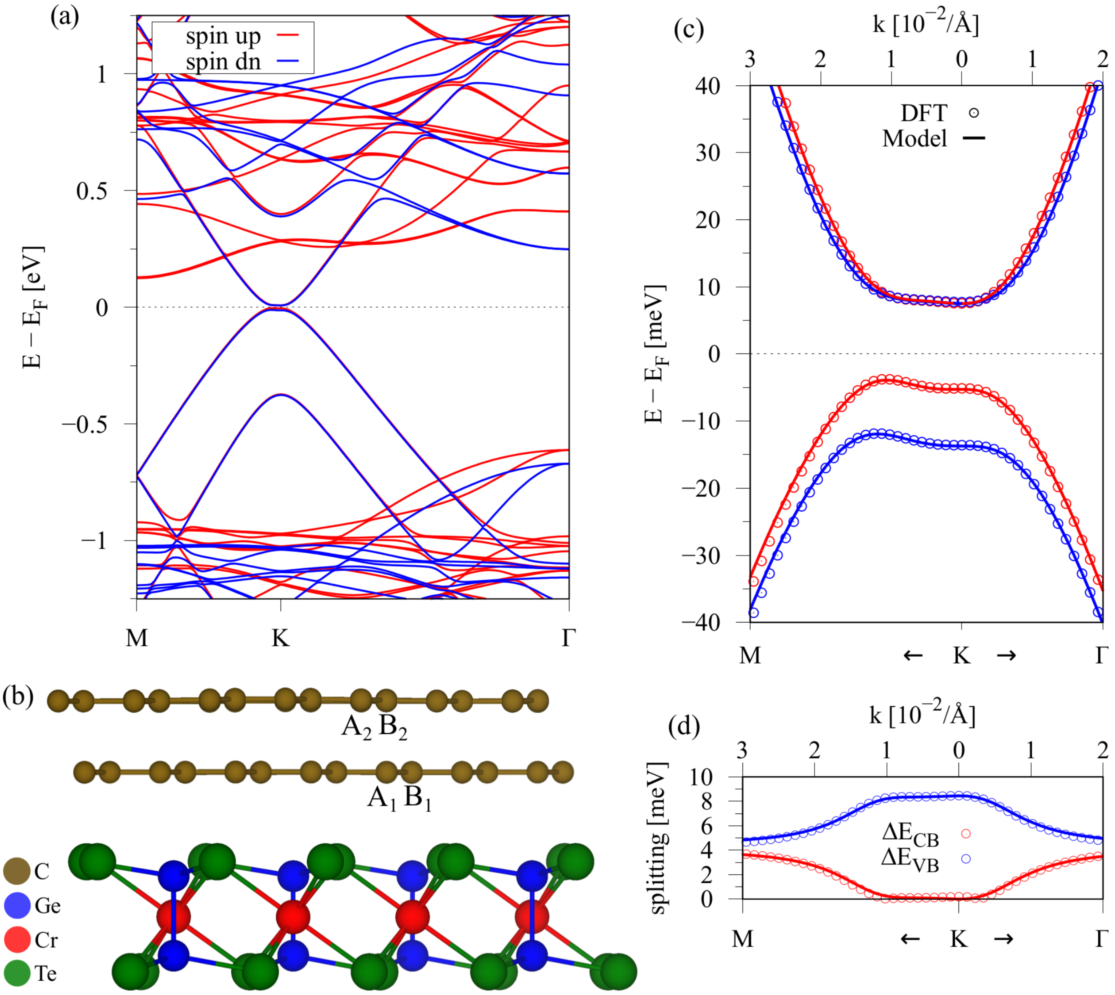

Figure 8.2: (a,b) Calculated band structure without SOC and geometry of BLG on CGT with labels for the sublattices. (c) Zoom to the calculated low energy bands (symbols) around the K point with a fit to the model Hamiltonian (solid lines) $\mathcal{H}_{\mathrm{BLG}}$, Eq. (7.1). Bands in red (blue) correspond to spin up (down). (d) Energy splittings of the CB and VB.

(parallel to the magnetic moments of the Te atoms), while the magnetization of Cr atoms in CGT points along the z direction. In Figs. 8.2(a,b) we show the DFT-calculated band structure and a side view of the geometry of BLG on CGT. Overall, the dispersion near the Fermi level closely resembles the band structure of bare BLG since we can identify the four parabolic low energy bands. Nearly all other bands originate from the CGT layer. By zooming into the fine structure around the Fermi level, see Fig. 8.2(c), we find an orbital band gap of about 10 meV. In addition, the VB is spin split by about 8 meV, while the CB splitting is negligible near the K point, see Fig. 8.2(d). How does this come about?

First of all, the low energy bands are formed by the non-dimer atoms B_1 and A_2. As demonstrated in the previous chapter, a transverse electric field opens the band gap of BLG because we introduce a potential difference between the two graphene layers. Here, no field is applied, but our considered structure has an intrinsic dipole, i. e., a built-in electric field, which essentially has the same effect as an external one. The built-in field of the structure is about 0.4 V/nm. In addition, the graphene layer adjacent to CGT experiences proximity-induced exchange coupling, splitting the VB in energy. In contrast, the CB is not split because its states are formed by the top graphene layer, which is far away from the magnetic substrate and short range proximity effects are nearly absent. The coupling to the magnetic substrate is limited to the bottom graphene layer. By fitting the low energy model Hamiltonian $\mathcal{H}_{\text{BLG}}$, Eq. (7.1), to the first-principles data, we find perfect agreement for the dispersion and band splittings, see Figs. 8.2(c,d). The fitted parameters are summarized in Tab. A.2 for the CGT/BLG heterostructure. In order to fit the DFT-data, most relevant are the exchange parameters corresponding to the bottom graphene layer, which are about -4 meV in magnitude. The ones for the top layer can be neglected. The negative sign originates from the fact that the proximity-induced magnetization of the bottom graphene layer points along the $-z$ direction, as mentioned above.

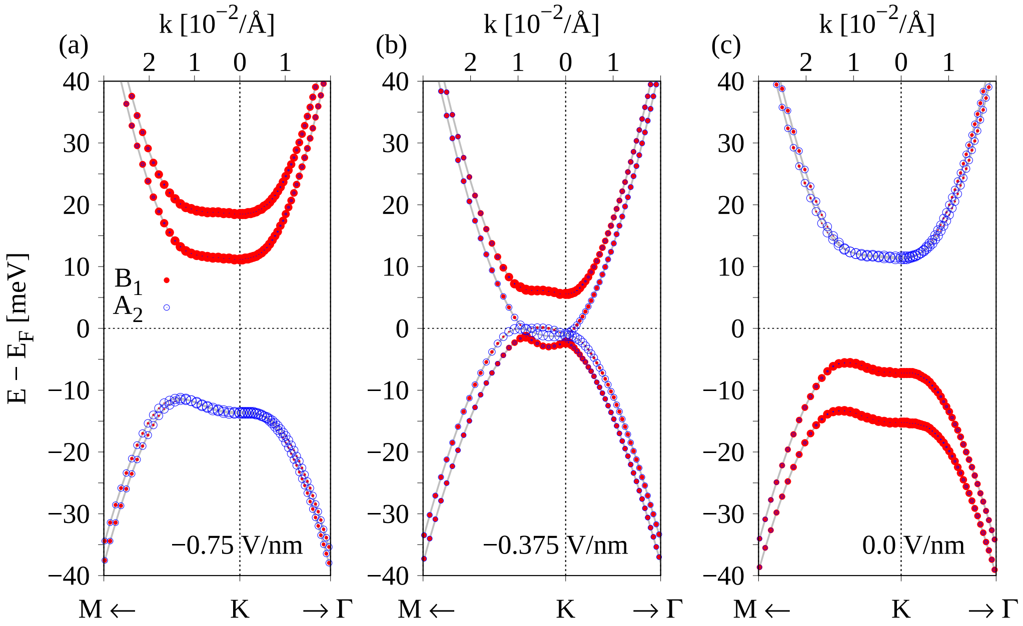

Figure 8.3: Calculated sublattice resolved band structures around the K valley for transverse electric fields of (a) -0.75 V/nm, (b) -0.375 V/nm, (c) 0.0 V/nm. The circles' radii correspond to the probability of the state being localized on the non-dimer atoms B_1 (red filled circles) and A_2 (blue open circles).

Let us now discuss the switching of the exchange coupling from the VB to the CB. In Fig. 8.3, we show the evolution of the low energy bands of BLG for a series of transverse electric fields. At zero field strength, see Fig. 8.3(c), the situation is as explained above; the exchange split VB is formed by p_z orbitals of B_1, while the nearly unsplit CB is formed by A_2 orbitals. Because of the short range proximity effect, only the atoms from the bottom graphene layer are affected by the exchange coupling. The built-in electric field (dipole), which points from CGT towards BLG, determines the band ordering such that states from B_1 form the VB at zero external field. Because we know that the built-in electric field points along the positive z direction, a positive external field would have an additive effect, simply increasing the orbital band gap and leaving the exchange splitting nearly unchanged. Here, we are interested in the switching behavior. By applying a negative field (along $-z$ direction), we can counter the built-in field. When the external field has roughly compensated the dipole field, the orbital gap closes. As we can see in Fig. 8.3(b), the band gap is closed for a field of -0.375 V/nm because the states from the non-dimer atoms B_1 and A_2 are almost at the same potential energy. By increasing the negative field further, we again introduce a potential difference between the graphene layers and the band gap reopens, see Fig. 8.3(a). In contrast to the zero field case, it is now the CB that is formed by B_1 orbitals, while A_2 atoms form the VB. Still, it is the lower graphene layer that experiences the proximity exchange coupling, splitting now the CB. This switching of the exchange splitting from VB to CB is only possible due to the short range proximity effect in combination with the layer-polarized low energy bands of BLG. *A proximity exchange valve is realized.*

What are the consequences of the switching and how can it be employed in devices? Simple model calculations predicted that BLG on a generic ferromagnetic insulator (FMI) substrate can be a platform for field-effect magnetic or spin devices [339, 342–345]. In dual gated BLG/CGT structures, where we can apply a transverse electric field across the structure and simultaneously tune the Fermi level, 100% spin polarization can be achieved. Imagine the Fermi level in Fig. 8.3(a) to lie in between the two spin-split CBs. If an unpolarized current is then injected into BLG, which is subject to proximity exchange from a FMI substrate, one spin component is perfectly filtered. A spin polarized current could be analyzed as well because, for a given spin-ordering of the bands, which is determined by the proximity magnetization, only one spin channel is addressed. By tuning the electric field, say to the situation shown in Fig. 8.3(c), no spin filtering occurs because both spin channels can be addressed in the CB. Therefore, BLG/FMI heterostructures could be employed as fully electrically operating spin-filters or detectors.

We have also considered CGT encapsulated BLG, see Fig. 8.4. In this case, both graphene layers are getting proximitized. Depending on the magnetization directions of the two individual CGT layers, different low energy band structures can be realized. Our results show that in the ferromagnetic configuration, where the magnetizations of both CGT layers point along the z direction, both graphene layers are getting equally proximitized, see Fig. 8.4(a). The full band structure, see Fig. 8.4(b), is similar to the non-encapsulated case, shown in Fig. 8.2(a). In contrast to before, this CGT/BLG/CGT sandwich structure is more or less z-mirror symmetric and the built-in dipole is almost zero. Consequently, the orbital band gap of BLG is closed, see Fig. 8.4(c). Moreover, now both graphene layers experience proximity exchange coupling, and the VB and the CB are spin split. As a consequence, the spin-split low energy bands cross the Fermi level and the system is conductive, see Fig. 8.4(c).

For the antiferromagnetic configuration, in which the magnetization of the bottom (top) CGT layer points along the z ($-z$) direction, see Fig. 8.4(d), the proximity effect is still present, but the sign of the exchange coupling for the top graphene layer changes. Consequently, the spin splitting will be of similar magnitude, but of opposite sign. Remarkably, the fine structure near the K point reveals that a sizable band gap of about 5 meV opens, such that no bands cross the Fermi level and zero in-plane conductance can be expected, see Fig. 8.4(f).

In this case, it is not an electric field that is responsible for the gap opening, but rather the unique sublattice- and layer-polarized low energy band structure of BLG itself, being subject to layered antiferromagnetic proximity exchange.

Our CGT/BLG/CGT geometry is similar to the recently proposed CrI_3/BLG/CrI_3 spin-valve heterostructure [340], in which the in-plane conductance can be controlled by switching the magnetic configuration. The advantage of our presented structure is that only the bands of the proximitized BLG are present at the Fermi level, while for the CrI_3/BLG/CrI_3 structure also bands originating from the CrI_3 layers reside near the Fermi level [340]. Moreover, we have also extracted the relevant fit parameters for both configurations, ferromagnetic and antiferromagnetic, of our sandwich structure by employing the model Hamiltonian $\mathcal{H}_{\mathrm{BLG}}$, Eq. (7.1). The results are summarized in Tab. A.2, and can be used for further spin and charge transport simulations.

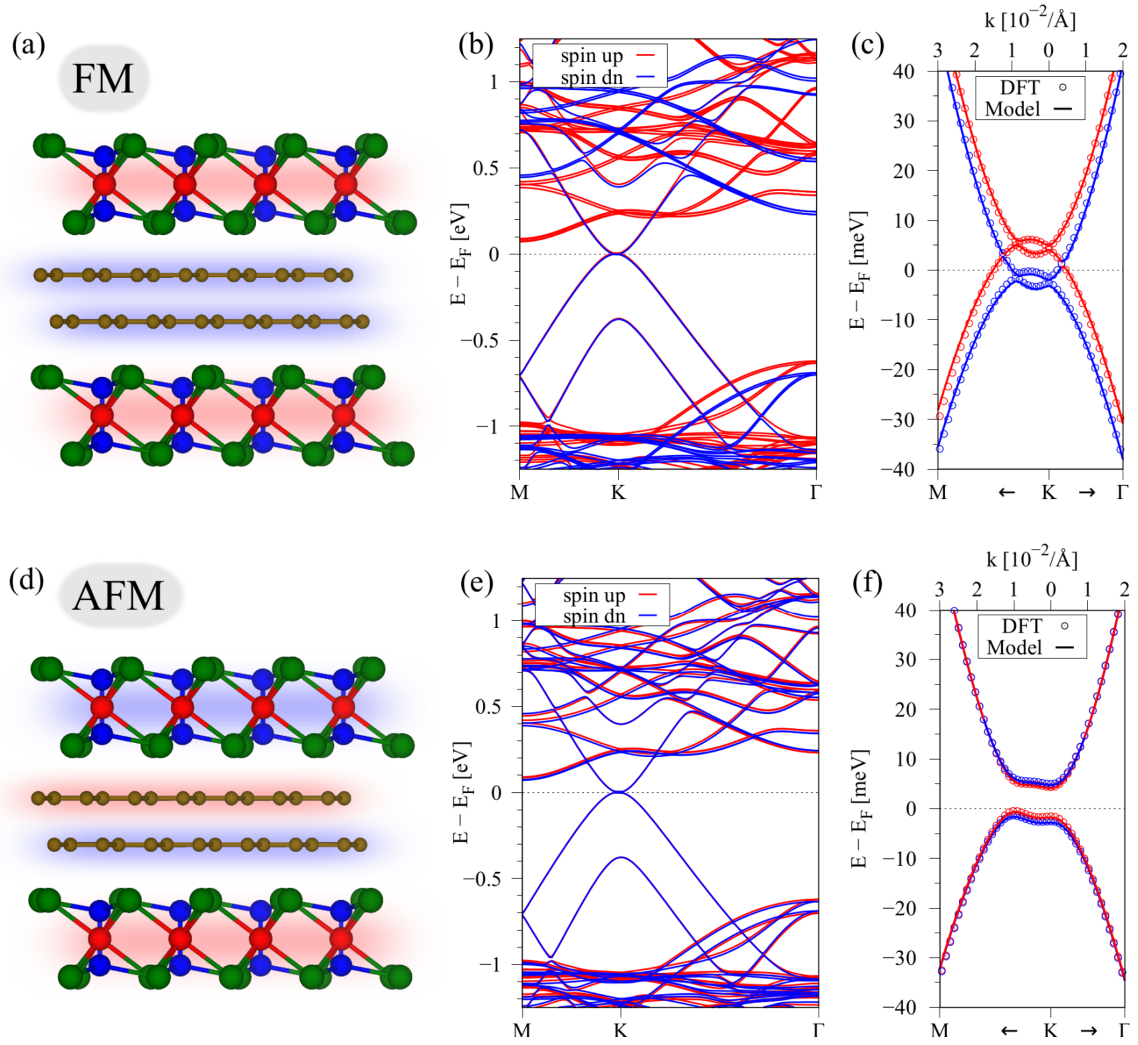

Figure 8.4: Band structure, geometry, and low energy model fit of BLG encapsulated by CGT for different magnetic configurations of the top and bottom CGT. In the geometries, the background color is the (proximity) magnetization of the corresponding layer (red = ↑, blue = ↓). (a)-(c) Ferromagnetic and (d)-(e) antiferromagnetic configuration of the two CGT layers.

8.4 Spin-orbit valve in bilayer graphene on WS$_2$

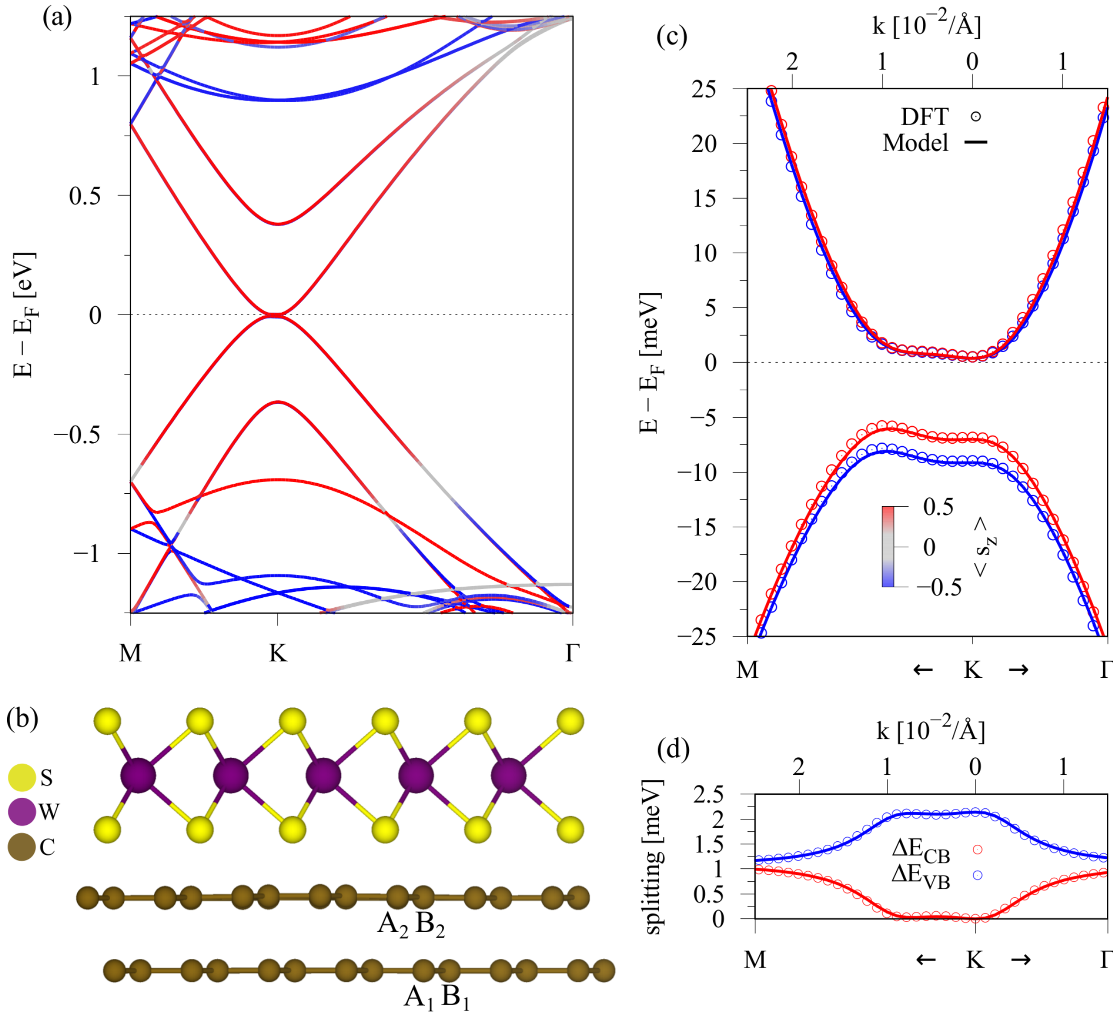

Figure 8.5: (a,b) Calculated band structure with SOC and geometry of WS$_2$ on BLG with labels for the sublattices. (c) Zoom to the calculated low energy bands (symbols) around the K point with a fit to the model Hamiltonian (solid lines) $\mathcal{H}_{\mathrm{BLG}}$, Eq. (7.1). The color of the bands corresponds to the s_z spin expectation value. (d) Energy splittings of the CB and VB.

Before we come to our most important and final CGT/BLG/WS$_2$ trilayer structure, we also summarize the findings for the BLG/WS$_2$ stack. For the WS$_2$/BLG heterostructure, we used a 5 × 5 supercell of BLG in Bernal stacking and a 4 × 4 supercell of WS$_2$. We stretched the lattice constant of the BLG by roughly 2% to 2.5 Å and the WS$_2$ lattice constant was compressed by about 1% from 3.153 Å [346] to 3.125 Å. The supercell of WS$_2$ on BLG has a lattice constant of 12.5 Å and contains 148 atoms in the unit cell.

In Figs. 8.5(a,b), we show the calculated band structure and a side view of the geometry of WS$_2$ on BLG. Similarly to before, we identify the four parabolic bands of BLG, located near the heterostructure Fermi level and within the band gap of the TMDC. The presented results are in perfect agreement with Ref. [31]. The low energy bands can be already understood from our previous analysis of the BLG/CGT structure. The orbital gap of about 5 meV is due to the built-in electric field of the heterostructure, introducing a potential difference between the graphene layers. In addition, the VB is spin split because of short range proximity-induced SOC, which is limited to the top graphene layer. The built-in field is oriented from the TMDC towards the BLG, dictating the given band ordering for zero external field. We would like to emphasize that the two systems, BLG/CGT and TMDC/BLG, indeed show similar low energy band structure features. Despite the similarity, we break time-reversal symmetry in the case of the FMI, and the spin-split bands at K and K′ are the same. In contrast, for the TMDC-based case, time-reversal symmetry is still preserved.

In addition to the mere prediction of this scenario in Ref. [31], we go one step further and fit our BLG low energy model Hamiltonian $\mathcal{H}_{\mathrm{BLG}}$, Eq. (7.1), to the DFT-calculated bands. As can be seen in Figs. 8.5(c,d), we find perfect agreement for the dispersion and the band splittings. The fitted parameters are also summarized in Tab. A.2 for the BLG/WS_2 heterostructure. In analogy to before, an external transverse electric field can be used to switch the spin-orbit splitting from the VB to the CB because of the layer-polarized low energy bands and short range proximity effects. Here, we do not explicitly show the electric field tunability, but refer the reader to Ref. [31].

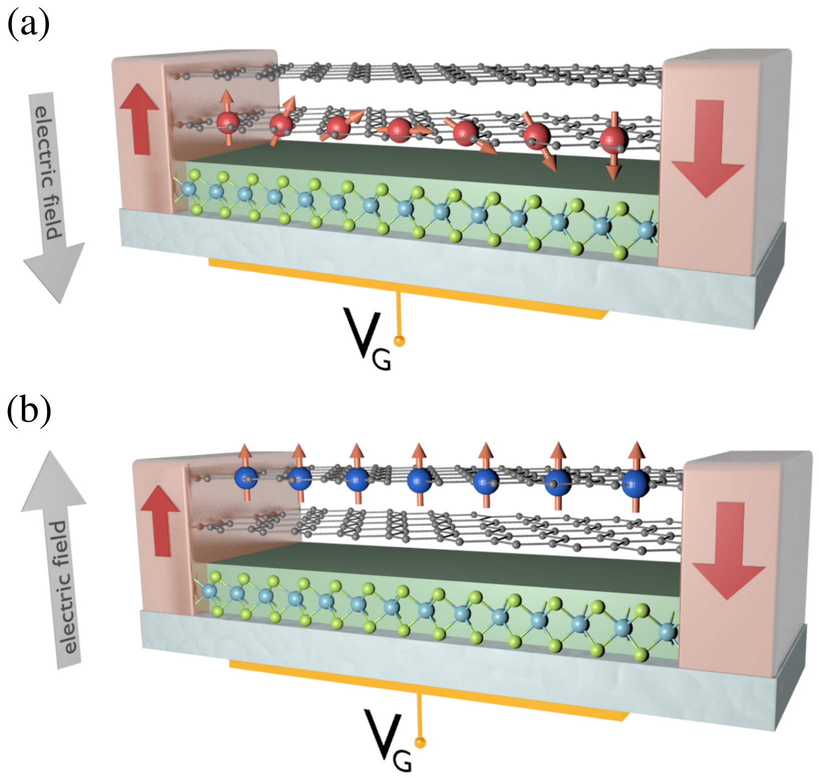

Figure 8.6: Spin field-effect transistor (FET) based on a BLG/TMDC heterostructure. The two ferromagnetic electrodes have opposite magnetization and serve as injector and detector for the spins. (a) In the ON state, spins effectively feel large SOC, spin precession is strong, and they can enter the ferromagnet. (b) In the OFF state, spins feel weak SOC, spin precession is absent and no current can flow. Figures are from Ref. [31].

Again, we can ask about application prospects of this switching behavior [31]. In Fig. 8.6, a particular device scheme for a BLG-based spin FET is illustrated, similar to the Datta-Das one in Fig. 1.2, but with opposite magnetization for injector and detector contacts. Essentially this device relies on the tunability of SOC of conduction electrons. Since the spin-orbit field components ω are proportional to the energy splitting ΔE of the bands, see Eq. (4.1), and the spin relaxation (SR) rate is proportional to ω^2, one can tune the spin precession of electrons by gating. For an electric field, pointing from BLG towards the TMDC, see Fig. 8.6(a), electron spins will be injected in the bottom graphene layer, which experiences strong proximity-induced SOC. Consequently, SR is strong, injected spins will precess, and the detected spin signal is large in case of antiparallel magnetized contacts. By switching the electric field direction, see Fig. 8.6(b), spins are injected in the top graphene layer, which is practically "free" from proximity SOC. No precession takes place and the detector signal is (in the ideal case) zero. *A spin-orbit valve can be realized.*

For completeness, we have also calculated and fitted the band structure of BLG encapsulated by WS_2, see Fig. A.1. Again, due to the roughly z-mirror symmetric structure, the orbital band gap is closed and both graphene layers experience the same amount of proximity-induced SOC. The corresponding fit parameters are also summarized in Tab. A.2. Remarkably, recent capacitance measurements, see Fig. 8.1, could confirm the gate tunable low energy band structure of the proximitized BLG for both scenarios, BLG/WS_2 and WS_2/BLG/WS_2 [336]. The experimental confirmation of the predicted spin-orbit switching [31, 336] unambiguously proves the importance of 2D material vdW heterostructures to tailor spin interactions.

8.5 Doubly proximitized bilayer graphene

Finally, we study the *trilayer* geometry consisting of BLG, WS_2, and CGT. For the considered heterostructure, we choose a 5×5 supercell of BLG in Bernal stacking, a $\sqrt{3} \times \sqrt{3}$ CGT supercell, and a 4×4 supercell of WS_2. We stretched the lattice constant of BLG by roughly 2% to 2.5 Å [321] and stretched the lattice constant of CGT by roughly 6% to 7.2169 Å [341]. The WS_2 lattice constant is compressed by about 1% to 3.125 Å [346]. The supercell of WS_2/BLG/CGT has a lattice constant of 12.5 Å and contains 178 atoms in the unit cell. In Fig. 8.7(b) we show the exact geometry of the WS_2/BLG/CGT hybrid structure, including the DFT-relaxed interlayer distances. The lower (upper) graphene layer, formed by sublattices A_1 and B_1 (A_2 and B_2), is proximitized by the CGT (WS_2) only due to the short-range proximity effects. With the knowledge from the previous sections, we expect to find proximity exchange (SOC) in the BLG bands originating from the lower (upper) graphene layer. In Fig. 8.7(a), we show the full band structure of the WS_2/BLG/CGT trilayer stack. In analogy to the previous sections, the bands near the Fermi level closely resemble the parabolic bands of pristine BLG. The low energy bands of BLG are now located within the band gaps from both surrounding materials, WS_2 and CGT. Keep in mind that time-reversal symmetry is broken in the trilayer structure due to the FMI.

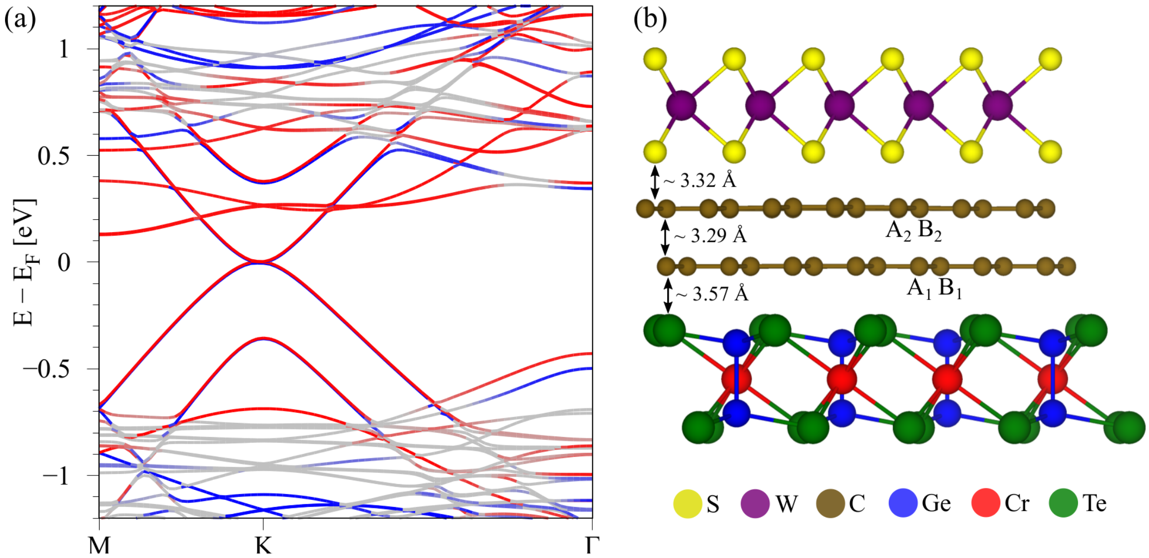

Figure 8.7: (a) Calculated electronic band structure of the WS_2/BLG/CGT heterostructure with SOC along the high symmetry path M-K-Γ. Color corresponds to the s_z spin expectation value. (b) Side view of the WS_2/BLG/CGT heterostructure. Different colored spheres correspond to the different atomic species. The lower (upper) graphene layer of BLG is formed by sublattices A_1 and B_1 (A_2 and B_2). The relaxed interlayer distances are also indicated.

In Fig. 8.8, we show the evolution of the gate tunable low energy bands of doubly proximitized BLG for a series of transverse electric fields between ±1 V/nm. In the upper (lower) row, we show the evolution of the bands near the K (K′) valley, and the external electric field is tuned from −1 V/nm to 1 V/nm from left to right. At first, we focus on the −1 V/nm case, where an orbital gap is present and the bands, originating from different layers, are well separated in energy. The orbital gap is due to the total, external plus built-in, transverse electric field. We find that the CB is split by about 10 meV, while the VB has only about 2 meV splitting. The spin ordering in the CB at K and K′ is the same, thus showing broken time-reversal symmetry. The VB spin ordering is different in both valleys with nearly preserved time-reversal symmetry, despite the magnetism in our structure. Our conclusion is that the CB is split by exchange and the VB by SOC due to short range proximity effects and layer-polarized bands. By decreasing the field amplitude to −0.5 V/nm, the orbital gap starts to close because we tune the potential difference between the graphene layers, while the band characters and their splittings remain nearly unchanged.

For a positive external electric field of 1 V/nm, the orbital gap is similar to the −1 V/nm case. However, we have switched the band characters. Now, the VB is split by exchange and the CB by SOC. Similarly, the exchange (SOC) split bands lack (nearly display) time-reversal symmetry, comparing them at K and K′ valleys. By decreasing the field amplitude to 0.4 V/nm, the band gap can be diminished with preserved band characters and splittings. For zero external electric field, the gap is then solely determined by the built-in electric field, which points from CGT towards the WS_2. The internal field is small, but finite, as BLG is sandwiched between two different materials, only approximately restoring the z-mirror

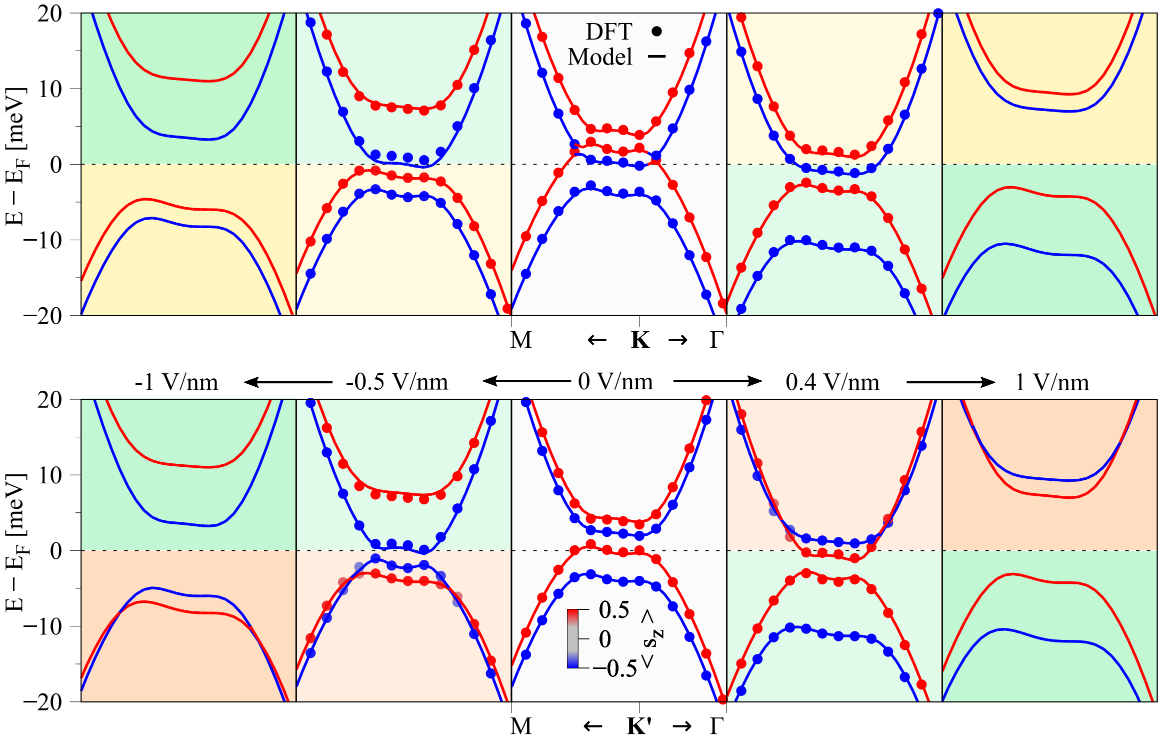

Figure 8.8: Low energy bands of BLG around the K (top) and K′ (bottom) points for the WS_2/BLG/CGT heterostructure. The color of the bands corresponds to the s_z spin expectation value. The yellowish (reddish) background color indicates that the bands are split by SOC with a down-up (up-down) spin ordering along increasing energy. The greenish background is for exchange split bands, where spin ordering is always up-down, as determined by the CGT magnetization. From left to right the transverse electric field is tuned from -1 V/nm to 1 V/nm. For electric fields of -0.5 V/nm, 0 V/nm, and 0.4 V/nm, we compare model (solid lines) and DFT data (symbols). For electric fields of ± 1 V/nm, we use the model parameters with extrapolated values for V, assuming a linear dependence on the field. Parameters $V = \{7.1, 3.2, -0.5, -3.6, -8.1\}$ meV correspond to the field values of $\{-1, -0.5, 0, 0.4, 1\}$ V/nm, respectively.

symmetry. The dispersion, near the K and K′ valleys is a result of this small built-in field in combination with the layer polarization and short-range proximity effects. As we have demonstrated in Fig. 8.8, an external electric field can be used to fully electrically swap the two proximity-induced spin interactions.

In the case of three electric field values, we have fitted our effective Hamiltonian $\mathcal{H}_{\mathrm{BLG}}$, Eq. (7.1), to the DFT-calculated low-energy dispersion, see Fig. 8.8. In all cases, we have obtained great agreement. A more detailed view, comparing model and DFT, is given in Fig. A.2 for zero electric field and in Fig. A.3 for fields of -0.5 V/nm and 0.4 V/nm. For the fitting itself, we first focused on the zero field case and obtained the orbital parameters γ, as well as the potential difference V and asymmetry Δ. In the second step, the relevant exchange and SOC parameters were determined. We have found large uniform proximity exchange ($\lambda_{\mathrm{ex}}^{\mathrm{A1}} = \lambda_{\mathrm{ex}}^{\mathrm{B1}}$) for the lower graphene layer and valley Zeeman SOC ($\lambda_{\mathrm{I}}^{\mathrm{A2}} = -\lambda_{\mathrm{I}}^{\mathrm{B2}}$) for the upper layer. Since the spin expectation values are predominantly out-of-plane, we

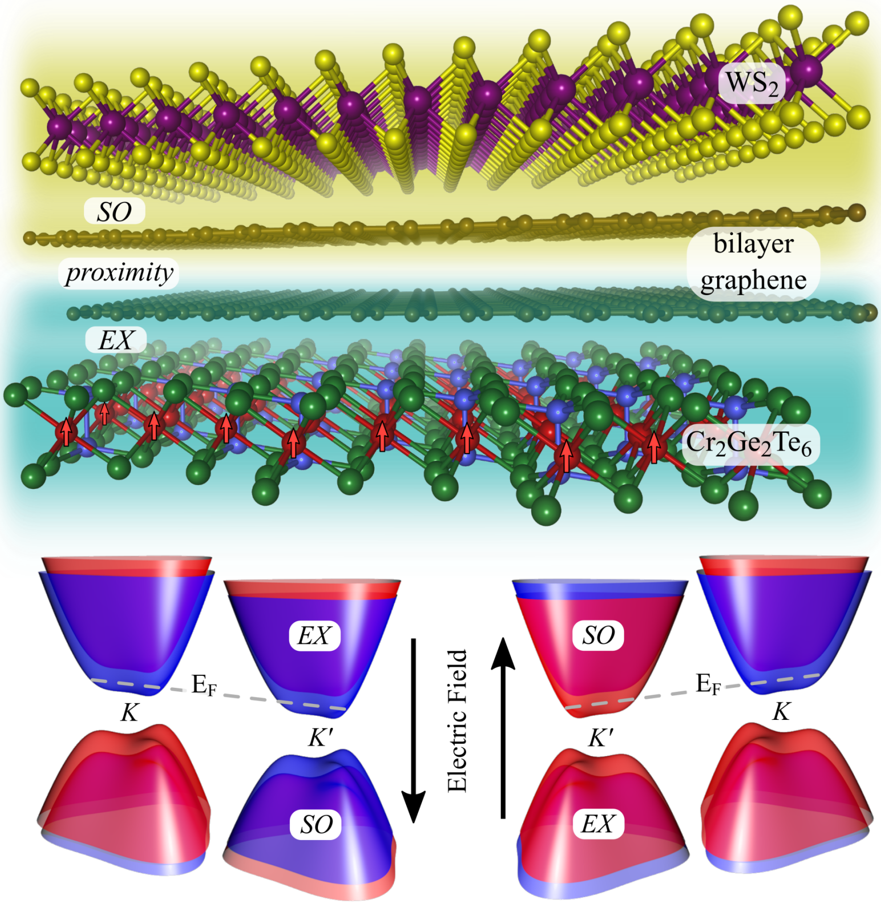

Figure 8.9: Ex-so-tic vdW heterostructure. Top: BLG sandwiched between a monolayer TMDC (such as WS_2 or $MoSe_2$) and a monolayer ferromagnetic semiconductor (such as CGT or CrI_3). The magnetization of the ferromagnet is indicated by the arrows. The top layer of BLG is proximitized by the TMDC, acquiring giant SOC, while the bottom layer of the BLG is proximitized by the ferromagnet, acquiring exchange coupling. Bottom: Electric tunability of the low-energy bands at K and K′. The colors red and blue indicate out-of-plane spin. For a fixed Fermi level (here in the CB), the Dirac electrons experience either exchange or SOC, depending on the electric field. *The figures were created with the help of M. Gmitra.*

could neglect the parameters λ_0 and λ_R. The fit parameters for the zero field case, with and without inclusion of SOC, are summarized in Tab. A.3. Turning on SOC in the calculation essentially activates the proximity effect from the WS_2. The parameter set yields an almost perfect agreement between model and DFT, see Fig. A.2.

Already the zero-field parameters can be used to study the charge and spin transport properties of the WS_2/BLG/CGT system. By considering two values of a finite electric field, −0.5 V/nm and 0.4 V/nm, we check the gate tunability of the parameters. As already discussed, the external field tunes the potential difference V between the graphene layers. Indeed, the investigated cases of a finite electric field can be fitted with the zero field parameters from Tab. A.3, just adapting V in our model. The agreement is shown in Fig. A.3 for −0.5 V/nm and 0.4 V/nm of external electric field. When a transverse electric field of 0.4 V/nm is applied, we use $V = -3.6$ meV, while for -0.5 V/nm of external field, we have $V = 3.2$ meV. The presented V tunability should be extendable to higher electric field values, a fact that we already exploited for the model band structures in Fig. 8.8 for ±1 V/nm, assuming a linear dependence of V on the external field. Most important, Fig. 8.8 demonstrates that proximity exchange and SOC can be switched from the VB to the CB fully electrically and reversibly, in agreement with our DFT analysis.

In Fig. 8.9, we summarize our findings in an illustrative picture. Each of the two materials, CGT and WS_2, induces a different spin interaction in only one of the two graphene layers, which will be imprinted on the low energy dispersion of BLG. We call it an *ex-so-tic* structure, as a reference to both exchange (ex) and spin-orbit (so) couplings blended into an "exotic" sounded sniglet[2]. One of the bands is split by exchange and the other by SOC due to short range proximity effects and layer polarization. An external gate voltage can be used to switch between the two interactions. With regard to experiments, this vdW heterostructure offers on-demand exchange and SOC, which are accessible by top and back gate electrodes, as already demonstrated for proximity SOC alone [336]. It is also worth to mention that the presented switching operation is not restricted to BLG sandwiched between TMDC and FMI *monolayers*. Also multilayers should work since proximity effects are short-ranged and limited to adjacent layers. In addition, any proximity-induced interaction can be in principle turned on and off with this approach. The swapping is a new milestone for vdW engineering that goes well beyond the two spin interactions.

8.6 Summary and conclusion

In this chapter, we have investigated proximity effects in BLG, induced by the FMI CGT and by the TMDC WS_2. The strong SOC material WS_2 induces significant amount of SOC in the adjacent graphene layer by the proximity effect. Similarly, the magnetic material CGT induces strong proximity exchange in the adjacent graphene layer only. Due to the layer polarization of the low energy BLG bands, only the VB is spin split because these bands are formed by the proximitized graphene layer. The orbital band gap of the BLG dispersion is determined by the total, built-in and external, transverse electric field and can be used to switch the splitting from the VB to the CB. Consequently, we can turn on and off either spin-orbit or exchange coupling in singly proximitized BLG.

Combining the knowledge in a doubly proximitized WS_2/BLG/CGT structure, results in a unique multifunctional device, in which two fundamental spin interactions, exchange and SOC, can be swapped fully electrically. As a consequence, we can also on-demand turn on and off time-reversal symmetry in the electronic states at a given doping. In principle, the demonstrated swapping behavior is not limited to the investigated structure. Due to the amount of available 2D materials, comprising ferro- and antiferromagnets, superconductors, and other strong SOC materials, the possibilities to achieve electrical tunability of other effects are endless.

---

[2] A *sniglet* is a word that does not appear in the dictionary.

PART IV

Transition-Metal Dichalcogenides

CHAPTER 9

The basics and strain effects of TMDCs

This chapter is based on the publication: K. Zollner, P. E. Faria Junior, and J. Fabian, Physical Review B ***100****, 195126 (2019), "Strain tunable orbital, spin-orbit, and optical properties of monolayer transition-metal dichalcogenides".*

In this chapter, we introduce the basic properties of semiconducting transition-metal dichalcogenides (TMDCs) such as their lattice geometry, band structure, and low energy Hamiltonian. The Hamiltonian is based on different d orbitals of the transition-metal atom that form the relevant band edges around the K and K$'$ valleys. The latter are important for the description of optical and excitonic properties of the monolayer TMDCs. We also include additional terms into the Hamiltonian that are due to a magnetic substrate material in close proximity to the TMDC. Proximity exchange effects will be important in the next chapter, when we discuss TMDC/CrI_3 heterostructures. In general, when considering TMDCs in van der Waals (vdW) heterostructures for periodic density functional theory (DFT) calculations, usually lattice mismatch is present and the TMDC needs to be strained. Here, we analyze the effects of biaxial strain on the orbital, spin-orbit, and optical properties of the monolayer TMDCs.

9.1 Introduction

Recent advances in condensed matter physics show, that two-dimensional (2D) vdW materials and their hybrids are vital for miniaturized spintronics devices [30]. As we have already mentioned in the previous chapters, TMDCs are an important material class. Monolayer TMDCs (MoS_2, $MoSe_2$, WS_2, and WSe_2) are direct band gap semiconductors with optical gaps in the visible spectrum [44, 289–293, 347, 348]. Especially their optical properties make them appealing for several theoretical and experimental considerations, such as in the fields of optoelectronics [349], optospintronics [88, 99, 194], and valleytronics [350–352]. For example, TMDCs have been used for optical spin injection in graphene [88, 99, 194] due to their helicity- and spin-selective optical excitations [353].

In general, 2D materials are sensitive to external influences, which can be used to control the electronic and related spin and optical properties. We have seen in the previous chapters that proximity effects modify the low energy bands of graphene within vdW heterostructures.

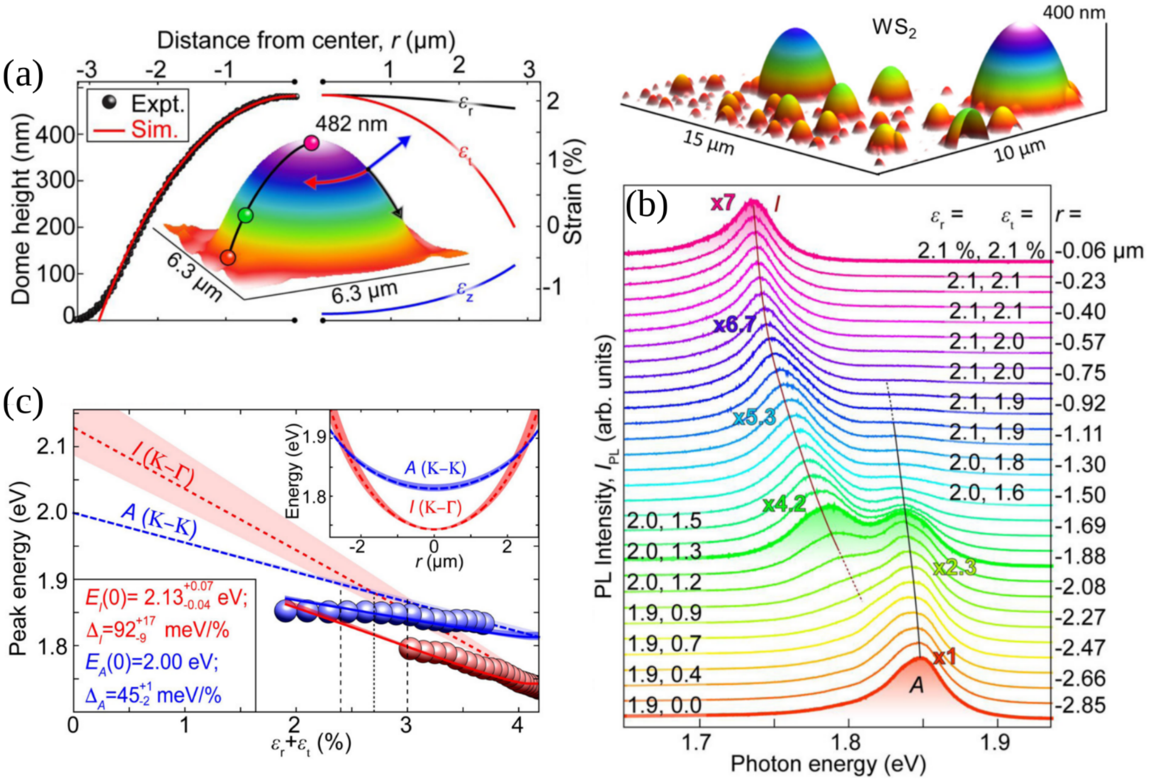

Figure 9.1: Strain-tunable direct-to-indirect band gap transition. (a) A three-dimensional (3D) atomic force microscopy image of one WS_2 dome or nanobubble (enlarged view of the upper right figure). The domes, which are filled with H_2 gas, form between the two uppermost monolayers of the TMDC after proton irradiation. At each position r away from the dome apex, the dome height as well as the principal components of the strain tensor — along the circumferential (ε_t) and radial (ε_r) in-plane directions and the perpendicular out-of-plane direction (ε_z) — are extracted. (b) The normalized micro-photoluminescence (PL) spectra across one dome, where the differently colored lines correspond to the different measurement positions, with the color-code as in (a). At the apex (purple), where strain is isotropic and large, an indirect band gap transition (I) is assigned, while at the edge of the dome (red) the direct transition (A) is assigned. (c) Energy dependence of the direct (blue dots) and indirect (red dots) transitions on the in-plane strain tensor, $\varepsilon_p = \varepsilon_t + \varepsilon_r$, as extracted from (b). The solid blue/red lines are linear fits to the data points according to $E_{\mathrm{A,I}}(\varepsilon_p) = E_{\mathrm{A,I}}(0) - \Delta_{\mathrm{A,I}}\varepsilon_p$, allowing to extract the zero strain transition energies $E_{\mathrm{A,I}}(0)$ and their shift rates $\Delta_{\mathrm{A,I}}$, taking into account the funnel effect (exciton drift towards regions of lower energy before recombination). The blue/red dashed lines display the actual (free from funneling) strain dependent exciton transition energies (shaded areas are due to fitting uncertainties). The upper right inset in (c) shows the evolution of the transition energies across the dome. Figures are from Ref. [354].

Gating and external pressure can be also used to even tune the proximity-induced phenomena. However, what often remains undiscussed in experimental and especially theoretical studies, is the fact that strain also plays an important role. For example, as demonstrated experimentally, straining the crystal can be used as an efficient knob to fully reversibly tune the optical transitions of TMDCs by hundreds of meV within accessible strain limits of a few percent [355–364]. In graphene, by combining doping with biaxial strain[1], one can significantly enhance the electron-phonon coupling [366], eventually leading to superconductivity. In the case of the 2D magnetic transition-metal trihalides (TMTHs), straining can be used to tune the magnetic anisotropy [367] and induce a ferromagnet-to-antiferromagnet phase transition.

Here, we focus on the biaxial strain engineering of monolayer TMDCs, which can be employed experimentally not only to spatially localize, but also spectrally tune the optical emission of those 2D materials [368–371]. In theoretical approaches, where we calculate the band structure of vdW heterostructures from DFT, strain plays an important role. Because one needs to fulfill the periodic boundary conditions, we need to rely on commensurate lattices and therefore typically strain the involved materials. In the previous chapters, we have seen that the material of interest was usually left unstrained (if possible) because we were mainly interested in proximity and not in strain effects. With biaxial strain, the electronic structure of the TMDC will be modified and a systematic analysis of its behavior might provide valuable insights and further understanding of experiments [354]. The main experimental results of Ref. [354] are summarized in Fig. 9.1, demonstrating the role of strain for the tunability of the optically active band gap transition from the direct to the indirect regime in monolayer TMDCs.

In this chapter, we first introduce the TMDC related basics such as their lattice structure, orbital resolved dispersion, and low energy Hamiltonian. Then, we proceed to study the effect of biaxial strain on the orbital, spin-orbit, and optical properties of pristine monolayer TMDCs. We find that by tuning the lattice constant, the orbital band gap, and the spin splittings of the valence band (VB) and conduction band (CB) drastically change. Specifically, the orbital gap can be tuned by about 100 meV/% with the applied biaxial strain. Also the VB and CB spin splittings are affected by strain in a nonlinear fashion. The observed behavior is universal for all studied TMDCs (MoS_2, $MoSe_2$, WS_2, WSe_2). Finally, we address the transition from the direct to the indirect band gap regime due to strain, as demonstrated in recent experiments of, for example, WS_2 nanobubbles [354], as shown in Fig. 9.1.

9.2 Geometry, band structure, and model Hamiltonian

In the following, we deal with TMDC monolayers that are biaxially strained and/or in proximity to magnetic substrates. Therefore, we need a Hamiltonian that describes the low energy bands of bare TMDCs around the K and K′ valleys, including spin-valley locking as well as proximity exchange effects. In Fig. 9.2(c), we show the orbital decomposed band structure of MoS_2, calculated from DFT and without inclusion of SOC, as a representative example of a TMDC, in general termed MX_2 (M for the transition-metal atom, X for the chalcogen atom). As expected, we find that there is a direct band gap at the K point. The VB and CB are formed by a combination of d_{z^2}, $d_{x^2-y^2}$, and d_{xy} orbitals of Mo, with an additional small contribution from S p orbitals.

---

[1] The graphene lattice can be strained up to 25% without breaking, making it the strongest material ever measured [365].

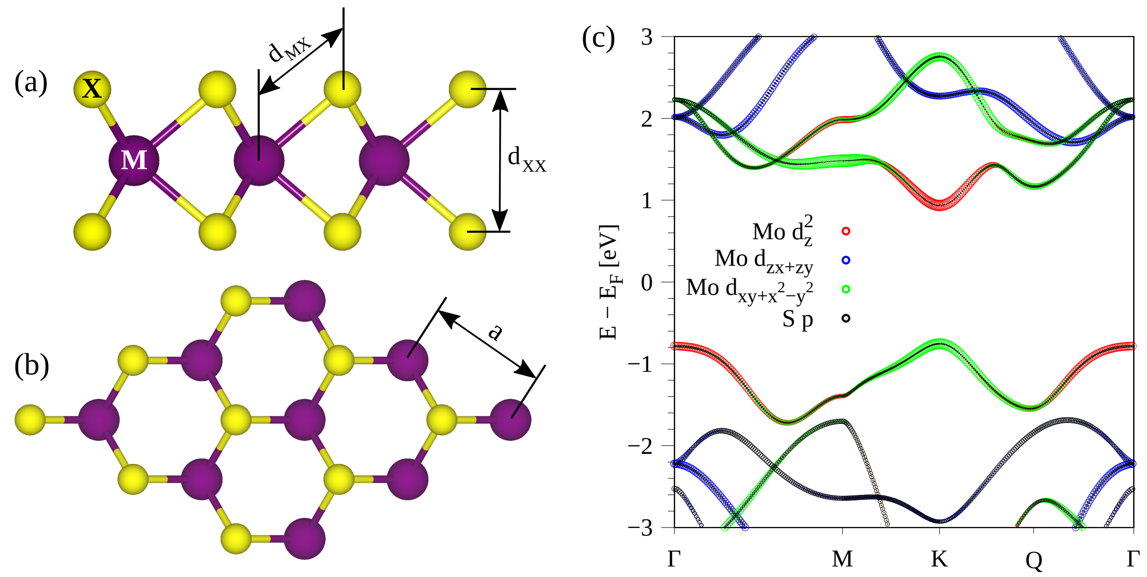

Figure 9.2: (a,b) Geometry of a TMDC monolayer with general structure MX_2, where M is the transition metal (Mo, W) and X is the chalcogen atom (S, Se). (a) Side and (b) top view of the geometry with labels for the lattice constant a, distance d_{MX} (between the transition metal and the chalcogen atom), and d_{XX} (between the two chalcogen atoms). (c) Calculated orbital decomposed band structure of MoS_2 as a representative example of a TMDC. Here, spin-orbit coupling (SOC) is not included and the different colors correspond to projections onto different atomic orbitals as indicated.

Since we are interested in the electronic, spin, and optical properties in the vicinity of the band edges (K and K′ points) and the chalcogen contribution is negligible compared to the transition-metal one, we use $|\Psi_{\mathrm{CB}}\rangle = |d_{z^2}\rangle$ and $|\Psi^{\tau}_{\mathrm{VB}}\rangle = \frac{1}{\sqrt{2}}(|d_{x^2-y^2}\rangle + \mathrm{i}\tau|d_{xy}\rangle)$ as the orbital basis for the Hamiltonian. These states correspond to the CB and VB at the K and K′ valleys, see Fig. 9.2(c), in agreement with literature [289]. The final basis set, including spin, is then $|\Psi_{\mathrm{CB}},\uparrow\rangle$, $|\Psi^{\tau}_{\mathrm{VB}},\uparrow\rangle$, $|\Psi_{\mathrm{CB}},\downarrow\rangle$, and $|\Psi^{\tau}_{\mathrm{VB}},\downarrow\rangle$. The model Hamiltonian to describe the low energy band structure — including SOC and proximity exchange — of the TMDC close to K ($\tau = 1$) and K′ ($\tau = -1$) is [335, 353, 372]

$$\mathcal{H}_{\mathrm{TMDC}} = \mathcal{H}_0 + \mathcal{H}_\Delta + \mathcal{H}_{\mathrm{soc}} + \mathcal{H}_{\mathrm{ex}} + \mathcal{H}_{\mathrm{R}}, \tag{9.1}$$

$$\mathcal{H}_0 = \hbar v_{\mathrm{F}} s_0 \otimes (\tau\sigma_x k_x + \sigma_y k_y), \tag{9.2}$$

$$\mathcal{H}_\Delta = \frac{\Delta}{2} s_0 \otimes \sigma_z, \tag{9.3}$$

$$\mathcal{H}_{\mathrm{soc}} = \tau s_z \otimes (\lambda_{\mathrm{c}}\sigma_+ + \lambda_{\mathrm{v}}\sigma_-), \tag{9.4}$$

$$\mathcal{H}_{\mathrm{ex}} = -s_z \otimes (B_{\mathrm{c}}\sigma_+ + B_{\mathrm{v}}\sigma_-), \tag{9.5}$$

$$\mathcal{H}_{\mathrm{R}} = \lambda_{\mathrm{R}}(\tau s_y \otimes \sigma_x - s_x \otimes \sigma_y), \tag{9.6}$$

which is reminiscent of the graphene Dirac Hamiltonian, introduced in Sec. 3.2. Similarly, v_{F} is the Fermi velocity, representing the effective mass of the bands, and can be seen as the effective hopping amplitude between d_{z^2} and $d_{xy+x^2-y^2}$ orbitals. The Cartesian components k_x and k_y of the electron wave vector are measured from K (K′). The pseudospin Pauli matrices are σ_{i}, acting on the (CB,VB) subspace and spin Pauli matrices are s_{i}, acting on the $(\uparrow, \downarrow)$ subspace, with $\mathrm{i} = \{0, x, y, z\}$. For shorter notation, we introduce $\sigma_{\pm} = \frac{1}{2}(\sigma_0 \pm \sigma_z)$. As already mentioned, TMDCs are semiconductors and the term $\mathcal{H}_{\Delta}$ introduces a gap in the band structure. In contrast to the graphene cases, the corresponding parameter Δ will be much larger here. The two terms $\mathcal{H}_0 + \mathcal{H}_{\Delta}$ describe a gapped spectrum with spin-degenerate parabolic CB and VB. In addition, the bands are spin-split due to SOC, which is captured by the term $\mathcal{H}_{\mathrm{soc}}$ with the parameters λ_{c} and λ_{v}, describing the spin splitting of the CB and VB, respectively. The Hamiltonian $\mathcal{H}_0 + \mathcal{H}_{\Delta} + \mathcal{H}_{\mathrm{soc}}$ is already suitable to describe the spectrum of bare monolayer TMDCs around the band edges at K and K′.

In the case when we have a magnetic substrate, such as mono- and few-layer $\mathrm{CrI_3}$ or a ferromagnet/hexagonal boron nitride (hBN) junction adjacent to the TMDC, proximity exchange effects will be present [373, 374]. The two parameters B_{c} and B_{v} describe the proximity-induced exchange splittings of the CB and VB, similarly to the sublattice resolved exchange parameters (λ_{ex}) in graphene. The Rashba SOC parameter (λ_{R}) is due to a z-mirror asymmetry when the TMDC forms a heterostructure with other 2D materials. Especially the term $\mathcal{H}_{\mathrm{ex}}$ will be important for the next chapter. In the following sections, we neglect the proximity exchange and the Rashba term since only biaxial strain effects in freestanding monolayer TMDCs are considered.

The electronic structure calculations and structural relaxation of our geometries were performed with DFT [204] employing the QUANTUM ESPRESSO [267] code. Self-consistent calculations were performed with the k-point sampling of $30 \times 30 \times 1$ for bare TMDC monolayers. We used an energy cutoff for charge density of 560 Ry and the kinetic energy cutoff for wavefunctions was 70 Ry for the scalar relativistic pseudopotential within the projector augmented wave (PAW) method [268] with the Perdew-Burke-Ernzerhof (PBE) exchange correlation functional [206]. When SOC was included, the fully relativistic versions of the pseudopotentials were used. In order to simulate quasi-2D systems, a vacuum of at least 16 Å was used to avoid interactions between periodic images in our slab geometries. Structural relaxations of the monolayers were performed with quasi-Newton algorithm based on trust radius procedure until all components of all forces were reduced below 10^{-4} $[\mathrm{Ry}/a_0]$, where a_0 is the Bohr radius.

Before we address the strain effects, we also introduce the exact geometry and discuss more aspects of the electronic structure of TMDCs. In Figs. 9.2(a,b), we show the lattice structure of a TMDC monolayer with general formula $\mathrm{MX_2}$, where M is the transition metal (Mo, W) and X is the chalcogen atom (S, Se). The distance between two chalcogen atoms is d_{XX}, the distance between the transition metal and the chalcogen atom is d_{MX}, and the distance between two transition metal atoms is the lattice constant a.

The calculated band structure of $\mathrm{MoS_2}$, including SOC, is shown in Fig. 9.3 as a representative example for all considered TMDCs. Compared to the situation without SOC, see Fig. 9.2(c), the band edges at the K point are now spin split. The VB edge is strongly split, by more than 100 meV, while the CB is split much less, by only a few meV, see Figs. 9.3(b,c). Due to time-reversal symmetry, the bands at the K and K′ points are energetically degenerate, but opposite in spin. In agreement with previous calculations [289, 290, 377, 378], we observe the spin-valley coupling at the K and K′ points, which arises due to the combination of strong

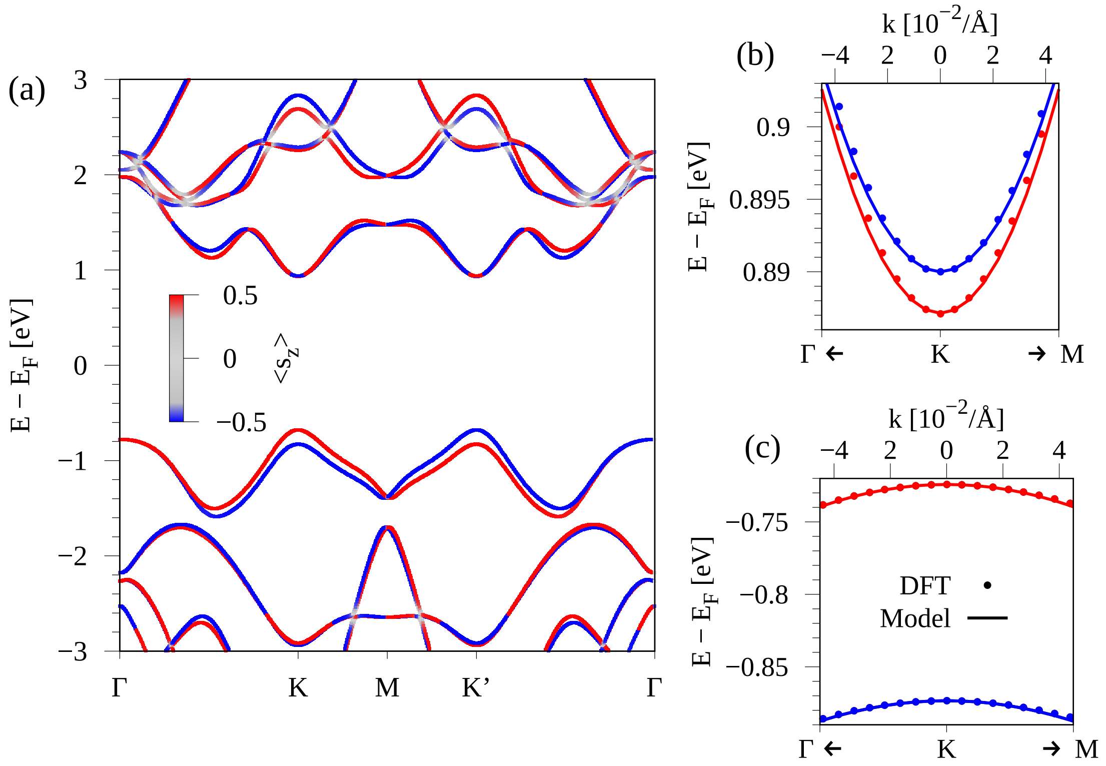

Figure 9.3: (a) Calculated band structure of MoS_2 including SOC. The color corresponds to the s_z spin expectation value. (b,c) Calculated low energy CB and VB around the K point (symbols) with a fit to the model Hamiltonian, Eq. (9.1) (solid line).

Table 9.1: Overview of the lattice parameters for all TMDCs, as well as the fit parameters of the Hamiltonian $\mathcal{H}_{\text{TMDC}}$, Eq. (9.1). The first-principles relaxed monolayer TMDC lattice constant a (calc.), distances d_{XX} and d_{MX}, as defined in Fig. 9.2. The orbital gap parameter Δ, the Fermi velocity v_{F}, and the SOC parameters λ_{c} and λ_{v}. The experimental lattice constants a (exp.) [346, 375, 376] of the bulk systems are given for comparison.

	MoS_2	WS_2	$MoSe_2$	WSe_2
a (exp.) [Å]	3.15	3.153	3.288	3.282
a (calc.) [Å]	3.185	3.18	3.319	3.319
d_{MX} (calc.) [Å]	2.417	2.417	2.547	2.550
d_{XX} (calc.) [Å]	3.138	3.145	3.357	3.364
Δ [eV]	1.687	1.812	1.461	1.525
v_{F} [$10^5 \frac{\text{m}}{\text{s}}$]	5.338	6.735	4.597	5.948
λ_{c} [meV]	−1.41	15.72	−10.45	19.86
λ_{v} [meV]	74.6	213.46	93.25	233.07

SOC and the lack of inversion symmetry in monolayer TMDCs. As a consequence, one can optically excite electrons with a certain spin in one valley using circularly polarized light of one helicity only. The other valley can be addressed by the other light helicity, exciting electrons with opposite spin at the same excitation energy. This can be attibuted to the optical selection rules in monolayer TMDCs in combination with the spin-valley coupling [33].

We are able to fit the Hamiltonian $\mathcal{H}_{\mathrm{TMDC}}$, Eq. (9.1), to the low energy band edges of the TMDC at the K and K′ valleys and obtain a very good agreement with the calculated band structure, as can be seen in Figs. 9.3(b,c). The fit parameters for the different TMDCs are summarized in Tab. 9.1, considering the equilibrium lattice constants obtained from first-principles lattice relaxation.

9.3 Strain effects on orbital and spin-orbit properties

The typical approach to consider vdW heterostructures from DFT, is to find a common unit cell for the individual materials because of lattice mismatch. For example, in the previously discussed case of graphene on hBN, we mentioned that the lattice constants differ by less than 2%. This small lattice mismatch leads to the formation of a moiré-pattern. Without straining the lattices, one would have to consider a 56×56 graphene supercell on a 55×55 hBN supercell, fulfilling the condition (ratio of lattice constants) $2.46/2.504 \approx 0.982 \approx 55/56$. Hence, one would have to deal with more than 10.000 atoms in the unit cell, which is an unpractical approach. Thus, it is better to use the lattice constant of pristine graphene, being the material of interest, and adapt the hBN lattice by about 1.8%. We end up with a heterostructure containing 4 atoms in the unit cell, which will significantly reduce the computational cost without altering the qualitative results[2] too much. In the case of proximity effects, where multiple 2D materials are interfaced, lattice mismatch can be even larger. It is sometimes unavoidable that all individual layers must be slightly strained to get a compromise between strain minimization, reduction of computational cost, and leaving the intrinsic electronic properties of the materials unchanged.

When we consider TMDC-based heterostructures and strain has to be applied (up to a reasonable limit), what are the physical consequences for the TMDC? In other words, will the biaxial strain influence the *intrinsic* properties such as orbital gap and spin-orbit splittings? In order to answer this, we consider the four monolayer TMDCs $\mathrm{MoS_2}$, $\mathrm{MoSe_2}$, $\mathrm{WS_2}$, and $\mathrm{WSe_2}$ in a 1×1 unit cell, and calculate their band structures for different lattice constants. The amount of strain we consider is about ±3% with respect to the theoretically predicted lattice constants, as listed in Tab. 9.1. Consequently, also the experimental lattice constants are covered within the considered strain limits.

For every lattice constant, we first perform a relaxation of the internal positions of the metal and chalcogen atoms within the unit cell. In our case, it is enough to relax the z positions of the chalcogen atoms since biaxial strain does not change the symmetry, but only the inter-atomic distances. Also in reality, when biaxial strain is applied to the monolayer TMDCs, the distances d_{XX} and d_{MX} will be affected. For the analysis of strain effects, we then calculate the low energy band structure near the K and K′ valleys for several lattice constants within our strain limits. In each case, we fit the model Hamiltonian $\mathcal{H}_{\mathrm{TMDC}}$, Eq. (9.1), to

---

[2] Of course, moiré-pattern effects are not captured, but proximity-induced SOC ones are.

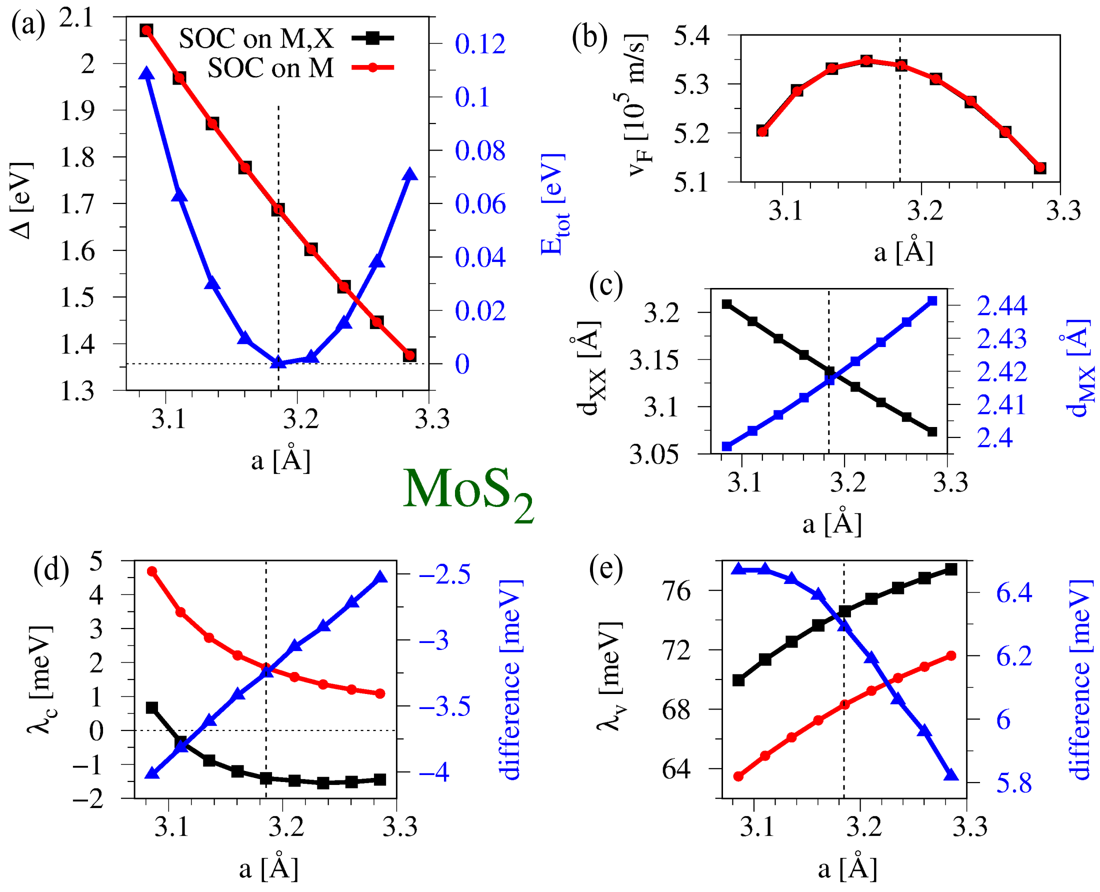

Figure 9.4: Summary of the fit parameters for MoS$_2$ as functions of the lattice constant. (a) The gap parameter Δ and the total energy E_{tot}. The black data (SOC on M,X) correspond to calculations where SOC is included for both atoms M and X, while for the red data (SOC on M), we turned off SOC on the X atoms, respectively. Dashed vertical lines indicate the equilibrium lattice constant. (b) The Fermi velocity v_F. (c) The distances d_{XX} and d_{MX}. (d,e) The SOC parameters λ_c and λ_v. The difference (blue curve) is between the black and the red cures.

the DFT-calculated bands and obtain the relevant orbital and SOC parameters that describe the band edges around the K and K′ points. By taking the spin expectation values of the bands and the fact that time-reversal symmetry is present into account, it is enough to fit the Hamiltonian only in one valley to determine the correct signs of the parameters λ_c and λ_v. In the following, we explicitly discuss the results for MoS$_2$ as the representative case.

In Fig. 9.4, we show the evolution of the inter-atomic distances, the total energy, and the fitted parameters as functions of the lattice constant, i. e., biaxial strain. Since we employ the PBE functional in the DFT calculations, the total energy E_{tot} is minimized for the theoretically predicted lattice constant [289] $a = 3.185$ Å, see Fig. 9.4(a). However, the total energy for the experimental lattice constant ($a = 3.15$ Å) is only about 20 meV higher in energy. In Fig. 9.4(c), we show the evolution of the distances d_{XX} and d_{MX} with respect to the lattice constant. By applying tensile strain, i. e., tuning from smaller to larger lattice constants, the distance between the two chalcogen atoms d_{XX} is getting smaller, while the distance between the transition-metal atom and the chalcogen atom d_{MX} is getting larger. If we remind ourselves about the orbital decomposed band structure in Fig. 9.2(c), combined with the fact that inter-atomic distances can be tuned with strain, one can easily understand that the whole band structure will be affected. The distances determine the overlap between the orbitals, and consequently the matrix elements in a tight-binding model perspective [379, 380]. As a result, the band energies at a given k point will be strongly strain dependent. We will see later in more detail that this will have significant consequences for the active optical transitions.

The orbital gap at the K point, represented by the parameter Δ, decreases linearly with increasing lattice constant, being consistent with literature [363, 381–385]. Remarkably, in between our considered range of lattice constants, the gap can be drastically tuned by about 0.7 eV with a maximal strain of only ±3%. As already mentioned, the overall band structure gets modified with strain. In the case of $\mathrm{MoS_2}$ and strains beyond ±1%, the band gap becomes indirect, in agreement with literature [382–384]. For the other TMDCs, different strain amplitudes are necessary to achieve this, as we will see. The Fermi velocity v_{F}, shown in Fig. 9.4(b), exhibits a maximum at around 3.16 Å and decreases for smaller or larger lattice constants. Remember that $v_{\mathrm{F}} \propto at$ [353], the product of the effective hopping amplitude t, between d_{z^2} and $d_{xy+x^2-y^2}$ orbitals, and the lattice constant a. It is therefore not surprising that v_{F} changes by tuning atomic distances.

The strain tunability of the SOC parameters λ_{c} and λ_{v} is shown in Figs. 9.4(d,e). We find that the CB spin splitting, represented by the SOC parameter λ_{c}, is on the order of a few meV. For the case of our smallest lattice constant, i. e., -3% of strain, λ_{c} is positive. With increasing lattice constant, the parameter first reduces in magnitude, then switches sign, and finally increases again and reaches about -1.5 meV in the equilibrium case. The transition from a positive to a negative value reflects a change in the ordering of the corresponding spin-split bands. For the VB splitting, the responsible SOC parameter is λ_{v}, which increases in a nonlinear fashion with increasing lattice constant.

For monolayer TMDCs, in general denoted as $\mathrm{MX_2}$, the unit cell consists of two different atoms, one metal atom M and two chalcogen atoms X. The two SOC parameters λ_{c} and λ_{v} represent the spin splitting of the CB and VB. How do the fit parameters depend on the SOC from the two different atomic species M and X? In order to answer this, we artificially turned off the SOC of the chalcogen atoms by using a scalar-relativistic pseudopotential. In this case, the only contribution to the spin splittings is given by the metal atom. Similarly to before, we extract the fit parameters from the low energy band structure for every lattice constant. The results are also summarized in Fig. 9.4, where the red data points represent the case with SOC on the metal atom M only.

Since v_{F} and Δ are orbital parameters, they are not affected by turning off SOC on the chalcogen atoms. In contrast, the spin splittings are strongly affected. Note that the blue curve (difference between black and red data points) in Figs. 9.4(d,e) represents the contribution from the chalcogen atoms to the SOC parameters. The qualitative behavior of λ_{c} and λ_{v} with respect to the lattice constant is unchanged. However, their values are different, which can be easily understood from the fact that spin splittings result from an interplay of the atomic SOCs [378]. By turning off the spin-orbit contribution from one atom (in our case from the two chalcogen atoms), the spin splittings and the corresponding parameters will be affected. In Fig. 9.4, we explicitly show how both atomic species contribute in the case of MoS_2. In agreement with perturbation theory [378], we can confirm that the chalcogen atoms give a negative (positive) contribution to the CB (VB) splitting [the blue curves in Figs. 9.4(d,e)], while the metal atom contributes to both splittings in a positive way [the red curves in Figs. 9.4(d,e)]. To gain an even better understanding, one would need to consider a microscopic orbital-based description and determine how the splittings depend on overlap matrix elements, which themselves depend on inter-atomic distances.

The fit parameters as functions of the lattice constant are summarized in Tab. A.4 for all TMDCs. In general, we notice that the SOC parameter λ_c for Mo-based systems is negative, while the one of W-based materials is positive, as already pointed out in the literature [289, 377, 378]. Consequently, the spin ordering in the CB is opposite. In addition, heavier elements (W, Se) result in larger spin splittings than lighter ones (Mo, S), which is reflected in the larger values of the SOC parameters λ_c and λ_v. Overall, the strain dependence of the fitted parameters and distances is similar for all TMDCs, as excplicitly shown in Ref. [386].

As stated in the beginning, we consider strain of $\pm 3\%$ with respect to the theoretically predicted lattice constants, which slightly deviates from the experimental values, see Tab. 9.1. In general, the employed PBE exchange correlation functional [206] is not the best to describe equilibrium crystal properties. For this purpose, we additionally employed the PBEsol functional [387] which is an improved version of the PBE one to properly describe crystallographic ground state properties. In Fig. A.4, we compare the two exchange correlation functionals for the case of MoS_2. From the total energy minimization, we find an equilibrium lattice constant of $a = 3.15$ Å for PBEsol, in agreement with the experimental value, while PBE overestimates the lattice constant by about 1%. Nevertheless, we find that both functionals predict a similar dependence of the fitted parameters and atomic distances on strain. Consequently, PBE and PBEsol are equally valid in terms of electronic structure, even though equilibrium lattice geometries differ a bit.

9.4 Strain tunable optical transitions

What are the consequences of straining the monolayer TMDC crystals, in terms of their optical properties? Recent experiments demonstrated, that strain not only tunes the band gap, as we have shown, but also influences the PL spectrum, exciton-phonon coupling, or circular dichroism [361, 388–390]. In addition, and technologically important, strain can be used to control the response time in MoS_2-based photodetectors [364]. Moreover, basic strain research is vital in the design of novel wearable electronic and optoelectronic devices [391], as 2D materials can withstand significantly more strain than conventional bulk semiconductors [391, 392]. As already mentioned, biaxial strain induces a direct to indirect band gap transition. Now, we want to explicitly discuss the strain dependence of the optical transitions for all TMDCs on the level of the single-particle DFT spectra. Excitonic[3] features and their strain tunabilities are discussed in more detail in Ref. [386], where also results from theory and experiments are compared. The following single-particle perspective is enough for a qualitative description of the main results. *The presented results in this section were obtained with the help of Paulo E. Faria Junior.*

---

[3] Excitons are strongly bound quasi-particles created due to the Coulomb interaction between electrons and holes [393, 394]. In 2D materials, excitons have large binding energies due to the weak screening and dominate the optical spectra [44, 347, 395, 396].

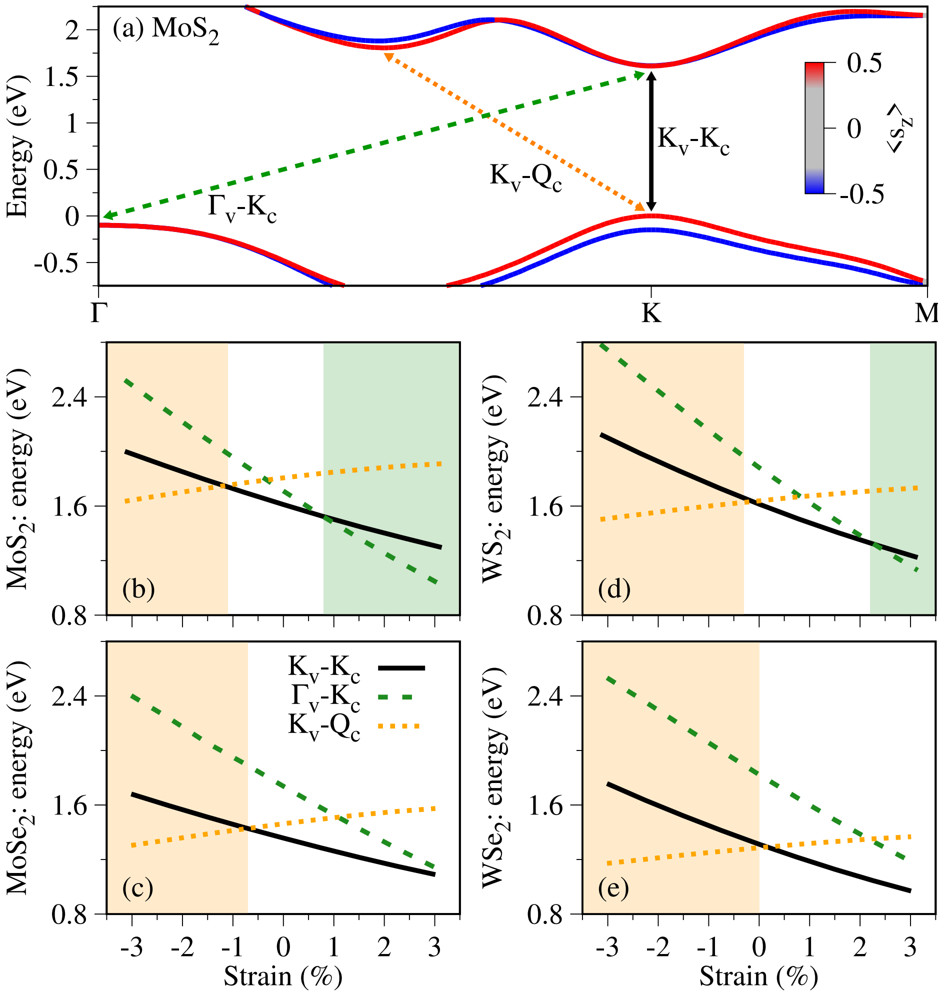

Figure 9.5: (a) Band structure of MoS$_2$ at zero strain, highlighting the important optical transitions mostly affected by strain. The transitions are identified by the reciprocal space point (K, Q, Γ) and by the energy band (subindices v and c for VB and CB). Evolution of the transition energies depicted in subfigure (a) as function of strain for (b) MoS$_2$, (c) MoSe$_2$, (d) WS$_2$, and (e) WSe$_2$. The shaded regions indicate indirect band gap regimes (K-Q for negative strain and Γ-K for positive strain).

In the previous section, we have demonstrated that strain can tune the direct band gap parameter Δ which is valid for the optical transition at the K point. However, the overall band structure modifications due to strain are more complicated. For example, in the case of MoS$_2$, we observe that the VB edge at the Γ point shifts up in energy by applying tensile strain. The VB edge at the Γ point lies higher in energy than the one at the K point for about 1% of tensile strain. Similarly, for about 1% compressive strain, the CB edge at the Q point is lower in energy than the one at the K point. In Fig. 9.5(a), we again show the band structure of monolayer MoS$_2$, indicating all relevant optical transitions. The strain evolution of the

Table 9.2: Gauge factors (in meV/%) for the single-particle transitions presented in Fig. 9.5, extracted by linear extrapolation within the whole considered strain region.

	MoS_2	$MoSe_2$	WS_2	WSe_2
K_v-K_c	-112.3	-98.2	-133.5	-118.8
Γ_v-K_c	-239.9	-210.2	-254.0	-213.4
K_v-Q_c	44.3	45.7	37.0	32.8

transitions is summarized in Figs. 9.5(b-e) for MoS_2, $MoSe_2$, WS_2, and WSe_2, respectively. For all TMDCs, compressive strain activates the K_v-Q_c transition, while tensile strain leads to the Γ_v-K_c transition. Without any strain, the K_v-K_c direct band gap optical transition has the lowest energy. For Se-based TMDCs, the amount of tensile strain that we considered is not large enough to activate the indirect transition. In addition, we notice that for all TMDCs, the K_v-Q_c transition energy increases, while the K_v-K_c and Γ_v-K_c transition energies decrease with strain.

For a more qualitative comparison, we extracted the rates at which strain changes the transition energies. Such a rate is commonly termed *gauge factor* and given in meV/%. In Tab. 9.2, we summarize the gauge factors for all TMDCs, assuming, for simplicity, a linear behavior of the transition energies with respect to strain. We find that the indirect Γ_v-K_c transition shows the largest gauge factors (between -200 to -250 meV/%), about twice as large as the direct K_v-K_c transition. The indirect K_v-Q_c transition has the smallest gauge factors, which are additionally opposite in sign compared to the other ones. In summary, the extracted gauge factors are important to identify and track the optically active transitions in TMDCs under the influence of strain.

How do our results compare with experimental data? Unfortunately, the amount of experimental results of biaxially strained TMDCs is very limited. Still, the available experimental gauge factors for MoS_2 range within -94 to -105 meV/% [357, 360, 363, 364], as determined from the A exciton peak in PL measurements. Experimentally, the gauge factors of the A exciton (the first allowed optical transition between the VB and CB) correspond to the ones of the direct K_v-K_c transition in our single particle picture. Note that our simple DFT approach does neither take into account a dielectric environment nor the Coulomb correlation between electrons and holes, which is important for excitons [44, 347, 395–397]. With that in mind, our extracted K_v-K_c gauge factor for MoS_2 of about -112 meV/% is in fairly good agreement.

9.5 Summary and conclusion

In this chapter, we have first introduced the basics of monolayer TMDCs such as lattice structure, dispersion, and effective low energy Hamiltonian. The Hamiltonian, comprising orbital and SOC parameters, can reasonably well describe the relevant band edges near the K and K′ valleys of unstrained and biaxially strained TMDCs. From the evolution of the fit parameters with respect to the lattice constant, we have found that the orbital band gap at the K point is strongly tunable by about 100 meV/% of applied strain. In addition, the SOC parameters, representing VB and CB spin splittings, are highly strain tunable in a nonlinear fashion. Both splittings result from an interplay of transition-metal and chalcogen atomic SOCs.

Most important, strain induces a direct to indirect band gap transition for all TMDCs. In the case of an unstrained TMDC, the optically active transition is at the K point, as expected from experiments. For tensile strain, the Γ_v-K_c transition gets active, while for compressive strain the K_v-Q_c transition energy is the lowest. Our results provide valuable insights on how strain modifies the optically active transitions of monolayer TMDCs. The extracted gauge factors are essential for a qualitative and quantitative assessment of strain effects, and should be helpful to interpret experimental PL spectra of strained TMDCs.

CHAPTER 10

Proximity exchange effects in $MoSe_2$ and WSe_2 on CrI_3

This chapter is based on the publication: K. Zollner, P. E. Faria Junior, and J. Fabian, Physical Review B ***100****, 085128 (2019), "Proximity exchange effects in* $MoSe_2$ *and* WSe_2 *on* CrI_3*: Twist angle, layer, and gate dependence".*

10.1 Introduction

The advantage of transition-metal dichalcogenides (TMDCs) is the fact that they are direct band gap semiconductors in the two-dimensional (2D) monolayer limit with their gaps in the visible part of the spectrum [43, 44, 289–293, 386]. Thus, they are well suited for device technologies such as photodetectors, light emitters, and field-effect transistors (FETs) [49, 398]. In addition, monolayer TMDCs have another interesting property, the so called spin-valley locking [353], which stems from spin-orbit coupling (SOC) and the lack of inversion symmetry, making them highly interesting for the field of valleytronics [92, 350–352, 399] that exploits the valley as an additional degree of freedom. With circularly polarized light, say σ_-, one can address charge carriers in the K valley with spin-up, while σ_+ addresses the K$'$ valley and spin-down carriers at the same energy. One major issue for persistent valley polarization is the limited lifetime of (optically created) excitons [400], which can be significantly enhanced by spatially separating the charge carriers. By combining two different monolayer TMDCs in a van der Waals (vdW) heterostructure, a type-II band alignment is formed. Then, e. g., electrons will flow into one layer, while holes reside in the other layer, both assigned to a certain valley and spin. These so-called interlayer excitons have much longer lifetimes [401, 402] compared to intralayer excitons, where electrons and holes reside in the same layer.

An alternative route to gain control over the valley polarization is to break the valley degeneracy in monolayer TMDCs. By breaking the time-reversal symmetry via a magnetic exchange field, the degeneracy of the valleys gets lifted. Initial studies have shown that an external magnetic field perpendicular to the TMDC layer leads to a valley splitting of about 0.1–0.2 meV per Tesla [403–406]. Hence, giant field amplitudes are required to get sizable effects, which seems unpractical for applications. As we have seen in the last chapters, proximity effects, could be highly suitable for this purpose being intrinsically present in vdW heterostructures. Recent experiments and density functional theory (DFT) calculations indeed demonstrated that giant valley splittings can be achieved, when placing the TMDC on a magnetic substrate [335, 352, 399, 407–414]. In the following, we focus on the layered compound CrI_3, which belongs to the family of chromium trihalides CrX_3 (X = Cl, Br, I) and should provide us with the necessary proximity-induced exchange coupling.

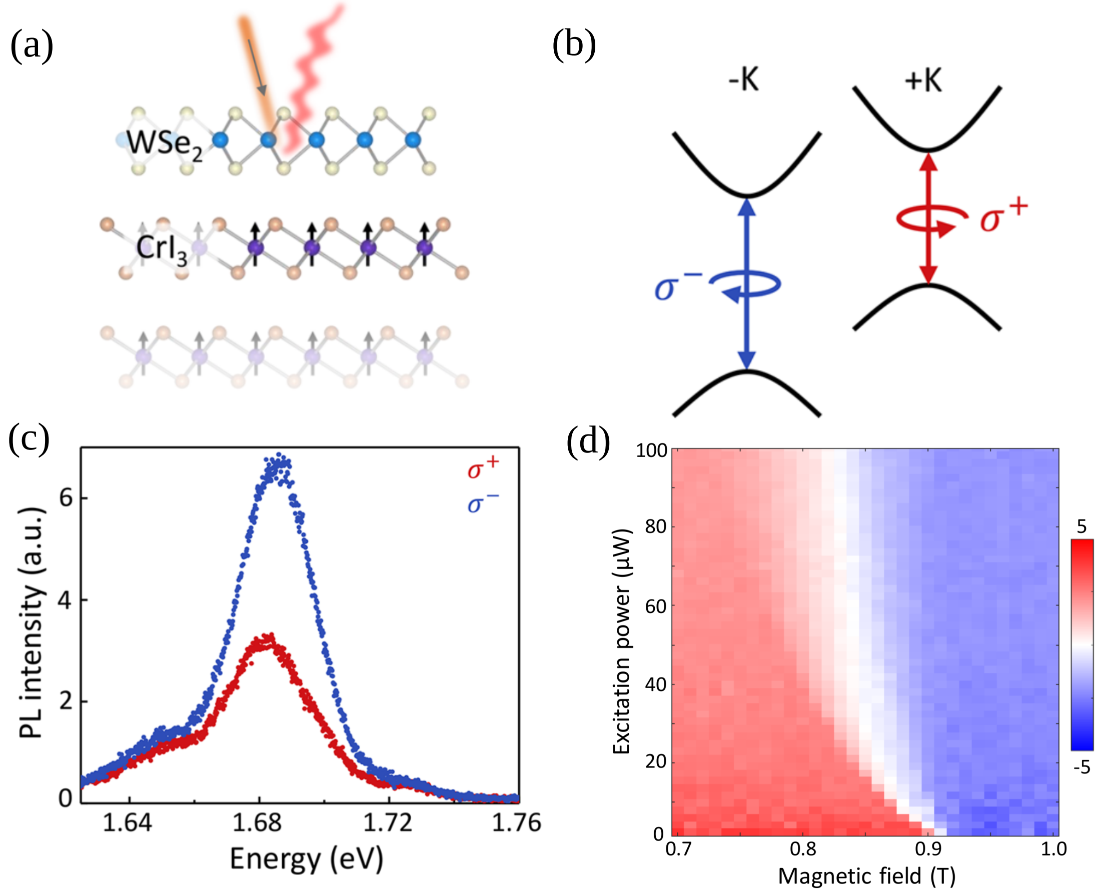

Figure 10.1: Tunable valley splitting in a WSe_2/CrI_3 heterostructure. (a) The geometry of monolayer WSe_2 on a magnetic CrI_3 multilayer sample for the photoluminescence (PL) measurement. (b) Schematic band structure diagram of WSe_2 in the presence of proximity-induced exchange coupling, showing the optical selection rules for the different valleys. (c) The σ_+ (σ_-) PL spectrum under σ_+ (σ_-) excitation at a fixed external magnetic field of 1 T, shown in red (blue). Due to proximity exchange, the peak positions of σ_+ and σ_- are at different energies. The peak intensity of one light helicity is quenched due to an additional nonradiative relaxation channel via spin-polarized CrI_3 in-gap states, see for example Fig. 10.2(c). (d) Colormap of the valley splitting Δ, as function of an external magnetic field and the laser excitation power. The valley splitting Δ is extracted from the energy difference of the $\sigma_\pm$ PL peak positions. Figures are from Ref. [412].

At around 2010, shortly after the advent of 2D materials, the chromium trihalides got rediscovered [415] and DFT calculations confirmed their ferromagnetic order found by early experiments [416–418]. The reexamination of the crystallographic and magnetic properties [55] of CrI_3 has finally given the starting shot for the triumph of 2D magnets. Nowadays, researchers show massive interest in magnetic chromium trihalides due to their easily cleavable and layered vdW structure. In particular, CrI_3 is a ferromagnetic semiconductor with a Curie temperature of $T_C = 68$ K and an optical band gap of about 1.2 eV [418]. A monolayer of CrI_3 maintains its ferromagnetic ground state with perpendicular magnetic anisotropy (PMA) [284, 419]. Comprehensive DFT calculations [420, 421], combined with experiments [55], are the foundation in understanding the electronic and magnetic properties of CrI_3. X-ray diffraction experiments on bulk CrI_3 [55] show that the crystal structure at low temperature is in the rhombohedral $R\bar{3}$ space group with lattice constants $a = 6.867$ Å and $c = 19.807$ Å. At around 220 K, a crystallographic phase transition occurs, transforming the crystal into the monoclinic $C2/m$ space group. Interestingly, bilayer CrI_3 is a layered antiferromagnet, as experiments demonstrated [96, 284, 422]. Apparently, the stacking of the individual monolayers strongly influences the type of interlayer exchange coupling [419, 423, 424], either favoring a ferromagnetic or an antiferromagnetic order in bilayer CrI_3.

Recent measurements [330, 352, 412, 425, 426] have already found a few meV of proximity exchange in TMDC/chromium-trihalide heterostructures, which has attracted also our interest. In particular, in Fig. 10.1 we summarize the main results from Ref. [412], where a monolayer of WSe_2 on multilayer CrI_3 was investigated. Due to proximity exchange, the valley degeneracy of the WSe_2 gets lifted, as schematically shown in Fig. 10.1(b), resulting in different excitation energies at K (σ_+) and $-$K (σ_-). This energy difference, defining the valley splitting, can be seen in the helicity-selective PL spectra, see Fig. 10.1(c), where the PL peak positions for σ_+ and σ_- are at different energies. The proximity-induced valley splitting can be tuned in the range of about ± 5 meV, see Fig. 10.1(d), either optically by varying the laser excitation power or via an external magnetic field. Essentially, the magnetization in the CrI_3 layer adjacent to the TMDC, being responsible for proximity exchange, can be tuned optically or magnetically.

In this chapter, we present results from extensive DFT calculations of TMDC/CrI_3 heterostructures. The TMDCs, $MoSe_2$ and WSe_2, couple weakly to the magnetic CrI_3 monolayer, as the heterostructure dispersions show. In addition, the relevant band edges of the TMDC experience spin splittings due to the combination of intrinsic SOC and proximity-induced exchange interaction, breaking the valley degeneracy. We quantify the proximity effect by a low energy model Hamiltonian for the TMDC, capturing both effects, and find exchange parameters of about 2 meV. Remarkably, twisting the layers changes the sign of the proximity spin splitting in the valence band (VB), leading to an enhanced valley splitting of the first intralayer exciton peak. The short-rangeness of the proximity-induced exchange is explicitly confirmed by investigating $MoSe_2$/bilayer-CrI_3 and $MoSe_2$/hexagonal boron nitride (hBN)/CrI_3 structures. In the former case, proximity exchange in the TMDC is only due to the magnetization of the adjacent CrI_3 layer. In contrast, the hBN buffer layer significantly reduces the induced spin splitting by an order of magnitude. Finally, we look at the gate tunability of proximity exchange by applying a transverse electric field across the TMDC/CrI_3 heterostructures. With experimentally accessible electric fields of a few V/nm, the valley splitting can be tuned by a few meV.

10.2 Geometry and computational details

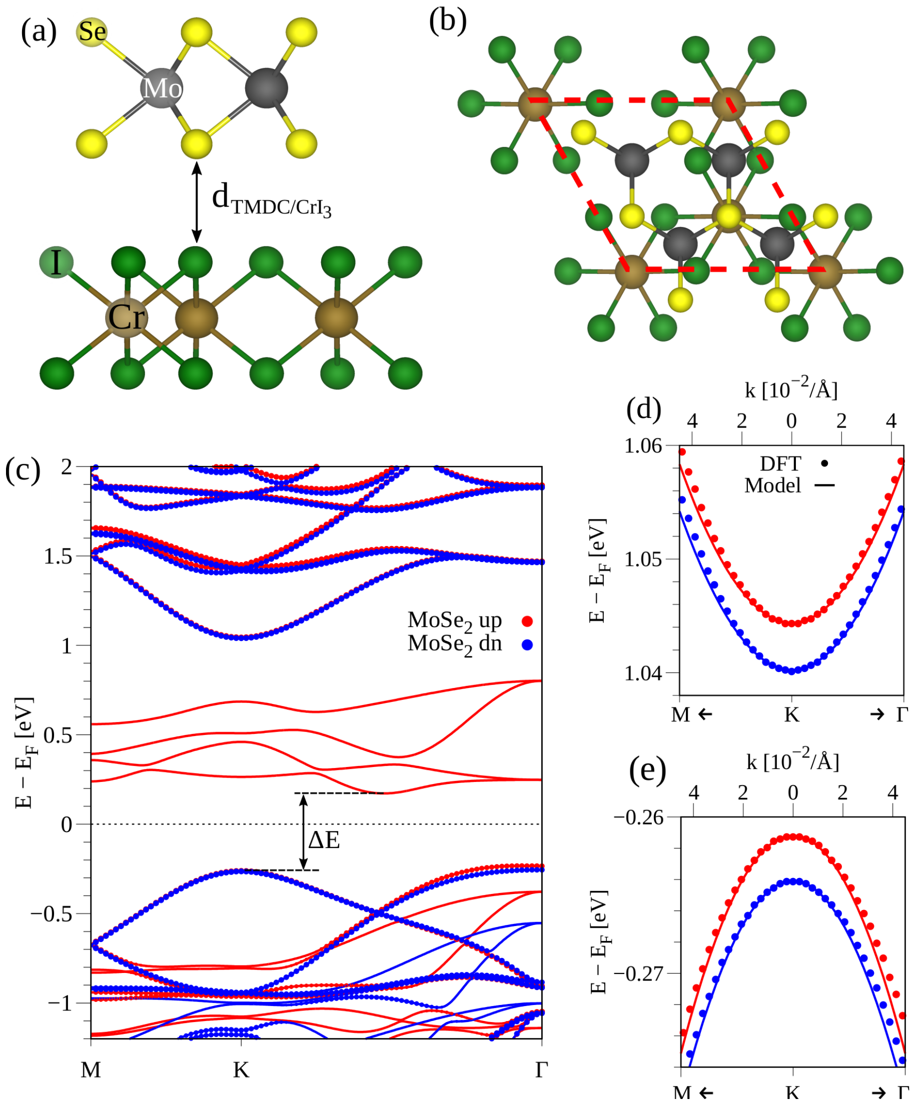

Figure 10.2: Calculated band structure without SOC and geometry of the MoSe$_2$/CrI$_3$ heterostructure. (a,b) Side and top view of the small supercell geometry (0° twist angle) with labels for the different atoms and the definition of the interlayer distance d_{TMDC/CrI_3}. The heterostructure unit cell is emphasized by the red dashed line in the top view. (c) Band structure along high symmetry points. The energy gap of the full heterostructure is ΔE. The bands corresponding to MoSe$_2$ are highlighted by red (spin up) and blue (spin down) filled circles. (d,e) Zoom to the conduction band (CB) and VB edge corresponding to MoSe$_2$. Symbols are DFT data and solid lines refer to the model Hamiltonian fit.

For our study of proximity exchange effects, we have set up TMDC/CrI$_3$ heterostructures with the atomic simulation environment (ASE) [265]. In general, we distinguish two kinds of unit cells with different twist angles. For 0° twist angle between the TMDC and CrI$_3$, we end up with 20 atoms in the heterostructure unit cell because we used a 2×2 supercell of the TMDC (MoSe$_2$ and WSe$_2$) and a 1×1 cell of CrI$_3$. The lattice constants of the individual materials need to be strained to get commensurate layers for periodic DFT calculations. For

CrI_3, we applied about -1.7% of tensile strain and compressed the lattice constant [55] from 6.867 Å to 6.748 Å. For the TMDC $MoSe_2$ (WSe_2), we stretched the lattice constant [346, 376] by around 2.6% (2.8%) from 3.288 Å (3.282 Å) to 3.374 Å. All strain values are still within an acceptable strain limit. However, as discussed in the previous chapter, this will have consequences for the band structures of the individual materials. In the case of the TMDCs, the orbital band gap will be diminished. The 0° twist angle heterostructure is built such that a chalcogen atom of the TMDC is located atop a Cr atom of the CrI_3 layer, see Figs. 10.2(a,b). Other stacking configurations can give slight variations in the band alignment and spin splittings [374, 427], and are not discussed here.

In addition to the 0° case, we consider a larger 7×7 supercell of $MoSe_2$ on top of a $(2\sqrt{3} \times 2\sqrt{3})$R30° supercell of CrI_3. We changed the lattice constant of $MoSe_2$ [376] to $a = 3.358$ Å and the one of CrI_3 [55] to $a = 6.785$ Å, resulting in strains of 2.13% and -1.19%, which is roughly equal to the strains in the 0° case. In a similar way, we considered such a large supercell for WSe_2 on CrI_3. These geometries contain then 243 atoms in the unit cell, where the two monolayers have a relative twist angle of 30° with respect to each other. We considered these two differently twisted geometries, 0° and 30°, because the exact layer alignment is typically hard to control experimentally. Consequently, we can give at least some qualitative insights on how the proximity exchange coupling depends on the twist angle. Here, we want to mention that the twist angle can have significant impact on proximity effects, as demonstrated in the case of proximity-induced SOC for graphene/topological insulator (TI) and graphene/TMDC heterostructures [218, 428].

The electronic band structure calculations and structural relaxation of our heterostructures were performed by DFT [204] with QUANTUM ESPRESSO [267]. Self-consistent calculations were performed with the k-point sampling of $36 \times 36 \times 1$ for the small non-twised TMDC/CrI_3 heterostrucures ($6 \times 6 \times 1$ for the large supercells with 30° twist angle). We performed open shell calculations that provide the spin polarized ground state of CrI_3 with the magnetization of Cr atoms pointing along the z direction. We used an energy cutoff for charge density of 500 Ry and the kinetic energy cutoff for wavefunctions was 60 Ry for the scalar relativistic pseudopotential within the projector augmented wave (PAW) method [268] with the Perdew-Burke-Ernzerhof (PBE) exchange correlation functional [206]. When SOC was included in the calculation the fully relativistic pseudopotentials were used. In addition, we included the Hubbard correction for Cr atoms with $U = 4$ eV [315], if not indicated otherwise. For the relaxation of the heterostructures, we added vdW corrections [269, 270] and used quasi-Newton algorithm based on trust radius procedure. In order to simulate quasi-2D systems, a vacuum of at least 20 Å was used to avoid interactions between periodic images in our slab geometry. Dipole corrections [271] were also included to get correct band offsets and internal electric fields. Structural relaxations were performed until all components of all forces were reduced below 10^{-3} [Ry/a_0], where a_0 is the Bohr radius. In order to gain proper interlayer distances, we allowed the atoms of the TMDC, as well as the Cr atoms of CrI_3, to relax their z positions, while the I atoms were allowed to move in all directions during relaxation since they form a distorted octahedral surrounding around the Cr atoms [429]. The relaxed interlayer distances $d_{\mathrm{TMDC/CrI_3}}$ are summarized in Tab. 10.1. They are about 3.5 Å and of typical size for vdW systems.

Since we will also show and discuss results from absorption spectra calculations of TMDCs being subject to proximity exchange, we provide the most important details in the following. If the reader is interested in more details, we refer him/her to Refs. [373, 374, 386], where the exact formalism is described. For the calculation of the absorption spectra, we employed the effective Bethe-Salpeter equation (BSE) [430–433], with the electron-hole interaction mediated by the Rytova-Keldysh potential [434–437], to gain insights into intralayer excitons and valley splittings. We considered TMDC layers with vacuum on top ($\varepsilon_t = 1$) and with CrI_3 underneath (with the dielectric constant $\varepsilon_b = 1.8$ estimated from experiment [284]). For the screening lengths of $MoSe_2$ and WSe_2, we used $r_0 = 5.1$ nm and $r_0 = 4.5$ nm, respectively, based on the values provided in Ref. [437]. *The BSE absorption spectra calculations were performed and analyzed by Paulo E. Faria Junior.*

10.3 Band structure and twist effects

At first, we focus on the results obtained for the non-twisted geometries. As a reference, we have calculated and fitted the band structure of the bare monolayer TMDCs with the strained lattice constants from the heterostructure. The results are summarized in Tab. 10.1. In Fig. 10.2(c), we show the DFT-calculated band structure of the $MoSe_2/CrI_3$ stack for the 0° twist angle without including SOC. The overall dispersion of the TMDC is preserved and proximity-induced exchange coupling, originating from the magnetic CrI_3 layer, spin splits the bands. Within the band edges of the TMDC, spin-polarized in-gap states are located, which originate solely from the CrI_3 layer. Recent experiments have already demonstrated that the PL spectrum of one light helicity gets quenched due to an additional nonradiative relaxation channel via these in-gap states [330, 352, 412], see Fig. 10.1(c). The band gap of the $MoSe_2$ in the heterostructure is about 1.3 eV, in agreement with the strain tunable band gap results from the previous chapter, see Tab. A.4, and with our reference calculation of the bare $MoSe_2$ monolayer. However, the band gap of the full $MoSe_2/CrI_3$ heterostructure is $\Delta E \approx 400$ meV, as defined in Fig. 10.2(c). The TMDC and CrI_3 form a type-II band alignment, where the CB is formed by the energetically lowest spin-polarized in-gap state from CrI_3 and the VB originates from the TMDC.

We are mainly interested in the proximity exchange coupling that is induced in $MoSe_2$ by CrI_3. The band edges of the TMDC are spin split by about 5 meV due to magnetic exchange, see Figs. 10.2(d,e). Our model Hamiltonian $\mathcal{H}_{\text{TMDC}}$, Eq. (9.1), can be used to fit the spectrum of the TMDC near the K valley. The parameters (without SOC) from Tab. 10.1 provide a reasonable match between DFT and model data, see Figs. 10.2(d,e). Most important here are the exchange parameters, being about 2 meV in magnitude and negative in sign. From the DFT calculation, we also extracted the average atomic magnetic moments and found: Cr ($+3.53\ \mu_B$), I ($-0.19\ \mu_B$), Mo ($-0.0039\ \mu_B$), and Se[1] ($-0.0046\ \mu_B$). This reveals that the proximity-induced magnetization of the TMDC points along the $-z$ direction, i. e., parallel to the I atoms, but opposite to the Cr atoms magnetization. As a consequence, we obtain *negative* proximity exchange parameters for a net CrI_3 magnetization pointing along the z direction.

---

[1] For the average, we considered only the Se atoms in the $MoSe_2$ layer which are closer to the CrI_3 substrate, as they mediate the proximity exchange coupling.

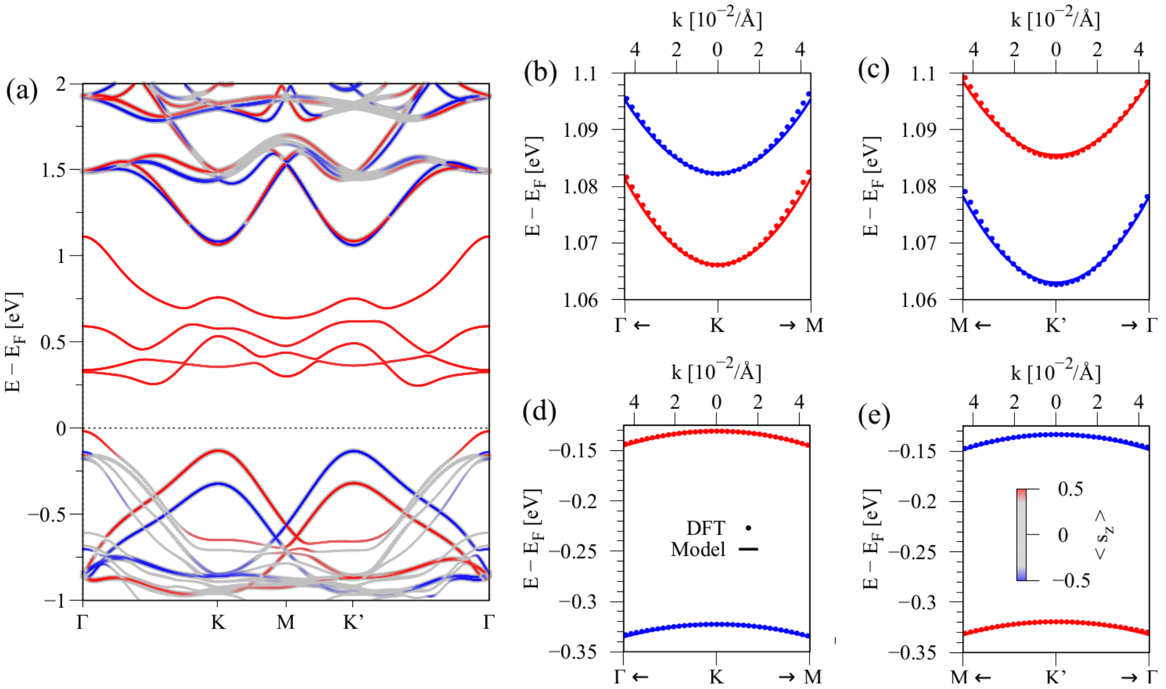

Figure 10.3: Calculated band structure of $MoSe_2/CrI_3$ with SOC for the 0° twist angle structure. (a) Band structure along high symmetry lines. Color corresponds to the s_z spin expectation value. (b,c) Zoom to the CB edge corresponding to $MoSe_2$ at K and K′. Symbols are DFT data and solid lines refer to the model Hamiltonian fit. (d,e) Same as (b,c) but for the VB edge.

Similarly to an external magnetic field, proximity exchange coupling breaks time-reversal symmetry and we must consider the band edges of the TMDC near both valleys, K and K′. As we have previously seen, SOC effects dominate the spin splittings of the TMDC band edges and we cannot neglect it for the calculation of the dispersion. In Fig. 10.3, we show the DFT-calculated band structure of the 0° twist angle $MoSe_2/CrI_3$ stack, now including SOC. Overall, turning on SOC, the dispersion is strongly modified but the TMDC bands are still well recognizable. One should keep in mind, that strain significantly modifies the band gaps of the TMDCs and the presented band alignments might differ from experiments. For example, in Sec. 9.4 we have seen that the direct band gap at the K point is tunable by about -100 meV/% of applied strain. Thus, the CBs of the TMDC are actually located at much higher energies than presented in Fig. 10.3. However, we are interested in proximity exchange effects in the TMDC and we can still extract the relevant band edges, see Figs. 10.3(b-e). The fit parameters (with SOC) from Tab. 10.1 lead to a satisfactory agreement between our model and the DFT data. We also find that the combination of the fit parameters of the bare monolayer and the ones from the heterostructure case without SOC barely differ from the results of the full calculation with SOC; compare the relevant columns in Tab. 10.1. Consequently, SOC is not important here to get realistic proximity exchange parameters and a full description of the relevant bands. We also want to mention that the Rashba parameter is not essential here, as spin expectation values near the band edges are predominantly out-of-plane.

Table 10.1: Summary of fit parameters, calculated dipoles, distances, and valley splittings for the TMDC/CrI_3 systems with different twist angles. The valley splitting extracted from the single-particle picture (s. p.) at K/K′ and from the absorption spectra of the A_{1s} exciton peak (*contribution from Paulo E. Faria Junior*). The orbital gap Δ of the TMDC and the Fermi velocity v_F. The parameters λ_c and λ_v describe the SOC splittings, and B_c and B_v are the proximity exchange parameters for the CB and VB. The built-in electric field of the heterostructure is the dipole. The distance d_{TMDC/CrI_3} is defined in Fig. 10.2(a). The individual columns are for calculations of the bare TMDC (B) with the modified lattice constant from the heterostructure, the heterostructure without SOC (no SOC), and with SOC.

TMDC	$MoSe_2$			WSe_2			$MoSe_2$	WSe_2
dipole [debye]	0.103			0.156			0.172	0.790
distance [Å]	3.506			3.497			3.517	3.529
twist angle [°]	0			0			30	30
s. p. [meV]	1.25			1.61			4.29	7.09
A_{1s} [meV]	1.13			1.43			3.89	6.35
calculation	B	no SOC	SOC	B	no SOC	SOC	no SOC	no SOC
Δ [eV]	1.302	1.305	1.301	1.327	1.358	1.327	1.351	1.417
v_F [10^5m/s]	4.591	4.579	4.591	5.863	5.799	5.845	4.597	5.863
λ_c [meV]	-9.647	-	-9.678	13.90	-	13.81	-	-
λ_v [meV]	94.56	-	94.43	241.79	-	240.99	-	-
B_c [meV]	-	-2.081	-1.592	-	-2.223	-1.783	-1.641	-1.648
B_v [meV]	-	-1.454	-1.426	-	-1.446	-1.583	0.502	1.896

Here is a good point to remind the reader about the spin-valley coupling. In pristine monolayer TMDCs, one can excite electrons at the K valley with a certain light helicity, say σ_-. Electrons at the K′ valley can be excited with σ_+. The excitation energy is the same for both valleys. In our calculated heterostructure dispersion, the valley degeneracy is broken especially when comparing the CB edges at the K and K′ valleys, see Figs. 10.3(b,c). Since the additional exchange field breaks the valley degeneracy of the bands, also the optical excitation energies will be different in different valleys. This energy difference between σ_+ and σ_- polarizations is the *valley splitting*. One can either look at this valley splitting from the single-particle perspective of the DFT-calculated band structure or, more realistically, take into account electron-hole pairs with Coulomb interaction and look at the splitting of the A_{1s} exciton peak[2]. The latter is extracted from the BSE calculated absorption spectra, employing the model Hamiltonian and the fitted parameters from Tab. 10.1.

---

[2] An exciton is a bound electron-hole pair due to their Coulomb interaction. In analogy to the hydrogen atom, the bound state energies are $E_b(n) = -R_x/n^2$ and follow a Rydberg series, where R_x is the exciton binding energy and n is the principal quantum number. The energy of the exciton is then $E(n) = E_g + E_b(n)$, where E_g is the band gap of the material. The A excitons are formed by holes in the first VB and electrons in the first (second) CB in pristine Mo(W)-based TMDCs. The subindex "1s" corresponds to the first s-like exciton state [33, 386].

The single particle spectrum provides a valley splitting of 1.25 meV, in good agreement with the exciton splitting of 1.13 meV. The numbers of the extracted valley splittings are also summarized in Tab. 10.1 for all relevant heterostructures. In contrast to an externally applied magnetic field, the valley splitting is intrinsically present in the heterostructure and due to the magnetic CrI_3 layer. In addition, an external field splits the valleys by only about 0.15 meV/T [403–406] such that large fields are necessary to get sizable effects. Our proximity exchange splitting would correspond to magnetic fields of about 10 T. The presented results are in agreement with recent experiments [330, 352, 412, 425] and other DFT calculations [414, 427, 438]. In Tab. 10.1, we also provide results for the WSe_2/CrI_3 structure with 0° twist angle. In contrast to $MoSe_2$, WSe_2 shows a bit larger exciton peak splitting of 1.43 meV.

Does the twist angle enhance the valley splitting? For our large heterostructure supercells (30°), we calculated the band structure only without SOC to extract the orbital and proximity exchange parameters, see Tab. 10.1. Including SOC is computationally too demanding due to the large number of atoms in the unit cell. Fortunately, based on the knowledge for the 0° twist case, the absorption calculations can be already performed by combining the fit results from the bare monolayers and the ones from the heterostructure without SOC. We find that the overall band structure features of the large supercell are nearly unchanged, see Ref. [374], compared to the small cell. Surprisingly, the VB proximity exchange parameter (B_{v}) has changed its sign, while the CB one (B_{c}) remains nearly unchanged compared to the 0° case, see Tab. 10.1. The averaged magnetic moments for the 30° twist angle case are also nearly unaffected: Cr ($+3.46\ \mu_B$), I ($-0.18\ \mu_B$), Mo ($-0.0029\ \mu_B$), and Se ($-0.0031\ \mu_B$). The origin of the sign change remains unknown and demands further investigations, especially with respect to different values of the twist angle. Nevertheless, this has significant consequences for the optical signatures. In the case of $MoSe_2$ (WSe_2), the twist angle strongly enhances the valley splitting of the first exciton peak by a factor of 3.4 (4.4) to 3.89 (6.35) meV. This would correspond to giant external magnetic fields of at minimum 25 T.

It is also important to analyze the effect of the Hubbard U, which is a tunable parameter in the DFT calculation, on the proximity-induced exchange splittings. Taking into account recent DFT calculations [421, 439–443], reasonable U values for Cr d orbitals of CrI_3 should lie between 1 eV and 4 eV. For several values of U, within these limits, we calculated the band structure of $MoSe_2$ on CrI_3 without SOC for the 0° structure, and fitted our Hamiltonian to extract the model parameters. In Fig. 10.4, we show the fitted parameters, as well as the average magnetic moments of the Cr, I, Mo, and Se atoms, as functions of the Hubbard U. The orbital parameters Δ and v_{F} barely depend on U since they are roughly fixed by the TMDC itself and are nearly independent of proximity effects. In contrast, the proximity exchange parameters B_{c} and B_{v} increase linearly in magnitude with increasing U. More specifically, the CB proximity exchange splitting being roughly $2B_{\mathrm{c}}$ changes from -2 meV to -4 meV within the considered U limits. Similarly, the VB exchange splitting ($\approx 2B_{\mathrm{v}}$) can be tuned from -1 meV to -3 meV. In addition, the band gap of the full heterostructure ΔE is very sensitive and can be tuned from 650 meV to 400 meV, by increasing U from 1 eV to 4 eV. This is not surprising since the Hubbard U affects the location of the Cr d levels in the band structure, i. e., the spin-polarized in-gap states shown in Fig. 10.2(c) are affected. We also show the evolution of the average magnetic moments, see Figs. 10.4(g,h), as functions of

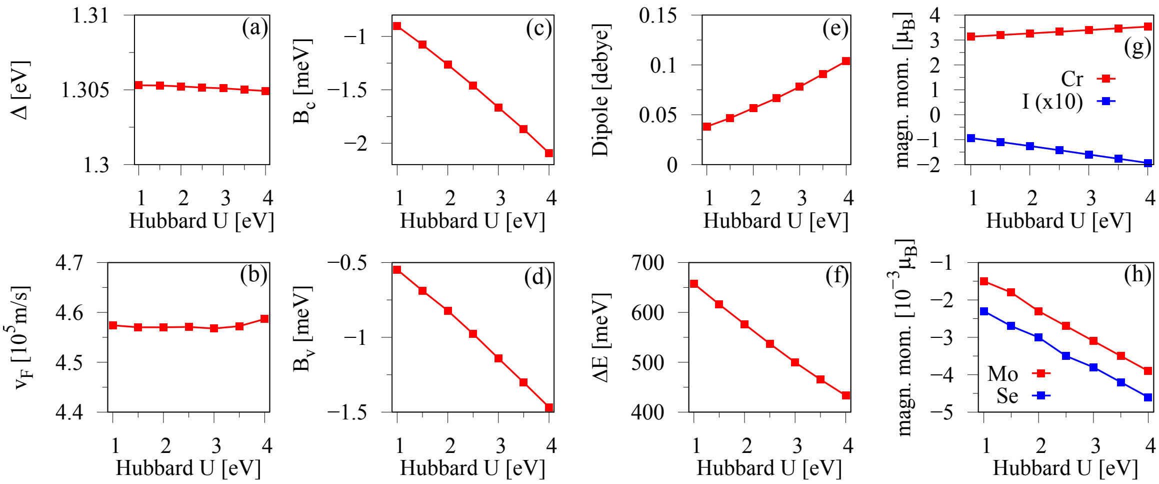

Figure 10.4: Fit parameters as functions of the Hubbard U for the MoSe$_2$/CrI$_3$ heterostructure and for 0° twist angle. Results are obtained from calculations without SOC. (a) The orbital gap Δ of the spectrum, (b) the Fermi velocity v_F, (c,d) the proximity exchange parameters B_c and B_v, (e) the dipole of the heterostructure, and (f) the band gap ΔE as defined in Fig. 10.2. (g,h) The average magnetic moments of the Cr, I, Mo, and Se atoms. We averaged only over the Se atoms closer to the CrI$_3$ substrate. The magnetic moment of the I atom is enhanced by a factor of 10.

the U value. All of them increase in magnitude with increasing U, but their directions do not change. The induced magnetic moment in Mo is directly connected to the amplitudes of the exchange parameters B_c and B_v. Even though the proximity exchange parameters depend linearly on U, their order of magnitude does not change. Therefore, we believe that our presented results will not be affected much; only the magnitudes may be somewhat different.

10.4 Short-rangeness of proximity effects

An important question is what happens if we add more layers to our bilayer heterostructure, that only consisted of TMDC and CrI$_3$ monolayers so far. In order to address this question, we first introduce a second CrI$_3$ layer, i. e., we consider a MoSe$_2$/bilayer-CrI$_3$ heterostructure. Experimentally, it has been demonstrated that monolayer CrI$_3$ is a ferromagnet [284, 419], while the bilayer is a layered antiferromagnet [96, 284, 422]. In contrast, theory predicted the ground state of bilayer CrI$_3$ to be also ferromagnetic for the low temperature rhombohedral phase [419, 423, 424]. The origin of this contradiction can be attributed to the interlayer exchange coupling between two CrI$_3$ layers, which is sensitive to the stacking order [419, 423, 424]. Remarkably, the magnetization of the CrI$_3$ can be tuned by optical excitation, external magnetic fields, gating, and current-induced spin-orbit torque (SOT) [98, 412, 444, 445]. Such diverse control possibilities open new avenues for novel technologies, such as gate tunable spin-filter tunnel junctions [96, 331, 446], and for antiferromagnetic spintronics devices [447, 448]. For our bilayer CrI$_3$ considerations, the most important feature is, that one can switch from ferromagnetically to antiferromagnetically coupled layers [98, 284, 445].

Table 10.2: Summary of the fit parameters for $MoSe_2$/bilayer-CrI_3 systems for 0° twist angle, where the bilayer-CrI_3 is in the ferromagnetic or antiferromagnetic configuration, and arrows ($\uparrow, \downarrow$) denote the magnetization of the first and second CrI_3 layer below $MoSe_2$. The orbital gap Δ of the TMDC and the Fermi velocity v_F. The parameters λ_c and λ_v are the SOC splittings, and B_c and B_v are the proximity exchange parameters for the CB and VB. The dipole of the structure is 0.072 debye for all configurations. The individual columns are calculations with and without SOC.

configuration	ferromagnetic ($\uparrow\uparrow$)		antiferromagnetic ($\uparrow\downarrow$)	
calculation	no SOC	SOC	no SOC	SOC
Δ [eV]	1.307	1.303	1.307	1.303
v_F [10^5m/s]	4.582	4.588	4.585	4.582
λ_c [meV]	-	-9.69	-	-9.66
λ_v [meV]	-	94.41	-	94.36
B_c [meV]	-1.766	-1.542	-1.703	-1.408
B_v [meV]	-1.184	-1.192	-1.191	-1.192

Here, we have calculated the band structure for $MoSe_2$ on top of bilayer CrI_3 with and without SOC. For the bilayer CrI_3, we consider the low temperature rhombohedral phase stacking [419, 423, 424]. Specifically, we are interested in the results for the ferro- and antiferromagnetically coupled bilayer CrI_3. In the ferromagnetic case, the magnetizations are along the z direction for both CrI_3 layers. In the antiferromagnetic case, the magnetization of the CrI_3 layer directly below the TMDC is pointing along z, while the magnetization of the other CrI_3 layer is pointing along $-z$. In agreement with other DFT calculations that considered bare bilayer CrI_3 [419, 423, 424], we find a total energy difference $E_{AFM} - E_{FM} \approx 24$ meV for the whole $MoSe_2$/bilayer-CrI_3 stack, predicting the ferromagnetic state to be energetically favorable for our rhombohedral stacking order. The overall band structure features are not very different compared to the monolayer CrI_3 case shown in Fig. 10.2. Thus, we only summarize the obtained fit results in Tab. 10.2, which describe the spin-split band edges of the TMDC. We find that the parameters Δ, v_F, and especially the proximity exchange couplings B_c and B_v are nearly independent of the magnetic configuration of the bilayer CrI_3. The parameters are also similar to the ones obtained for the case of $MoSe_2$ on monolayer CrI_3, presented in Tab. 10.1. In principle, one could have expected that the total magnetization of the bilayer CrI_3 somewhat influences the proximity-induced exchange in the TMDC. However, this does not seem to be the case, given the fit parameters extracted from realistic DFT calculations. *Even though the antiferromagnetic bilayer CrI_3 has no net magnetization, we still find proximity exchange in $MoSe_2$.* We conclude that proximity exchange is limited to adjacent layers [412] and of short-range nature.

From the experimental perspective, the stability of CrI_3 under ambient conditions is very poor [449]. The stability can be significantly improved by minimizing the exposure to light, while simultaneously encapsulating CrI_3 in hBN to protect it from environmental impurities and degradation [449]. As a consequence, we ask the question whether the $MoSe_2$ on top of the hBN-protected CrI_3 still experiences proximity exchange?

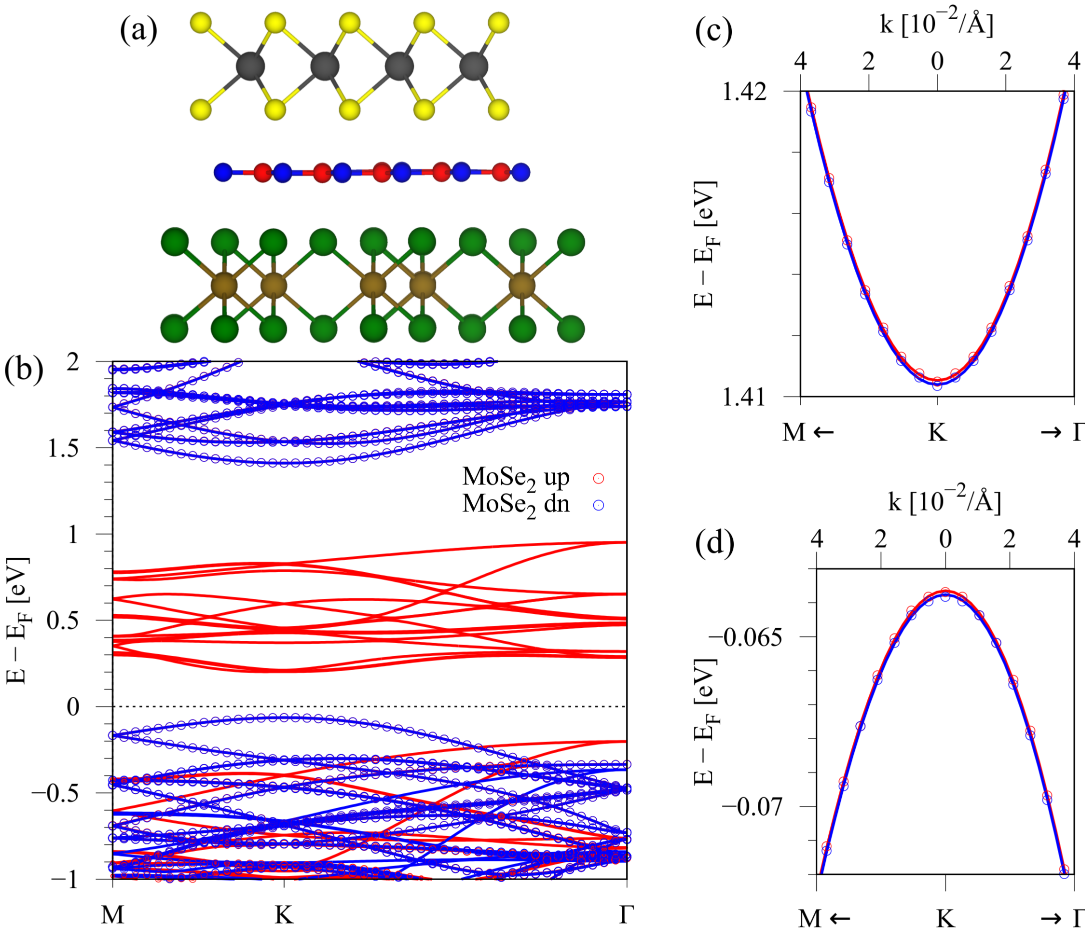

Figure 10.5: (a) Side view of the $MoSe_2/hBN/CrI_3$ stack. (b) Calculated band structure along high symmetry lines. The bands corresponding to $MoSe_2$ are emphasized by red (spin up) and blue (spin down) open circles. (b) Zoom to the $MoSe_2$ CB edge around the K point. (c) Same as (b), but for the VB edge.

Therefore, we considered a $MoSe_2/hBN/CrI_3$ heterostructure, which consists of a 4×4 cell of $MoSe_2$, a 5×5 cell of hBN, and a 2×2 cell of CrI_3. In Fig. 10.5(a), we show the geometry of the stack. We adapted the lattice constant of $MoSe_2$ [376] to $a = 3.314$ Å, the one of hBN [198] to $a = 2.651$ Å, and the one of CrI_3 [55] to $a = 6.627$ Å, resulting in strains of 0.79%, 5.87%, and −3.49%. Even though the hBN layer is strained beyond the typical limits, we can still get an insight on how the buffer layer influences the proximity exchange. The full $MoSe_2/hBN/CrI_3$ geometry contains 130 atoms in the supercell. Interlayer distances were relaxed to 3.46 Å (3.36 Å) between the hBN and CrI_3 ($MoSe_2$). Self consistent calculations were performed with a k-point sampling of $12 \times 12 \times 1$.

The calculated averaged magnetic moments for the case of $MoSe_2/hBN/CrI_3$ are: Cr ($+3.50\ \mu_B$), I ($-0.19\ \mu_B$), N ($-0.0016\ \mu_B$), B ($0.0\ \mu_B$), Mo ($-0.0001\ \mu_B$), and Se ($-0.0001\ \mu_B$). Already here, we notice that the magnetic moments in the TMDC are reduced by one order of magnitude compared to the case without the hBN layer. In Fig. 10.5(b), we show the DFT-calculated band structure of the $MoSe_2/hBN/CrI_3$ stack. Similarly to before, the TMDC bands are recognizable and preserved. The spin-polarized bands of CrI_3 reside within the band gap of $MoSe_2$. Only the number of in-gap states has increased, which can be attributed to the larger supercell size of CrI_3 within this heterostructure. The relevant TMDC band edges are shown in Figs. 10.5(c,d), where nearly no spin splitting is visible. Even though the hBN buffer layer might protect the CrI_3, it also significantly reduces the proximity exchange and the resulting valley splitting. The spin splittings are drastically diminished to about 100 μeV compared to several meV without the hBN layer. The fit parameters are $\Delta = 1.474$ eV, $v_F = 4.638 \times 10^5$m/s, $B_c = -0.069$ meV, and $B_v = -0.057$ meV. The hBN layer reduces the proximity exchange by one order of magnitude. We believe that additional protection layers would even further decrease the coupling between the TMDC and the magnetic substrate, as demonstrated for graphene on hBN/ferromagnet junctions [141].

10.5 Gate tunable proximity exchange and valley splitting

Another important point that we would like to address here is the gate tunability of proximity exchange in our $MoSe_2/CrI_3$ and WSe_2/CrI_3 heterostructures. In the following, we consider only DFT calculations without SOC, as this already suffices to give reasonable proximity exchange parameters. In addition, we focus on the 0° twist angle structures only. As already mentioned, gating can control the magnetism in CrI_3 [284, 444, 445]. Does a transverse electric field, applied across the TMDC/CrI_3 heterostructure, also influence proximity exchange?

For several electric field values, we calculate the band structure, fit our model Hamiltonian to the spin split TMDC band edges, and extract the relevant parameters. In Figs. 10.6(a,b) we show the electric field evolution of the orbital parameters Δ and v_F, which are barely affected by the field. Since the TMDCs are semiconductors, their band gaps Δ and the band edge curvatures, captured by v_F, are independent of external gating. However, what drastically changes is the full band gap ΔE of the band structure, see Fig. 10.6(f), which is defined in Fig. 10.2(c). The explanation is as follows. The materials are weakly coupled and in the simplest picture the full band structure is just an overlay of the individual band structures of the TMDC and the CrI_3. As already mentioned, the materials form a type-II band alignment. The gap ΔE is defined as the energy difference between the spin-polarized in-gap states from CrI_3 and the VB edge of the TMDC, see Fig. 10.2(c). A transverse electric field introduces a potential difference between the monolayers, thus shifting the bands that originate from the individual materials, relative to each other in energy. One can conclude that the field tunes the band alignment. Important for us is the fact that the CrI_3 in-gap states are shifted within the TMDC band gap, which drastically influences ΔE. The tunability of the band alignment could have important consequences for the lifetime of interlayer excitons, i. e., electron-hole pairs localized in different layers. Since the in-gap states are also spin-polarized, one could speculate about additional valley control, having the spin-valley coupling of the TMDC in mind.

Essential for technological applications is the gate tunability of the proximity exchange parameters B_c and B_v, see Figs. 10.6(d,e). Within the experimentally accessible field range of ± 4 V/nm, the CB spin splitting ($\approx 2B_c$) can be tuned between 2 meV to 8 meV, while the VB splitting ($\approx 2B_v$) changes from 2 meV to 5 meV. In general, the proximity exchange

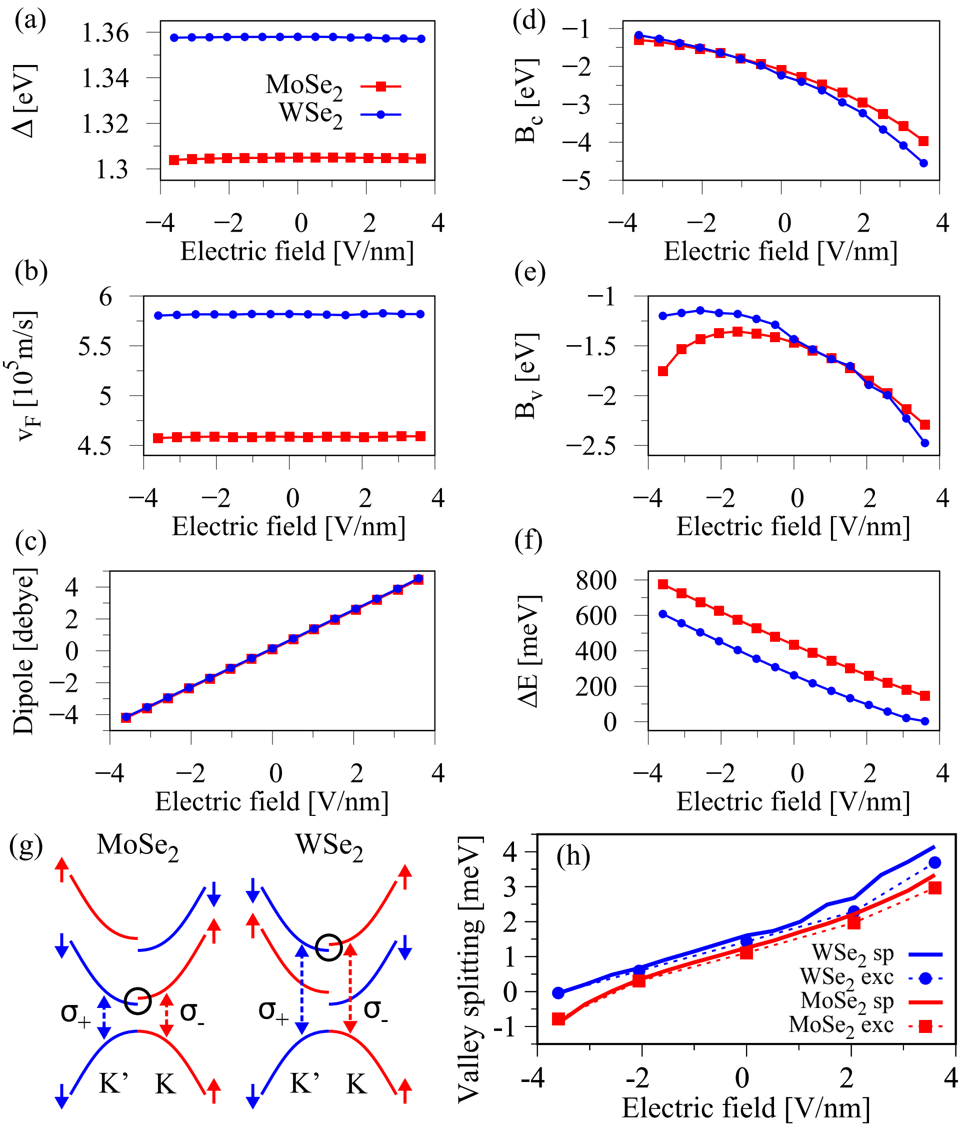

Figure 10.6: Fit parameters as functions of a transverse electric field for TMDC/CrI$_3$ heterostructures and for calculations without SOC. (a) The gap Δ of the TMDC spectrum, (b) the Fermi velocity v_F, (c) the dipole of the heterostructure, (d,e) the proximity exchange parameters B_c and B_v and (f) the full band gap ΔE, as defined in Fig. 10.2(c). (g) Schematic representation of the exchange interaction in the band structure of MoSe$_2$ and WSe$_2$ at K and K′ points, indicating the lowest energy optically allowed transitions (vertical dashed arrows). (h) Single-particle and intralayer exciton valley splitting as functions of the external electric field. *Figures (g) and (h) are contributions from Paulo E. Faria Junior.*

increases when the external field is tuned from −4 V/nm to 4 V/nm, which also enables gate control of the valley splitting. In Fig. 10.6(g), we sketch the energy levels for the top VB and the first two CBs at K and K′ valleys for MoSe$_2$ and WSe$_2$. The top of the VB is set to zero. We look at the lowest energy optical transitions, which are from the VB to the first (second) CB in MoSe$_2$ (WSe$_2$). As stated earlier, the optical selection rules allow transitions with different light helicity in different valleys. Due to the interplay of proximity exchange and SOC, the valley degeneracy is broken, and the energy difference between σ_+ and σ_-

excitations represents the valley splitting. In Fig. 10.6(h), we show the electric field evolution of the valley splitting, as calculated from the first exciton absorption peaks within the BSE framework[3] and from the single-particle picture. Despite the nonlinear behavior of the exchange parameters, the valley splitting shows a roughly linear tunability with respect to the applied field. The results from the single-particle picture show the same trends as the ones from the absorption spectra calculations. Remarkably, we find not only a strong tunability for both TMDCs, but also a sign change in the valley splitting of $MoSe_2$ at around -2.5 V/nm. For WSe_2, a further increase of the field amplitude could also lead to such a transition. In reality, we expect and interplay of both the electric field tunability and the previously discussed twist angle dependence of the valley splitting.

At the end of this chapter, we want to mention a few words of precaution when comparing our results to experiments. From our considerations and from recent results [450, 451], we conclude that twisting, gating, and stacking influences the proximity exchange. Experimentally, when moirè-patterns are present in relatively large samples, an interplay of all effects occur and local variations in the proximity exchange strength can be expected. Since the overall electrostatics play a role for the band alignment, additional SiO_2 or hBN substrates and capping layers can influence the results as well. Apparently, for both materials, TMDCs and CrI_3, the optical spectra are dominated by strongly bound excitons [347, 452], which certainly complicates the analysis of the heterostructure spectra. In conclusion, further extensive considerations are necessary to gain a full understanding of experimental data.

10.6 Summary and conclusion

In this chapter, we have considered vdW heterostructures consisting of TMDCs ($MoSe_2$ and WSe_2) and CrI_3. The magnetic CrI_3 substrate induces significant proximity exchange coupling in the monolayer TMDCs, which spin splits the relevant VB and CB edges. With the help of a low energy model Hamiltonian, we were able to extract proximity exchange parameters and valley splittings of a few meV. Remarkably, twisting the layers changes the sign of the VB spin splitting, which significantly enhances the valley splitting, as we found by comparing 0° and 30° twist angle cases. Another efficient tuning knob for the valley splitting is a transverse electric field, through which band offsets and the proximity-induced spin splittings can be controlled. More precisely, twisting from 0° to 30° can enhance the valley splitting roughly by a factor of 3–4, depending on the TMDC. Tuning the electric field from -4 V/nm to 4 V/nm can change the valley splitting from -1 meV to 4 meV. From our considerations of bilayer-CrI_3 and an additional hBN-buffer layer, we found that proximity exchange coupling is short-ranged. One can expect, that these observations are generally valid for 2D vdW heterostructures, where proximity effects play a role.

---

[3] For the absorption spectra calculations, we employed the model Hamiltonian together with the fixed values of Δ, v_{F}, λ_{c}, and λ_{v}, given in Tab. 10.1, and the electric field tunable parameters B_{c} and B_{v} presented in Figs. 10.6(d,e).

PART V

Summary and Outlook

CHAPTER 11

Recapitulation

Throughout this thesis, we discussed several two-dimensional (2D) materials and van der Waals (vdW) heterostructures with the potential for novel spin-based device technologies. Some of the most important results obtained in this thesis are summarized in Fig. 11.1. In all considered cases, an effective low energy model Hamiltonian was fitted to the first-principles data in order to quantify the relevant proximity effects. In the first part, we have seen that proximity-induced spin-orbit coupling (SOC) and exchange effects are a valuable and simple route to modify the Dirac states of monolayer graphene according to our needs. In addition, an external transverse electric field can be used to tune the magnitude of proximity effects. In the second part, we have shown that the major advantage of bilayer graphene (BLG) is its gate-tunable band gap. Since proximity effects are short-ranged and the low energy bands of BLG are layer-polarized, spin-orbit and exchange coupling of conduction electrons can be switched on and off. In the last part, we have seen that, by straining monolayer transition-metal dichalcogenides (TMDCs), one can gain control over the type (direct or indirect) and size of the band gap, which has a great impact on optical properties. Moreover, with proximity exchange effects, originating from a magnetic substrate, one can break the valley degeneracy of a TMDC, which is tunable by gating and twisting.

More precisely, in Ch. 4 we have seen that, when graphene is encapsulated by the wide band gap insulator hexagonal boron nitride (hBN), the linear dispersion can be well preserved. Moreover, proximity-induced SOC effects are weak and graphene's intrinsic electronic and spin transport properties are only barely affected. We concluded that in ultraclean graphene/hBN heterostructure devices, one can expect high mobility charge carriers with ultralong spin lifetimes well beyond a few nanoseconds. In addition, the spin lifetimes exhibit giant and gate-tunable anisotropies, which are experimentally detectable fingerprints of our results. From our studies of monolayer graphene on the three-dimensional (3D) topological insulator (TI) material Bi_2Se_3 in Ch. 5, we have seen that a strong valley Zeeman type SOC is induced by the proximity effect, in analogy to graphene/TMDC heterostructures. The magnitude of the proximity-induced SOC can be strongly controlled by the interlayer distance, as well as by gating the heterostructures. Moreover, for a different TI material, e. g., Bi_2Te_2Se, band offsets are significantly different, while the induced SOC strength stays similar in magnitude. In Ch. 6, we studied graphene on the antiferromagnetic Ising semiconductor $MnPSe_3$. In contrast to all previously reported graphene-based proximity-induced

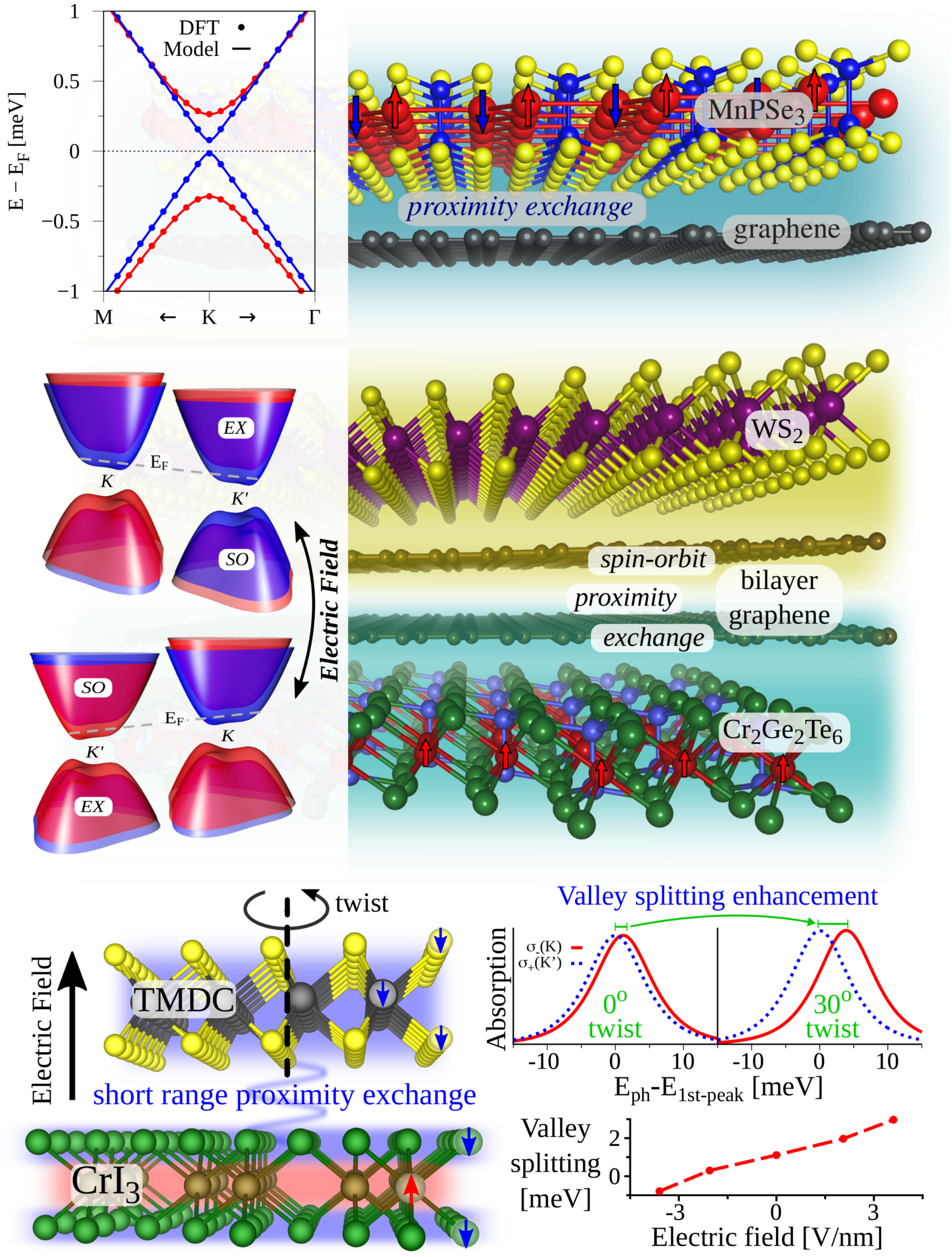
1
0.5
0
−0.5
−1
E − E_F [meV]
DFT •
Model —
M
←
K
→
Γ
MnPSe3
proximity exchange
graphene
EX
E_F
K
K'
SO
Electric Field
SO
E_F
K'
K
EX
WS2
spin-orbit
proximity
exchange
bilayer
graphene
Cr2Ge2Te6
twist
TMDC
Electric Field
short range proximity exchange
CrI3
Valley splitting enhancement
Absorption
σ−(K)
σ+(K')
0° twist
30° twist
-10
0
10
-10
0
10
E_ph-E_1st-peak [meV]
Valley splitting [meV]
2
0
-3
0
3
Electric field [V/nm]

Figure 11.1: Pictorial summary of some important results obtained in this thesis. Top: Proximity exchange in graphene on the Ising antiferromagnet $MnPSe_3$. Middle: On-demand spin-orbit and exchange in doubly proximitized bilayer graphene. Bottom: Twist-angle and gate-tunable valley splitting in TMDC/CrI_3 heterostructures.

exchange studies, we could demonstrate staggered exchange coupling in graphene. This new type of proximity exchange leads to opportunities in designing novel graphene-based devices that potentially host topologically protected edge states. By reducing the vdW gap between the monolayers or eventually employing another member of the MPX_3 family, the antiferromagnetic proximity effect might even be further enhanced.

The second main part of this thesis was dedicated to BLG structures. In Ch. 8, we first recapitulated the spin-orbit valve effect in BLG/TMDC and the exchange valve effect in BLG/$Cr_2Ge_2Te_6$ (CGT) heterostructures. With the help of our low energy BLG model Hamiltonian, we also quantified the proximity effects in these structures, which is vital for further theoretical studies. As the next logical step, we considered a trilayer heterostructure consisting of BLG sandwiched between monolayers of WS_2 and CGT such that each graphene layer of BLG almost exclusively experiences one kind of proximity effect. The low energy bands of the doubly proximitized BLG display an exchange split valence band (VB) and a spin-orbit split conduction band (CB) for a positive electric field of 1 V/nm. The band structure can be swapped by tuning the electric field to negative values, say -1 V/nm, where now the CB is split by exchange and the VB by spin-orbit. Doubly proximitized BLG is a unique platform for investigating fundamental spin physics and demonstrates the potential of vdW engineering using 2D crystal multilayers.

In the last part of this thesis, we considered TMDCs. In Ch. 9, we investigated bare TMDC monolayers under the influence of biaxial strain. We provided a systematic assessment of biaxial strain effects on the orbital, spin-orbit, and optical properties of the monolayer TMDCs. Most important, strain induces a direct-to-indirect band gap transition and our results are particularly useful for interpreting experiments that study strain-tunable optical spectra of TMDCs. Finally, in Ch. 10, we considered proximity exchange effects in TMDCs due to the magnetic transition-metal trihalide (TMTH) CrI_3. We have shown that proximity exchange splittings can be strongly tuned by gating the TMDC/monolayer-CrI_3 heterostructures, but also twisting is an efficient control knob to tune the valley splitting of the proximitized TMDC. Moreover, the TMDC is only affected by the adjacent magnetic layer, as we found by considering bilayer-CrI_3 as the substrate, which is a layered antiferromagnet. Even though a hBN layer on top of the CrI_3 substrate can protect it from environmental influences and degradation, the proximity exchange effect on the TMDC is strongly weakened. The observed twist angle dependence, electric field tunability, and short-rangeness of proximity exchange can be verified experimentally in optical reflectance or transmittance measurements, and should be generally valid for other 2D vdW heterostructures.

CHAPTER 12

Novel 2D materials

Physicists and engineers are striving to design novel spintronics devices with extraordinary functionalities. Thus, basic research is challenged more than ever to find the most suitable two-dimensional (2D) material candidates and their heterostructure combinations for whatever applicative reason. Moreover, new materials have to be found, synthesized, and characterized, which can potentially outperform known materials and additionally broaden the spectrum of combination possibilities. A very nice example are the atomically thin magnets, which have just recently opened new avenues for basic research on magnetism in the 2D limit, as well as for applications in spintronics. What kind of innovative 2D materials are explored at the moment?

A whole bunch of interesting van der Waals (vdW) layered magnetic materials can be summarized in the MPX_3 family, which are currently under intense investigations [312, 318, 453–459]. As we have seen in Ch. 6 of this thesis, $MnPSe_3$ is an Ising-type antiferromagnetic semiconductor with the potential to induce staggered exchange coupling in graphene. Generally, the magnetic properties of the MPX_3 crystals can be tuned by gating and straining [460]. Remarkably, in Ni-based transition-metal trichalcogenides (TMTCs), there is evidence of topological superconductivity [457] and a coherent many-body exciton state [461]. However, one limiting issue of the known 2D ferro- and antiferromagnets, such as CrI_3, VI_3, $Cr_2Ge_2Te_6$ (CGT), and $MnPSe_3$, are their Curie and Néel temperatures, which are well below ambient conditions [55, 319, 341, 462] and thus limiting their application prospects. Fortunately, there are now candidates such as $Cr_{5+x}Te_8$ [463] and $Fe_{3+x}GeTe_2$ [464–467], which hold promise for room temperature applications due to their intrinsically high and tunable Curie temperature. In both of them, the transition metal concentration x can be used to tune T_C, while it can be additionally tuned by gating in $Fe_{3+x}GeTe_2$, see Figs. 12.1(a,b). Besides them, monolayers of VSe_2 [468] and MnSe [469] already intrinsically show evidence for strong room temperature ferromagnetism.

Also the family of non-magnetic 2D materials is growing almost every day. The ultrathin insulator hexagonal boron nitride (hBN) was roughly the first material that soon followed after the discovery of graphene. Remarkably, hBN has become one of the most important materials for electronics and spintronics. Especially in the 2D limit, it is frequently used as tunnel barrier to overcome the conductivity mismatch or as protection layer for other materials. In analogy to hBN, there are now similar insulating materials, hexagonal alu-

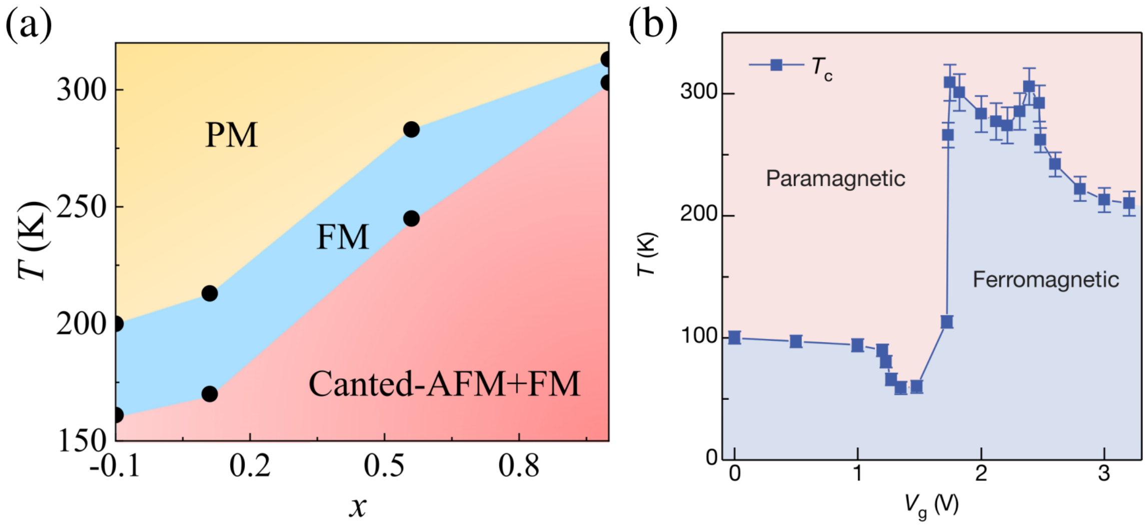

Figure 12.1: Tunable Curie temperature in magnetic vdW materials. (a) Magnetic phase diagram (FM = ferromagnet, AFM = antiferromagnet, PM = paramagnet) of $Cr_{5+x}Te_8$ as function of temperature and Cr-concentration x. (b) Magnetic phase diagram of a trilayer Fe_3GeTe_2 sample as function of temperature and gate voltage. Figure (a) from Ref. [463] and (b) from Ref. [464].

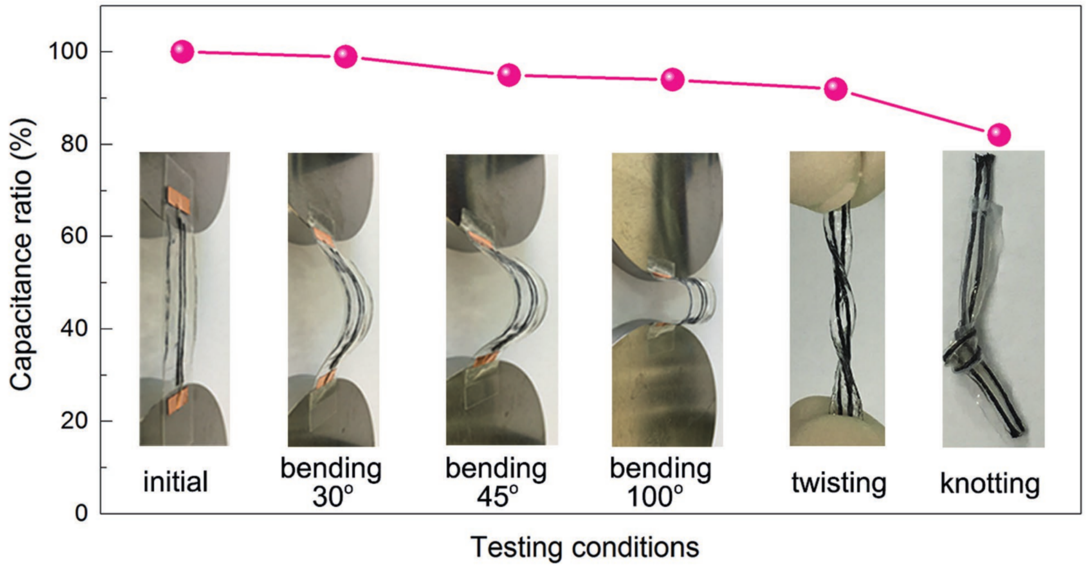

Figure 12.2: The normalized capacitance of an all-solid-state, flexible, and fiber-based MXene supercapacitor after bending, twisting, and knotting. Figure taken from Ref. [470].

minum nitride (hAlN) and hexagonal gallium nitride (hGaN) [471–477], which seem to be very promising 2D monolayers. For example, heterostructures consisting of hAlN combined with a transition-metal dichalcogenide (TMDC) or blue phosphorene are predicted to be important visible-light-driven photocatalysts for water splitting [478, 479]. Also excitonic effects have been studied in hAlN and hGaN [475, 480], with absorption spectra dominated by strongly bound excitons, similarly to TMDCs. Both materials are becoming of interest for optoelectronic applications [481] due to their 2D nature, while also their heterostructure stacks [482] show novel electronic and optical properties. G_0W_0-calculations provide indirect band gaps for hAlN (5.8 eV [483]) and hGaN (4.55 eV [484]) comparable to the one of hBN (6.0 eV [485]). Based on these results, one may argue that hAlN and hGaN are an alternative to hBN, even though few- and monolayers are hard to synthesize at the moment.

Elemental 2D materials, such as germanene, stanene, and silicene, are also very interesting, displaying extraordinary electronic, mechanical, optical, and thermal properties [486–492]. In analogy to graphene, they form a honeycomb lattice, but with a buckled structure, and feature a Dirac-like linear dispersion. In addition, and in contrast to graphene, their intrinsic spin-orbit coupling (SOC) is large, which is inevitable for topological transport properties. For example, monolayer stanene shows a large ($\approx$ 100 meV) intrinsic spin-orbit gap [486], thus potentially hosting quantum spin Hall (QSH) and, under the right conditions, quantum anomalous Hall (QAH) states at room temperature [487]. Furthermore, theory predicts enhanced thermoelectric performance, topological superconductivity, and perfect spin filtering for those 2D topological insulators (TIs) [487, 488, 491].

Another relevant and highly discussed 2D material family are the MXenes [493, 494], which are promising and long-awaited candidates for miniaturized energy storage solutions, see Fig. 12.2(a). The above examples are by far not a complete overview about all currently known 2D materials. In this context, it is worth to mention the work of Mounet *et al.* [495], in which hundreds of potential 2D materials were identified by first-principles calculations. Even though most of them show prominent features and are important for basic research, only some of them will find their way to mass market industry. At the moment, 2D material research is a platform for novel low power device designs at the nanoscale.

PART VI

Appendix

APPENDIX A

Supplementary Material

A.1 Supporting Information for chapter 6

Table A.1: The fit parameters of the model Hamiltonian $\mathcal{H}_{\mathrm{GR}}$, Eq. (3.7), for the graphene/MnPSe$_3$ heterostructure as functions of the interlayer distance. The Fermi velocity is v_{F}, Δ is the staggered potential gap, $\lambda_{\mathrm{ex}}^{\mathrm{A}}$ and $\lambda_{\mathrm{ex}}^{\mathrm{B}}$ are the sublattice-resolved exchange parameters, E_{D} is the Dirac point energy, and E_{tot} is the total energy of the system, relative to the lowest energy case. FM/AFM denotes the ferromagnetic/antiferromagnetic configuration of MnPSe$_3$.

dist.	FM/AFM	v_{F} [$10^5\frac{\mathrm{m}}{\mathrm{s}}$]	Δ [μeV]	$\lambda_{\mathrm{ex}}^{\mathrm{A}}$ [μeV]	$\lambda_{\mathrm{ex}}^{\mathrm{B}}$ [μeV]	E_{D} [meV]	E_{tot} [meV]
3.56	AFM	8.187	22	-31	45	0.111	36.2
3.46	AFM	8.171	32	-45	65	0.233	0
3.36	AFM	8.148	49	-66	95	-0.420	33.4
3.26	AFM	8.114	76	-96	137	0.0320	180.5
3.16	AFM	8.064	123	-140	201	0.001	497.9
3.06	AFM	7.991	210	-200	292	-0.356	1050.5
3.36	FM	8.149	51	-251	-205	0.476	244.1

A.2 Supporting Information for chapter 8

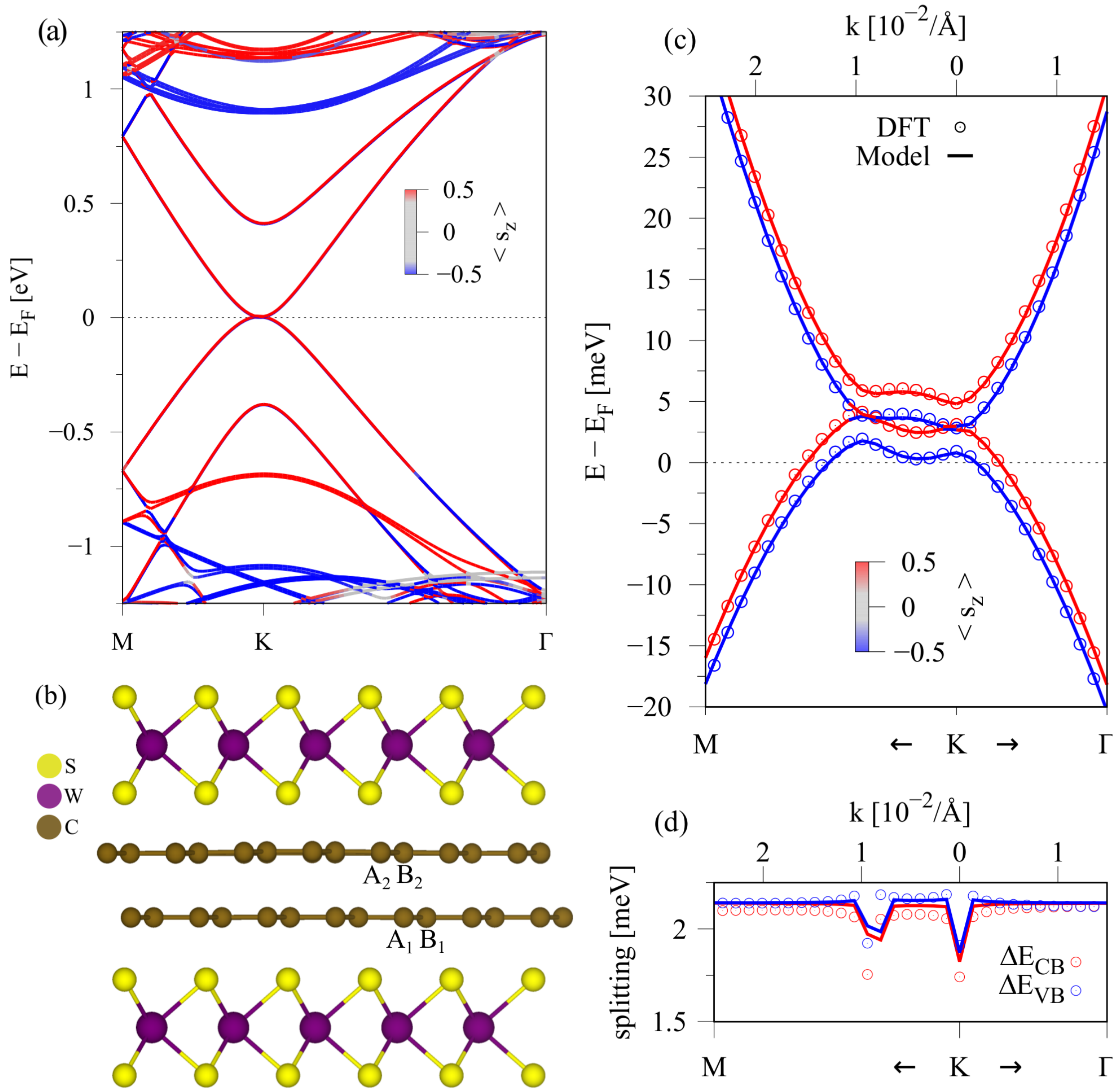

Figure A.1: (a,b) Band structure with spin-orbit coupling (SOC) and geometry of bilayer graphene (BLG) encapsulated by WS_2. (c) Zoom to the calculated low energy bands (symbols) around the K point with a fit to the model Hamiltonian (solid lines). The color corresponds to the s_z expectation value. (d) Energy splittings of the conduction band (CB) and valence band (VB).

Table A.2: Most relevant fit parameters of the model Hamiltonian $\mathcal{H}_{\mathrm{BLG}}$, Eq. (7.1), for the ($WS_2$/)BLG/$WS_2$ structures including SOC and for the $Cr_2Ge_2Te_6$ (CGT)/BLG(/CGT) structures without SOC.

system	BLG/WS_2 (SOC)	WS_2/BLG/WS_2 (SOC)	CGT/BLG (no SOC)	CGT/BLG/CGT (no SOC, FM)	CGT/BLG/CGT (no SOC, AFM)
γ_0 [eV]	2.453	2.444	2.541	2.519	2.524
γ_1 [eV]	0.372	0.395	0.384	0.387	0.387
γ_3 [eV]	−0.269	−0.288	−0.296	−0.296	−0.295
γ_4 [eV]	−0.162	−0.170	−0.179	−0.189	−0.189
V [meV]	4.226	0.924	−8.499	−0.495	−0.423
Δ [meV]	10.208	12.331	10.434	9.303	9.255
λ_{R} [meV]	−0.059	0	0	0	0
$\lambda_{\mathrm{I}}^{\mathrm{A1}}$ [meV]	0	1.082	0	0	0
$\lambda_{\mathrm{I}}^{\mathrm{B1}}$ [meV]	0	−1.058	0	0	0
$\lambda_{\mathrm{I}}^{\mathrm{A2}}$ [meV]	1.070	1.082	0	0	0
$\lambda_{\mathrm{I}}^{\mathrm{B2}}$ [meV]	−1.179	−1.058	0	0	0
$\lambda_{\mathrm{ex}}^{\mathrm{A1}}$ [meV]	0	0	−4.567	−3.447	−3.254
$\lambda_{\mathrm{ex}}^{\mathrm{B1}}$ [meV]	0	0	−4.224	−3.625	−3.460
$\lambda_{\mathrm{ex}}^{\mathrm{A2}}$ [meV]	0	0	0	−3.447	3.254
$\lambda_{\mathrm{ex}}^{\mathrm{B2}}$ [meV]	0	0	0	−3.625	3.460
E_D [meV]	−3.844	2.815	−1.003	0.987	1.051
dipole [debye]	−1.089	0.020	1.527	0.051	0.054

Table A.3: Most relevant fit parameters of the model Hamiltonian $\mathcal{H}_{\mathrm{BLG}}$, Eq. (7.1), for the WS_2/BLG/CGT heterostructure. The parameters fit the first-principles results with and without SOC. Based on the fit parameters for the individual BLG/CGT and WS_2/BLG subsystems, we assumed $\lambda_{\mathrm{I}}^{\mathrm{A2}} = -\lambda_{\mathrm{I}}^{\mathrm{B2}}$ and $\lambda_{\mathrm{ex}}^{\mathrm{A1}} = \lambda_{\mathrm{ex}}^{\mathrm{B1}}$ for the fit when SOC is included.

	no SOC	SOC
γ_0 [eV]	2.434	2.432
γ_1 [eV]	0.365	0.365
γ_3 [eV]	−0.269	−0.273
γ_4 [eV]	−0.165	−0.164
V [meV]	−0.479	−0.474
Δ [meV]	8.649	8.854
$\lambda_{\mathrm{I}}^{\mathrm{A2}}$ [meV]	0	1.132
$\lambda_{\mathrm{I}}^{\mathrm{B2}}$ [meV]	0	−1.132
$\lambda_{\mathrm{ex}}^{\mathrm{A1}}$ [meV]	−4.257	−3.874
$\lambda_{\mathrm{ex}}^{\mathrm{B1}}$ [meV]	−3.997	−3.874
E_D [meV]	−0.336	0.348
dipole [debye]	0.366	0.398

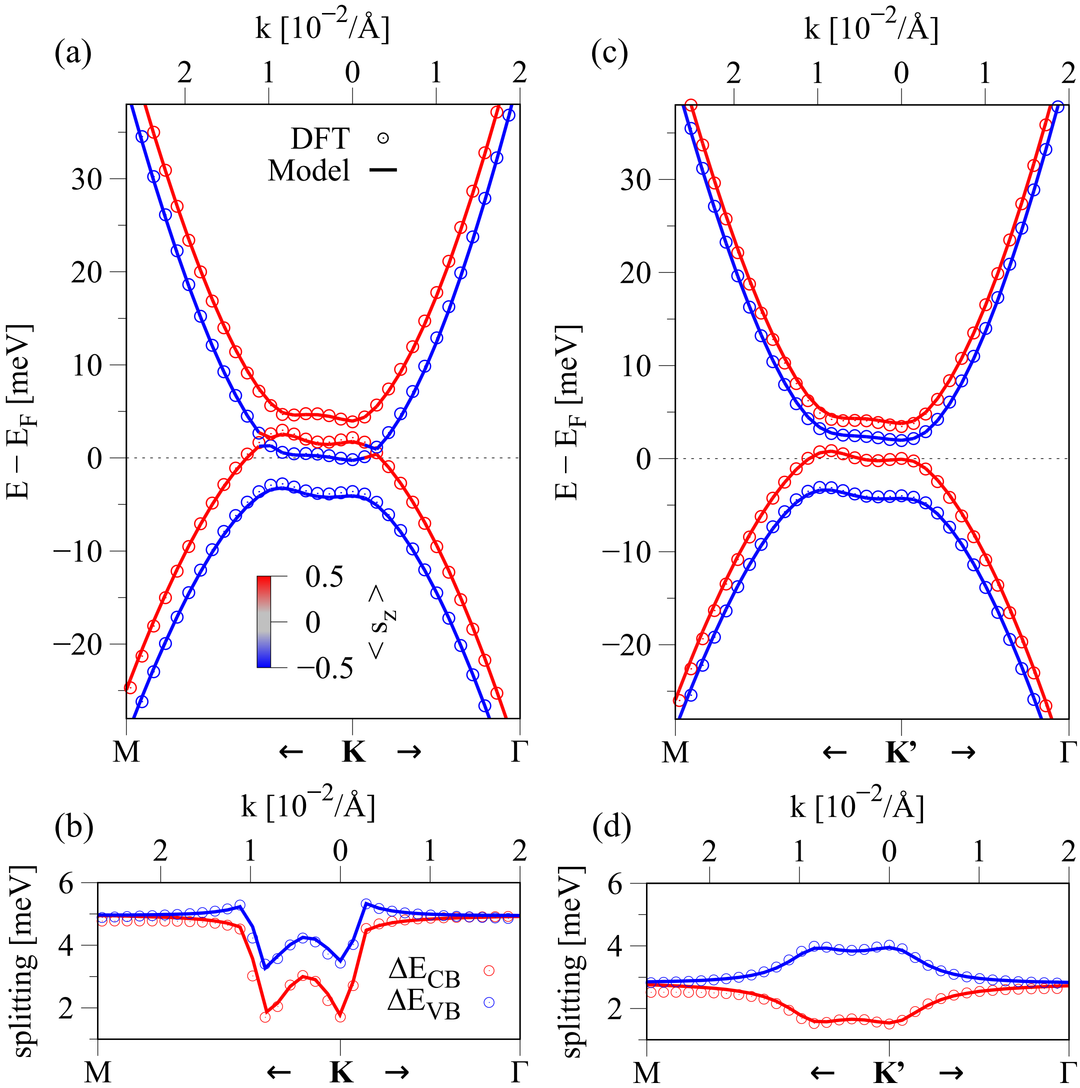

Figure A.2: (a) Zoom to the calculated low energy bands (symbols) around the K point with a fit to the model Hamiltonian (solid lines) for the WS_2/BLG/CGT heterostructure and zero external electric field. (b) Energy splittings of the CB and VB. (c,d) Same as (a,b), but for the K′ point.

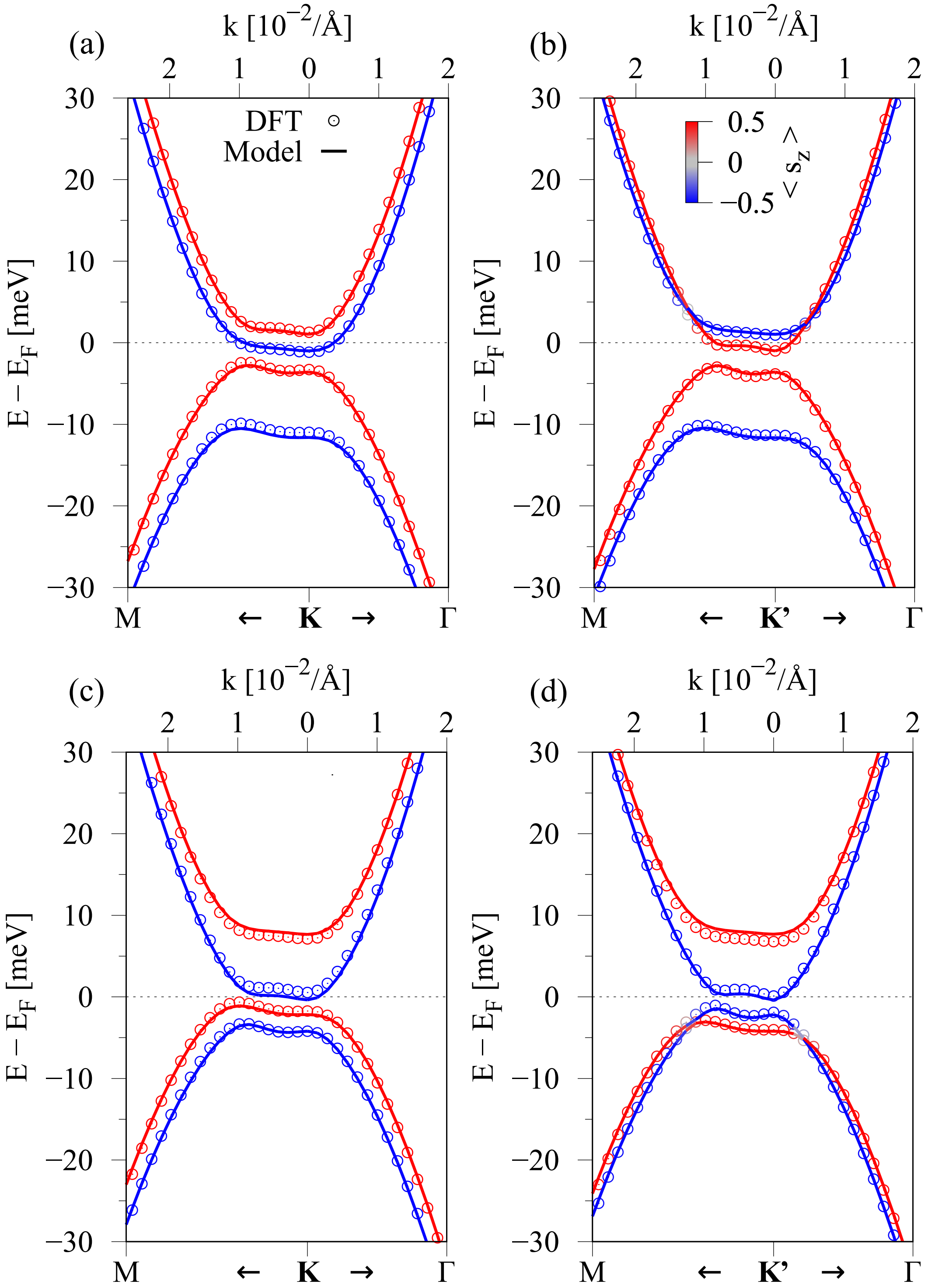

Figure A.3: Calculated (symbols) low energy band structures with a fit to the model Hamiltonian (solid lines) around K and K′ points for WS$_2$/BLG/CGT heterostructure. (a,b) For a transverse electric field of +0.4 V/nm and a resulting dipole of 2.755 debye. (c,d) For a transverse electric field of −0.5 V/nm and a resulting dipole of −2.649 debye.

A.3 Supporting Information for chapter 9

Table A.4: Fit parameters of the model Hamiltonian $\mathcal{H}_{\mathrm{TMDC}}$, Eq. (9.1), for all four transition-metal dichalcogenides (TMDCs) and different values of biaxial strain. The lattice parameter a is given in Å, Δ is given in eV, v_{F} is given in 10^5 m/s, and λ_{c}, λ_{v} are given in meV.

MoS_2					$MoSe_2$				
a	Δ	v_{F}	λ_{c}	λ_{v}	a	Δ	v_{F}	λ_{c}	λ_{v}
3.0854	2.071	5.205	0.666	69.95	3.219	1.779	4.429	-9.120	89.10
3.1104	1.969	5.287	-0.336	71.34	3.244	1.696	4.507	-10.22	90.39
3.1354	1.871	5.331	-0.887	72.54	3.269	1.615	4.560	-10.59	91.54
3.1604	1.777	5.347	-1.207	73.64	3.294	1.536	4.587	-10.64	92.50
3.1854	1.687	5.338	-1.410	74.60	3.319	1.461	4.597	-10.45	93.25
3.2104	1.602	5.310	-1.479	75.43	3.344	1.389	4.589	-10.15	93.95
3.2354	1.522	5.263	-1.550	76.16	3.369	1.320	4.564	-9.760	94.42
3.2604	1.446	5.202	-1.518	76.82	3.394	1.255	4.526	-9.309	94.78
3.2854	1.375	5.128	-1.450	77.42	3.419	1.194	4.480	-8.780	94.98

WS_2					WSe_2				
a	Δ	v_{F}	λ_{c}	λ_{v}	a	Δ	v_{F}	λ_{c}	λ_{v}
3.080	2.274	6.752	43.08	191.46	3.219	1.917	5.964	51.18	212.16
3.105	2.153	6.815	31.80	197.68	3.244	1.816	6.011	38.40	218.12
3.130	2.035	6.820	24.40	203.40	3.269	1.716	6.019	29.87	223.60
3.155	1.921	6.795	19.35	208.64	3.294	1.619	5.995	24.00	228.56
3.180	1.812	6.735	15.72	213.46	3.319	1.525	5.948	19.86	233.07
3.205	1.710	6.655	13.07	217.83	3.344	1.437	5.881	16.85	237.10
3.230	1.614	6.542	11.11	221.81	3.369	1.353	5.798	14.63	240.72
3.255	1.526	6.437	9.62	225.37	3.394	1.276	5.702	13.02	243.86
3.280	1.443	6.311	8.46	228.57	3.419	1.203	5.596	11.81	246.58

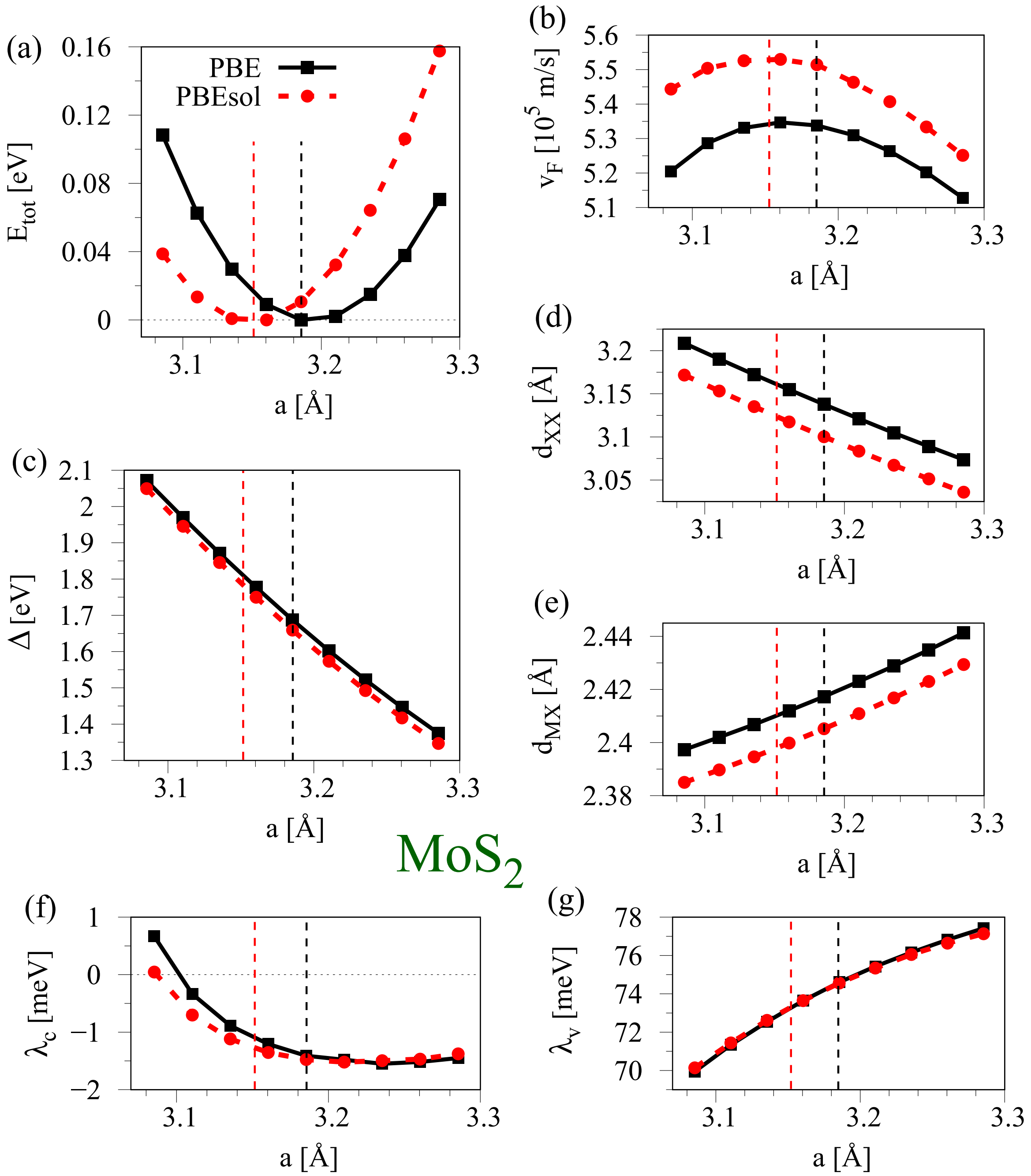

Figure A.4: Comparison between the Perdew-Burke-Ernzerhof (PBE) (black squares) and PBEsol (red dots) functional for MoS_2 as a function of the lattice constant. Dashed vertical lines indicate the equilibrium lattice constants. (a) Total energy E_{tot}, (b) the Fermi velocity v_F, (c) the gap parameter Δ, (d,e) the distances d_{XX} and d_{MX}, and (f,g) the SOC parameters λ_c and λ_v.

APPENDIX B

Employed program packages

The **Atomic Simulation Environment** (ASE) is a set of tools and Python modules for setting up, manipulating, running, visualizing, and analyzing atomic simulations [265]. It was used to create the individual two-dimensional (2D) monolayers, the van der Waals (vdW) heterostructures, and to set up the input files for the calculations.

XCrySDen is a crystalline and molecular structure visualization program aiming to display isosurfaces and contours, which can be superimposed on crystalline structures, and interactively rotated and manipulated [496]. It was used to view the structures we generated and to produce the k-path for band structure calculations. After relaxation of atomic positions, it was used to measure the distances between the single layers in the vdW systems.

VESTA is a three-dimensional (3D) visualization program for structural models and volumetric data such as electron/nuclear densities, and crystal morphologies [497]. It was used to visualize the crystal structures, spin polarizations, or other volumetric data. All figures, showing crystal structures, were produced with VESTA.

QUANTUM ESPRESSO is an integrated suite of Open-Source computer codes for electronic-structure calculations and materials modeling at the nanoscale. It is based on density functional theory (DFT)[1], plane waves, and pseudopotentials. It is able to calculate ground state properties, perform structural optimizations, quantum transport, and many more [267, 500]. It was used for structural relaxation of the systems and the calculation of electronic properties, such as band structure and density of states (DOS).

The program package **WIEN2k** allows to perform electronic structure calculations of solids employing DFT. It is based on the full potential linearized augmented plane wave (FLAPW) plus local orbitals method, one among the most accurate schemes for band structure calculations. WIEN2K is an all-electron scheme including relativistic effects [205]. It was mainly used to crosscheck the results obtained from QUANTUM ESPRESSO suite.

The fitting of the model Hamiltonians to the calculated band structures was performed with the `lmfit` package implemented in **Python**, employing the least-squares method. For accurate fit results, we took into account the relevant band energies, their energy differences, and spin expectation values where possible and necessary.

---

[1] A detailed introduction to DFT and its methodologies can be found in Refs. [498, 499]

Acronyms

2D	two-dimensional
3D	three-dimensional
ASE	atomic simulation environment
ARPES	angle resolved photoemission spectroscopy
BZ	Brillouin zone
BLG	bilayer graphene
BSE	Bethe-Salpeter equation
CB	conduction band
CDW	charge density wave
CGT	$Cr_2Ge_2Te_6$
CVD	chemical vapour deposition
DFT	density functional theory
DOS	density of states
FET	field-effect transistor
FLAPW	full potential linearized augmented plane wave
FMI	ferromagnetic insulator
GGA	generalized gradient approximation
GMR	giant magnetoresitance
hAlN	hexagonal aluminum nitride
hBN	hexagonal boron nitride
hGaN	hexagonal gallium nitride
MBE	molecular beam epitaxy
MRAM	magnetic random access memory
PAW	projector augmented wave
PBE	Perdew-Burke-Ernzerhof
PIA	pseudospin inversion asymmetry
PL	photoluminescence

PMA	perpendicular magnetic anisotropy
QL	quintuple layer
QAH	quantum anomalous Hall
QSH	quantum spin Hall
REE	Rashba-Edelstein effect
RHEED	reflection high-energy electron diffraction
TI	topological insulator
TMDC	transition-metal dichalcogenide
TMR	tunneling magnetoresitance
TMTC	transition-metal trichalcogenide
TMTH	transition-metal trihalide
SHE	spin Hall effect
SR	spin relaxation
SOC	spin-orbit coupling
SOT	spin-orbit torque
STT	spin-transfer torque
VB	valence band
vdW	van der Waals

References

[1] M. D. Amipara, “Nano Technology - Spintronics”, IOSR-JECE, SICETE **3**, 14 (2013).

[2] I. Zutic, J. Fabian, and S. Das Sarma, “Spintronics: Fundamentals and applications”, Rev. Mod. Phys. **76**, 323 (2004).

[3] J. Fabian et al., “Semiconductor spintronics”, Acta Phys. Slov. **57**, 565 (2007).

[4] A. Avsar et al., “Colloquium: Spintronics in graphene and other two-dimensional materials”, Rev. Mod. Phys. **92**, 021003 (2020).

[5] W. Gerlach and O. Stern, “Der experimentelle Nachweis der Richtungsquantelung im Magnetfeld”, Z. Phys. **9**, 349 (1922).

[6] W. Pauli, “Zur Quantenmechanik des magnetischen Elektrons”, Z. Phys. **43**, 601 (1927).

[7] N. F. Mott, “The electrical conductivity of transition metals”, Proc. R. Soc. A **153**, 699 (1936).

[8] N. F. Mott, “The resistance and thermoelectric properties of the transition metals”, Proc. R. Soc. A **156**, 368 (1936).

[9] T. Kasuya and A. Yanase, “Anomalous transport phenomena in Eu-chalcogenide alloys”, Rev. Mod. Phys. **40**, 684 (1968).

[10] J. Moodera et al., “Electron-spin polarization in tunnel junctions in zero applied field with ferromagnetic EuS barriers”, Phys. Rev. Lett. **61**, 637 (1988).

[11] X. Hao, J. S. Moodera, and R. Meservey, “Spin-filter effect of ferromagnetic europium sulfide tunnel barriers”, Phys. Rev. B **42**, 8235 (1990).

[12] L. Esaki, P. J. Stiles, and S. v. Molnar, “Magnetointernal Field Emission in Junctions of Magnetic Insulators”, Phys. Rev. Lett. **19**, 852 (1967).

[13] P. M. Tedrow and R. Meservey, “Spin-Dependent Tunneling into Ferromagnetic Nickel”, Phys. Rev. Lett. **26**, 192 (1971).

[14] R. Meservey and P. Tedrow, “Spin-polarized electron tunneling”, Phys. Rep. **238**, 173 (1994).

[15] M. Julliere, “Tunneling between ferromagnetic films”, Phys. Lett. A **54**, 225 (1975).

[16] A. Fert and P. Grünberg, *The Nobel Prize in Physics 2007*, (2007) `https://www.nobelprize.org/prizes/physics/2007/summary/`.

[17] M. N. Baibich et al., “Giant Magnetoresistance of (001)Fe/(001)Cr Magnetic Superlattices”, Phys. Rev. Lett. **61**, 2472 (1988).

[18] G. Binasch et al., "Enhanced magnetoresistance in layered magnetic structures with antiferromagnetic interlayer exchange", Phys. Rev. B **39**, 4828 (1989).

[19] S. M. Thompson, "The discovery, development and future of GMR: The Nobel Prize 2007", J. Phys. D: Appl. Phys. **41**, 093001 (2008).

[20] J. C. Slonczewski, "Current-driven excitation of magnetic multilayers", J. Magn. Magn. Mater. **159**, L1 (1996).

[21] Y. Zhang et al., "Spintronics for low-power computing", in Des. autom. test eur. conf. exhib. (date) (2014).

[22] IBM, *20th century disk storage chronology*, (2003) `https://www.ibm.com/ibm/history/exhibits/storage/storage_chrono20b.html`.

[23] B. Dieny et al., "Opportunities and challenges for spintronics in the microelectronic industry", Nature Electronics **3**, 446 (2020).

[24] G. Schmidt et al., "Fundamental obstacle for electrical spin injection from a ferromagnetic metal into a diffusive semiconductor", Phys. Rev. B **62**, R4790 (2000).

[25] I. Appelbaum, B. Huang, and D. J. Monsma, "Electronic measurement and control of spin transport in silicon", Nature **447**, 295 (2007).

[26] T. Taniyama et al., "Electrical and optical spin injection in ferromagnet/semiconductor heterostructures", NPG Asia Mater. **3**, 65 (2011).

[27] S. Takahashi, "Physical Principles of Spin Pumping", in *Handbook of spintronics* (Springer Netherlands, Dordrecht, 2016), p. 1445.

[28] M. Dyakonov and V. Perel, "Current-induced spin orientation of electrons in semiconductors", Phys. Lett. A **35**, 459 (1971).

[29] S. Datta and B. Das, "Electronic analog of the electro-optic modulator", Appl. Phys. Lett. **56**, 665 (1990).

[30] I. Zutic et al., "Proximitized materials", Mater. Today **22**, 85 (2019).

[31] M. Gmitra and J. Fabian, "Proximity Effects in Bilayer Graphene on Monolayer WSe_2: Field-Effect Spin Valley Locking, Spin-Orbit Valve, and Spin Transistor", Phys. Rev. Lett. **119**, 146401 (2017).

[32] Z. Wang et al., "Tunneling spin valves based on Fe_3GeTe_2/hBN/Fe_3GeTe_2 van der Waals heterostructures", Nano Lett. **18**, 4303 (2018).

[33] C. Schüller, *Lecture notes on Light Matter Interaction (University of Regensburg)*, 2019.

[34] A. K. Geim and I. V. Grigorieva, "Van der Waals heterostructures", Nature **499**, 419 (2013).

[35] A. H. Castro Neto et al., "The electronic properties of graphene", Rev. Mod. Phys. **81**, 109 (2009).

[36] M. J. Allen, V. C. Tung, and R. B. Kaner, "Honeycomb Carbon: A Review of Graphene", Chem. Rev. **110**, 132 (2010).

[37] J. de La Fuente, *Properties of Graphene*, (2019) `https://www.graphenea.com/pages/graphene-properties`.

[38] J. Wang, F. Ma, and M. Sun, “Graphene, hexagonal boron nitride, and their heterostructures: properties and applications”, RSC Adv. **7**, 16801 (2017).

[39] F. Schedin et al., “Detection of individual gas molecules adsorbed on graphene”, Nat. Mater. **6**, 652 (2007).

[40] H. Jang et al., “Graphene-Based Flexible and Stretchable Electronics”, Adv. Mater. **28**, 4184 (2016).

[41] K. Zhang et al., “Two dimensional hexagonal boron nitride (2D-hBN): synthesis, properties and applications”, J. Mater. Chem. C **5**, 11992 (2017).

[42] Y. J. Zhang et al., “2D crystals of transition metal dichalcogenide and their iontronic functionalities”, 2D Mater. **2**, 044004 (2015).

[43] A. Splendiani et al., “Emerging Photoluminescence in Monolayer MoS_2”, Nano Lett. **10**, 1271 (2010).

[44] K. F. Mak et al., “Atomically Thin MoS_2: A New Direct-Gap Semiconductor”, Phys. Rev. Lett. **105**, 136805 (2010).

[45] B. Sipos et al., “From Mott state to superconductivity in 1T-TaS_2”, Nat. Mater. **7**, 960 (2008).

[46] R. G. Dickinson and L. Pauling, “The Crystal Structure of Molybdenite”, J. Am. Chem. Soc. **45**, 1466 (1923).

[47] S. J. McDonnell and R. M. Wallace, “Atomically-thin layered films for device applications based upon 2D TMDC materials”, Thin Solid Films **616**, 482 (2016).

[48] K. Mak and J. Shan, “Photonics and optoelectronics of 2D semiconductor transition metal dichalcogenides”, Nat. Photonics **10**, 216 (2016).

[49] D. Jariwala et al., “Emerging device applications for semiconducting two-dimensional transition metal dichalcogenides”, ACS nano **8**, 1102 (2014).

[50] W. Zhang et al., “Van der Waals magnets: Wonder building blocks for two-dimensional spintronics?”, InfoMat **1**, 479 (2019).

[51] M. Gibertini et al., “Magnetic 2D materials and heterostructures”, Nat. Nanotechnol. **14**, 408 (2019).

[52] C. Gong and X. Zhang, “Two-dimensional magnetic crystals and emergent heterostructure devices”, Science **363**, eaav4450 (2019).

[53] M.-C. Wang et al., “Prospects and Opportunities of 2D van der Waals Magnetic Systems”, Ann. Phys. **532**, 1900452 (2020).

[54] N. D. Mermin and H. Wagner, “Absence of Ferromagnetism or Antiferromagnetism in One- or Two-Dimensional Isotropic Heisenberg Models”, Phys. Rev. Lett. **17**, 1133 (1966).

[55] M. A. McGuire et al., “Coupling of crystal structure and magnetism in the layered, ferromagnetic insulator CrI_3”, Chem. Mater. **27**, 612 (2015).

[56] M. Yi and Z. Shen, “A review on mechanical exfoliation for the scalable production of graphene”, J. Mater. Chem. A **3**, 11700 (2015).

[57] K. S. Novoselov et al., "Two-dimensional atomic crystals", PNAS **102**, 10451 (2005).

[58] V. Nicolosi et al., "Liquid Exfoliation of Layered Materials", Science **340**, 1226419 (2013).

[59] Y. Xu et al., "Liquid-Phase exfoliation of graphene: An overview on exfoliation media, techniques, and challenges", Nanomaterials **8**, 942 (2018).

[60] A. Ciesielski and P. Samori, "Graphene via sonication assisted liquid-phase exfoliation", Chem. Soc. Rev. **43**, 381 (2014).

[61] Z. Cai et al., "Chemical Vapor Deposition Growth and Applications of Two-Dimensional Materials and Their Heterostructures", Chem. Rev. **118**, 6091 (2018).

[62] J.-O. Carlsson and P. M. Martin, "Chapter 7 - Chemical Vapor Deposition", in *Handbook of deposition technologies for films and coatings (third edition)* (William Andrew Publishing, Boston, 2010), p. 314.

[63] J. Yu et al., "Synthesis of high quality two-dimensional materials via chemical vapor deposition", Chem. Sci. **6**, 6705 (2015).

[64] S. Bae et al., "Roll-to-roll production of 30-inch graphene films for transparent electrodes", Nat. Nanotechnol. **5**, 574 (2010).

[65] L. A. Walsh and C. L. Hinkle, "Van der Waals epitaxy: 2D materials and topological insulators", Appl. Mater. Today **9**, 504 (2017).

[66] M. Nakano et al., "Layer-by-Layer Epitaxial Growth of Scalable WSe_2 on Sapphire by Molecular Beam Epitaxy", Nano Lett. **17**, 5595 (2017).

[67] R. Yue et al., "$HfSe_2$ Thin Films: 2D Transition Metal Dichalcogenides Grown by Molecular Beam Epitaxy", ACS Nano **9**, 474 (2015).

[68] M. Mattinen et al., "Van der Waals epitaxy of continuous thin films of 2D materials using atomic layer deposition in low temperature and low vacuum conditions", 2D Mater. **7**, 011003 (2019).

[69] A. Summerfield et al., "Strain-Engineered Graphene Grown on Hexagonal Boron Nitride by Molecular Beam Epitaxy", Sci. Rep. **6**, 22440 (2016).

[70] Y.-J. Cho et al., "Hexagonal Boron Nitride Tunnel Barriers Grown on Graphite by High Temperature Molecular Beam Epitaxy", Sci. Rep. **6**, 34474 (2016).

[71] K. S. Novoselov and A. H. C. Neto, "Two-dimensional crystals-based heterostructures: materials with tailored properties", Physica Scripta **T146**, 014006 (2012).

[72] P. Bøggild, "The war on fake graphene", Nature **562**, 502 (2018).

[73] N. Briggs et al., "A roadmap for electronic grade 2D materials", 2D Mater. **6**, 022001 (2019).

[74] Y.-M. Lin et al., "100-GHz Transistors from Wafer-Scale Epitaxial Graphene", Science **327**, 662 (2010).

[75] N. Waldron, "Chapter 7 - III-V Devices and Technology for CMOS", in *High Mobility Materials for CMOS Applications*, Woodhead Publishing Series in Electronic and Optical Materials (Woodhead Publishing, 2018), p. 231.

[76] F. Schwierz, J. Pezoldt, and R. Granzner, "Two-dimensional materials and their prospects in transistor electronics", Nanoscale **7**, 8261 (2015).

[77] L. Banszerus et al., "Ultrahigh-mobility graphene devices from chemical vapor deposition on reusable copper", Sci. Adv. **1**, 1500222 (2015).

[78] L. Banszerus et al., "Extraordinary high room-temperature carrier mobility in graphene/WSe_2 heterostructures", arXiv:1909.09523 (2019).

[79] E. H. Hwang and S. Das Sarma, "Acoustic phonon scattering limited carrier mobility in two-dimensional extrinsic graphene", Phys. Rev. B **77**, 115449 (2008).

[80] H. Lyu et al., "Deep-submicron Graphene Field-Effect Transistors with State-of-Art f_{max}", Sci. Rep. **6**, 35717 (2016).

[81] M. Bonmann et al., "Graphene Field-Effect Transistors With High Extrinsic f_T and f_{max}", IEEE Electron Device Letters **40**, 131 (2018).

[82] M. Houssa, A. Dimoulas, and A. Molle, *2D Materials for Nanoelectronics*, Series in Materials Science and Engineering (CRC Press, 2016).

[83] H. Liu et al., "Semiconducting black phosphorus: synthesis, transport properties and electronic applications", Chem. Soc. Rev. **44**, 2732 (2015).

[84] A. Castellanos-Gomez, "Black phosphorus: narrow gap, wide applications", J. Phys. Chem. Lett. **6**, 4280 (2015).

[85] W. Zhu et al., "Flexible black phosphorus ambipolar transistors, circuits and AM demodulator", Nano Lett. **15**, 1883 (2015).

[86] M. Akhtar et al., "Recent advances in synthesis, properties, and applications of phosphorene", npj 2D Mater. Appl. **1**, 5 (2017).

[87] M. Z. Rahman et al., "2D phosphorene as a water splitting photocatalyst: fundamentals to applications", Energy Environ. Sci. **9**, 709 (2016).

[88] M. Gmitra and J. Fabian, "Graphene on transition-metal dichalcogenides: A platform for proximity spin-orbit physics and optospintronics", Phys. Rev. B **92**, 155403 (2015).

[89] F. Herling et al., "Gate tunability of highly efficient spin-to-charge conversion by spin Hall effect in graphene proximitized with WSe_2", APL Mater. **8**, 071103 (2020).

[90] S. Jiang et al., "Spin tunnel field-effect transistors based on two-dimensional van der Waals heterostructures", Nat. Electronics **2**, 159 (2019).

[91] S. Manzeli et al., "2D transition metal dichalcogenides", Nat. Rev. Mater. **2**, 17033 (2017).

[92] S. A. Vitale et al., "Valleytronics: Opportunities, Challenges, and Paths Forward", Small **14**, 1801483 (2018).

[93] K. Thakar and S. Lodha, "Optoelectronic and photonic devices based on transition metal dichalcogenides", Materials Research Express **7**, 014002 (2020).

[94] A. Krasnok, S. Lepeshov, and A. Alú, "Nanophotonics with 2D transition metal dichalcogenides", Opt. Express **26**, 15972 (2018).

[95] H. Li, S. Ruan, and Y.-J. Zeng, "Intrinsic Van Der Waals Magnetic Materials from Bulk to the 2D Limit: New Frontiers of Spintronics", Adv. Mater. **31**, 1900065 (2019).

[96] T. Song et al., "Giant tunneling magnetoresistance in spin-filter van der Waals heterostructures", Science **360**, 1214 (2018).

[97] R. Holm and W. Meissner, "Messungen mit Hilfe von flüssigem Helium. XIII", Z. Phys. **74**, 715 (1932).

[98] K. Dolui et al., "Proximity Spin-Orbit Torque on a Two-Dimensional Magnet within van der Waals Heterostructure: Current-Driven Antiferromagnet-to-Ferromagnet Reversible Nonequilibrium Phase Transition in Bilayer CrI_3", Nano Lett. **20**, 2288 (2020).

[99] A. Avsar et al., "Optospintronics in Graphene via Proximity Coupling", ACS Nano **11**, 11678 (2017).

[100] A. W. Cummings et al., "Giant Spin Lifetime Anisotropy in Graphene Induced by Proximity Effects", Phys. Rev. Lett. **119**, 206601 (2017).

[101] T. S. Ghiasi et al., "Charge-to-Spin Conversion by the Rashba–Edelstein Effect in Two-Dimensional van der Waals Heterostructures up to Room Temperature", Nano Lett. **19**, 5959 (2019).

[102] L. A. Benitez et al., "Tunable room-temperature spin galvanic and spin Hall effects in van der Waals heterostructures", Nat. Mater. **19**, 170 (2020).

[103] A. M. Hoque et al., "All-electrical creation and control of giant spin-galvanic effect in 1T-$MoTe_2$/graphene heterostructures at room temperature", arXiv:1908.09367 (2019).

[104] Y. Chen et al., "High-Performance Photovoltaic Detector Based on $MoTe_2$/MoS_2 Van der Waals Heterostructure", Small **14**, 1703293 (2018).

[105] S. Kang et al., "2D semiconducting materials for electronic and optoelectronic applications: potential and challenge", 2D Mater. **7**, 022003 (2020).

[106] C.-H. Lee et al., "Atomically thin p-n junctions with van der Waals heterointerfaces", Nat. Nanotechnol. **9**, 676 (2014).

[107] N. Petrone et al., "Chemical vapor deposition-derived graphene with electrical performance of exfoliated graphene", Nano Lett. **12**, 2751 (2012).

[108] V. E. Calado et al., "Ballistic transport in graphene grown by chemical vapor deposition", Appl. Phys. Lett. **104**, 023103 (2014).

[109] C. Soldano, A. Mahmood, and E. Dujardin, "Production, properties and potential of graphene", Carbon **48**, 2127 (2010).

[110] M. Losurdo et al., "Graphene CVD growth on copper and nickel: role of hydrogen in kinetics and structure", Phys. Chem. Chem. Phys. **13**, 20836 (2011).

[111] M. Gmitra et al., "Band-structure topologies of graphene: Spin-orbit coupling effects from first principles", Phys. Rev. B **80**, 235431 (2009).

[112] D. Kochan, S. Irmer, and J. Fabian, "Model spin-orbit coupling Hamiltonians for graphene systems", Phys. Rev. B **95**, 165415 (2017).

[113] D. R. Cooper et al., “Experimental Review of Graphene”, ISRN Cond. Mat. Phys. **2012**, 501686 (2012).

[114] D. Kochan, M. Gmitra, and J. Fabian, “Spin Relaxation Mechanism in Graphene: Resonant Scattering by Magnetic Impurities”, Phys. Rev. Lett. **112**, 116602 (2014).

[115] T. Frank, M. Gmitra, and J. Fabian, “Theory of electronic and spin-orbit proximity effects in graphene on Cu(111)”, Phys. Rev. B **93**, 155142 (2016).

[116] T. Frank et al., “Copper adatoms on graphene: Theory of orbital and spin-orbital effects”, Phys. Rev. B **95**, 035402 (2017).

[117] M. Gmitra, D. Kochan, and J. Fabian, “Spin-Orbit Coupling in Hydrogenated Graphene”, Phys. Rev. Lett. **110**, 246602 (2013).

[118] C. L. Kane and E. J. Mele, “Quantum Spin hall effect in graphene”, Phys. Rev. Lett. **95**, 226801 (2005).

[119] D. Huertas-Hernando, F. Guinea, and A. Brataas, “Spin-orbit coupling in curved graphene, fullerenes, nanotubes, and nanotube caps”, Phys. Rev. B **74**, 155426 (2006).

[120] C. Ertler et al., “Electron spin relaxation in graphene: The role of the substrate”, Phys. Rev. B **80**, 041405 (2009).

[121] D. Pesin and A. H. MacDonald, “Spintronics and pseudospintronics in graphene and topological insulators”, Nat. Mater. **11**, 409 (2012).

[122] H. Min et al., “Intrinsic and Rashba spin-orbit interactions in graphene sheets”, Phys. Rev. B **74**, 165310 (2006).

[123] V. K. Dugaev, E. Y. Sherman, and J. Barnas, “Spin dephasing and pumping in graphene due to random spin-orbit interaction”, Phys. Rev. B **83**, 085306 (2011).

[124] D. Huertas-Hernando, F. Guinea, and A. Brataas, “Spin-Orbit-Mediated Spin Relaxation in Graphene”, Phys. Rev. Lett. **103**, 146801 (2009).

[125] W. Han et al., “Tunneling Spin Injection into Single Layer Graphene”, Phys. Rev. Lett. **105**, 167202 (2010).

[126] M. Popinciuc et al., “Electronic spin transport in graphene field-effect transistors”, Phys. Rev. B **80**, 214427 (2009).

[127] W. Han and R. K. Kawakami, “Spin Relaxation in Single-Layer and Bilayer Graphene”, Phys. Rev. Lett. **107**, 047207 (2011).

[128] W. Han et al., “Spin relaxation in single-layer graphene with tunable mobility”, Nano Lett. **12**, 3443 (2012).

[129] X. F. Fan et al., “Interaction between graphene and the surface of SiO_2”, J. Phys.: Cond. Mat. **24**, 305004 (2012).

[130] W. Gao et al., “Interfacial adhesion between graphene and silicon dioxide by density functional theory with van der Waals corrections”, J. Phys. D: Appl. Phys. **47**, 255301 (2014).

[131] Y. J. Kang, J. Kang, and K. J. Chang, “Electronic structure of graphene and doping effect on SiO_2”, Phys. Rev. B **78**, 115404 (2008).

[132] L. Wang et al., “One-dimensional electrical contact to a two-dimensional material”, Science **342**, 614 (2013).

[133] T. Maassen et al., “Comparison between charge and spin transport in few-layer graphene”, Phys. Rev. B **83**, 115410 (2011).

[134] T.-. Y. Yang et al., “Observation of Long Spin-Relaxation Times in Bilayer Graphene at Room Temperature”, Phys. Rev. Lett. **107**, 047206 (2011).

[135] N. Tombros et al., “Electronic spin transport and spin precession in single graphene layers at room temperature”, Nature **448**, 571 (2007).

[136] H. González-Herrero et al., “Atomic-scale control of graphene magnetism by using hydrogen atoms”, Science **352**, 437 (2016).

[137] J. C. Boettger and S. B. Trickey, “First-principles calculation of the spin-orbit splitting in graphene”, Phys. Rev. B **75**, 121402 (2007).

[138] S. Konschuh, M. Gmitra, and J. Fabian, “Tight-binding theory of the spin-orbit coupling in graphene”, Phys. Rev. B **82**, 245412 (2010).

[139] J. Sichau et al., “Resonance Microwave Measurements of an Intrinsic Spin-Orbit Coupling Gap in Graphene: A Possible Indication of a Topological State”, Phys. Rev. Lett. **122**, 046403 (2019).

[140] M. Gmitra et al., “Trivial and inverted Dirac bands and the emergence of quantum spin Hall states in graphene on transition-metal dichalcogenides”, Phys. Rev. B **93**, 155104 (2016).

[141] K. Zollner et al., “Theory of proximity-induced exchange coupling in graphene on hBN/(Co, Ni)”, Phys. Rev. B **94**, 155441 (2016).

[142] K. Zollner, M. Gmitra, and J. Fabian, “Heterostructures of graphene and hBN: Electronic, spin-orbit, and spin relaxation properties from first principles”, Phys. Rev. B **99**, 125151 (2019).

[143] D. Di Sante et al., “Towards topological quasifreestanding stanene via substrate engineering”, Phys. Rev. B **99**, 035145 (2019).

[144] C. L. Kane and E. J. Mele, “Z2 topological order and the quantum spin hall effect”, Phys. Rev. Lett. **95**, 146802 (2005).

[145] S. Irmer, “Theoretical investigations of orbital and spin-orbital effects in functionalized graphene”, PhD thesis (University of Regensburg, 2018).

[146] V. T. Phong, N. R. Walet, and F. Guinea, “Effective interactions in a graphene layer induced by the proximity to a ferromagnet”, 2D Mater. **5**, 014004 (2017).

[147] T. Frank et al., “Protected Pseudohelical Edge States in $\mathbb{Z}_2$-Trivial Proximitized Graphene”, Phys. Rev. Lett. **120**, 156402 (2018).

[148] J. Zhang et al., “Robust quantum anomalous Hall effect in graphene-based van der Waals heterostructures”, Phys. Rev. B **92**, 165418 (2015).

[149] Z. Qiao et al., “Quantum Anomalous Hall Effect in Graphene Proximity Coupled to an Antiferromagnetic Insulator”, Phys. Rev. Lett. **112**, 116404 (2014).

[150] J. Zhang et al., “Strong magnetization and Chern insulators in compressed graphene/CrI_3 van der Waals heterostructures”, Phys. Rev. B **97**, 085401 (2018).

[151] P. Högl et al., “Quantum anomalous hall effects in graphene from proximity-induced uniform and staggered spin-orbit and exchange coupling”, Phys. Rev. Lett. **124**, 136403 (2020).

[152] J. C. Leutenantsmeyer et al., “Proximity induced room temperature ferromagnetism in graphene probed with spin currents”, 2D Mater. **4**, 014001 (2016).

[153] K. Zollner et al., “Scattering-induced and highly tunable by gate damping-like spin-orbit torque in graphene doubly proximitized by two-dimensional magnet $Cr_2Ge_2Te_6$ and monolayer WS_2”, Phys. Rev. Research **2**, 043057 (2020).

[154] W. Han et al., “Graphene spintronics”, Nat. Nanotechnol. **9**, 794 (2014).

[155] D. Van Tuan et al., “Spin dynamics and relaxation in graphene dictated by electron-hole puddles”, Sci. Rep. **6**, 21046 (2016).

[156] J. Martin et al., “Observation of electron–hole puddles in graphene using a scanning single-electron transistor”, Nat. Phys. **4**, 144 (2008).

[157] J. Sabio et al., “Electrostatic interactions between graphene layers and their environment”, Phys. Rev. B **77**, 195409 (2008).

[158] J.-H. Chen et al., “Charged-impurity scattering in graphene”, Nat. Phys. **4**, 377 (2008).

[159] B. Raes et al., “Determination of the spin-lifetime anisotropy in graphene using oblique spin precession”, Nat. Commun. **7**, 11444 (2016).

[160] S. Ringer et al., “Measuring anisotropic spin relaxation in graphene”, Phys. Rev. B **97**, 205439 (2018).

[161] T. Zhu and R. K. Kawakami, “Modeling the oblique spin precession in lateral spin valves for accurate determination of the spin lifetime anisotropy: Effect of finite contact resistance and channel length”, Phys. Rev. B **97**, 144413 (2018).

[162] S. Irmer et al., “Resonant scattering due to adatoms in graphene: Top, bridge, and hollow positions”, Phys. Rev. B **97**, 075417 (2018).

[163] V. Miranda, E. Mucciolo, and C. Lewenkopf, “Spin relaxation in disordered graphene: Interplay between puddles and defect-induced magnetism”, J. Phys. Chem. Solids **128**, 169 (2019).

[164] T. S. Ghiasi et al., “Large Proximity-Induced Spin Lifetime Anisotropy in Transition-Metal Dichalcogenide/Graphene Heterostructures”, Nano Lett. **17**, 7528 (2017).

[165] S. Zihlmann et al., “Large spin relaxation anisotropy and valley-Zeeman spin-orbit coupling in WSe_2/graphene/*h*-BN heterostructures”, Phys. Rev. B **97**, 075434 (2018).

[166] M. H. D. Guimaraes et al., “Spin Transport in High-Quality Suspended Graphene Devices”, Nano Lett. **12**, 3512 (2012).

[167] X. Du et al., “Approaching ballistic transport in suspended graphene”, Nat. Nanotechnol. **3**, 491 (2008).

[168] W. Bao et al., “Controlled ripple texturing of suspended graphene and ultrathin graphite membranes”, Nat. Nanotechnol. **4**, 562 (2009).

[169] S. Roche et al., “Graphene spintronics: the European Flagship perspective”, 2D Mater. **2**, 030202 (2015).

[170] M. V. Kamalakar et al., “Spintronics with graphene-hexagonal boron nitride van der Waals heterostructures”, Appl. Phys. Lett. **105**, 212405 (2014).

[171] M. Gurram, S. Omar, and B. J. van Wees, “Electrical spin injection, transport, and detection in graphene-hexagonal boron nitride van der Waals heterostructures: progress and perspectives”, 2D Mater. **5**, 032004 (2018).

[172] M. H. D. Guimaraes et al., “Controlling Spin Relaxation in Hexagonal BN-Encapsulated Graphene with a Transverse Electric Field”, Phys. Rev. Lett. **113**, 086602 (2014).

[173] S. Singh et al., “Nanosecond spin relaxation times in single layer graphene spin valves with hexagonal boron nitride tunnel barriers”, Appl. Phys. Lett. **109**, 122411 (2016).

[174] M. Drögeler et al., “Spin Lifetimes Exceeding 12 ns in Graphene Nonlocal Spin Valve Devices”, Nano Lett. **16**, 3533 (2016).

[175] M. Drögeler et al., “Simulations on the Influence of Spatially Varying Spin Transport Parameters on the Measured Spin Lifetime in Graphene Non-Local Spin Valves”, PSS (B) **254**, 1700293 (2017).

[176] P. J. Zomer et al., “Long-distance spin transport in high-mobility graphene on hexagonal boron nitride”, Phys. Rev. B **86**, 161416 (2012).

[177] J. Ingla-Aynés et al., “$24-\mu$m spin relaxation length in boron nitride encapsulated bilayer graphene”, Phys. Rev. B **92**, 201410 (2015).

[178] M. Drögeler et al., “Nanosecond Spin Lifetimes in Single- and Few-Layer Graphene/hBN Heterostructures at Room Temperature”, Nano Lett. **14**, 6050 (2014).

[179] C. Dean et al., “Graphene based heterostructures”, Solid State Commun. **152**, 1275 (2012).

[180] C. R. Dean et al., “Boron nitride substrates for high-quality graphene electronics”, Nat. Nanotechnol. **5**, 722 (2010).

[181] J. Xue et al., “Scanning tunnelling microscopy and spectroscopy of ultra-flat graphene on hexagonal boron nitride”, Nat. Mater. **10**, 282 (2011).

[182] N. Mishra et al., “Rapid and catalyst-free van der Waals epitaxy of graphene on hexagonal boron nitride”, Carbon N. Y. **96**, 497 (2016).

[183] S. Tang et al., “Precisely aligned graphene grown on hexagonal boron nitride by catalyst free chemical vapor deposition”, Sci. Rep. **3**, 2666 (2013).

[184] H. Arjmandi-Tash et al., “Large scale graphene/h-BN heterostructures obtained by direct CVD growth of graphene using high-yield proximity-catalytic process”, J. Phys. Mater. **1**, 015003 (2018).

[185] P. J. Zomer et al., “A transfer technique for high mobility graphene devices on commercially available hexagonal boron nitride”, Appl. Phys. Lett. **99**, 2009 (2011).

[186] M. Gurram et al., “Spin transport in fully hexagonal boron nitride encapsulated graphene”, Phys. Rev. B **93**, 115441 (2016).

[187] A. S. Mayorov et al., “Micrometer-scale ballistic transport in encapsulated graphene at room temperature”, Nano Lett. **11**, 2396 (2011).

[188] M. Gurram, S. Omar, and B. J. van Wees, “Bias induced up to 100% spin-injection and detection polarizations in ferromagnet/bilayer-hBN/graphene/hBN heterostructures”, Nat. Commun. **8**, 248 (2017).

[189] M. Gurram et al., “Spin transport in two-layer-CVD-hBN/graphene/hBN heterostructures”, Phys. Rev. B **97**, 045411 (2018).

[190] L. Britnell et al., “Field-Effect Tunneling Transistor Based on Vertical Graphene Heterostructures”, Science **335**, 947 (2012).

[191] J. Wang et al., “Magnetics and spintronics on two-dimensional composite materials of graphene/hexagonal boron nitride”, Mater. Today Phys. **3**, 93 (2017).

[192] C. C. Lin et al., “Spin transfer torque in a graphene lateral spin valve assisted by an external magnetic field”, Nano Lett. **13**, 5177 (2013).

[193] C. C. Lin et al., “Improvement of spin transfer torque in asymmetric graphene devices”, ACS Nano **8**, 3807 (2014).

[194] Y. K. Luo et al., “Opto-valleytronic spin injection in monolayer MoS_2/few-layer graphene hybrid spin valves”, Nano Lett. **17**, 3877 (2017).

[195] H. Wen et al., “Experimental Demonstration of xor Operation in Graphene Magnetologic Gates at Room Temperature”, Phys. Rev. Appl. **5**, 044003 (2016).

[196] I. Zutic, J. Fabian, and S. C. Erwin, “Bipolar spintronics: Fundamentals and applications”, IBM J. Res. Dev. **50**, 121 (2006).

[197] B. Behin-Aein et al., “Proposal for an all-spin logic device with built-in memory”, Nat. Nano. **5**, 266 (2010).

[198] A. Catellani et al., “Bulk and surface electronic structure of hexagonal boron nitride”, Phys. Rev. B **36**, 6105 (1987).

[199] G. Giovannetti et al., “Substrate-induced band gap in graphene on hexagonal boron nitride: Ab initio density functional calculations”, Phys. Rev. B **76**, 073103 (2007).

[200] J. Jung et al., “Ab initio theory of moire superlattice bands in layered two-dimensional materials”, Phys. Rev. B **89**, 205414 (2014).

[201] P. Moon and M. Koshino, “Electronic properties of graphene/hexagonal-boron-nitride moiré superlattice”, Phys. Rev. B **90**, 155406 (2014).

[202] G. Argentero et al., “Unraveling the 3D Atomic Structure of a Suspended Graphene/hBN van der Waals Heterostructure”, Nano Lett. **17**, 1409 (2017).

[203] R. Quhe et al., “Tunable and sizable band gap of single-layer graphene sandwiched between hexagonal boron nitride”, NPG Asia Mater. **4**, e6 (2012).

[204] P. Hohenberg and W. Kohn, “Inhomogeneous Electron Gas”, Phys. Rev. **136**, B864 (1964).

[205] P. Blaha et al., *WIEN2K, an augmented plane wave + local orbitals program for calculating crystal properties* (Prof. Dr. Karlheinz Schwarz, Vienna University of Technology, Institute of Materials Chemistry, Wien, Austria, 2001).

[206] J. P. Perdew, K. Burke, and M. Ernzerhof, "Generalized Gradient Approximation Made Simple", Phys. Rev. Lett. **77**, 3865 (1996).

[207] S. Grimme et al., "A consistent and accurate ab initio parametrization of density functional dispersion correction (DFT-D) for the 94 elements H-Pu", J. Chem. Phys. **132**, 154104 (2010).

[208] H. Tang et al., "Density functionals combined with van der waals corrections for graphene adsorbed on layered materials", Phys. Rev. B **101**, 195426 (2020).

[209] D. L. Miller et al., "Real-space mapping of magnetically quantized graphene states", Nat. Phys. **6**, 811 (2010).

[210] B. Hunt et al., "Massive dirac fermions and hofstadter butterfly in a van der Waals heterostructure", Science **340**, 1427 (2013).

[211] M. Kindermann, B. Uchoa, and D. L. Miller, "Zero-energy modes and gate-tunable gap in graphene on hexagonal boron nitride", Phys. Rev. B **86**, 115415 (2012).

[212] M. Yankowitz et al., "Dynamic band-structure tuning of graphene moiré superlattices with pressure", Nature **557**, 404 (2018).

[213] J. C. Leutenantsmeyer et al., "Observation of Spin-Valley-Coupling-Induced Large Spin-Lifetime Anisotropy in Bilayer Graphene", Phys. Rev. Lett. **121**, 127702 (2018).

[214] J. Xu et al., "Strong and Tunable Spin-Lifetime Anisotropy in Dual-Gated Bilayer Graphene", Phys. Rev. Lett. **121**, 127703 (2018).

[215] S. Omar, B. N. Madhushankar, and B. J. van Wees, "Large spin-relaxation anisotropy in bilayer-graphene/WS_2 heterostructures", Phys. Rev. B **100**, 155415 (2019).

[216] S. Omar and B. J. van Wees, "Spin transport in high-mobility graphene on WS_2 substrate with electric-field tunable proximity spin-orbit interaction", Phys. Rev. B **97**, 045414 (2018).

[217] S. Konschuh et al., "Theory of spin-orbit coupling in bilayer graphene", Phys. Rev. B **85**, 115423 (2012).

[218] K. Song et al., "Spin Proximity Effects in Graphene/Topological Insulator Heterostructures", Nano Lett. **18**, 2033 (2018).

[219] J. H. Garcia et al., "Spin transport in graphene/transition metal dichalcogenide heterostructures", Chem. Soc. Rev. **47**, 3359 (2018).

[220] B. Raes et al., "Spin precession in anisotropic media", Phys. Rev. B **95**, 085403 (2017).

[221] N. Tombros et al., "Anisotropic Spin Relaxation in Graphene", Phys. Rev. Lett. **101**, 046601 (2008).

[222] L. Banszerus et al., "Observation of the Spin-Orbit Gap in Bilayer Graphene by One-Dimensional Ballistic Transport", Phys. Rev. Lett. **124**, 177701 (2020).

[223] K. S. Novoselov et al., “2D materials and van der Waals heterostructures”, Science **353**, aac9439 (2016).

[224] D. L. Duong, S. J. Yun, and Y. H. Lee, “Van der Waals Layered Materials: Opportunities and Challenges”, ACS Nano **11**, 11803 (2017).

[225] H. Zhang et al., “Topological insulators in Bi_2Se_3, Bi_2Te_3 and Sb_2Te_3 with a single Dirac cone on the surface”, Nat. Phys. **5**, 438 (2009).

[226] D. Hsieh et al., “A tunable topological insulator in the spin helical Dirac transport regime”, Nature **460**, 1101 (2009).

[227] M. Z. Hasan and C. L. Kane, “Colloquium: Topological insulators”, Rev. Mod. Phys. **82**, 3045 (2010).

[228] T. Zhang et al., “Experimental Demonstration of Topological Surface States Protected by Time-Reversal Symmetry”, Phys. Rev. Lett. **103**, 266803 (2009).

[229] N. Koirala et al., “Record Surface State Mobility and Quantum Hall Effect in Topological Insulator Thin Films via Interface Engineering”, Nano Lett. **15**, 8245 (2015).

[230] Y. Zhang et al., “Crossover of the three-dimensional topological insulator Bi_2Se_3 to the two-dimensional limit”, Nat. Phys. **6**, 584 (2010).

[231] C.-X. Liu et al., “Oscillatory crossover from two-dimensional to three-dimensional topological insulators”, Phys. Rev. B **81**, 041307 (2010).

[232] O. V. Yazyev, J. E. Moore, and S. G. Louie, “Spin Polarization and Transport of Surface States in the Topological Insulators Bi_2Se_3 and Bi_2Te_3 from First Principles”, Phys. Rev. Lett. **105**, 266806 (2010).

[233] K. Park et al., “Robustness of Topologically Protected Surface States in Layering of Bi_2Te_3 Thin Films”, Phys. Rev. Lett. **105**, 186801 (2010).

[234] S.-Y. Xu et al., “Hedgehog spin texture and Berry’s phase tuning in a magnetic topological insulator”, Nat. Phys. **8**, 616 (2012).

[235] Y. L. Chen et al., “Massive Dirac Fermion on the Surface of a Magnetically Doped Topological Insulator”, Science **329**, 659 (2010).

[236] R. Yu et al., “Quantized Anomalous Hall Effect in Magnetic Topological Insulators”, Science **329**, 61 (2010).

[237] C.-Z. Chang et al., “Experimental Observation of the Quantum Anomalous Hall Effect in a Magnetic Topological Insulator”, Science **340**, 167 (2013).

[238] S. V. Eremeev et al., “Magnetic proximity effect at the three-dimensional topological insulator/magnetic insulator interface”, Phys. Rev. B **88**, 144430 (2013).

[239] A. T. Lee, M. J. Han, and K. Park, “Magnetic proximity effect and spin-orbital texture at the Bi_2Se_3/EuS interface”, Phys. Rev. B **90**, 155103 (2014).

[240] Y. Hou and R. Wu, “Axion Insulator State in a Ferromagnet/Topological Insulator/Antiferromagnet Heterostructure”, Nano Lett. **19**, 2472 (2019).

[241] X.-L. Qi, T. L. Hughes, and S.-C. Zhang, “Topological field theory of time-reversal invariant insulators”, Phys. Rev. B **78**, 195424 (2008).

[242] M. Mogi et al., “A magnetic heterostructure of topological insulators as a candidate for an axion insulator”, Nat. Mater. **16**, 516 (2017).

[243] Q. L. He et al., “Chiral Majorana fermion modes in a quantum anomalous Hall insulator-superconductor structure”, Science **357**, 294 (2017).

[244] L. Fu and C. L. Kane, “Superconducting proximity effect and majorana fermions at the surface of a topological insulator”, Phys. Rev. Lett. **100**, 096407 (2008).

[245] M. He, H. Sun, and Q. L. He, “Topological insulator: spintronics and quantum computations”, Front. Phys. **14**, 43401 (2019).

[246] B. Lian et al., “Topological quantum computation based on chiral Majorana fermions”, PNAS **115**, 10938 (2018).

[247] D. Khokhriakov et al., “Tailoring emergent spin phenomena in Dirac material heterostructures”, Sci. Adv. **4**, eaat9349 (2018).

[248] S. Jafarpisheh et al., “Proximity-induced spin-orbit coupling in graphene/$Bi_{1.5}Sb_{0.5}Te_{1.7}Se_{1.3}$ heterostructures”, Phys. Rev. B **98**, 241402 (2018).

[249] J. Zhang, C. Triola, and E. Rossi, “Proximity Effect in Graphene/Topological-Insulator Heterostructures”, Phys. Rev. Lett. **112**, 096802 (2014).

[250] A. Zalic, T. Dvir, and H. Steinberg, “High-density carriers at a strongly coupled interface between graphene and a three-dimensional topological insulator”, Phys. Rev. B **96**, 075104 (2017).

[251] H. Steinberg et al., “Tunneling in graphene-topological insulator hybrid devices”, Phys. Rev. B **92**, 241409 (2015).

[252] C.-L. Song et al., “Topological insulator Bi_2Se_3 thin films grown on double-layer graphene by molecular beam epitaxy”, Appl. Phys. Lett. **97**, 143118 (2010).

[253] W. Dang et al., “Epitaxial heterostructures of ultrathin topological insulator nanoplate and graphene”, Nano Lett. **10**, 2870 (2010).

[254] P. Lee et al., “Proximity effect induced electronic properties of graphene on Bi_2Te_2Se”, Acs Nano **9**, 10861 (2015).

[255] L. Kou et al., “Proximity enhanced quantum spin Hall state in graphene”, Carbon **87**, 418 (2015).

[256] L. Kou et al., “Graphene-based topological insulator with an intrinsic bulk band gap above room temperature”, Nano Lett. **13**, 6251 (2013).

[257] M. Rodriguez-Vega et al., “Giant Edelstein effect in topological-insulator–graphene heterostructures”, Phys. Rev. B **96**, 235419 (2017).

[258] W. Cao et al., “Heavy Dirac fermions in a graphene/topological insulator heterojunction”, 2D Mater. **3**, 034006 (2016).

[259] H. Qiao et al., “Broadband photodetectors based on graphene–Bi_2Te_3 heterostructure”, ACS Nano **9**, 1886 (2015).

[260] S. Rajput et al., “Indirect interlayer bonding in graphene–topological insulator van der Waals heterostructure: Giant spin–orbit splitting of the graphene Dirac states”, ACS Nano **10**, 8450 (2016).

[261] K. Vaklinova et al., “Current-induced spin polarization in topological insulator–graphene heterostructures”, Nano Lett. **16**, 2595 (2016).

[262] I. Popov et al., “Proximity-induced topological state in graphene”, Phys. Rev. B **90**, 035418 (2014).

[263] D. Khokhriakov et al., “Gate-tunable spin-galvanic effect in graphene-topological insulator van der Waals heterostructures at room temperature”, Nat. Commun. **11**, 3657 (2020).

[264] B. Karpiak et al., “Magnetic proximity in a van der Waals heterostructure of magnetic insulator and graphene”, 2D Mater. **7**, 015026 (2019).

[265] S. R. Bahn and K. W. Jacobsen, “An object-oriented scripting interface to a legacy electronic structure code”, Comput. Sci. Eng. **4**, 56 (2002).

[266] S. Nakajima, “The crystal structure of $Bi_2Te_{3-x}Se_x$”, J. Phys. Chem. Solids **24**, 479 (1963).

[267] P. Giannozzi et al., “QUANTUM ESPRESSO: a modular and open-source software project for quantum simulations of materials”, J. Phys.: Cond. Mat. **21**, 395502 (2009).

[268] G. Kresse and D. Joubert, “From ultrasoft pseudopotentials to the projector augmented-wave method”, Phys. Rev. B **59**, 1758 (1999).

[269] S. Grimme, “Semiempirical GGA-type density functional constructed with a long-range dispersion correction”, J. Comput. Chem. **27**, 1787 (2006).

[270] V. Barone et al., “Role and effective treatment of dispersive forces in materials: Polyethylene and graphite crystals as test cases”, J. Comput. Chem. **30**, 934 (2009).

[271] L. Bengtsson, “Dipole correction for surface supercell calculations”, Phys. Rev. B **59**, 12301 (1999).

[272] C.-Y. Hou, C. Chamon, and C. Mudry, “Electron Fractionalization in Two-Dimensional Graphene-like Structures”, Phys. Rev. Lett. **98**, 186809 (2007).

[273] G. Giovannetti et al., “Kekulé textures, pseudospin-one Dirac cones, and quadratic band crossings in a graphene-hexagonal indium chalcogenide bilayer”, Phys. Rev. B **91**, 121417 (2015).

[274] Z. Lin et al., “Competing gap opening mechanisms of monolayer graphene and graphene nanoribbons on strong topological insulators”, Nano Lett. **17**, 4013 (2017).

[275] C. Gutiérrez et al., “Imaging chiral symmetry breaking from Kekulé bond order in graphene”, Nat. Phys. **12**, 950–958 (2016).

[276] Y. Ren et al., “Single-valley engineering in graphene superlattices”, Phys. Rev. B **91**, 245415 (2015).

[277] S. Basak et al., “Spin texture on the warped Dirac-cone surface states in topological insulators”, Phys. Rev. B **84**, 121401 (2011).

[278] M. Vanin et al., “Graphene on metals: A van der Waals density functional study”, Phys. Rev. B **81**, 081408 (2010).

[279] Z. Ren et al., "Optimizing $Bi_{2-x}Sb_xTe_{3-y}Se_y$ solid solutions to approach the intrinsic topological insulator regime", Phys. Rev. B **84**, 165311 (2011).

[280] T. Arakane et al., "Tunable Dirac cone in the topological insulator $Bi_{2-x}Sb_xTe_{3-y}Se_y$", Nat. Commun. **3**, 636 (2012).

[281] S. Carr et al., "Pressure dependence of the magic twist angle in graphene superlattices", Phys. Rev. B **98**, 085144 (2018).

[282] P. Xu et al., "New scanning tunneling microscopy technique enables systematic study of the unique electronic transition from graphite to graphene", Carbon **50**, 4633 (2012).

[283] C. Gong et al., "Discovery of intrinsic ferromagnetism in two-dimensional van der Waals crystals", Nature **546**, 265 (2017).

[284] B. Huang et al., "Layer-dependent ferromagnetism in a van der Waals crystal down to the monolayer limit", Nature **546**, 270 (2017).

[285] K. S. Burch, D. Mandrus, and J.-G. Park, "Magnetism in two-dimensional van der Waals materials", Nature **563**, 47 (2018).

[286] D. L. Cortie et al., "Two-Dimensional Magnets: Forgotten History and Recent Progress towards Spintronic Applications", Adv. Funct. Mater. **30**, 1901414 (2019).

[287] M. Alghamdi et al., "Highly Efficient Spin–Orbit Torque and Switching of Layered Ferromagnet Fe_3GeTe_2", Nano Lett. **19**, 4400 (2019).

[288] X. Wang et al., "Current-driven magnetization switching in a van der Waals ferromagnet Fe_3GeTe_2", Sci. Adv. **5**, eaaw8904 (2019).

[289] A. Kormányos et al., "K.P Theory for Two-Dimensional Transition Metal Dichalcogenide Semiconductors", 2D Mater. **2**, 022001 (2014).

[290] G.-B. Liu et al., "Electronic structures and theoretical modelling of two-dimensional group-VIB transition metal dichalcogenides", Chem. Soc. Rev. **44**, 2643 (2015).

[291] P. Tonndorf et al., "Photoluminescence emission and Raman response of monolayer MoS_2, $MoSe_2$, and WSe_2", Opt. Express **21**, 4908 (2013).

[292] S. Tongay et al., "Thermally driven crossover from indirect toward direct bandgap in 2D Semiconductors: $MoSe_2$ vs. MoS_2", Nano Lett. **12**, 5576 (2012).

[293] G. Eda et al., "Photoluminescence from chemically exfoliated MoS_2", Nano Lett. **11**, 5111 (2011).

[294] M. Yoshida et al., "Electrostatic and electrochemical tuning of superconductivity in two-dimensional $NbSe_2$ crystals", Appl. Phys. Lett. **108**, 202602 (2016).

[295] Y. Noat et al., "Quasiparticle spectra of $2H - NbSe_2$: Two-band superconductivity and the role of tunneling selectivity", Phys. Rev. B **92**, 134510 (2015).

[296] X. Zhu et al., "Signature of coexistence of superconductivity and ferromagnetism in two-dimensional $NbSe_2$ triggered by surface molecular adsorption", Nat. Commun. **7**, 11210 (2016).

[297] S.-Y. Xu et al., "Electrically switchable Berry curvature dipole in the monolayer topological insulator WTe_2", Nat. Phys. **14**, 900 (2018).

[298] S. Omar and B. J. van Wees, “Graphene-WS_2 heterostructures for tunable spin injection and spin transport”, Phys. Rev. B **95**, 081404 (2017).

[299] T. Völkl et al., “Magnetotransport in heterostructures of transition metal dichalcogenides and graphene”, Phys. Rev. B **96**, 125405 (2017).

[300] L. A. Benitez et al., “Strongly anisotropic spin relaxation in graphene-transition metal dichalcogenide heterostructures at room temperature”, Nat. Phys. **14**, 303 (2018).

[301] K. Zollner and J. Fabian, “Single and bilayer graphene on the topological insulator Bi_2Se_3: Electronic and spin-orbit properties from first principles”, Phys. Rev. B **100**, 165141 (2019).

[302] P. Lazić, K. D. Belashchenko, and I. Zutic, “Effective gating and tunable magnetic proximity effects in two-dimensional heterostructures”, Phys. Rev. B **93**, 241401 (2016).

[303] Z. Wang et al., “Proximity-Induced Ferromagnetism in Graphene Revealed by the Anomalous Hall Effect”, Phys. Rev. Lett. **114**, 016603 (2015).

[304] J. B. S. Mendes et al., “Spin-Current to Charge-Current Conversion and Magnetoresistance in a Hybrid Structure of Graphene and Yttrium Iron Garnet”, Phys. Rev. Lett. **115**, 226601 (2015).

[305] A. G. Swartz et al., “Integration of the ferromagnetic insulator EuO onto graphene”, ACS Nano **6**, 10063 (2012).

[306] P. Wei et al., “Strong interfacial exchange field in the graphene/EuS heterostructure”, Nat. Mater. **15**, 711 (2016).

[307] H. Haugen, D. Huertas-Hernando, and A. Brataas, “Spin transport in proximity-induced ferromagnetic graphene”, Phys. Rev. B **77**, 115406 (2008).

[308] H. X. Yang et al., “Proximity Effects Induced in Graphene by Magnetic Insulators: First-Principles Calculations on Spin Filtering and Exchange-Splitting Gaps”, Phys. Rev. Lett. **110**, 046603 (2013).

[309] A. Hallal et al., “Tailoring magnetic insulator proximity effects in graphene: first-principles calculations”, 2D Mater. **4**, 025074 (2017).

[310] A. Dyrdal and J. Barnas, “Anomalous, spin, and valley Hall effects in graphene deposited on ferromagnetic substrates”, 2D Mater. **4**, 034003 (2017).

[311] K. Zollner, M. Gmitra, and J. Fabian, “Electrically tunable exchange splitting in bilayer graphene on monolayer $Cr_2X_2Te_6$ with X = Ge, Si, and Sn”, New J. Phys. **20**, 073007 (2018).

[312] N. Sivadas et al., “Magnetic ground state of semiconducting transition-metal trichalcogenide monolayers”, Phys. Rev. B **91**, 235425 (2015).

[313] B. L. Chittari et al., “Electronic and magnetic properties of single-layer MPX_3 metal phosphorous trichalcogenides”, Phys. Rev. B **94**, 184428 (2016).

[314] M. Cococcioni and S. de Gironcoli, “Linear response approach to the calculation of the effective interaction parameters in the LDA + U method”, Phys. Rev. B **71**, 035105 (2005).

[315] A. I. Liechtenstein, V. I. Anisimov, and J. Zaanen, “Density-functional theory and strong interactions: Orbital ordering in Mott-Hubbard insulators”, Phys. Rev. B **52**, R5467 (1995).

[316] Q. Pei et al., “Superior Electronic Structure in Two-Dimensional $MnPSe_3/MoS_2$ van der Waals Heterostructures”, Sci. Rep. **7**, 9504 (2017).

[317] Q. Pei et al., “Efficient band structure modulations in two-dimensional $MnPSe_3/CrSiTe_3$ van der Waals heterostructures”, Nanotechnology **29**, 214001 (2018).

[318] Q. Pei et al., “Tunable electronic structure and magnetic coupling in strained two-dimensional semiconductor $MnPSe_3$”, Front. Phys. **13**, 137105 (2018).

[319] A. Wiedenmann et al., “Neutron diffraction study of the layered compounds $MnPSe_3$ and $FePSe_3$”, Solid State Commun. **40**, 1067 (1981).

[320] V. Grasso and L. Silipigni, “Optical absorption and reflectivity study of the layered $MnPSe_3$ seleniophosphate”, J. Opt. Soc. Am. B **16**, 132 (1999).

[321] Y. Baskin and L. Meyer, “Lattice Constants of Graphite at Low Temperatures”, Phys. Rev. **100**, 544 (1955).

[322] Y. Cao et al., “Unconventional superconductivity in magic-angle graphene superlattices”, Nature **556**, 43 (2018).

[323] Y. Cao et al., “Correlated insulator behaviour at half-filling in magic-angle graphene superlattices”, Nature **556**, 80 (2018).

[324] E. McCann and M. Koshino, “The electronic properties of bilayer graphene”, Rep. Prog. Phys. **76**, 056503 (2013).

[325] E. McCann, “Asymmetry gap in the electronic band structure of bilayer graphene”, Phys. Rev. B **74**, 161403 (2006).

[326] H. Min et al., “Ab initio theory of gate induced gaps in graphene bilayers”, Phys. Rev. B **75**, 155115 (2007).

[327] A. Ramasubramaniam, D. Naveh, and E. Towe, “Tunable band gaps in bilayer graphene-BN heterostructures”, Nano Lett. **11**, 1070 (2011).

[328] Y. Zhang et al., “Direct observation of a widely tunable bandgap in bilayer graphene”, Nature **459**, 820 (2009).

[329] Z. Wang et al., “Strong interface-induced spin-orbit interaction in graphene on WS_2”, Nat. Commun. **6**, 8339 (2015).

[330] D. Zhong et al., “Layer-resolved magnetic proximity effect in van der Waals heterostructures”, Nat. Nanotechnol. **15**, 187 (2020).

[331] D. Ghazaryan et al., “Magnon-assisted tunnelling in van der Waals heterostructures based on $CrBr_3$”, Nat. Electron. **1**, 344 (2018).

[332] C. Safeer et al., “Room-temperature spin Hall effect in graphene/MoS_2 van der Waals heterostructures”, Nano Lett. **19**, 1074 (2019).

[333] N. Cortés et al., “Tunable Spin-Polarized Edge Currents in Proximitized Transition Metal Dichalcogenides”, Phys. Rev. Lett. **122**, 086401 (2019).

[334] Y. Guo et al., "Magnetic two-dimensional layered crystals meet with ferromagnetic semiconductors", InfoMat **2**, 639 (2020).

[335] J. Qi et al., "Giant and tunable valley degeneracy splitting in $MoTe_2$", Phys. Rev. B **92**, 121403 (2015).

[336] J. O. Island et al., "Spin–orbit-driven band inversion in bilayer graphene by the van der Waals proximity effect", Nature **571**, 85 (2019).

[337] J. Y. Khoo, A. F. Morpurgo, and L. Levitov, "On-Demand Spin-Orbit Interaction from Which-Layer Tunability in Bilayer Graphene", Nano Lett. **17**, 7003 (2017).

[338] S. L. Tomarken et al., "Electronic Compressibility of Magic-Angle Graphene Superlattices", Phys. Rev. Lett. **123**, 046601 (2019).

[339] P. Michetti, P. Recher, and G. Iannaccone, "Electric field control of spin rotation in bilayer graphene", Nano Lett. **10**, 4463 (2010).

[340] C. Cardoso et al., "Van der Waals Spin Valves", Phys. Rev. Lett. **121**, 067701 (2018).

[341] V. Carteaux et al., "Crystallographic, magnetic and electronic structures of a new layered ferromagnetic compound $Cr_2Ge_2Te_6$", J. Phys.: Condens. Mat. **7**, 69 (1995).

[342] P. Michetti and P. Recher, "Spintronics devices from bilayer graphene in contact to ferromagnetic insulators", Phys. Rev. B **84**, 125438 (2011).

[343] K. Jatiyanon, I.-M. Tang, and B. Soodchomshom, "Perfect spin filtering controlled by an electric field in a bilayer graphene junction: Effect of layer-dependent exchange energy", Chin. Phys. B **25**, 078104 (2016).

[344] Y. Yu, Q. Liang, and J. Dong, "Controllable spin filter composed of ferromagnetic AB-stacking bilayer graphenes", Phys. Lett. A **375**, 2858 (2011).

[345] Z. Rashidian et al., "Conductance and Fano factor in normal/ferromagnetic/normal bilayer graphene junction.", J. Phys.: Cond. Mat. **26**, 255302 (2014).

[346] W. J. Schutte, J. L. De Boer, and F. Jellinek, "Crystal structures of tungsten disulfide and diselenide", J. Solid State Chem. **70**, 207 (1987).

[347] A. Chernikov et al., "Exciton Binding Energy and Nonhydrogenic Rydberg Series in Monolayer WS_2", Phys. Rev. Lett. **113**, 076802 (2014).

[348] M. Gibertini et al., "Spin-resolved optical conductivity of two-dimensional group-VIB transition-metal dichalcogenides", Phys. Rev. B **90**, 245411 (2014).

[349] Q. H. Wang et al., "Electronics and optoelectronics of two-dimensional transition metal dichalcogenides", Nat. Nanotechnol. **7**, 699 (2012).

[350] J. R. Schaibley et al., "Valleytronics in 2D materials", Nat. Rev. Mater. **1**, 16055 (2016).

[351] F. Langer et al., "Lightwave valleytronics in a monolayer of tungsten diselenide", Nature **557**, 76 (2018).

[352] D. Zhong et al., "Van der Waals engineering of ferromagnetic semiconductor heterostructures for spin and valleytronics", Sci. Adv. **3**, e1603113 (2017).

[353] D. Xiao et al., "Coupled Spin and Valley Physics in Monolayers of MoS_2 and Other Group-VI Dichalcogenides", Phys. Rev. Lett. **108**, 196802 (2012).

[354] E. Blundo et al., “Evidence of the direct-to-indirect band gap transition in strained two-dimensional WS_2, MoS_2, and WSe_2”, Phys. Rev. Research **2**, 012024 (2020).

[355] K. He et al., “Experimental demonstration of continuous electronic structure tuning via strain in atomically thin MoS_2”, Nano Lett. **13**, 2931 (2013).

[356] H. J. Conley et al., “Bandgap engineering of strained monolayer and bilayer MoS_2”, Nano Lett. **13**, 3626 (2013).

[357] G. Plechinger et al., “Control of biaxial strain in single-layer molybdenite using local thermal expansion of the substrate”, 2D Mater. **2**, 015006 (2015).

[358] J. Ji et al., “Strain-modulated excitonic gaps in mono- and bilayer $MoSe_2$”, Chin. Phys. B **25**, 077802 (2016).

[359] R. Schmidt et al., “Reversible uniaxial strain tuning in atomically thin WSe_2”, 2D Mater. **3**, 21011 (2016).

[360] D. Lloyd et al., “Band Gap Engineering with Ultralarge Biaxial Strains in Suspended Monolayer MoS_2”, Nano Lett. **16**, 5836 (2016).

[361] O. B. Aslan, M. Deng, and T. F. Heinz, “Strain tuning of excitons in monolayer WSe_2”, Phys. Rev. B **98**, 115308 (2018).

[362] O. B. Aslan et al., “Probing the Optical Properties and Strain-Tuning of Ultrathin $Mo_{1-x}W_xTe_2$”, Nano Lett. **18**, 2485 (2018).

[363] R. Frisenda et al., “Biaxial strain tuning of the optical properties of single-layer transition metal dichalcogenides”, npj 2D Mater. Appl. **1**, 10 (2017).

[364] P. Gant et al., “A strain tunable single-layer MoS_2 photodetector”, Mater. Today **27**, 8 (2019).

[365] C. Lee et al., “Measurement of the elastic properties and intrinsic strength of monolayer graphene”, Science **321**, 385 (2008).

[366] C. Si, Z. Sun, and F. Liu, “Strain engineering of graphene: a review”, Nanoscale **8**, 3207 (2016).

[367] L. Webster and J.-A. Yan, “Strain-tunable magnetic anisotropy in monolayer $CrCl_3$, $CrBr_3$, and CrI_3”, Phys. Rev. B **98**, 144411 (2018).

[368] A. Castellanos-Gomez et al., “Local strain engineering in atomically thin MoS_2”, Nano Lett. **13**, 5361 (2013).

[369] S. Kumar, A. Kaczmarczyk, and B. D. Gerardot, “Strain-induced spatial and spectral isolation of quantum emitters in mono-and bilayer WSe_2”, Nano Lett. **15**, 7567 (2015).

[370] A. Branny et al., “Discrete quantum dot like emitters in monolayer $MoSe_2$: Spatial mapping, magneto-optics, and charge tuning”, Appl. Phys. Lett. **108**, 142101 (2016).

[371] N. V. Proscia et al., “Near-deterministic activation of room-temperature quantum emitters in hexagonal boron nitride”, Optica **5**, 1128 (2018).

[372] H. Ochoa and R. Roldán, “Spin-orbit-mediated spin relaxation in monolayer MoS_2”, Phys. Rev. B **87**, 245421 (2013).

[373] K. Zollner, P. E. Faria Junior, and J. Fabian, "Giant proximity exchange and valley splitting in transition metal dichalcogenide/*h*BN/(Co, Ni) heterostructures", Phys. Rev. B **101**, 085112 (2020).

[374] K. Zollner, P. E. Faria Junior, and J. Fabian, "Proximity exchange effects in $MoSe_2$ and WSe_2 heterostructures with CrI_3: Twist angle, layer, and gate dependence", Phys. Rev. B **100**, 085128 (2019).

[375] N. Wakabayashi, H. G. Smith, and R. M. Nicklow, "Lattice dynamics of hexagonal MoS_2 studied by neutron scattering", Phys. Rev. B **12**, 659 (1975).

[376] P. B. James and M. T. Lavik, "The crystal structure of $MoSe_2$", Acta Cryst. **16**, 1183 (1963).

[377] A. Kormányos et al., "Spin-Orbit Coupling, Quantum Dots, and Qubits in Monolayer Transition Metal Dichalcogenides", Phys. Rev. X **4**, 011034 (2014).

[378] K. Kosmider, J. W. González, and J. Fernández-Rossier, "Large spin splitting in the conduction band of transition metal dichalcogenide monolayers", Phys. Rev. B **88**, 245436 (2013).

[379] E. Cappelluti et al., "Tight-binding model and direct-gap/indirect-gap transition in single-layer and multilayer MoS_2", Phys. Rev. B **88**, 075409 (2013).

[380] G.-B. Liu et al., "Three-band tight-binding model for monolayers of group-VIB transition metal dichalcogenides", Phys. Rev. B **88**, 085433 (2013).

[381] C.-H. Chang et al., "Orbital analysis of electronic structure and phonon dispersion in MoS_2, $MoSe_2$, WS_2, and WSe_2 monolayers under strain", Phys. Rev. B **88**, 195420 (2013).

[382] L. Wang, A. Kutana, and B. I. Yakobson, "Many-body and spin-orbit effects on direct-indirect band gap transition of strained monolayer MoS_2 and WS_2", Ann. Phys. **526**, L7 (2014).

[383] P. Johari and V. B. Shenoy, "Tuning the Electronic Properties of Semiconducting Transition Metal Dichalcogenides by Applying Mechanical Strains", ACS Nano **6**, 5449 (2012).

[384] D. Muoi et al., "Electronic properties of WS_2 and WSe_2 monolayers with biaxial strain: A first-principles study", Chem. Phys. **519**, 69 (2019).

[385] G. H. Ahn et al., "Strain-engineered growth of two-dimensional material", Nat. Commun. **8**, 608 (2017).

[386] K. Zollner, P. E. F. Junior, and J. Fabian, "Strain-tunable orbital, spin-orbit, and optical properties of monolayer transition-metal dichalcogenides", Phys. Rev. B **100**, 195126 (2019).

[387] J. P. Perdew et al., "Restoring the Density-Gradient Expansion for Exchange in Solids and Surfaces", Phys. Rev. Lett. **100**, 136406 (2008).

[388] I. Niehues et al., "Strain Control of Exciton–Phonon Coupling in Atomically Thin Semiconductors", Nano Lett. **18**, 1751 (2018).

[389] M. Feierabend et al., "Impact of strain on the optical fingerprint of monolayer transition-metal dichalcogenides", Phys. Rev. B **96**, 045425 (2017).

[390] S. Aas and C. Bulutay, "Strain dependence of photoluminescence and circular dichroism in transition metal dichalcogenides: a k.p analysis", Opt. Express **26**, 28672 (2018).

[391] J. Yao and G. Yang, "2D group 6 transition metal dichalcogenides toward wearable electronics and optoelectronics", J. Appl. Phys. **127**, 030902 (2020).

[392] S. Bertolazzi, J. Brivio, and A. Kis, "Stretching and breaking of ultrathin MoS_2", ACS Nano **5**, 9703 (2011).

[393] S. L. Chuang, *Physics of optoelectronic devices* (John Wiley, New York, 1995).

[394] H. Haug and S. W. Koch, *Quantum Theory of the Optical and Electronic Properties of Semiconductors: Fifth Edition* (World Scientific Publishing Company, 2009).

[395] D. Y. Qiu, F. H. da Jornada, and S. G. Louie, "Optical Spectrum of MoS_2: Many-Body Effects and Diversity of Exciton States", Phys. Rev. Lett. **111**, 216805 (2013).

[396] G. Wang et al., "Colloquium: Excitons in atomically thin transition metal dichalcogenides", Rev. Mod. Phys. **90**, 021001 (2018).

[397] F. Bechstedt, *Many-Body Approach to Electronic Excitations*, Vol. 181 (Springer, Berlin, Heidelberg, 2016).

[398] S. Ahmed and J. Yi, "Two-Dimensional Transition Metal Dichalcogenides and Their Charge Carrier Mobilities in Field-Effect Transistors", Nano-Micro Lett. **9**, 50 (2017).

[399] Y. Ye et al., "Electrical generation and control of the valley carriers in a monolayer transition metal dichalcogenide", Nat. Nanotechnol. **11**, 598 (2016).

[400] C. Robert et al., "Exciton radiative lifetime in transition metal dichalcogenide monolayers", Phys. Rev. B **93**, 205423 (2016).

[401] P. Nagler et al., "Giant magnetic splitting inducing near-unity valley polarization in van der Waals heterostructures", Nat. Commun. **8**, 1551 (2017).

[402] P. Rivera et al., "Observation of long-lived interlayer excitons in monolayer $MoSe_2$–WSe_2 heterostructures", Nat. Commun. **6**, 6242 (2015).

[403] A. Srivastava et al., "Valley Zeeman effect in elementary optical excitations of monolayer WSe_2", Nat. Phys. **11**, 141 (2015).

[404] G. Aivazian et al., "Magnetic control of valley pseudospin in monolayer WSe_2", Nat. Phys. **11**, 148 (2015).

[405] Y. Li et al., "Valley Splitting and Polarization by the Zeeman Effect in Monolayer $MoSe_2$", Phys. Rev. Lett. **113**, 266804 (2014).

[406] D. MacNeill et al., "Breaking of Valley Degeneracy by Magnetic Field in Monolayer $MoSe_2$", Phys. Rev. Lett. **114**, 037401 (2015).

[407] Y. Ji et al., "Spin splitting and p-/n-type doping of two-dimensional $WSe_2/BiIrO_3(111)$ heterostructures", Phys. Chem. Chem. Phys. **20**, 6100 (2018).

[408] N. Li et al., "Large valley polarization in monolayer $MoTe_2$ on a magnetic substrate", Phys. Chem. Chem. Phys. **20**, 3805 (2018).

[409] Q. Zhang et al., "Large Spin-Valley Polarization in Monolayer $MoTe_2$ on Top of EuO(111)", Adv. Mater. **28**, 959 (2016).

[410] L. Xu et al., "Large valley splitting in monolayer $\mathbf{WS_2}$ by proximity coupling to an insulating antiferromagnetic substrate", Phys. Rev. B **97**, 041405 (2018).

[411] C. Zhao et al., "Enhanced valley splitting in monolayer WSe_2 due to magnetic exchange field", Nat. Nanotechnol. **12**, 757 (2017).

[412] K. L. Seyler et al., "Valley Manipulation by Optically Tuning the Magnetic Proximity Effect in WSe_2/CrI_3 Heterostructures", Nano Lett. **18**, 3823 (2018).

[413] B. Peng et al., "Valley Polarization of Trions and Magnetoresistance in Heterostructures of MoS_2 and Yttrium Iron Garnet", ACS Nano **11**, 12257 (2017).

[414] Z. Zhang et al., "Valley splitting in the van der Waals heterostructure WSe_2/CrI_3: The role of atom superposition", Phys. Rev. B **99**, 115441 (2019).

[415] H. Wang, V. Eyert, and U. Schwingenschlögl, "Electronic structure and magnetic ordering of the semiconducting chromium trihalides $CrlC_3$, $CrBr_3$, and CrI_3 ", J. Phys.: Cond. Mat. **23**, 116003 (2011).

[416] W. J. de Haas, B. H. Schultz, and J. Koolhaas, "Further measurements of the magnetic properties of some salts of the iron group at low temperatures", Physica **7**, 57 (1940).

[417] W. N. Hansen, "Some Magnetic Properties of the Chromium (III) Halides at 4.2°K", J. Appl. Phys. **30**, S304 (1959).

[418] J. F. Dillon and C. E. Olson, "Magnetization, Resonance, and Optical Properties of the Ferromagnet CrI_3", J. Appl. Phys. **36**, 1259 (1965).

[419] P. Jiang et al., "Stacking tunable interlayer magnetism in bilayer CrI_3", Phys. Rev. B **99**, 144401 (2019).

[420] W.-B. Zhang et al., "Robust intrinsic ferromagnetism and half semiconductivity in stable two-dimensional single-layer chromium trihalides", J. Mater. Chem. C **3**, 12457 (2015).

[421] J. Liu et al., "Exfoliating biocompatible ferromagnetic Cr-trihalide monolayers", Phys. Chem. Chem. Phys. **18**, 8777 (2016).

[422] S. Jiang, J. Shan, and K. F. Mak, "Electric-field switching of two-dimensional van der Waals magnets", Nat. Mater. **17**, 406 (2018).

[423] D. Soriano, C. Cardoso, and J. Fernández-Rossier, "Interplay between interlayer exchange and stacking in CrI_3 bilayers", Solid State Commun. **299**, 113662 (2019).

[424] N. Sivadas et al., "Stacking-Dependent Magnetism in Bilayer CrI_3", Nano Lett. **18**, 7658 (2018).

[425] L. Ciorciaro et al., "Observation of Magnetic Proximity Effect Using Resonant Optical Spectroscopy of an Electrically Tunable $MoSe_2/CrBr_3$ Heterostructure", Phys. Rev. Lett. **124**, 197401 (2020).

[426] T. P. Lyons et al., "Interplay between spin proximity effect and charge-dependent exciton dynamics in $MoSe_2$ / $CrBr_3$ van der Waals heterostructures", Nature communications **11**, 6021 (2020).

[427] T. Hu et al., “Manipulation of valley pseudospin in WSe_2/CrI_3 heterostructures by the magnetic proximity effect”, Phys. Rev. B **101**, 125401 (2020).

[428] A. David et al., “Induced spin-orbit coupling in twisted graphene–transition metal dichalcogenide heterobilayers: Twistronics meets spintronics”, Phys. Rev. B **100**, 085412 (2019).

[429] P. Jiang et al., “Spin direction controlled electronic band structure in two dimensional ferromagnetic CrI_3”, Nano Lett. **18**, 3844 (2018).

[430] M. Rohlfing and S. G. Louie, “Electron-hole excitations and optical spectra from first principles”, Phys. Rev. B **62**, 4927 (2000).

[431] B. Scharf et al., “Magnetic Proximity Effects in Transition-Metal Dichalcogenides: Converting Excitons”, Phys. Rev. Lett. **119**, 127403 (2017).

[432] D. Tedeschi et al., “Unusual spin properties of InP wurtzite nanowires revealed by Zeeman splitting spectroscopy”, Phys. Rev. B **99**, 161204 (2019).

[433] P. E. Faria Junior et al., “$k.p$ theory for phosphorene: Effective g-factors, Landau levels, and excitons”, Phys. Rev. B **100**, 115203 (2019).

[434] N. S. Rytova, “The screened potential of a point charge in a thin film”, Mosc. Univ. Phys. Bull. **3**, 18 (1967).

[435] L. Keldysh, “Coulomb interaction in thin semiconductor and semimetal films”, Sov. J. Exp. Theo. Phys. Lett. **29**, 658 (1979).

[436] P. Cudazzo, I. V. Tokatly, and A. Rubio, “Dielectric screening in two-dimensional insulators: Implications for excitonic and impurity states in graphane”, Phys. Rev. B **84**, 085406 (2011).

[437] T. C. Berkelbach, M. S. Hybertsen, and D. R. Reichman, “Theory of neutral and charged excitons in monolayer transition metal dichalcogenides”, Phys. Rev. B **88**, 045318 (2013).

[438] C. Lin et al., “Enhanced Valley Splitting of Transition-Metal Dichalcogenide by Vacancies in Robust Ferromagnetic Insulating Chromium Trihalides”, ACS Appl. Mater. Interfaces **11**, 18858 (2019).

[439] L. Webster, L. Liang, and J. A. Yan, “Distinct spin-lattice and spin-phonon interactions in monolayer magnetic CrI_3”, Phys. Chem. Chem. Phys. **20**, 23546 (2018).

[440] J. L. Lado and J. Fernández-Rossier, “On the origin of magnetic anisotropy in two dimensional CrI_3”, 2D Mater. **4**, 035002 (2017).

[441] W. Jiang et al., “First-principles calculations of magnetic edge states in zigzag CrI_3 nanoribbons”, Phys. Lett. A **383**, 754 (2019).

[442] V. Kumar Gudelli and G.-Y. Guo, “Magnetism and magneto-optical effects in bulk and few-layer CrI_3: a theoretical GGA+U study”, New J. Phys. **21**, 053012 (2019).

[443] A. K. Behera, S. Chowdhury, and S. R. Das, “Magnetic skyrmions in atomic thin CrI_3 monolayer”, Appl. Phys. Lett. **114**, 232402 (2019).

[444] S. Jiang et al., “Controlling magnetism in 2D CrI_3 by electrostatic doping”, Nat. Nanotechnol. **13**, 549 (2018).

[445] B. Huang et al., “Electrical control of 2D magnetism in bilayer CrI_3”, Nat. Nanotechnol. **13**, 544 (2018).

[446] D. R. Klein et al., “Probing magnetism in 2D van der Waals crystalline insulators via electron tunneling”, Science **360**, 1218 (2018).

[447] V. Baltz et al., “Antiferromagnetic spintronics”, Rev. Mod. Phys. **90**, 015005 (2018).

[448] T. Jungwirth et al., “Antiferromagnetic spintronics”, Nat. Nanotechnol. **11**, 231 (2016).

[449] D. Shcherbakov et al., “Raman spectroscopy, photocatalytic degradation, and stabilization of atomically thin chromium tri-iodide”, Nano Lett. **18**, 4214 (2018).

[450] M. Ge et al., “Interface depended electronic and magnetic properties of vertical CrI_3/WSe_2 heterostructures”, RSC Adv. **9**, 14766 (2019).

[451] J. Xie et al., “Electric field mediated large valley splitting in the van der Waals heterostructure WSe_2/CrI_3”, Jpn. J. Appl. Phys. **58**, 010906 (2018).

[452] M. Wu et al., “Physical origin of giant excitonic and magneto-optical responses in two-dimensional ferromagnetic insulators”, Nat. Commun. **10**, 2371 (2019).

[453] D. Lancon et al., “Magnetic exchange parameters and anisotropy of the quasi-two-dimensional antiferromagnet $NiPS_3$”, Phys. Rev. B **98**, 134414 (2018).

[454] D. Lancon et al., “Magnetic structure and magnon dynamics of the quasi-two-dimensional antiferromagnet $FePS_3$”, Phys. Rev. B **94**, 214407 (2016).

[455] R. R. Rao and A. Raychaudhuri, “Magnetic studies of a mixed antiferromagnetic system $Fe_{1-x}Ni_xPS_3$”, J. Phys. Chem. Solids **53**, 577 (1992).

[456] G. L. Flem et al., “Magnetic interactions in the layer compounds MPX_3 (M = Mn, Fe, Ni; X = S, Se)”, J. Phys. Chem. Solids **43**, 455 (1982).

[457] Y. Li et al., “Topological superconductivity in Ni-based transition metal trichalcogenides”, Phys. Rev. B **100**, 214513 (2019).

[458] J.-U. Lee et al., “Ising-Type Magnetic Ordering in Atomically Thin $FePS_3$”, Nano Lett. **16**, 7433 (2016).

[459] W. Klingen, G. Eulenberger, and H. Hahn, “ Über Hexathio- und Hexaselenohypodiphosphate vom Typ $M_2P_2X_6$”, Naturwissenschaften **55**, 229 (1968).

[460] B. L. Chittari et al., “Carrier- and strain-tunable intrinsic magnetism in two-dimensional MAX_3 transition metal chalcogenides”, Phys. Rev. B **101**, 085415 (2020).

[461] S. Kang et al., “Coherent many-body exciton in van der Waals antiferromagnet $NiPS_3$”, Nature **n/a**, n/a (2020).

[462] K. Yang et al., “VI_3: A two-dimensional Ising ferromagnet”, Phys. Rev. B **101**, 100402 (2020).

[463] L.-Z. Zhang et al., “Tunable Curie temperature in layered ferromagnetic $Cr_{5+x}Te_8$ single crystals”, APL Mater. **8**, 031101 (2020).

[464] Y. Deng et al., “Gate-tunable room-temperature ferromagnetism in two-dimensional Fe_3GeTe_2”, Nature **563**, 94 (2018).

[465] A. May et al., "Ferromagnetism Near Room Temperature in the Cleavable van der Waals Crystal Fe_5GeTe_2", ACS Nano **13**, 4436 (2019).

[466] A. F. May, C. A. Bridges, and M. A. McGuire, "Physical properties and thermal stability of $Fe_{5-x}GeTe_2$ single crystals", Phys. Rev. Materials **3**, 104401 (2019).

[467] J. Stahl, E. Shlaen, and D. Johrendt, "The van der Waals Ferromagnets $Fe_{5-\delta}GeTe_2$ and $Fe_{5-\delta-x}Ni_xGeTe_2$ - Crystal Structure, Stacking Faults, and Magnetic Properties", Z. anorg. allg. Chem. **644**, 1923–1929 (2018).

[468] M. Bonilla et al., "Strong room-temperature ferromagnetism in VSe_2 monolayers on van der Waals substrates", Nat. Nanotechnol. **13**, 289 (2018).

[469] D. J. O'Hara et al., "Room Temperature Intrinsic Ferromagnetism in Epitaxial Manganese Selenide Films in the Monolayer Limit", Nano Lett. **18**, 3125 (2018).

[470] M. Hu et al., "All-Solid-State Flexible Fiber-Based MXene Supercapacitors", Adv. Mater. Technol. **2**, 1700143 (2017).

[471] D. Kecik et al., "Layer- and strain-dependent optoelectronic properties of hexagonal AlN", Phys. Rev. B **92**, 165408 (2015).

[472] C. Bacaksiz et al., "Hexagonal AlN: Dimensional-crossover-driven band-gap transition", Phys. Rev. B **91**, 085430 (2015).

[473] H. L. Zhuang, A. K. Singh, and R. G. Hennig, "Computational discovery of single-layer III-V materials", Phys. Rev. B **87**, 165415 (2013).

[474] H. Sahin et al., "Monolayer honeycomb structures of group-IV elements and III-V binary compounds: First-principles calculations", Phys. Rev. B **80**, 155453 (2009).

[475] D. Vahedi Fakhrabad, N. Shahtahmasebi, and M. Ashhadi, "Optical excitations and quasiparticle energies in the AlN monolayer honeycomb structure", Superlattices Microstruct. **79**, 38 (2015).

[476] Q. Peng et al., "Mechanical stabilities and properties of graphene-like aluminum nitride predicted from first-principles calculations", RSC Adv. **3**, 7083 (2013).

[477] C. L. Freeman et al., "Graphitic Nanofilms as Precursors to Wurtzite Films: Theory", Phys. Rev. Lett. **96**, 066102 (2006).

[478] J. Liao et al., "Design of High-Efficiency Visible-Light Photocatalysts for Water Splitting: MoS_2/AlN(GaN) Heterostructures", J. Phys. Chem. C **118**, 17594 (2014).

[479] K. Ren et al., "Strain-enhanced properties of van der Waals heterostructure based on blue phosphorus and g-GaN as a visible-light-driven photocatalyst for water splitting", RSC Adv. **9**, 4816 (2019).

[480] M. S. Prete et al., "Giant excitonic absorption and emission in two-dimensional group-III nitrides", Sci. Rep. **10**, 10719 (2020).

[481] D. Kecik et al., "Fundamentals, progress, and future directions of nitride-based semiconductors and their composites in two-dimensional limit: A first-principles perspective to recent synthesis", Appl. Phys. Rev. **5**, 011105 (2018).

[482] A. Onen et al., "In-plane commensurate GaN/AlN junctions: Single-layer composite structures, single and multiple quantum wells and quantum dots", Phys. Rev. B **95**, 155435 (2017).

[483] M. S. Prete et al., "Tunable electronic properties of two-dimensional nitrides for light harvesting heterostructures", Appl. Phys. Lett. **110**, 012103 (2017).

[484] A. Onen et al., "GaN: From three- to two-dimensional single-layer crystal and its multilayer van der Waals solids", Phys. Rev. B **93**, 085431 (2016).

[485] F. Ferreira et al., "Excitons in hexagonal boron nitride single-layer: a new platform for polaritonics in the ultraviolet", J. Opt. Soc. Am. B **36**, 674111 (2019).

[486] M. Kurpas et al., "Spin-orbit coupling in elemental two-dimensional materials", Phys. Rev. B **100**, 125422 (2019).

[487] J.-K. Lyu et al., "Stanene: A Promising Material for New Electronic and Spintronic Applications", Ann. Phys. **531**, 1900017 (2019).

[488] S. K. Sahoo and K.-H. Wei, "A Perspective on Recent Advances in 2D Stanene Nanosheets", Adv. Mater. Interfaces **6**, 1900752 (2019).

[489] J. Zhao et al., "Rise of silicene: A competitive 2D material", Prog. Mater. Sci. **83**, 24 (2016).

[490] A. Acun et al., "Germanene: the germanium analogue of graphene", J. Phys.: Cond. Mat. **27**, 443002 (2015).

[491] M. Ezawa, "Electronic and Topological Properties of Silicene, Germanene and Stanene", in *Silicene: Prediction, Synthesis, Application* (Springer International Publishing, Cham, 2018), p. 43.

[492] T. Hartman and Z. Sofer, "Beyond Graphene: Chemistry of Group 14 Graphene Analogues: Silicene, Germanene, and Stanene", ACS Nano **13**, 8566 (2019).

[493] B.-M. Jun et al., "Review of MXenes as new nanomaterials for energy storage/delivery and selected environmental applications", Nano Res. **12**, 471 (2019).

[494] Q. Jiang et al., "Review of MXene electrochemical microsupercapacitors", Energy Storage Mater. **27**, 78 (2020).

[495] N. Mounet et al., "Two-dimensional materials from high-throughput computational exfoliation of experimentally known compounds", Nat. Nanotechnol. **13**, 246 (2018).

[496] A. Kokalj, "XCrySDen—a new program for displaying crystalline structures and electron densities", J. Mol. Graph. Model. **17**, 176 (1999).

[497] K. Momma and F. Izumi, "VESTA3 for three-dimensional visualization of crystal, volumetric and morphology data", J. Appl. Cryst. **44**, 1272 (2011).

[498] T. Frank, "Ab initio studies of extrinsic spin-orbit coupling effects in graphene and quantum Monte Carlo simulations of phosphorene", PhD thesis (University of Regensburg, 2019).

[499] S. Cottenier, *Density Functional Theory and the family of (L)APW-methods: a step-by-step introduction* (2002).

[500] P. Giannozzi et al., "Advanced capabilities for materials modelling with Quantum ESPRESSO", J. Phys.: Cond. Mat. **29**, 465901 (2017).

List of Publications

1. **Klaus Zollner**, Aron W. Cummings, Stephan Roche, and Jaroslav Fabian, `arXiv:2011.14588 (2020)` "Graphene on two-dimensional hexagonal BN, AlN, and GaN: Electronic, spin-orbit, and spin relaxation properties"
2. **Klaus Zollner**, Martin Gmitra, and Jaroslav Fabian, `Physical Review Letters` **`125,`** `196402 (2020),` "Swapping Exchange and Spin-Orbit Coupling in 2D van der Waals Heterostructures"
3. Dietmar Czubak, Samuel Gaucher, Lars Oppermann, Jens Herfort, **Klaus Zollner**, Jaroslav Fabian, Holger T. Grahn, and Manfred Ramsteiner `Physical Review Materials` **`4,`** `104415 (2020)` "Electronic and magnetic properties of α-$FeGe_2$ films embedded in vertical spin valve devices"
4. **Klaus Zollner**, Marko D. Petrović, Kapildeb Dolui, Petr Plecháč, Branislav K. Nikolić, and Jaroslav Fabian, `Physical Review Research` **`2,`** `043057 (2020),` "Scattering-induced and highly tunable by gate damping-like spin-orbit torque in graphene doubly proximitized by two-dimensional magnet $Cr_2Ge_2Te_6$ and monolayer WS_2"
5. **Klaus Zollner** and Jaroslav Fabian, `Physica Status Solidi (b)` **`258,`** `2000081 (2020),` "Heterostructures of graphene and topological insulators Bi_2Se_3, Bi_2Te_3, and Sb_2Te_3"
6. Kapildeb Dolui, Marko D. Petrović, **Klaus Zollner**, Petr Plecháč, Jaroslav Fabian, and Branislav K. Nikolić, `Nano Letters` **`20,`** `2288 (2020),` "Proximity spin-orbit torque on a two-dimensional magnet within van der Waals heterostructure: Current-driven antiferromagnet-to-ferromagnet reversible nonequilibrium phase transition in bilayer CrI_3"
7. Petra Högl, Tobias Frank, **Klaus Zollner**, Denis Kochan, Martin Gmitra, and Jaroslav Fabian, `Physical Review Letters` **`124,`** `136403 (2020),` "Quantum Anomalous Hall Effects in Graphene from Proximity-Induced Uniform and Staggered Spin-Orbit and Exchange Coupling"

8. **Klaus Zollner**, Paulo E. Faria Junior, and Jaroslav Fabian,
   `Physical Review B` **`101,`** `085112 (2020),`
   "Giant proximity exchange and valley splitting in transition-metal dichalcogenide/hBN/(Co, Ni) heterostructures"
9. **Klaus Zollner**, Paulo E. Faria Junior, and Jaroslav Fabian,
   `Physical Review B` **`100,`** `195126 (2019),`
   "Strain tunable orbital, spin-orbit, and optical properties of monolayer transition-metal dichalcogenides"
10. **Klaus Zollner** and Jaroslav Fabian,
   `Physical Review B` **`100,`** `165141 (2019),`
   "Single- and bilayer graphene on the topological insulator Bi_2Se_3: Electronic and spin-orbit properties from first principles"
11. Bogdan Karpiak, Aron W. Cummings, **Klaus Zollner**, Marc Vila, Dmitrii Khokhriakov, Anamul Md. Hoque, André Dankert, Peter Svedlindh, Jaroslav Fabian, Stephan Roche, and Saroj P. Dash,
   `2D Materials` **`7,`** `015026 (2019),`
   "Magnetic proximity in a van der Waals heterostructure of magnetic insulator and graphene"
12. **Klaus Zollner**, Paulo E. Faria Junior, and Jaroslav Fabian,
   `Physical Review B` **`100,`** `085128 (2019),`
   "Proximity exchange effects in $MoSe_2$ and WSe_2 on CrI_3: Twist angle, layer, and gate dependence"
13. **Klaus Zollner**, Martin Gmitra, and Jaroslav Fabian,
   `Physical Review B` **`99,`** `125151 (2019),`
   "Heterostructures of graphene and hBN: Electronic, spin-orbit, and spin relaxation properties from first principles"
14. **Klaus Zollner**, Martin Gmitra, and Jaroslav Fabian,
   `New Journal of Physics` **`20,`** `073007 (2018),`
   "Electrically tunable exchange splitting in bilayer graphene on monolayer $Cr_2X_2Te_6$ with X = Ge, Si, and Sn"
15. **Klaus Zollner**, Tobias Frank, Martin Gmitra, and Jaroslav Fabian,
   `Physical Review B` **`94,`** `155441 (2016),`
   "Theory of proximity-induced exchange coupling in graphene on hBN/(Co, Ni)"
16. **Klaus Zollner**, Tobias Frank, Susanne Irmer, Denis Kochan, Martin Gmitra, and Jaroslav Fabian,
   `Physical Review B` **`93,`** `045423 (2016),`
   "Spin-orbit coupling in methyl functionalized graphene"

Acknowledgements

At the end of this thesis, I would like to thank all people that supported me during my PhD. I want to thank Prof. Jaroslav Fabian for giving me the opportunity to work in his research group and for his excellent scientific guidance. Many thanks also to my colleagues Andreas Costa, Paulo E. Faria Junior, and Tobias Frank for proofreading this thesis.

I also want to thank the research groups conducted by Saroj P. Dash (Chalmers University of Technology), Stephan Roche (Catalan Institute of Nanoscience and Nanotechnology), Manfred Ramsteiner (Paul-Drude-Institut Berlin), and Branislav K. Nikolic (University of Delaware) for the excellent collaborations.

I acknowledge financial support through the German Research Foundation (Deutsche Forschungsgemeinschaft, DFG) through the priority program SPP 1666 (Topolgical Insulators) and the collaborative research center SFB 1277 (Emergent Relativistic Effects in Condensed Matter), as well as from the European Unions Horizon 2020 research and innovation program (Graphene Flagship).

Finally, I also want to thank my family, friends, and especially my wife. Their support and care helped me to stay focused during my studies.

Regensburg,

Zollner Klaus